Cellular Ionic Concentration Dynamics and Wave Propagation in Spatial Media

by

Michelle Louise Goodman

A thesis submitted in partial fulfilment of the requirements for the

Degree of Doctor of Philosophy in Mechanical Engineering at

The University of Canterbury

February 2018

Acknowledgement

"Ehara taku toa, he takitahi, he toa takitini"

"My success should not be bestowed onto me alone, as it was not individual success but success of a collective" Māori Whakataukī

First and foremost, I would like to show great appreciation and many thanks to my amazing team of supervisors: Professor Tim David, Associate Professor Rua Murray and Senior Lecturer Dr. Paul Docherty. In particular, I would like to thank my primary supervisor, Professor Tim David, for his leadership, guidance, outstanding knowledge and continual support. I would like to thank my co-supervisor, Associate Professor Rua Murray, for his in depth insights and reliability. Finally, I would like to show appreciation to my other co-supervisor, Senior Lecturer Dr. Paul Docherty, for his outstanding support throughout my studies, guidance and advice both technical and otherwise.

I would like to give thanks, love and appreciation to my supportive parents: Lois and Graham Goodman. I would not be who I am, what I am or where I am today without you. You can not be thanked enough. I would like to thank Denise Rowland, you are not just my sister but my team-mate, friend and editor. I want to thank my little sister Nicole Goodman for having my back without fail. I would also like to thank the rest of my extended whānau including my new brothers in law.

I would like to thank my partner and fellow researcher Tim van Ginkel for standing by me especially through my late nights and helping to edit my work. I would additionally like to thank my friends from all walks of life and my other fellow researchers, past and present. Your expertise and support did not go unnoticed: Dr. Katharina Dormanns, Dr. Jaijus Pallippadan Johny, Dr. Christine French, Dr. Elshin Mathias, Stewart Dowding, Allanah Kenny and Grace Strijbis.

Finally, I would like to thank the institutions, societies and funding bodies that supported my research: The University of Canterbury for The Ngata Centenary Doctoral Scholarship, Brain Research New Zealand (BRNZ) for their valued collaborations and PhD Top-Up Scholarship, The Royal Society of New Zealand for their RHT Bates Scholarship and the Health Research Society of Canterbury (HRSC) for the Rutherford Prize. Additionally, the Society for Industrial and Applied Mathematics (SIAM), the New Zealand Neurological Foundation, and the Te Punenga Grant from the office of the Assistant Vice-Chancellor Māori for conference travel related funding.

Abstract

In the context of cranial cellular modelling, mathematical techniques have been applied to model oscillations of concentration over time. Models were made for different cell types to match data and known chemical reactions within the cell over time. The ability to oscillate the concentration over time provides the necessary environment for waves of concentration to traverse across space and time. Whilst experimental procedures have advanced in recent years, there still exists a gap in knowledge that computational modelling attempts to fill.

Five Simplified Generic Oscillatory Cell Model/s (SGOCM) are described in detail: the Goldbeter model, the Dupont model, the Ermentrout model, the FitzHugh-Nagumo model and the Koenigsberger model. All of these models exhibit either steady state or oscillatory dynamics altered by a bifurcation parameter. They all exhibit periods of oscillation generally increasing alongside the bifurcation parameter towards at least one of the bifurcation points (labelled the lower bifurcation point). Each of these 5 microscale models were converted, via homogenisation, to a spatially orientated macroscale system and applied with a spatially varying stimulus. On the addition of Fickian Diffusion (FD) excursions of high concentration 'waves' were seen to propagate through space over time into the previously non-oscillatory low concentration region beyond the lower bifurcation point. These excursions were made the focus of this research.

A hypothesis was made indicating a link between the shape of the concentration oscillation of the variable being diffused over time ('Wave Shape') and its ability to produce excursions into the previously non-oscillatory region. It was theorised that a Front Heavy (FH) asymmetric profile was needed in order to produce excursions. This was further quantified via a mathematical derivation as the Front Heavy Score (FH-score) whereby a FH-score> 0 predicted excursions. This theory was then tested, and held true, for all the models and subsequently held true on three additional Toy models designed to produce specific desired outcomes. The ability to predict excursion allows for an aim to modify the single cell dynamics such that this wave movement would or would not occur in the surrounding cells.

Next, a tool was developed, known as the Excitability Profile (E-Profile) to compare across models. The E-Profile was used to view the dependence of the bifurcation parameter and an applied perturbation from the steady state value on the excitability of a system. The E-Profile was used to further understand the aforementioned models' spatio-temporal results on the addition of diffusion. This tool was then related to the depth of excursions on the spatio-temporal solutions via an Excitability Path (E-Path). This was then used to accurately predict either the diffusion coefficient (with a standard deviation of 1.8% from the true D) given a spatio-temporal solution of a known model or to predict the depth (to $\pm 1.1\%$ of the macroscale length) and maximum concentration over space of the excursions from the single cell dynamics and spatial stimulus profile alone.

Foreword

The content within this research has been broken up into 9 chapters. Chapters 1-2 are a literature review. Chapter 3 is a review, reproduction and comparison of existing cellular dynamics mathematical models. Chapters 4-5 combine techniques individually investigated with the previously defined mathematical models and finally Chapter 6 onwards contain entirely my own work, unless otherwise stated.

Chapter 1 includes an introduction to mammalian cells, cerebral cell modelling and the cerebral vasculature that supplies the cells in the brain with oxygenated blood and glucose. This chapter provides the surrounding context and the reasoning for this research. Chapter 2 provides a review of the important and necessary mathematical modelling techniques used within this research and provides the building blocks to be built upon.

Chapter 3 is a review, reproduction and comparison of existing mathematical models describing specified cellular dynamics. Whilst the mathematical models are not my work, the reproduction, additional analysis, review and comparison is my own work. Chapter 4, whilst short, is a necessary model adaptation for the later introduced component (Electro-diffusion) to be compared across more models.

Chapter 5 introduces the spatial context and, in particular, the time dependent spatial diffusion. This chapter applies previously defined diffusion, of cited

sources, to an emergent area of a spatially varying stimulus to all of the review models from Chapter 3.

In Chapter 6, I propose a hypothesis indicating a link between the shape of a wave and its ability to produce excursions into the previously non-oscillatory region. The hypothesis is then quantified (as the Front Heavy Score (FH-score)) and tested on three toy models I generated. In addition, it was also tested on all the reviewed models, to give the theory evidence and strength.

Chapter 7 introduces a tool I developed, the Excitability Profile (E-Profile), which allows further investigation of the aforementioned models. The tool provides understanding of the models' spatio-temporal results on the addition of diffusion. The E-Profile creates a relationship between the bifurcation parameter and its excitability to an applied perturbation from the steady state solution. This chapter then utilised the created tool (the E-Profile), and through a technique I developed, compares it to the depth of an excursion and formulates mathematical relationships not previously known.

Chapter 8 uses the created tool (the E-Profile) in addition to the newly developed relationships and backwardly applies them as prediction techniques (via the Excitability Path (E-Path)) in order to predict the diffusion coefficient, depth and concentration of the excursions seen in the spatio-temporal solutions.

Finally, Chapter 9 is a review of the work completed, its importance and relevance to cerebral cell understanding. Chapter 9 also includes possible future work.

Contents

List of Figures

List of Tables

Acronyms

$\bar{\iota}$	Wave Front Number
β	bifurcation parameter
1D	One Dimension
AC	astrocyte
BBB	Blood Brain Barrier
BH	Backwards Heavy
BRNZ	Brain Research New Zealand
Ca^{2+}	Calcium ion
CBF	Cerebral Blood Flow
CICP	Calcium Induced Calcium Pump
CICR	Calcium Induced Calcium Release
CNS	Central Nervous System
CSD	Cortical Spreading Depression
ER	Endoplasmic Reticulum
E	Excitability
E-Path	Excitability Path
E-Profile	Excitability Profile

ED	Electro-Diffusion
FD	Fickian Diffusion
FFT	Fast Fourier Transform
FH	Front Heavy
FH-score	Front Heavy Score
HRSC	Health Research Society of Canterbury
IP_3	Inositol trisphosphate
K^+	Potassium ion
mGluR	Metabotropic Glutamate Receptor
MOL	Method of Lines
N	Open Probability of the Potassium Channel
NVU	Neuro-Vascular Unit
ODE	Ordinary Differential Equation
PDE	Partial Differential Equation
PLC	Phospholipase C
SERCA-Pump	Sarco/Endoplasmic Reticulum $Ca^{2+}-$ATPase Pump
SGOCM	Simplified Generic Oscillatory Cell Model/s
SMC	Smooth Muscle Cell
SIAM	Society for Industrial and Applied Mathematics
SR	Sarcoplasmic Reticulum
TBI	Traumatic Brain Injury
TM1	Toy Model 1

TM2	Toy Model 2
TM3	Toy Model 3
V	Cellular Membrane Potential
VICR	Voltage Induced Calcium Release
VOCC	Voltage Operated Calcium Channel
Y	ionic calcium concentration in the intracellular store
Z	ionic calcium concentration in the cytosol

1 Introduction

1.1 Mammalian Brain

Throughout the ages, in depth understanding of the mammalian brain has eluded scientists. Early civilisations lacked adequate means to obtain the knowledge and as such their understanding of the inner workings of the brain were not accurate. Andreas Vesalius in the 1500s was one of the first to provide detailed drawings and anatomical features of the human brain (Scatliff and Johnston, 2014). Vesalius' research was the first to propose that the brain was made up of pairs of cranial nerves, each with a specialized function.

Thomas Willis in 1664 was the first to use the term 'Neurology' (in Greek) in his text 'Cerebri Anatome' (Donaldson, 2010). His research focused on the arterial circle, later famously known as the 'Circle of Willis', the structure of cerebral vessels that supply blood to the brain (Feindel, 1962). His research used the anatomy of the brain as a tool to 'investigate the nature of the soul'. Although his description of the anatomy of the brain remains important for contemporary neurological science, Willis's understanding of the brain was very different from that of modern scientific thought (O'Connor, 2003).

The next major advances in the understanding of cells came in the 18th century by Luigi Galvani. Galvani, through his experiments on frogs, gave birth to electro-physiology (Piccolino, 1998). His research noted the effect of electrical stimulants on, in particular, nerves and muscles. He was the first to provide evidence for the electrical nature of mysterious fluid involved in nerve conduction and muscle contraction.

Studies of the brain became more sophisticated after the invention of the microscope and identification techniques for human tissue. Nobel prize winners Santiago Ramón y Cajal and Camillo Golgi, developed and used staining techniques in the late 1890s to identify individual neurons and make hypothesis surrounding the neuron being the main functional unit of the brain. Their work included proving that each nerve cell is an independent entity and nerve synapses transfer nerve impulses from one cell to another (Biography.com, 2014).

There have been many Nobel prize winners in the field of Physiology or Medicine relating to the brain. A notable mention is Nobel prize winners (1963) Sir John Carew Eccles, Alan Lloyd Hodgkin and Andrew Fielding Huxley for "their discoveries concerning the ionic mechanisms involved in excitation and inhibition in the peripheral and central portions of the nerve cell membrane" (Raju, 1999). Their research developed the widely known 'Hodgkin-Huxley' cell model still built on today (Schwiening, 2012). Another notable mention is Nobel prize winners Erwin Neher and Bert Sakmann in 1991 for their discoveries concerning the function of single ion channels in cells. In particular, their patch clamping technique is widely used in cell biology today.

The twentieth century saw a rise in neuroscience and it became a distinct unified academic discipline. Francis O. Schmitt helped to found the Neurosciences Research Program in 1962 within the Biology Department at the Massachusetts

Institute of Technology. Neuroscience was noted as a combination of biology, chemistry, physics, and mathematics (Quarton et al., 1967).

55 years later it is of no surprise that neuroscience is still at the forefront of technology. Recent advances in the understanding of the mammalian brain are edging us closer to comprehending the inner workings of the human brain.

1.1.1 Anatomy and Histology

The human brain is comprised of three main components: brainstem, cerebellum, and cerebrum. The brainstem forms the connection between the brain and the spinal cord. It maintains vital control of the heart and lungs, and coordinates many important reflexes. The cerebellum, located behind the brainstem, is mainly concerned with the maintenance of posture, balance and the coordination of movement. The cerebrum, the largest mass of the brain, controls all other functions behind creating concious life. The cerebrum is divided into two masses: the left and right hemispheres.

The surface of the cerebrum, called the cortex, has a folded appearance with 2 main purposes. First, this folded morphology provides an increased surface area, allowing the maximum number of cells to fit within the limited cranial volume imposed by the skull (Fernández et al., 2016). Second, the folded morphology provides divisions to separate types of brain functions (Bailey, 2017). The cortex is home to approximately 70 of the 100 billion nerve cells in the brain (Herculano-Houzel, 2009). These nerve cells bodies have a grey-brown body colour and thus collectively are called the grey matter. Beneath this is the white matter consisting of long connecting fibres between neurons called axons. Figure 1.1 depicts the folds of the brain tissue called gyrus, with each grove called a sulcus.

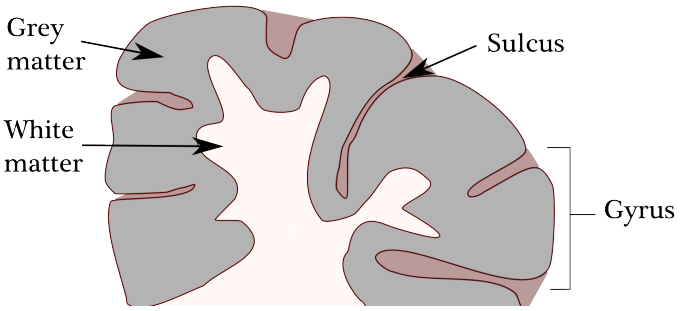

Figure 1.1: Describing the structure of the cortex. Each fold is called a gyrus, and each groove between folds is called a sulcus. Each fold is uniquely named to indicate location and function.

Histology is the study of the microscopic anatomy of cells and tissues in both plants and animals. Within the grey matter in the brain there are two types of cells; nerve cells (neurons) and glia cells. Glia (the Greek word meaning glue) cells provide the brain with nourishment, protection, and structural support (Jäkel and Dimou, 2017). There are roughly 10 to 50 times more glia than nerve cells. Astroglia or astrocytes, a glia type cell, transport nutrients to neurons, hold neurons in place, digest parts of dead neurons, and regulate the blood brain barrier (Jäkel and Dimou, 2017). Astrocytes play a key role in the connection between the neurons and arteries in the brain (Nedergaard et al., 2003).

1.1.2 Cerebral Vasculature

The Cerebral Blood Flow (CBF), the blood supplied to the tissue in the brain, is on average 750 millilitres every minute or approximately 15% of the cardiac output (Pace, 2015). This blood is supplied via the cerebral arteries carrying oxygen, glucose and other nutrients to the brain. The de-oxygenated blood, along with any waste, is then transported back to the heart via the veins.

From the heart, the blood travels via the aorta to the basilar artery located at

the base of the brain (Cloud and Markus, 2003). From there the blood flow is divided via the Circle of Willis (Ustun, 2005) to be distributed to the different areas of the brain. The Circle of Willis consists of three main (paired) arteries: the anterior cerebral arteries, the internal carotid arteries and the posterior cerebral arteries (Weerakkody et al., 2017). The anterior cerebral arteries supply the 'front' of the cerebrum, the internal carotid arteries (along with the middle cerebral arteries) supply the mid section (inner and outer) of the cerebrum and the posterior cerebral arteries (along with the superior cerebral arteries) supply the 'back/top' of the cerebrum with blood. The arteries supplying the blood then bifurcate (split in two) multiple times in order to reduce the diameter and thus supply to each individual gyrus in the brain. Figure 1.2 gives a colour coded pictorial of this.

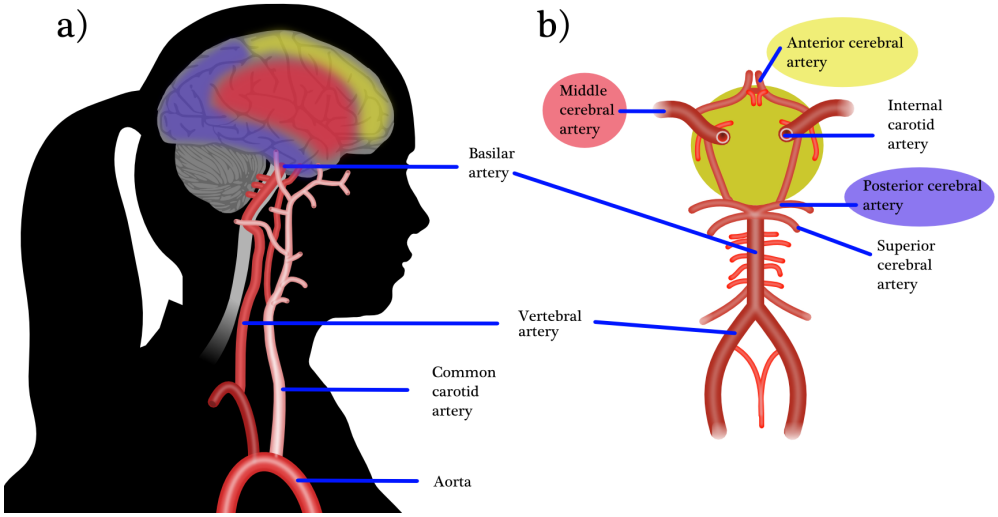

Figure 1.2: Pictorial of components leading to the cerebral vasculature. a) Indicates the main vessels in the supply of oxygenated blood from the aorta to the basilar artery. b) shows a detailed depiction of the circle of willis (green circle) which divides the blood flow into the different regions of the brain. Notably the anterior, middle and posterior regions colour coded to indicate approximate regions of the brain on Figure a). Figure created by M. Goodman from multiple sources of information: Ustun (2005), Cloud and Markus (2003) Weerakkody et al. (2017).

The CBF is further regulated by the diameter of the arterioles which affects the perfusion rate to the surrounding cells. Neuronal activation can stimulate the blood vessels causing contraction/dilation to adjust the blood supply as required (Purves et al., 2001). The CBF is heavily regulated in order to keep the brain within acceptable levels. Large blood flow into the brain (hyperemia) can raise intracranial pressure, causing compression and damage to delicate brain tissue. Conversely, too little blood flow (ischemia) can starve cells and lead to tissue death. In brain tissue, a biochemical cascade known as the ischemic cascade can be triggered when the tissue becomes ischemic, potentially resulting in damage or death of a large area of brain cells.

1.2 Neuro-Vascular Unit (NVU)

The Neuro-Vascular Unit (NVU), which includes the Blood Brain Barrier (BBB), is a collection of multiple different types of cells that connect the Neurons to the blood vessels in the brain. This connection is important to the supply of oxygenated blood and glucose to the cells in the brain. Principally, the unit can be broken down into 8-9 compartments: 4-5 cell types and 4 connecting spaces (of which one in the lumen) as shown in Figure 1.3.

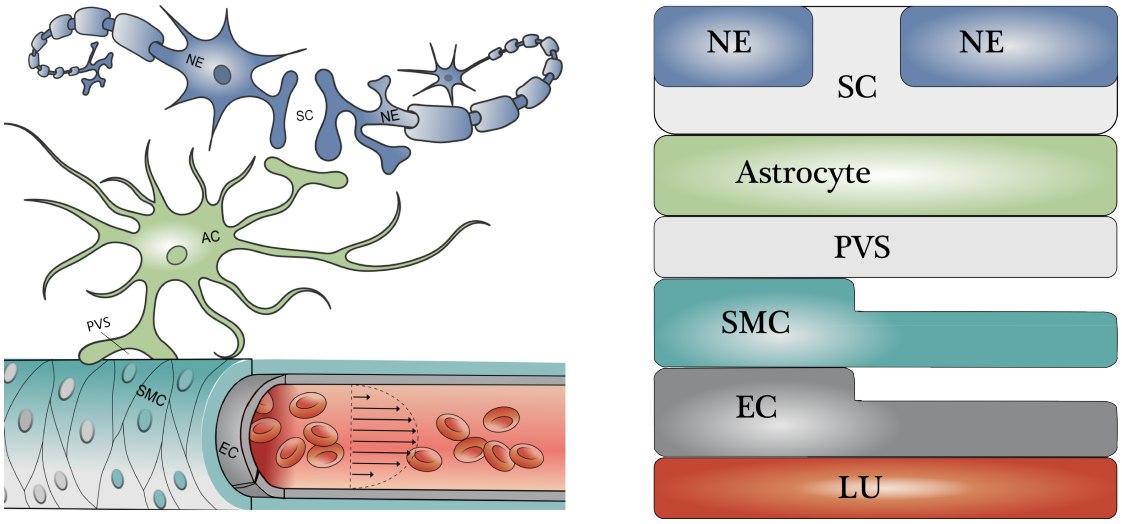

Figure 1.3: Pictorial alongside compartment model of the NVU consisting of the Neuron (NE), Synaptic Cleft (SC), Astrocyte (AC), Perivascular space (PVS), Smooth Muscle Cell (SMC), Endothelial cells (EC), and the Lumen (LU). Figure adapted with permission from Dormanns (2015). Pericytes are not included.

1.2.1 Cell Types

Throughout the literature the NVU has been described as a combination of three to five principle cell types (McConnell et al., 2017; Montagne et al., 2017; Filosa et al., 2016; Iadecola, 2017; Dormanns et al., 2015; Hawkins and Davis, 2005). Typically, the minimum expression includes at least a Neuron (NE), an Astrocyte (AC) and a Smooth Muscle Cell (SMC) (Filosa and Blanco, 2007). This is added to with the inclusion of Endothelial cells (EC) and, the newest addition, pericytes.

Endothelial cells, pericytes and SMCs are together grouped as vascular cells (Filosa et al., 2016). They act to regulate the BBB and perfusion of oxygen and glucose to the surrounding cells. Endothelial cells line the vasculature and play key roles in diverse processes such as “coagulation, inflammation, barrier

function, blood flow regulation and synthesis/degradation of the extracellular matrix" (Calcagno et al., 2016). The SMCs regulate the blood vessel diameter, vascular tone, and hence blood flow by dynamically contracting and relaxing in response to vasoactive stimuli (Metz et al., 2011). SMCs are nonstriated with tapered ends that wrap around the endothelial cells and run perpendicular to the blood flow in the lumen. Pericytes, both instead of SMC (Calcagno et al., 2016) and in combination (Filosa et al., 2016), are more common on the smaller diameter blood vessels, called capillaries (Hawkins and Davis, 2005) and as such are not included on Figure 1.3. Vascular cells allow the correct ionic concentrations to exchange with the blood flow. This is done dynamically and heterogeneously (Michiels, 2003).

A neuron, also known as a nerve cell, is an electrically excitable cell that receives, processes, and transmits information through electrical and chemical signals (Lodish et al., 2000). Finally, astrocytes, as previously mentioned, are glia type cells that transport nutrients to neurons, hold neurons in place, digest parts of dead neurons, and regulate the BBB (Jäkel and Dimou, 2017). In recent years, the astrocyte's role in the Central Nervous System (CNS) has changed as new studies have been completed. Astrocytes, originally thought to only provide structure and transmission of signals, are contested to also regulate the signal to and from the blood supply via information processing within the cell (Sofroniew and Vinters, 2010).

Both astrocytes and SMCs contain intracellular stores known as the endoplasmic reticulum and the sarcoplasmic reticulum, respectively. The intracellular stores contain specific ions, for immediate release, when action potentials are fired. The sarcoplasmic reticulum contains proteins specifically responsible for calcium ion uptake, storage and release to the cytosol to mediate quick cell

responses to external stimuli (Volpe et al., 1992).

1.2.2 Connecting Spaces

The synaptic cleft denotes the space between the cell membrane of an axon terminal and that of a neighboring cell with which it forms a synapse (The American Heritage, 2007). The perivascular space, also known as Virchow-Robin spaces, is a pial-lined interstitial fluid-filled space in the brain that surrounds perforating vessels. The perivascular space does not directly connect to the extracellular space due to the different spaces having variations in composition (Kwee and Kwee, 2007).

The extracellular space denotes the unconsumed space left within the NVU (Syková et al., 2008). The extracellular space allows for spatial diffusion of ions and absorbs or supplies ions needed for cellular uptake, binding and other mechanisms. Finally, the lumen (word derived from Latin meaning 'an opening') defines the space inside the tubular structure that contains the flow of blood of which the diameter is controlled by the SMCs.

1.2.3 Ionic Pathways

The cells and connecting spaces (Sections 1.2.1 and 1.2.2) interact with each other via exchanging electrically charged ions across the cell membrane. There are three main ways for an ion to pass across the cell membrane: leak, release and pump. The leak of an ion refers to the unintentional release of an ion from a high concentration compartment to a low concentration compartment. The release of ions is the passive opening of a channel and allowing the concentration to flow from a high concentration to a lower concentration and thirdly, the pump or exchanger entails a movement of ions against its concentration gradient. The

channels are typically mediated by either the membrane potential, the unequal pressure, or the concentration of another ion or neurotransmitter on at least one side of the channel. Figure 1.4 shows a pictorial of a concentration mediated release pathway across a membrane.

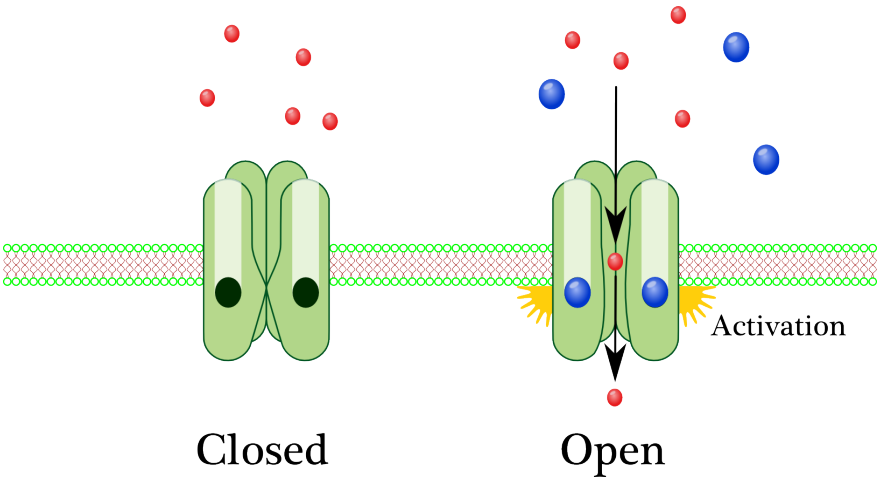

Figure 1.4: Pictorial of passive activation ionic pathway across a membrane. This ion channel is gated by the molecules (blue) above to provide channel activation and allow the ions (red) to cross. Figure produced with direction from Nature Education (2010) free to use image.

Some examples of ionic pathways in the NVU include: the Calcium Induced Calcium Release (CICR), which releases calcium ions depending on the existing concentration of calcium ions. The Voltage Induced Calcium Release (VICR) also known as the Voltage Operated Calcium Channel (VOCC), that opens depending on the membrane potential (the difference in electrical potential across the membrane), the more complex Sarco/Endoplasmic Reticulum $Ca^{2+}-$ATPase Pump (SERCA-Pump) and many more.

1.2.4 Buffering

Buffers are chemicals that help the fluid within a cell maintain its equilibrium when other chemicals are added that would normally cause a change in its properties. Buffering reduces the free concentration of an ion within the cell, which could go on to react or be transmitted to the next cell. For example, high-affinity calcium-binding proteins (such as calbindin-D28k, calretinin, and the α and β isoforms of parvalbumin) serve as diffusible Calcium ion (Ca^{2+}) buffers in order to reduce the free concentration and resist large changes to the properties of the cytoplasm within SMCs (Hackney, 2005).

1.3 Waves in Tissue Media

Throughout research into physiological tissue there exist many different types of 'waves' moving in space and time; so many in fact that this research could not attempt to do it justice. Some examples include vasomotion, peristalsis (eg. digestive tract movement) or uterine contractions to name a few. Here, instead, this research will introduce one such case of Calcium ion (Ca^{2+}) waves in cerebral tissue media. A wave in this research refers to a large increase in the concentration of an ion which then is seen to move across space over time. The movement of calcium ions has been chosen to be elaborated on, as many of the mathematical models (yet to be introduced) investigated within this research include an in depth look at cellular calcium ion concentrations.

It is widely believed that intercellular (between multiple cells) Ca^{2+} waves are a mechanism by which a group of cells can communicate with one another (Wilkins and Sneyd, 1998; Falcke, 2003). This communication allows for a co-ordinated, multicellular response to local events. It is believed by Wilkins and

Sneyd (1998) that understanding this intercellular Ca^{2+} communication could lead to the better understanding of a wide range processes such as mucociliary clearance, wound healing, mechanical transduction, cell growth, and information processing (Wilkins and Sneyd, 1998).

To understand the movement of Ca^{2+} waves over space, first one must understand at least one example of what initiates the dramatic change in concentration. Initially, upon a small addition of Ca^{2+}, Inositol trisphosphate (IP_3) or some other stimulus into the cell, a chain of reactions can occur. The large change in the cytosolic Ca^{2+} concentration is due to the release of ions from the intracellular store such as the Endoplasmic Reticulum (ER). The main purpose of the intracellular store is to mediate and offer quick release of ions used in signalling without affecting the extracellular concentration. This change is initially greatest near the ionic pathway outlet near the plasma membrane within the cell (Falcke, 2003). The opening and closing of these Ca^{2+} channels on the ER membrane controls the release of Ca^{2+}. The CICR ionic pathway is one of the widely recognised channels responsible for the large release in Ca^{2+} concentration (Falcke, 2003; Thul, 2014; Stern, 1990; Wilkins and Sneyd, 1998; Dawson et al., 1999) (also see Section 1.2.3). This pathway acts as a self amplifying release mechanism (Falcke, 2003), which upon a small external addition of calcium will release Ca^{2+} from the ER.

From the initial release site, intracellular (within the cell) spatial calcium oscillations occur throughout the cytosol. This can lead to whole cell spiking or stable oscillation depending on the rate and frequency of the CICR channels opening. Stern (1990) described the desire to initiate intracellular waves externally for cells that are not spontaneously oscillating. This can be done by means of ‘subthreshold field stimulation, local application of caffeine, or local-

ized photo-release of caged calcium'. However, intracellular waves created by these mechanisms often do not propagate the full length of the cell. Stern (1990) goes on to say that intracellular data measurement techniques lack the resolution necessary to fully comprehend this phenomenon.

Finally, the larger tissue scale is considered to view the interaction across multiple cells (intercellular). Each intercellular wave consists of a sequence of intracellular waves, and the delay in intercellular transmission decreases with increasing stimuli concentration (Wilkins and Sneyd, 1998). Data sources for comparison are limited to ethically obtainable methods. For example, intercellular waves of ionic calcium concentration, Ca^{2+}, have been proven to occur in hippocampal astrocyte networks of rats in situ by Dani et al. (1992). Charles (1994) indicated glial cells in culture with neurons showed frequent spontaneous Ca^{2+} oscillations and intercellular waves and Sanderson et al. (1994) showed that intercellular Ca^{2+} waves initiated by mechanical or chemical stimuli propagated between cells via gap junctions.

An example of the purpose of intercellular Ca^{2+} communication is described by Wilkins and Sneyd (1998); if a monolayer of epithelial cells is mechanically damaged, the resultant intercellular Ca^{2+} wave sets up intercellular Ca^{2+} gradients which influence the initiation and direction of cell migration. Another important aspect of Ca^{2+} waves, investigated by Charles (1994), is that intercellular Ca^{2+} waves in glial cells can be communicated to neurons, and thus glial cells could play an active role in information processing. Importantly, as Filosa and Blanco (2007) describe: "Neuronal stimulation increases intracellular calcium concentration (Ca^{2+}) in astrocytes via activation of voltage-dependent Ca^{2+} channels and Metabotropic Glutamate Receptor (mGluR) induced activation of Phospholipase C (PLC), production of IP_3 and Ca^{2+} release

from intracellular stores. The rise in Ca^{2+} ...[goes on to cause] .. vasoconstriction ...[or conversely]... vasodilatation".

The mechanical and chemical mechanisms that lead to Ca^{2+} oscillations and spatial wave propagations can be related to simple and elegant mathematical approximations. These approximations are used to calculate the effect of cell dynamics on the intracellular and intercellular Ca^{2+} concentrations. In combination with obtainable data, mathematical modelling of cells can provide a greater understanding of a cell's ability to communicate and its comprehension of signalling.

1.3.1 Spatially Varying Stimulus

As explained in Section 1.2.1 there are two types of cells (SMCs and Astrocytes) with intracellular stores within the NVU. Additionally, as previously mentioned, upon a stimuli the intracellular store is utilised to rapidly supply additional Ca^{2+} without affecting the extracellular Ca^{2+} concentration. This feedback is used to efficiently and effectively pass information to another type of cell, and thus communicate a large scale response to regulate the blood supply to cells in the NVU.

As the stimulus to regulate the blood flow changes over time, it is expected that this stimulus will additionally vary over a spatial arrangement on the macroscale. There exist many examples of spatial stimuli variations occurring in physiology, and again more than this research could hope to do justice to as it falls on the outskirts of the scope. Nevertheless, a brief example of Cortical Spreading Depression (CSD) is used.

CSD is characterised as a macroscale 'wave' of a high concentration of Potassium ion (K^+) traversing the extracellular space in the brain (Lauritzen

et al., 2011). This gradient of K^+ over space moves at a slow rate of 2-5mm/min, allowing time for fast intracellular responses to occur. As the high concentration of K^+ progresses the neurons become depolarised, creating an efflux of excitatory amino acids including Glutamate (Lauritzen et al., 2011; Fabricius et al., 1993). Glutamate activates PLC, inducing an additional increase to the concentration of IP_3 (Endoh, 2004). This is transmitted through the NVU and acts as the applied stimuli to the astrocytes and SMCs (Goldbeter et al., 1990). Thus, CSD creates a spatially varying stimulus (eg. Glutamate and IP_3) for astrocytes and SMCs on a time scale of 10-100 seconds.

2 Mathematical Modelling in Cell Biology

2.1 Cell Modelling Approach

2.1.1 Lumped Parameter Model

Many of the models described within this research use a lumped parameter model. A lumped parameter model assumption, in this context, is used to approximate the typically spatially distributed concentration as a single concentration within a closed compartment (Beeman, 2005). This assumption is typically valid within a small compartment with a large diffusive ability. This assumption is often contested, as it ignores the effect of local ionic concentration upon ionic concentration dependent channels, but is generally accepted for cellular modelling.

2.1.2 Mass Conservation

Cellular modelling is often based upon the assumption of mass conservation; mass is neither created nor destroyed in chemical reactions. This is applied to the movement of mass across the cell compartments through conservation of ionic concentration. More specifically, the change in ionic concentration ($[S]$)

over time, for some fixed volume (Vol), is equal to the influx minus the efflux of ions over time, Equation 2.1.

$$\left.\frac{d[S]}{dt}\right|_{Vol} = \sum_{k=1}^{n}[\dot{S}]_k - \sum_{l=1}^{m}[\dot{S}]_l \tag{2.1}$$

where k denotes the ionic concentration entering the cell over time through n pathways and l denotes the ionic concentration exiting the cell over time through m pathways. Note that cell waste, a degradation of an ionic concentration within a cell over time, is mathematically approximated as an efflux over time ($[\dot{S}]_l$).

2.1.3 Kirchhoff's Circuit Law

Kirchhoff's circuit law or Kirchhoff's first law states that current is preserved at a junction. The law is derived from the conservation of charge C which is the product of current, I, and time, t. In the context of cellular modelling the partial rate of change of the membrane potential (V) over time in a compartment, using $V = IR$, is proportional to the sum of currents entering minus the sum of currents leaving (Equation 2.2). Whereby the cell compartments are approximated as junctions using the lumped parameter model (Section 2.1.1).

$$C_m\frac{dV}{dt} = \sum_{k=1}^{n} I_k - \sum_{l=1}^{m} I_l \tag{2.2}$$

where, again, k denotes the currents entering the cell through n pathways, l denotes the currents exiting the cell over time through m pathways and C_m is the capacitance of the cell. From this, the membrane voltage can be tracked via the current induced by the electrically charged ions moving across the membrane of the cell.

The membrane potential or voltage is measured as the difference in electric

potential between the intracellular ionic concentration and the extracellular ionic concentration. As the electrically charged ions travel across the membrane, the membrane potential adjusts accordingly using the assumption of Kirchhoff's first law.

2.1.4 Oscillatory Behaviour in Cell Models

Section 1.3 described the mechanism in which calcium, in particular, achieved an oscillatory behaviour of its ionic concentration over time. One way this behaviour can be translated into mathematical models is by detailing the rate of change of a variable over time, with at least one other variable and at least two channels: a fast rate channel and a slow rate channel. Equation 2.3 describes the a basic mathematical description of this process.

$$\frac{d\Phi}{dt}(\Phi,\Psi,t) = J_{Fast} - J_{Slow} \quad \frac{d\Psi}{dt}(\Phi,\Psi,t) = -\delta\left(J_{Fast} - J_{Slow}\right) \tag{2.3}$$

where for example Φ is the concentration of one compartment and Ψ is the concentration of the other compartment and δ represents a fractional concentration conversion depending on the volumes ratio of the compartments. In the case of calcium oscillations from Section 1.3, Φ would represent the ionic calcium concentration in the cytosol and Ψ would represent the calcium concentration in the intracellular store. For this example, J_{Fast} represents fast release of calcium from the store to the cytosol and J_{Slow} represents the slow pump of calcium back to the higher concentration store.

Should either J_{Fast} be a periodic function or, the more likely case, when the J_{Fast} is of magnitude comparable to J_{Slow} but the latter exhibits a time delay, the concentration in both the cytosol and the store would oscillate over time.

Oscillatory behaviour can be represented in cell modelling via other approaches. The most common detailed alternative is the VOCC and its effect on the membrane potential, followed by the time delayed effect on the open probability of the VOCC channel (Gonzalez-Fernandez and Ermentrout, 1994).

2.1.5 Brief Homogenisation Theory

Homogenisation theory will be discussed in further detail later, but for now it is necessary to introduce the basic concept. Homogenization theory is concerned with the derivation of equations of averages. The word homogenisation means to make uniform or similar in composition or function. In application to cell modelling it is a process required to obtain a smoothed ('homogenized' or 'effective') macroscopic approximation, for example a concentration, even though the concentration can have a fine microscopic structure or changes. The theory is, thus, similar to the lumped parameter model assumptions (Section 2.1.1) on a different scale.

2.2 Cell Modelling Components

2.2.1 Molar Concentration

Careful consideration to units is important to the understanding of the surrounding literature. One case in particular is the difference between the Number of moles, n, with units $[mol]$ and Molar concentration, C, with units $[M]$. It is possible to convert between the two with Equation 2.4.

$$n = C \times Vol \tag{2.4}$$

where Vol is the volume such that $1mol = 1M \times 1L$. The dimensionless conversion c_c (Equation 2.5) is found given the standard unit for Molar concentration in cell modelling is $[\mu M]$ and the desired volume is often $[cm^3]$.

$$c_c = 10^9 \frac{\mu M cm^3}{mol} \tag{2.5}$$

2.2.2 Michaelis–Menten Kinetics

Michaelis–Menten kinetics is a scientific community recognised model to describe the rate of an enzymatic reaction. Michaelis and Menten (1913) proposed a mathematical model of the reaction involving an enzyme, E, binding to a substrate, S, to form a complex, ES, which in turn releases a product, P, and the original enzyme (Equation 2.6).

$$E + S \underset{k_2}{\overset{k_1}{\rightleftharpoons}} ES \xrightarrow{k_3} E + P \tag{2.6}$$

Michaelis and Menten (1913) assumes that the substrate becomes in instantaneous chemical equilibrium with the complex. This implies that the rate of formation of ES is equal the the rate of breakdown of ES to $E + S$ (Equation 2.7).

$$k_1[S][E] = k_2[ES] \tag{2.7}$$

In addition to this, the rate formation of E and P is $k_3[ES]$. From the enzyme conservation law Equation 2.8 is obtained.

$$[E] = [E]_0 - [ES] \tag{2.8}$$

Substituting Equation 2.8 into Equation 2.7 gives Equation 2.9.

$$k_1[S]\left([E]_0 - [ES]\right) = k_2[ES] \tag{2.9}$$

rearranging Equation 2.9 gives:

$$[ES] = \frac{[E]_0[S]}{[S] + \frac{k_2}{k_1}} \tag{2.10}$$

Finally, using the dissociation constant $K_M = \frac{k_2}{k_1}$ the rate of which P is formed is given by Equation 2.11. This is known as the Michaelis-Menten equation.

$$\frac{d[P]}{dt} = \frac{V_{max}[S]}{K_M + [S]} \tag{2.11}$$

where V_{max} is the maximum asymptotic rate the system can achieve with increasing concentration and K_M is the concentration required to reach 50% of the maximum rate. Figure 2.1 describes this relationship.

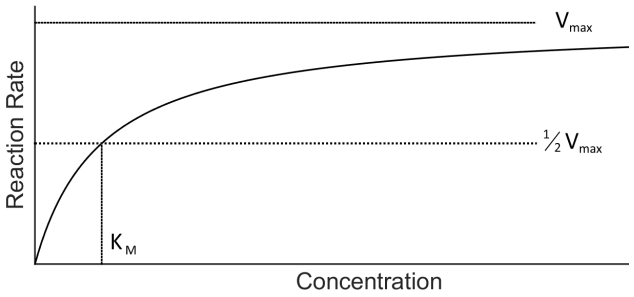

Figure 2.1: Relationship between parameters $[S]$, V_{max} and K_M in the Michaelis-Menten equation.

In cellular modelling the Michaelis-Menten equation is used for some ionic pathways which depend upon chemical reactions that proportionally slow the

rate of the channel.

2.2.3 Hill Kinetics

An alternative to Michaelis-Menten kinetics is Hill kinetics. The Hill Equation quantifies the effect of cooperative binding. The rate of binding of a ligand, L, to a macromolecule, P, increases with the number of ligands, n, already bound to the macromolecule. Equation 2.12 describes this chemical reaction.

$$P + nL \underset{k_2}{\overset{k_1}{\rightleftharpoons}} PL_n \tag{2.12}$$

Following a similar derivation as the Michaelis-Menten equation, the Hill Equation, written as an expression for the concentration $[PL_n]$ of bound protein, is given by Equation 2.13.

$$\theta = \frac{[L]^n}{(K_A)^n + [L]^n} \tag{2.13}$$

where θ is the fraction of the receptor protein concentration that is bond to the ligand, $[L]$ is the unbound ligand concentration and K_A is the ligand concentration required to achieve 50% occupied ligand binding sites. Finally, n is the Hill coefficient and the primary difference to the Michaelis-Menten equation. n represents the degree of cooperative binding obtained from experiments for each binding reaction. Similar to the Michaelis-Menten equation, the Hill equation is multiplied to an ionic concentration to determine the rate of an ion crossing an ionic pathway, where it is dependent on the occurrence of this type of chemical reaction.

2.2.4 Nernst Membrane Equilibrium Potential

The derivation of the equation of the Nernst Equilibrium Potential starts with the assumption that the free energy difference between the inside and the outside of the cell at equilibrium must be zero. Thus, at equilibrium, the change in free energy due to electrical difference (due to the membrane potential) must be equal to the change in energy due to the chemical difference between the inside and outside of the cell. i.e. Equation 2.14 must be true (Endresen et al., 1998; Malmivuo and Plonsey, 1995).

$$\Delta G_{Electrical} = \Delta G_{Chemical} \tag{2.14}$$

where the membrane potential is the difference in electrical potential across the membrane. Therefore, for a specific ion the electrical free energy can be described by Equation 2.15.

$$\Delta G_{Electrical} = z_X F V \tag{2.15}$$

where z_X is the valance of the ion X, F is Faraday's constant and V is the membrane potential. The free energy due to the chemical difference of a specific ionic species can be described by the Gibbs free energy (Equation 2.16) (Greiner et al., 1997).

$$\Delta G_{Chemical} = RTln\left(\frac{[X]_o}{[X]_i}\right) \tag{2.16}$$

where R is the universal gas constant, T is the temperature, and $[X]_o$ and $[X]_i$ are the concentrations of the ion X in the extracellular fluid and intracellular fluid respectively. Finally, substituting Equations 2.15 and 2.16 into 2.14 and

rearranging gives the Nernst Equilibrium Potential as shown in Equation 2.17.

$$V_{eq} = \frac{RT}{z_X F} ln\left(\frac{[X]_o}{[X]_i}\right) \tag{2.17}$$

Some examples of possible cellular ionic concentrations and their respective equilibrium potentials are described in Table 2.1. Note that the intracellular ionic concentrations vary across different mammalian cells and therefore so does the equilibrium potential.

Table 2.1: Some examples of their Equilibrium Potential given approximate intracellular and extracellular concentration for a typical mammalian cell in its natural environment (310 K). Note the concentrations vary depending on cell type so these should be used with caution.

Ionic Species	**Intracellular Concentration**	**Extracellular Concentration**	**Equilibrium Potential**
Sodium, Na^+	$15mM$	$145mM$	$+60.60mV$
Potassium, K^+	$150mM$	$4mM$	$-96.81mV$
Calcium, Ca^{2+}	$70nM$	$2mM$	$+137.04mV$
Chloride, Cl^-	$10mM$	$110mM$	$-64.05mV$

When there is more than one ionic species moving through a channel the equation increases in complexity to become the Goldman-Hodgkin-Katz equation (Equation 2.18) (Malmivuo and Plonsey, 1995).

$$V_{eq} = \frac{RT}{F} ln\left(\frac{\sum_{i=1}^{n}(p_i[X_i]_o)}{\sum_{i=1}^{n}(p_i[X_i]_i)}\right) \tag{2.18}$$

where i denotes the ion considered and p_i is the relative membrane permeability of the ion considered.

2.2.5 Resting Membrane Potential

The resting membrane potential, described as the difference in electrical potential across the membrane at rest (described in Section 2.1.3), also varies with cell type. The membrane potential of a neuron at rest is approximately $-70mV$ (Purves et al., 2001). The negative convention infers that the ionic potential inside the neuron is less than in the extracellular space. Furthermore, at rest, there is on average a higher concentration of potassium ions ($[K^+]$) and calcium ions $[Ca^{2+}]$ and a lower concentration of sodium ions ($[Na^+]$) and chloride ions ($[Cl^-]$) within the cell compared to the extracellular space. Vascular smooth muscle and endothelial cells typically have a resting membrane potential between $-40mV$ and $-70mV$ (Félétou and San, 2011).

2.2.6 Ion Channel Open Probability

An ion channel is a type of ionic pathway that allows the passive transport of ions from a high concentration compartment to a low concentration compartment. The open state probability of a channel denotes the probability that the channel is in its open state at any given time. A channel's open probability can be affected by the presence, or lack of, a specific antagonist. The process of a substance or agent affecting the opening of a channel is known as modulation and varies with the sensitivity of an ionic channel. The opening of an ion channel can be found via four different ways (or as a combination) (Dormanns, 2015).

- A voltage gated ion channel opens depending on the membrane potential (Section 2.1.3).
- A ligand gated ion channel opens depending on a transmitter binding such

as glutamate.

- A mechano-sensitive gating ion channel opens in response to a mechanical stretch, pressure or shear.
- A second-messenger-activated ion channel or a concentration mediated release is described in Section 1.2.3.

The open probability is determined by measuring the length of time a channel is open during a specified period or as a snapshot in time of multiple channels (Equation 2.19).

$$P_o = \frac{n_o}{n_o + n_c} \tag{2.19}$$

where P_o is the open probability, and n_o and n_c are the number of channels open or closed at any given time. Normally, the channels stay open for only a fraction of a second, allowing tens of thousands of ions through the pore. The open probability can be measured for a specific channel under specific conditions via a patch clamp test (Anantharam et al., 2006). An in-depth derivation of the change in the open probability can be found in Fall et al. (2002).

2.2.7 Types of Models and The Hodgkin and Huxley (1952) Model

Within this research there exist two approaches to modelling a cell: a conductance based model and a chemical reaction based model. The approaches are often used separately, but can also used in collaboration, depending on the mechanism modelled.

A conductance based model approximates the cell membrane as a sum of resistors and capacitors. The ionic pathways (Section 1.2.3) provide resistance to the movement of ions based on the concentration gradient and the lipid bi-

layer of the membrane is approximated as a capacitor. Hodgkin and Huxley (1952) provided one of the first examples of this, as depicted in Figure 2.2.

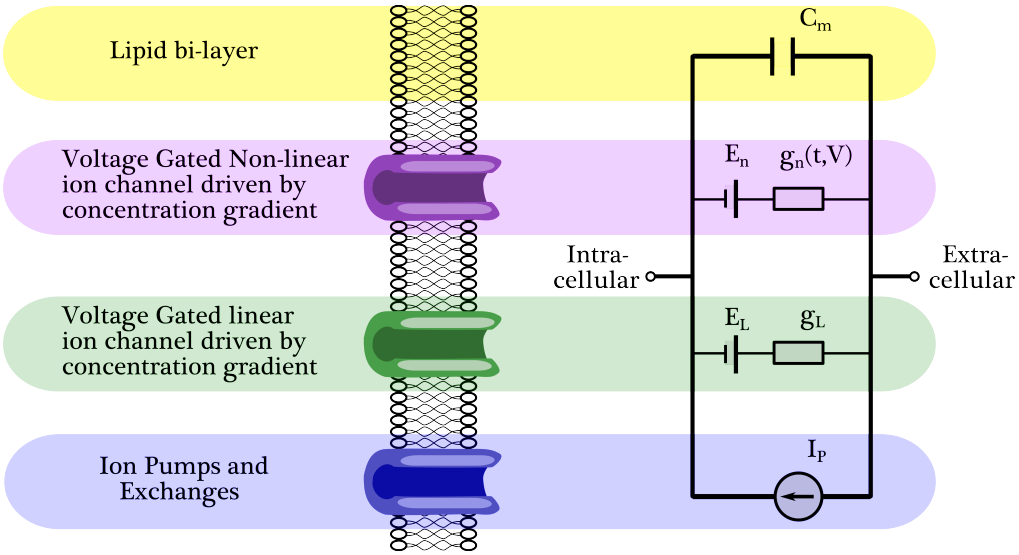

Figure 2.2: Breakdown of the famous Hodgkin and Huxley (1952) conductance based model. Figure created by M. Goodman with direction from Hodgkin and Huxley (1952).

Figure 2.2 shows a conductance based modelling approach to the modelling of the membrane potential and thus the ionic concentration changes based upon the different pathways. The current through a given ion channel within this type of model can be approximated via Equation 2.20.

$$I_i = g_n(V - V_i) \tag{2.20}$$

where V is the membrane potential, V_i is the reversal potential of the given ion channel, and g_n is the conductance per unit area which often includes a probability of the type of channel being open (Section 2.2.6). This resultant change in the membrane potential (using Equation 2.2) then drives a change in concentration for each ion that was said to move.

The other type of modelling approach, a chemical reaction based model, attempts to first and foremost quantify the concentration that passes across the membrane based upon the type of channel, which often includes a chemical reaction. Distinguishably, these types of modelling do not use the membrane potential in the calculations but rather the direct concentrations. For example, an ionic pathway which utilises Michaelis–Menten Kinetics (Section 2.2.2) or Hill Kinetics (Section 2.2.3) is a chemical reaction based modelling technique.

These two types of modelling approaches can be used separately or together depending on the mechanisms desired to be modelled.

2.3 Numerical Solving Methods

From Sections 2.1.2, 2.1.3, 2.1.4 and 2.2.2 it is clear that the main modelling equations used are coupled differential equations. This section describes the numerical method to solve coupled differential equations. An example of such a coupled differential equations set is defined by Equations 2.21 from Dokos (2017).

$$\begin{aligned} \frac{d\Phi_1}{dt} &= f_1(\Phi_1, \Phi_2 ... \Phi_n, t) \\ \frac{d\Phi_2}{dt} &= f_2(\Phi_1, \Phi_2 ... \Phi_n, t) \\ &... \\ \frac{d\Phi_n}{dt} &= f_n(\Phi_1, \Phi_2 ... \Phi_n, t) \end{aligned} \tag{2.21}$$

with

$$\Phi_1(0) = \Phi_{1,0}, \quad \Phi_2(0) = \Phi_{2,0}, \quad ... \quad \Phi_n(0) = \Phi_{n,0},$$

where f_1, f_2,..., f_n represent linear or non-linear functions and Φ_i is either different ionic species, membrane potential or open probability and are dependent on themselves and/or the other variables over time. The Runge-Kutta fourth order method is used as a means of solving the non-linear ODE equation sets. The Runge-Kutta family of methods includes the well-known Euler Method, which is the simplest explicit ODE solver. Equation 2.22 depicts Euler's explicit solver method of the Equation set detailed by Equation 2.21 in vector form.

$$\begin{bmatrix} \Phi_1 \\ \Phi_2 \\ \vdots \\ \Phi_n \end{bmatrix}_{t=i+\Delta t} = \begin{bmatrix} \Phi_1 \\ \Phi_2 \\ \vdots \\ \Phi_n \end{bmatrix}_{t=i} + \Delta t \begin{bmatrix} \frac{d\Phi_1}{dt} \\ \frac{d\Phi_2}{dt} \\ \vdots \\ \frac{d\Phi_n}{dt} \end{bmatrix}_{t=i} \tag{2.22}$$

By construct Eulers method introduces an error of approximation dependent upon Δt. As such, a pre-established reliable adaptive time step approximation MATLAB ODE45 which utilises the Runge-Kutta method was employed (Section 2.3.1) to give a fourth order accuracy. The fourth order accuracy indicates local truncation error is on the order of $Error_{LTE} \leq \mathcal{O}(h^5)$ and the total accumulated error is of the order $Error_{total} \leq \mathcal{O}(h^4)$ where h is the step size. The Runge-Kutta method uses a weighted average of the rate of change solved at the beginning, the midpoint and the end of the interval to approximate the more accurate change over the time step (Nur Adila Faruk Senan, 2017).

2.3.1 MATLAB ODEXX solver

ODE45 is a versatile, explicit ODE solver (Shampine and Reichelt, 1997; Nur Adila Faruk Senan, 2017) that fits most differential equation types and uses the

Runge-Kutta fourth order method. An expansion to ODE45 is ODE15s, which is a solver designed specifically for stiff problems. A stiff system experiences instability in the solution for small changes in the adaptive time step and often results in incorrect solutions. Should the specified approximate time step be sufficiently smaller than the time of any sudden changes in the result, an appearingly stiff model can be approximated as a non-stiff model. Thus, MATLAB ODE45 solver method was used given that for a non-stiff model ODE45 is strictly more efficient than ODE15s.

There are many benefits of this ODE solver in the context of numerical cell modelling. First, ODE45 employs an adaptive time step such that if the solution is not rapidly changing, the time step will increase. Conversely, should the solution suddenly experience changes, a finer time step is employed. This adaptive time step eliminates the majority of the error associated with a user selected Δt. Second, ODE45 allows the desired accuracy of the solution to be specified. For the purpose of this research it was determined that an absolute tolerance of $AbsTol = |Y_a - Y_b| = 1 \times 10^{-6}$ was sufficient in producing detailed results. Note that for an unspecified relative tolerance ($|Y_a - Y_b|/(min(|Y_a|, |Y_b|))$) the relative tolerance defaults to the absolute tolerance. This optimises the computation time spent to find the solution. Third, since ODE45 dynamically and iteratively adjusts the computations required it can also optimise the RAM usage. This is done by computing the smaller increment time steps as necessary to obtain the correct solution, then deleting them from the RAM. This is particularly critical to computations involving many differential equations and for a long detailed time.

Another benefit of the inbuilt ODE45 solver is the ability to fix the solutions as non negative variables. In cellular modelling this is desirable as a negative

ionic concentration is physiologically impossible. Finally, whilst the time step is adaptive there is the option to employ a suggested initial step size. This option allows an experienced used to predict the necessary time step and reduce computation time further.

Along with all the options specified above ODE45 also requires the $d\Phi_i/dt$ vector from Equation 2.22, the time span and the initial conditions to be set out in Section 2.3.2. For the reasons specified here ODE45 was used as the primary ODE solver unless otherwise stated for this research.

2.3.2 Initial Conditions

Correct initial condition choices to the Equation set 2.21 are necessary to efficiently find the desired equilibrium states and stable oscillatory solutions over time. The models used in this research (yet to be introduced) individually indicate their reliance on the initial conditions. The initial conditions, unless otherwise stated, have been set to recognised resting ionic concentrations within a generic cell. For example, the free intracellular ionic concentration of calcium in mammalian cells is approximately $0.1\mu M$ (Schumacher and Friml, 2009) and the ionic calcium concentration in the intracellular store is of the order 100 to 1000 times that of the cytoplasm (Bygravel and Benedetti, 1996). In comparison, the intracellular potassium ion concentration is approximately $100mM$ (Schumacher and Friml, 2009). Finally, the membrane potential resting state as described in Section 2.2.4 is approximately $-70mV$ (Purves et al., 2001). For other non physiological quantities the initial conditions are specified as used.

2.4 Analysing Tools

2.4.1 Bifurcation Analysis

The solutions to the time dependent differential equation sets can be one of two states depending on the applied stimulus (β) in this research: steady state or stable oscillations over time. A steady state solution over time refers to the system reaching a single value for the rest of time if unperturbed. A stable oscillatory solution refers to an oscillation with defined period and an identifiable maximum and minimum.

To quantify the difference between different dynamics bifurcation analysis was undertaken. This was achieved by determining either the steady state solution or the maximum, minimum and period of the stable oscillations. As the bifurcation parameter is varied through a threshold, topologically inequivalent behaviour occurs. Additionally, the type of bifurcations were found, which included identifying if the bifurcation point was a Hopf bifurcation. A Hopf bifurcation is defined as a change in stability of a fixed point, and the creation/destruction of a periodic orbit (which may or may not be attracting).

A bifurcation diagram, in this instance, depicts the effect of the bifurcation parameter (β) on the considered concentration or membrane potential. It indicates either a single value for the steady state solution or two values, the maximum and minimum, of the stable oscillations.

The bifurcations diagrams, bifurcation types and period of oscillation within this research were all found using the software program AUTO07p. AUTO is publicly available software for analysing continuation and bifurcation problems of Ordinary Differential Equation (ODE), originally written in 1980 and with the most recent update in 2007 (Champneys et al., 2000).

3 Review of Existing Simple Oscillatory Models

3.1 Introduction

Cellular modelling is at the forefront of cerebral disease understanding and over the past century many advances have been made in the modelling techniques. In order to progress the understanding of the reaction dynamics of mammalian cells under an applied stimuli, an in-depth review of existing models is necessary. There exist multiple distinctly different mathematical models of mammalian cells. Thus, in order to focus on the desired dynamics only, Simplified Generic Oscillatory Cell Model/s (SGOCM) (to be described) have been chosen. Not all the models chosen within this chapter meet all the requirements of a SGOCM, but rather they meet most of the requirements.

A SGOCM refers to a model that is, firstly, simple. A simple model is defined here to consist of 4 or less ODEs in its definition, giving rise to 4 or less variables. This criteria is imposed to strictly exclude models of unnecessary complexity introduced by less influential ionic concentrations and their ionic pathways' open probabilities. Examples of this would include the cell models (within the NVU) described by Dormanns et al. (2015) or the detailed SMC

model detailed by Johny et al. (2015).

A SGOCM secondly refers to a generic cell model. A generic model is negatively defined by virtue of not modelling any particular cell type. The purpose of this criteria is to investigate types of dynamics a cell can experience that are apparent across multiple types of cells. This selection attempts to broaden the applicability of the results across multiple areas.

Thirdly, and most importantly, a SGOCM defines an oscillatory model. As described in Section 2.1.4, in order to provide an environment for which waves in tissue media can occur the single cell must exhibit oscillatory properties for a specific stimulus, β. Thus, there must be at least 2 interconnected properties, with at least two fluxes, which exchange in a time dependent manner. In addition to this, the model must go to a stable solution, again depending on the applied stimulus.

Finally, a SGOCM needs to be of a single cell type. The purpose of this criteria is to exclude models of multiple different types of cells connected together that could add unnecessary complexity to the equation set. A single cell type can include intracellular stores such as an ER so oscillatory dynamics (mentioned in Section 2.1.4) can occur. This criteria excludes models such as that by Farr and David (2011) and Dormanns et al. (2015) which model the entire NVU.

An advantage, of a SGOCM is the ability to apply the overall results to more intricate, larger scale models such as by Dormanns et al. (2015). By breaking down the dynamic behaviour into its principle components, the more intricate, larger scale models can attribute or isolate desired (or undesirable) behaviours. A disadvantage of a SGOCM is the possibility to miss the desired components/dynamics by a skewed selection of models. To mitigate this, five models have been chosen to obtain a variety of SGOCMs. The five models selected

for further in-depth analysis are described by: Goldbeter et al. (1990), Dupont and Goldbeter (1994), Gonzalez-Fernandez and Ermentrout (1994), FitzHugh (1961) and Koenigsberger et al. (2004).

The first two models under examination are described by Goldbeter et al. (1990) and Dupont and Goldbeter (1994) and will be, henceforth, known as the Goldbeter model and the Dupont model respectively. The Goldbeter model, described as the *'two pool model'*, is an early variation of the Dupont model which is described as the *'one pool model'*. Both have been modelled by a lumped parameter method (Section 2.1.1) tracking calcium ion transfer between the cytosol and the intracellular store. The Goldbeter model included an assumption of an 'infinite store' (to be further detailed) which propagated into other models. This assumption was later removed in the Dupont model.

The third and fourth models described by Gonzalez-Fernandez and Ermentrout (1994) and FitzHugh (1961) are variations on the Hodgkin-Huxley conductance based model (Hodgkin and Huxley (1952), Section 2.2.7). Conductance based models primarily track changes to the membrane potential which depends on the movement of ions and a channel's open probability. The model described by Gonzalez-Fernandez and Ermentrout (1994), known as the Ermentrout model, is focused on the changes depending on the movement of potassium and calcium ions as well as a lumped leak term. The Ermentrout model refers to the cells ion dynamics only and can be separated cleanly from the cell mechanics also described in Gonzalez-Fernandez and Ermentrout (1994). In comparison, the model described by FitzHugh (1961), known as the FitzHugh-Nagumo model, is significantly less physiological in its formation. The FitzHugh-Nagumo model was created to match the generic outline of data collect from a squid axon and is considered a minimal model. The dynamics

of the squid axons minimal model can be approximately related to a cell's oscillatory dynamics. This approximation allows the dynamics of the FitzHugh (1961) model to better fit the SGOCM classification.

Finally, the fifth model is described by Koenigsberger et al. (2004) and is known as the Koenigsberger model. This model is the most intricate of the 5 models and is often considered to not be a simple model. However, the Koenigsberger model is one of the simplest models to include both conductance based modelling techniques and chemical reaction based modelling techniques, making it an ideal comparison tool. Accordingly, the Koenigsberger model tracks both membrane potential and intracellular ionic calcium levels in both the cytosol and the store.

Importantly, although some of the original papers have a spatial component included in their source material, it has been excluded within this chapter and will be reinvestigated in a later chapter. In addition, some parameters have been renamed from the original content to keep consistent parameter names and avoid clashes over this chapter. Furthermore, most of the original sources did not include proper bifurcation analysis of the models. This was forgone by instead giving examples of the time dependent solution with variations of the bifurcation parameter. This chapter includes continuation based bifurcation diagrams (Section 2.4.1), in order to give a full picture of the model behaviour and set the scene for the spatially coupled work in later chapters.

3.2 The Goldbeter model

The Goldbeter model introduced in Goldbeter et al. (1990) was one of the first simplified three compartment cell models to match data trends. It was formed to indicate physiological ionic species movement through channels across the

membranes. The Goldbeter model consists of two coupled ODEs dedicated to the ionic calcium concentration in the cytosol (Z) and the ionic calcium concentration in the intracellular store (Y). This model, like the other 4 detailed models, includes a primary bifurcation parameter (β), which Goldbeter et al. (1990) state that:

> *'The magnitude of the influx from the* IP_3*-sensitive pool is taken as proportional to the saturation function* β *of the receptor for* IP_3 *[the cooperative nature of this saturation function is expressed implicitly in* β*]; the level of* IP_3 *established upon stimulation increases with the magnitude of the external signal'*

The wording of Goldbeter et al. (1990) is important for correct interpretation of the β parameter. β is related to the magnitude of the external stimuli and the saturation function of the IP_3 receptor. It should be made clear that the β parameter does not measure directly the IP_3 concentration. Finally, the concentrations of ionic calcium in the two compartments are seen to oscillate over time. This oscillation is due to the natural feedback loop between the cytosol and the store formed by the CICR channel for specific values of β. Figure 3.1 depicts a pictorial representation of the Goldbeter model including all the ionic pathways.

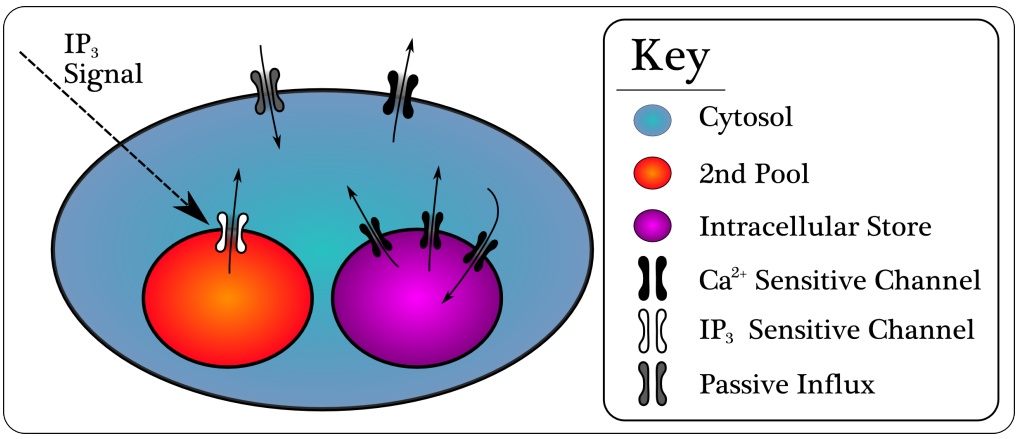

Figure 3.1: Diagram describing the dynamics of the Goldbeter model often referred to as a 2 pool model. Where Z measures the ionic calcium concentration in the cytosol and Y measures the ionic calcium concentration in the intracellular store.

Figure 3.1 shows three compartments: the cytosol, intracellular store and a second infinite intracellular store. The saturation of the IP_3 receptor due to the external signal (β) affects the release of calcium concentration from the IP_3 sensitive store. This store is often referred to as an infinite store due to there being no detailed feedback of concentration and the fact that it will not reduce in concentration (v_1) over time.

3.2.1 Goldbeter Equations

Using mass conservation within the compartments (Section 2.1.2) the rate of change equations of Z and Y over time were formed (Equations 3.1 and 3.2 respectively).

$$\frac{dZ}{dt} = V_{in} - V_2 + V_3 + k_f Y - kZ \tag{3.1}$$

$$\frac{dY}{dt} = V_2 - V_3 - k_f Y \tag{3.2}$$

where $k_f Y$ is the passive rate of calcium ion efflux from the intracellular store to the cytosol based on the calcium ion concentration in the intracellular store, and kZ is the passive rate of calcium ion efflux from the cytosol to the extracellular space based on the calcium ion concentration in the cytosol. V_{in} describes the calcium flux into the cell from both the passive influx and the second IP_3 sensitive store (Equation 3.3). This includes an assumption that the second IP_3 sensitive store has a high, constantly replenished calcium concentration and is often referred to as an infinite store. Therefore, it is not necessary to create a rate of change equation for the concentration within this compartment.

$$V_{in} = v_0 + v_1\beta \tag{3.3}$$

V_2 defines the rate of calcium ion concentration pumped back into the intracellular store via the calcium sensitive pump. The rate of the V_2 pump is determined by the Hill kinetics reaction (Section 2.2.3) and is defined by Equation 3.4.

$$V_2 = v_{M2}\frac{Z^n}{k_2^n + Z^n} \tag{3.4}$$

Finally, V_3 denotes the rate of calcium ion concentration release from the intracellular store via the calcium sensitive channel (the CICR channel). This channel is defined as the combination of Hill kinetics (Section 2.2.3) of both the intracellular store calcium ion concentration and the calcium ion concentration in the cytosol (Equation 3.5).

$$V_3 = v_{M3}\frac{Y^m}{k_R^m + Y^m}\frac{Z^p}{k_a^p + Z^p} \tag{3.5}$$

where all constants detailed in Equations 3.1 to 3.5 are defined by Table 3.1.

Table 3.1: Constants used in the Goldbeter model defined by Goldbeter et al. (1990). Described by Equations 3.1 to 3.5.

Constant	Value	Units	Description
v_0	1	$\mu M s^{-1}$	Passive rate calcium from background extracellular medium
v_1	7.3	$\mu M s^{-1}$	Maximum IP_3 stimulated calcium influx from the IP_3 sensitive store
v_{M2}	65	$\mu M s^{-1}$	Maximum rate exchange via pumping from store V_2
v_{M3}	500	$\mu M s^{-1}$	Maximum rate exchange via release from store V_3
k	10	s^{-1}	Passive efflux constant of calcium from cytosol to extracellular space
k_f	1	s^{-1}	Passive efflux constant of calcium from store to cytosol
k_2	1	μM	Threshold constant pumping
k_R	2	μM	Threshold constant release
k_a	0.9	μM	Threshold constant activation
n	2	–	Hill Coefficient pumping
m	2	–	Hill Coefficient release
p	4	–	Hill Coefficient activation

3.2.2 Goldbeter Results

First, to get an idea of the oscillatory dynamics of the Goldbeter model the ODE system of equations described by Equations 3.1 to 3.5 were integrated over time using the ODE solver in the software MATLAB as per Section 2.3.1. One example of $\beta = 0.4$ was used to compute the integral and display the results for some time such that any effect of the initial conditions is negligible.

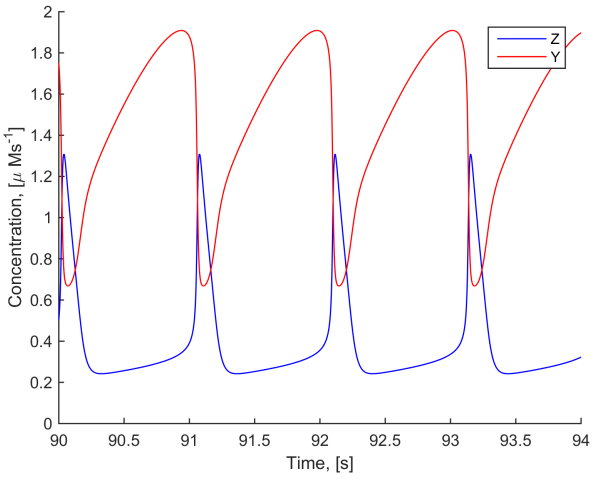

Figure 3.2: Example oscillatory dynamics of Goldbeter model ODEs (Equations 3.1 to 3.5) with $\beta = 0.4$.

Figure 3.2 shows the time dependent relationship between the two variables Z and Y. As previously mentioned, Goldbeter et al. (1990) did not include a complete bifurcation analysis of the Goldbeter model. This has been included here to compare and contrast the existing simple mathematical models. Bifurcation diagrams for each of the variables, Z and Y, were found as described by Section 2.4.1 using the continuation software AUTO.

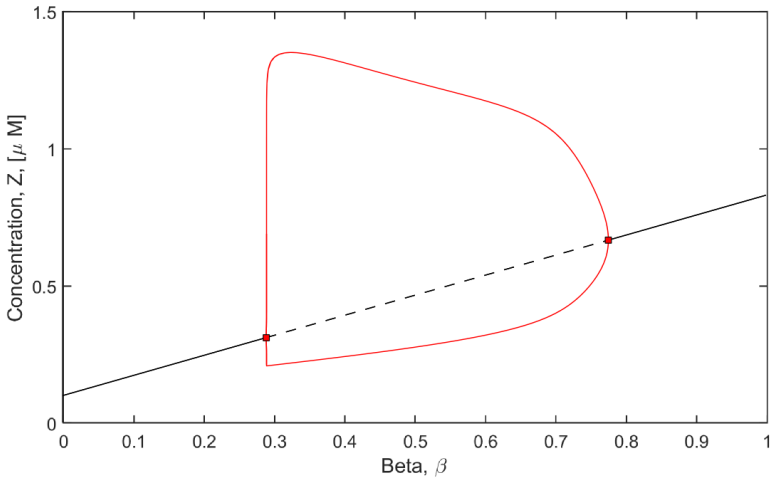

Figure 3.3: Bifurcation diagram of the Goldbeter model for the calcium concentration in the cytosol, representing the maximum/minimum concentration experienced for the single cell model. Black solid lines indicate stable fixed points, black dashed lines indicate unstable fixed points, red lines indicate stable limit cycles and red squares indicate bifurcation points.

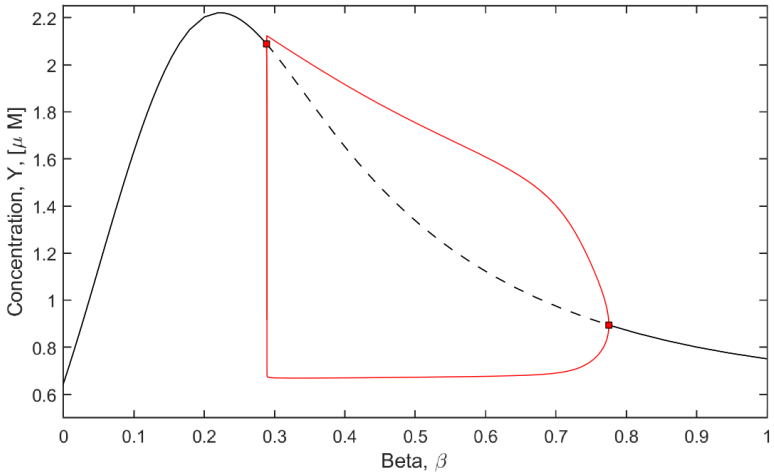

Figure 3.4: Bifurcation diagram of the Goldbeter model for the calcium concentration in the intracellular store, representing the maximum/minimum concentration experienced for the single cell model. Black solid lines indicate stable fixed points, black dashed lines indicate unstable fixed points, red lines indicate stable limit cycles and red squares indicate bifurcation points.

From the software package AUTO (Section 2.4.1) it is clear that the Goldbeter model contains two Hopf bifurcations occurring at $\beta = 0.289$ and $\beta = 0.775$. For values of β between these bifurcations ($0.289 < \beta < 0.775$) the calcium ion concentration oscillates over time. Conversely, the concentrations (Z and Y) both come to a steady state value over time for β values outside this region ($\beta < 0.289 \bigcap \beta > 0.775$). During the low β values steady state region the calcium concentration in the cytosol is up to 10 times smaller than that of the calcium concentration in the intracellular store. This is similar to experimental values described in Section 2.3.2.

The near vertical lines on the bifurcation diagrams (Figure 3.3 and 3.4) are attributed to the similar profiles of the nullclines separating with a change in β. This nullcline behaviour is described in detail by Kenny et al. (2016) and as such is not included here. Next, the stable oscillation associated periods were found using the continuation software AUTO.

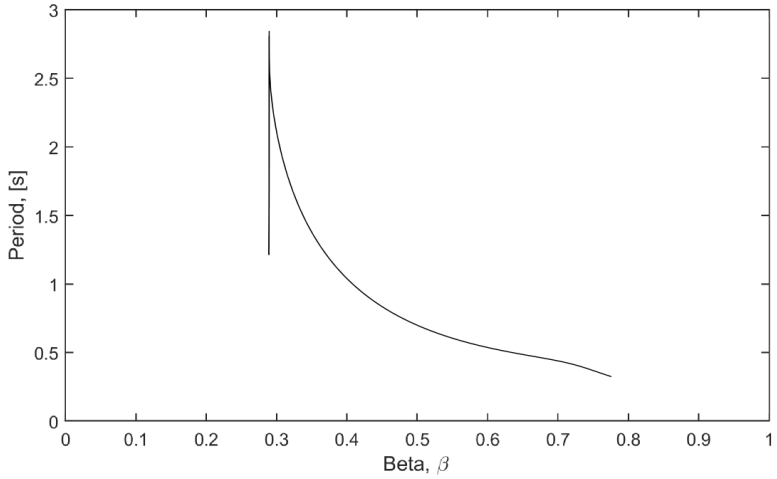

Figure 3.5: Period of oscillation for the single cell Goldbeter model. Note that a period is only found when the solution oscillates (See Figure 3.3).

The oscillations that occur on the range ($0.289 < \beta < 0.775$) have an associated period of oscillation (Figure 3.5). In particular, as β decreases towards the 'lower Hopf bifurcation' (occurring at $\beta = 0.289$) the period of oscillation increases rapidly.

3.3 The Dupont model

Dupont and Goldbeter (1993) and additionally Dupont and Goldbeter (1994) initially describe the Goldbeter model (the two pool model) and then compare it to a one pool model. Dupont and Goldbeter (1993) cited the reason for the change between a two pool and a one pool model was because:

> *'Recent experiments indicate that* Ca^{2+} *channels may sometimes be sensitive to both* IP_3 *and* Ca^{2+}*. Such a regulation may be viewed as* Ca^{2+}*-sensitized* IP_3*-induced* Ca^{2+} *release or, alternatively, as a form of* IP_3*-sensitized* CICR*'*

This variation model is henceforth known as the Dupont model. The Dupont model (similar to the Goldbeter model) tracks the ionic calcium concentration in the cytosol (Z) and the ionic calcium concentration in the intracellular store (Y). The major difference between these two models is the removal of the second infinite intracellular store and adding an IP_3 sensitivity to the CICR channel. For the Dupont model the definition of the parameter β is slightly altered (Dupont and Goldbeter, 1994):

> *'*β *represents the degree of saturation by* IP_3 *of this "bi-activated" receptor'*

Figure 3.6 gives the pictorial representation of the Dupont model which contains one pool, for comparison to the two pool model (Figure 3.1).

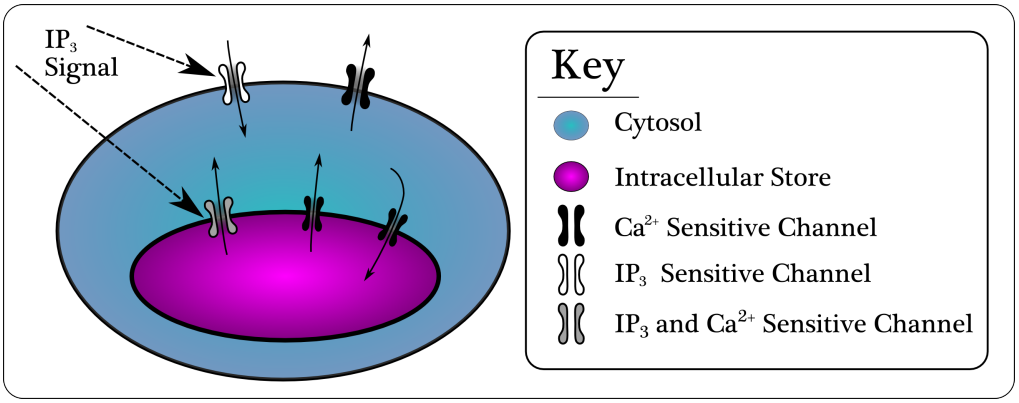

Figure 3.6: Diagram describing the dynamics of the Dupont model referred to as a 1 pool model. Diagram shows a single intracellular store with the presence of IP_3 effecting the extracellular pump into the cell and the CICR.

3.3.1 Dupont Equations

The rates of change of ionic calcium concentration in the cytosol (Z) and ionic calcium concentration in the intracellular store (Y) are defined by Equations 3.6 and 3.7 respectively (see Figure 3.6).

$$\frac{dZ}{dt} = V_{in} - V_2 + V_3 + k_f Y - kZ \tag{3.6}$$

$$\frac{dY}{dt} = V_2 - V_3 - k_f Y \tag{3.7}$$

where, again similar to the Goldbeter model, $k_f Y$ is the passive rate of calcium ion efflux from the intracellular store to the cytosol based on the calcium ion concentration in the intracellular store and kZ is the passive rate of calcium

ion efflux from the cytosol to the extracellular space based on the calcium ion concentration in the cytosol.

The flux into the cell, V_{in} (Equation 3.8), has been renamed to the extracellular passive influx and the extracellular influx through the IP_3 sensitive channel.

$$V_{in} = v_0 + v_1\beta \tag{3.8}$$

The definition of V_2 remains the same, being the rate of calcium ion concentration pumped back into the intracellular store via the calcium sensitive pump. The rate of the V_2 pump is determined by the Hill kinetics reaction (Section 2.2.3) and is defined by Equation 3.9.

$$V_2 = v_{M2}\frac{Z^n}{k_2^n + Z^n} \tag{3.9}$$

Finally, V_3 now denotes the rate of calcium ion concentration release from the intracellular store via the IP_3 and calcium sensitive channel, the IP_3-sensitized CICR. This channel is defined as the combination of Hill kinetics (Section 2.2.3) of both the intracellular store calcium ion concentration and the calcium ion concentration in the cytosol and additionally multiplied by β (Equation 3.5).

$$V_3 = \beta v_{M3}\frac{Y^m}{k_R^m + Y^m}\frac{Z^p}{k_A^p + Z^p} \tag{3.10}$$

The constants described in Equations 3.6 to 3.10 are the same as described in Section 3.2 (Table 3.1).

The difference in the equations is seen only in Equation 3.10, with the addition of an IP_3 sensitivity on the CICR channel. The new definition is now the rate of calcium ion concentration release from the calcium and IP_3 sensitive store via the CICR channel. V_{in} is also redefined to the rate of calcium ion con-

centration entering the cell from both passive influx and the IP_3 sensitive influx. This addition was made to make the model fit a different physiological situation.

3.3.2 Dupont Results

First, to get a rough idea of the oscillatory dynamics of the Dupont model, the system was integrated over time. The ODEs (described by Equations 3.6 to 3.10) was integrated over time using the the software MATLAB as per Section 2.3.1. One example of $\beta = 0.45$ was used to compute the integral and display the results for some time such that any effect of the initial conditions is negligible.

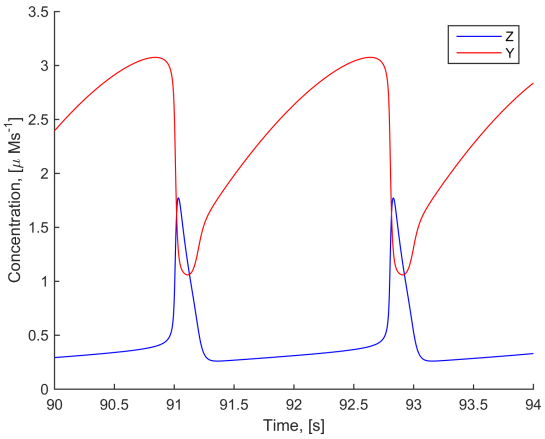

Figure 3.7: Example oscillatory dynamics of Dupont model ODEs (Equations 3.6 to 3.10) with $\beta = 0.45$.

Figure 3.7 shows the time dependent relationship between the two variables Z and Y. A complete bifurcation analysis of the Dupont model has been included here to obtain a complete review of these existing simple mathematical models. Bifurcation diagrams for each of the variables, Z and Y, were found as described in Section 2.4.1 using the continuation software AUTO.

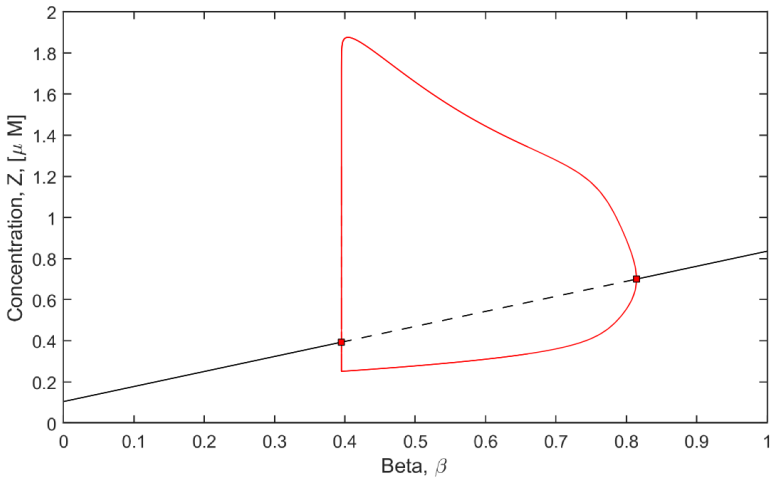

Figure 3.8: Bifurcation diagram of the Dupont model for the ionic calcium concentration in the cytosol (Z), representing the maximum/minimum concentration experienced for the single cell model. Black solid lines are stable fixed points, black dashed lines are unstable fixed points, red lines are stable limit cycles and red squares are bifurcation points.

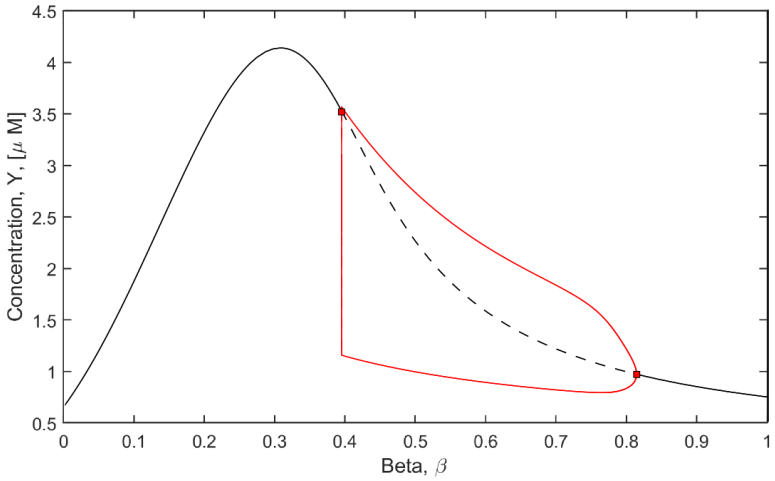

Figure 3.9: Bifurcation diagram of the Dupont model for the ionic calcium concentration in the intracellular store (Y), representing the maximum/minimum concentration experienced for the single cell model. Black solid lines are stable fixed points, black dashed lines are unstable fixed points, red lines are stable limit cycles and red squares are bifurcation points.

Using the software AUTO, the Dupont model was shown to have two Hopf bifurcations occurring at $\beta = 0.395$ and $\beta = 0.814$. For values of β between these bifurcations ($0.395 < \beta < 0.814$) the system oscillates in calcium ion concentration with the period shown in Figure 3.10. For β values outside this region ($\beta < 0.395 \bigcap \beta > 0.814$) the concentrations come to a steady state value over time. The calcium concentration in the cytosol is approximately $0.1 - 1.9\mu M$ compared to that of the intracellular store's $0.4 - 4.3\mu M$. Again, for the oscillatory interval, $0.395 < \beta < 0.814$, the oscillations have an associated period detailed by Figure 3.10.

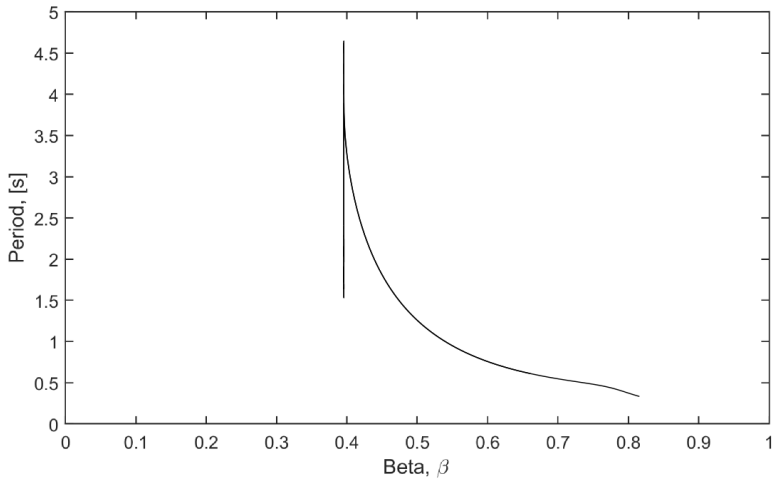

Figure 3.10: Period of oscillation for the single cell Dupont model. Note that a period is only found when the solution oscillates (See Figure 3.8).

Figure 3.10 shows that overall as β decreases towards the 'lower Hopf bifurcation' the period increases rapidly. Figure 3.10 shows the overall detail of the period of oscillation. This level of detail is sufficient for later comparisons on

the macroscale. Thus, additional detailed zooms were considered surplus to the needs of the model.

3.3.3 Extension to One and Two Pool Model

Dupont and Goldbeter (1994) refer to an extension to both the two pool Goldbeter model (Section 3.2), and the one pool Dupont model (Section 3.3). The extension is in reference to redefining the saturation level of the IP_3 receptor (β). Equation 3.11 redefines how β is found.

$$\beta = \frac{A^3}{K_1^3 + A^3} \tag{3.11}$$

where K_1 is the dissociation constant of the IP_3 receptor and A is the concentration of IP_3. A is then found by a new additional differential equation, Equation 3.12.

$$\frac{\partial A}{\partial t} = v_p R - k_d A \tag{3.12}$$

The change in IP_3 concentration is dependent on the fractional decrease in IP_3 via degradation (k_d) and the forced increase from external sources (v_p). Finally, R denotes the "degree of PLC activation" [-]. The constants in Equations 3.11 and 3.12 are defined in Table 3.2.

Table 3.2: Constants used in the Dupont and Goldbeter (1994) Extension model equation set. Described by Equations 3.11 to 3.12.

Constant	Value	Units	Description
K_1	0.1	μM	Dissociation Constant of IP_3 Receptor
v_p	30^{-1}	$\mu M s^{-1}$	Maximal Rate IP_3 Production
k_d	60^{-1}	s^{-1}	First order kinetic constant IP_3 degradation

It is important to note that neither the calcium concentration in the cytosol, nor the intracellular store, feeds back into this equation, making it independent of Z and Y. The model has therefore simply moved the unknown bifurcation parameter from the degree of saturation of the IP_3 channel to the degree of PLC activation. Subsequently, the extension to these models is added complexity with insufficient additional information about the dynamics. Therefore, this extension to the Goldbeter model and the Dupont model is not necessary in the understanding of the underlying cell oscillatory mechanics.

3.4 The Ermentrout model

The model described by Gonzalez-Fernandez and Ermentrout (1994) is principally similar to the Hodgkin and Huxley (1952) conductance-based model (Section 2.2.7). The dynamics associated with the cell defined by Gonzalez-Fernandez and Ermentrout (1994) is hereafter named the Ermentrout model. The Ermentrout model tracks the rate of change of membrane potential of a SMC based on the transfer of calcium and potassium ions across the cell membrane. Although Gonzalez-Fernandez and Ermentrout (1994) specify a specific type of cell (the SMC) the dynamics and equations are generic enough to still fit the definition of a SGOCM.

The Ermentrout model, unlike the Goldbeter model and the Dupont model, does not consider an intracellular store to be necessary to create oscillations in the cytosolic calcium ion concentration. Gonzalez-Fernandez and Ermentrout (1994) state “The vessel’s stationary cyclic concentrations and steady state tone are ...not contributed to by the intracellular stores”. What the Ermentrout model does measure, in addition to the membrane potential and the cytosolic free calcium, is the probability of the open states of the channels associated with the

movement of potassium ions across the membrane (Section 2.2.6).

Gonzalez-Fernandez and Ermentrout (1994) also go on to couple these dynamics to the vessel mechanics to understand the effect on the blood vessel diameter. They found that the stress on the blood vessel and therefore the vessel diameter, strictly lags the calcium ion concentration oscillation. These dynamics were based upon experimental data. Given that the vessel dynamics strictly lag the ionic concentration dynamics they can be decoupled without negative consequences. Thus, for the purpose of this investigation on SGOCMs, the Ermentrout model only refers to the generic ionic cell dynamics.

3.4.1 Ermentrout Equations

There are three coupled ODE equations, Equations 3.13, 3.14 and 3.15, which represent the rate of change of the ionic calcium concentration in the cytosol (Z), the Cellular Membrane Potential (V) and the Open Probability of the Potassium Channel (N) respectively.

$$\frac{dZ}{dt} = (-\alpha g_{Ca} m_\infty (V - v_{Ca}) - k_{Ca} Z)\rho \tag{3.13}$$

$$\frac{dV}{dt} = \frac{1}{C_m}(-g_L(V - v_L) - g_K N(V - v_k) - g_{Ca} m_\infty (V - v_{Ca})) \tag{3.14}$$

$$\frac{dN}{dt} = \lambda_n (n_\infty - N) \tag{3.15}$$

The membrane potential equation (Equation 3.14) is formed by three separate ions movement and thus three currents across the cell membrane: leak, potassium and calcium. In accordance with Equation 2.20 from Section 2.2.7 (the Hodgkin and Huxley (1952) model) the current is found by multiplying the maximum change in voltage (if free movement were applied) by the probability of the channel being open and the rate conversion coefficients (g_i). m_∞ (Equation

3.16), n_∞ (Equation 3.17) and N define the equilibrium distribution of the open states depending on membrane potential, cytoplasmic free calcium and fraction of potassium respectively.

$$m_\infty = 0.5\left(1+\tanh\left(\frac{V-(v_{1a}+v_{1b}\beta_2)}{v_2}\right)\right) \tag{3.16}$$

$$n_\infty = 0.5\left(1+\tanh\left(\frac{V-v_3}{v_4}\right)\right) \tag{3.17}$$

In order to account for the buffering of calcium (Section 1.2.4) the ratio of free to bounded calcium is defined by Equation 3.18 (ρ).

$$\rho = \frac{(K_d+Z)^2}{(K_d+Z)^2+K_dB_T} \tag{3.18}$$

The concept of buffering is explicitly noted by Gonzalez-Fernandez and Ermentrout (1994), while the previous models factor the buffering ratio into their constants proceeding each term, making them proportionally smaller results. Next, v_3 represents the membrane potential associated with opening half the population of channels with respect to the cytoplasmic free calcium concentration (Equation 3.19).

$$v_3 = -\frac{v_5}{2}\tanh\left(\frac{Z-Ca_3}{Ca_4}\right)+v_6 \tag{3.19}$$

λ_n, according to Morris and Lecar (1981), is the rate constant for opening the K^+ channel. It based on statistical considerations (Equation 3.20).

$$\lambda_n = \phi_n\cosh\left(\frac{V-v_3}{2v_4}\right) \tag{3.20}$$

Lastly, in order to convert the rate of change of membrane potential to a rate of change of calcium, a constant conversion, α [μMC^{-1}], was applied (Equation

3.21).

$$\alpha = \frac{c_c}{z_{Ca} f_{Vol} Vol_{Cell} F} \tag{3.21}$$

where c_c is a conversion factor defined by Equation 2.5 in Section 2.2. Finally, the bifurcation parameter, β_2, is notably different from previous models (β). Here, β_2 represents the fractional amount of voltage associated with the opening of half the population of channels dependent on cytosolic free calcium (v_1). This is desired to be adjustable between $-13mV$ and $-36mV$ (hence the breakdown of v_1 to v_{1a} and v_{1b}) dependent on the transmural pressure as described in Gonzalez-Fernandez and Ermentrout (1994). Physically, this suggests that cytosolic calcium concentration oscillation is induced by multiple different pathways; either IP_3 channel saturation (Goldbeter model, Dupont model) or the transmural pressure (Ermentrout model). Although β_2 is distinguishable different than β in the other models from this point forward β_2 will simply be known as β representing the bifurcation parameter. All other constants described by Equations 3.13 to 3.21 are defined in Table 3.3.

Table 3.3: Constants used in the Gonzalez-Fernandez and Ermentrout (1994) model equation set. Described by Equations 3.13 to 3.21.

Constant	Value	Units	Description
g_{Ca}	1.57×10^{-13}	$Cs^{-1}mV^{-1}$	Maximum Whole-cell Membrane Calcium Conductance
v_{Ca}	80	mV	Nernst reversal potential Calcium
k_{Ca}	1.3567537×10^{2}	s^{-1}	First order rate constant for cytosolic calcium concentration
K_d	1	μM	Ratio of k_- to k_+
B_T	1.0×10^{2}	μM	Calcium Buffering Total Concentration
g_L	7.854×10^{-14}	$Cs^{-1}mV^{-1}$	Maximum Whole-cell Membrane Leak Conductance
v_L	-70	mV	Nernst reversal potential Leak
g_K	3.1416×10^{-13}	$Cs^{-1}mV^{-1}$	Maximum Whole-cell Membrane Potassium Conductance
v_k	-90	mV	Nernst reversal potential Potassium
v_{1a}	-13	mV	Base level voltage associated opening half the population Calcium Channels
v_{1b}	-23	mV	Potential change in voltage associated opening half the population Calcium Channels
v_2	25	mV	Measure of distribution for v_1
v_4	14.5	mV	Measure of distribution for v_3
v_5	8	mV	Range of n_{inf} with Z
v_6	-15	mV	Shift of n_{inf} with Z
Ca_3	0.4	μM	Calcium concentration associated opening half the population Calcium Channels
Ca_4	0.15	μM	Measure of distribution for Ca_3
ϕ_n	2.664	s^{-1}	Amplitude of λ_n
C_m	1.9635×10^{-14}	CmV^{-1}	Membrane Capacitance Coefficient
f_{Vol}	5.5×10^{-1}	–	Fraction of Cytosol to Cell Volume
Vol_{Cell}	1.1781×10^{-9}	cm^3	Cell Volume
F	9.6487×10^{4}	$Cmol^{-1}$	Faraday Constant
z_{Ca}	2	–	Valance of a Calcium ion

3.4.2 Ermentrout Results

Again, to get a rough idea of the oscillatory dynamics of the Ermentrout model, the ODE system described by Equations 3.13 to 3.21 were integrated over time using the ODE solver in the software MATLAB as per Section 2.3.1. One example of $\beta = 0.4$ was used to compute the integral and display the results for some time such that any effect of the initial conditions is negligible.

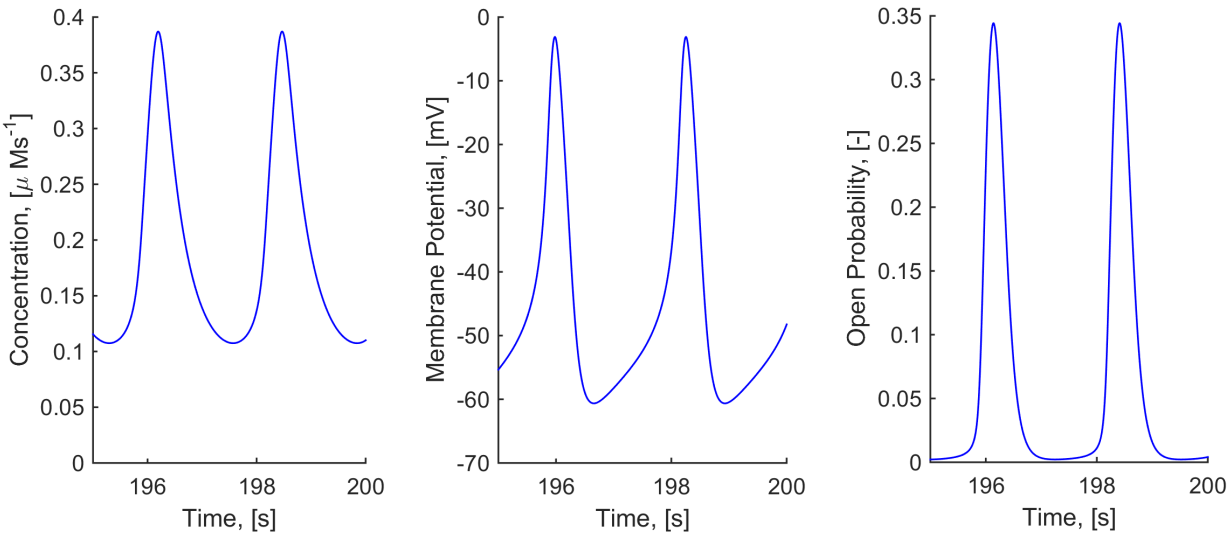

(a) Z *(b) V* *(c) N*

Figure 3.11: Example oscillatory dynamics of Ermentrout model ODEs (Equations 3.13 to 3.21) with $\beta = 0.4$.

Figure 3.11 shows the time dependent relationship between the three variables Z, V and N and shows that the peaks are not aligned over time. Again, to complete the review of existing models it is important to understand the bifurcation analysis of each detailed model. Figures 3.12, 3.13 and 3.14 define the relationship between Z, V, N and the bifurcation parameter β respectively.

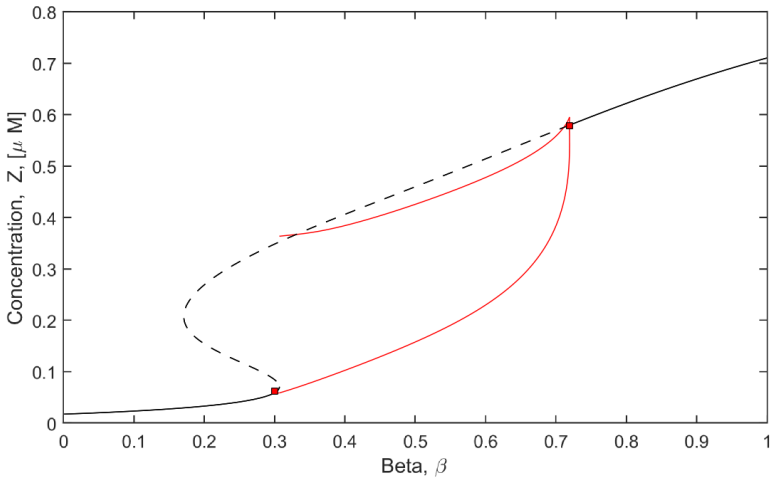

Figure 3.12: Bifurcation diagram of the Ermentrout model for the calcium concentration in the cytosol, representing the maximum/minimum concentration experienced for the single cell model. Black solid lines indicate stable fixed points, black dashed lines indicate unstable fixed points, red lines indicate stable limit cycles and red squares indicate bifurcation points.

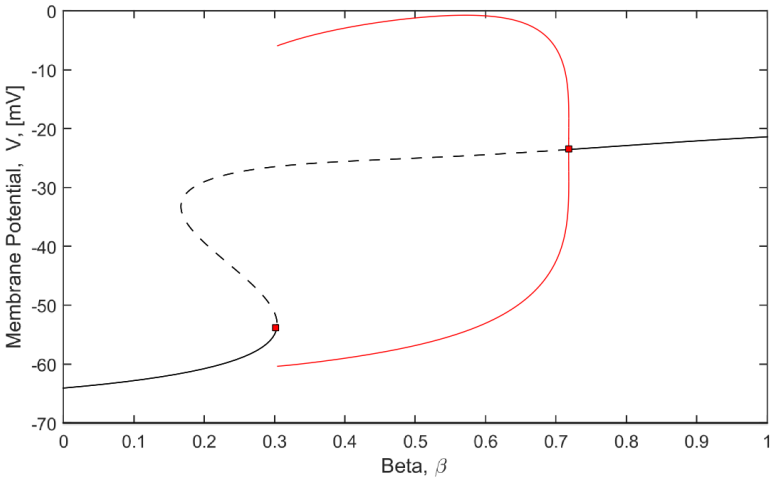

Figure 3.13: Bifurcation diagram of the Ermentrout model for the membrane potential, representing the maximum/minimum experienced for the single cell model. Black solid lines indicate stable fixed points, black dashed lines indicate unstable fixed points, red lines indicate stable limit cycles and red squares indicate bifurcation points.

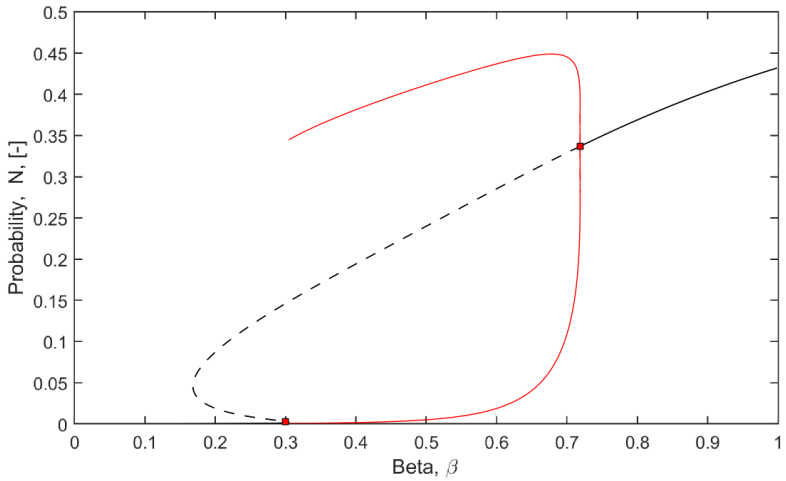

Figure 3.14: Bifurcation diagram of the Ermentrout model for the open probability, representing the maximum/minimum experienced for the single cell model. Black solid lines indicate stable fixed points, black dashed lines indicate unstable fixed points, red lines indicate stable limit cycles and red squares indicate bifurcation points.

The continuation software AUTO determined there exists a Hopf bifurcation point at $\beta = 0.719$ and a limit point bifurcation point at $\beta = 0.299$. According to Kenny et al. (2016) this limit point bifurcation can be categorised as a *"saddle node infinite cycle bifurcation point"*. A steady state solution occurs for a range of low and high β values ($\beta < 0.299 \bigcap \beta > 0.719$). For $0.299 < \beta < 0.719$ the Ermentrout model experiences oscillations and as such has an associated period, as described in Figure 3.15.

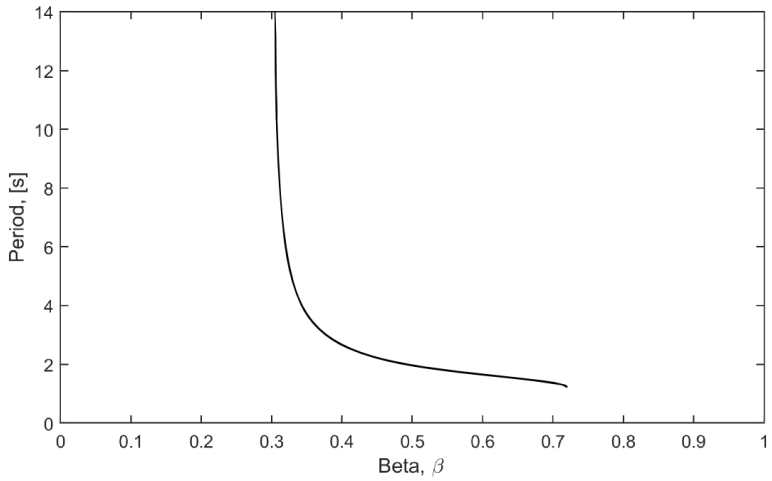

Figure 3.15: The Ermentrout model period of the oscillation. Note that a period is only found when the solution oscillates (See Figure 3.12).

Figure 3.15 shows that the Ermentrout model, similar to the Goldbeter model and the Dupont model, has a period of oscillation increasing (to infinity) with reducing β towards the lower bifurcation point located at $\beta = 0.299$.

The ionic calcium concentration in the cytosol (Z) ranges from 0 to $0.7\mu M$, which is within acceptable values (Section 2.3.2). The Ermentrout model has a membrane potential within acceptable levels for a vascular smooth muscle cell or a endothelial cell according to Section 2.2.4. The open probability of between 0 to 0.4 is within expected values according to Gonzalez-Fernandez and Ermentrout (1994). On the whole, the Ermentrout model relatively accurately describes the cytosolic calcium concentration and membrane potential as it set out to do.

3.5 The FitzHugh-Nagumo model

The model described independently by both FitzHugh (1961) and Nagumo et al. (1962) is an extremely simplified version of the Hodgkin and Huxley (1952) conductance-based model and has been aptly named the FitzHugh-Nagumo model. The model described by FitzHugh (1961) is a minimal model to match data produced from a squid axon. The dynamics are simplified to a point where the two tracked variables are not to be identified physically, except to say that one relates to "electrical potential and excitability" and the other to "accommodation and refractoriness". Nagumo et al. (1962) confirms this by saying the model is "one of the simplest mathematical models of the nerve axon". As such, the equations do not consider dimensional analysis. Therefore, minor adjustments were made to make the equations dimensionally correct without changing the dynamics.

Instead of being based on ion movement, the equations in FitzHugh (1961) and Nagumo et al. (1962) model, are based on the relationship between two rates of change: a fast and a slow rate. The rate of change of the electrical potential (W) is considerably faster than that of the recovery voltage (U). It was formed originally as a Lienard's transformation to a simple mass spring-damper-system and is now recognised as a simple oscillatory model.

Although this model was not created to align with cell mechanics, it does capture the overall oscillatory dynamics of the membrane potential in time. This makes the model useful to compare mathematically to the former three models (Sections 3.2, 3.3 and 3.4) as it does not contain any additional unnecessary complexity. It will also be used in later chapters to compare to toy models (Chapter 6) and to show an important phenomenon yet to be introduced.

Multiple different sources have previously completed bifurcation analysis and travelling wave analysis on the FitzHugh-Nagumo model. In particular, Guckenheimer and Kuehn (2009), Krupa et al. (1997), Liu and Van Vleck (2006) and Hsu et al. (2009), to name a few, all investigated the FitzHugh-Nagumo model. The level of detail at which the FitzHugh-Nagumo model is presented within this research will, thus, be minimal in comparison to show only the overall desired dynamics.

3.5.1 FitzHugh-Nagumo model Equations

As mentioned previously the two main equations, 3.22 and 3.23, are related to electrical potential, W, and recovery voltage, U, respectively.

$$\frac{dW}{dt} = c(W - \frac{W^3}{d} - U + \beta_3 I) \tag{3.22}$$

$$\frac{dU}{dt} = \frac{1}{\tau}(W + a - bU) \tag{3.23}$$

where all constants in Equations 3.22 and 3.23 are defined in Table 3.4. W models the faster changes of the electrical potential and U is the recovery variable related to the gating mechanism of the membrane channels. I is the maximum magnitude of stimulus current that can be applied to the system and β_3 (different to the previous 3 models) represents the fraction of this stimuli. Again, although β_3 is distinguishable different than β_i in the other models from this point forward β_3 will simply be known as β representing the bifurcation parameter.

Table 3.4: Constants used FitzHugh-Nagumo model equation set. Described by Equations 3.22 and 3.23.

Constant	Value	Units	Description
a	0.7	$[W]$	No description *
b	0.8	$-$	No description
c	1	s^{-1}	Dimensional accuracy †
d	3	$[W]^2$	No description *
τ	12.5	s	No description †
I	1	$[W]$	External Stimulus *

3.5.2 FitzHugh-Nagumo Results

First, to get a rough idea of the oscillatory dynamics of the FitzHugh-Nagumo model, the ODE system described by Equations 3.22 and 3.23 was integrated over time using the ODE solver in the software MATLAB as per Section 2.3.1. One example of $\beta = 0.4$ was used to compute the integral and display the results for some time such that any effect of the initial conditions is negligible.

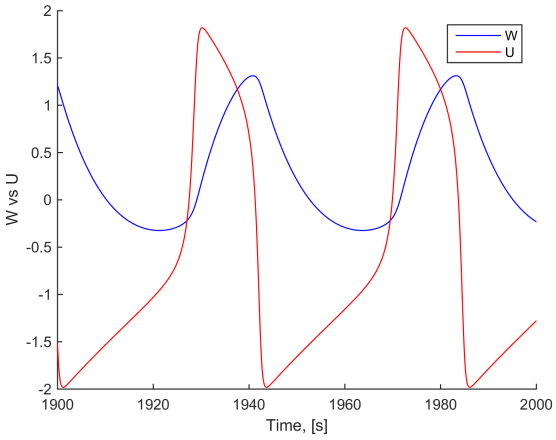

Figure 3.16: Example oscillatory dynamics of FitzHugh-Nagumo model ODEs (Equations 3.22 to 3.23) with $\beta = 0.4$.

* $[W]$ denotes the same units as the variable W which along with U is not specified.

† Time assumed dimensions of seconds. Not confirmed

Again, to compare the FitzHugh-Nagumo model to the previous three defined models, bifurcation analysis in the software AUTO (Section 2.4.1) was completed. Figure 3.17 and Figure 3.18 represent the variables response to the bifurcation parameter β.

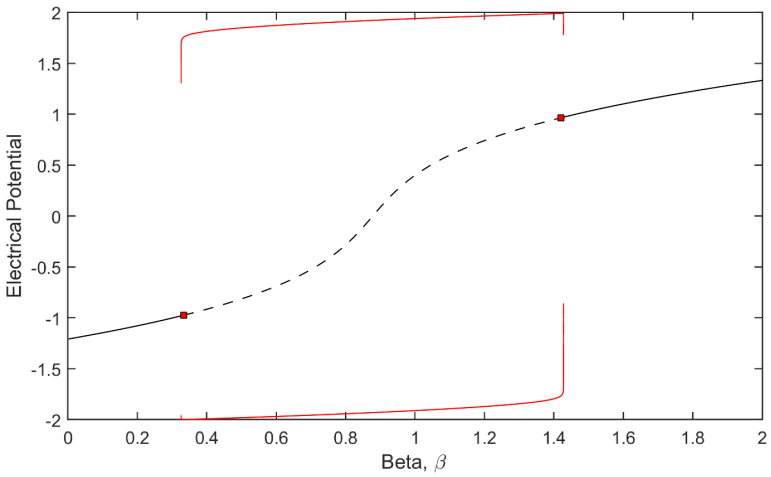

Figure 3.17: Bifurcation diagram of the FitzHugh-Nagumo model for the electrical potential, representing the maximum/minimum experienced for the single cell model. Black solid lines indicate stable fixed points, black dashed lines indicate unstable fixed points, red solid lines indicate stable limit cycles and red squares indicate bifurcation points.

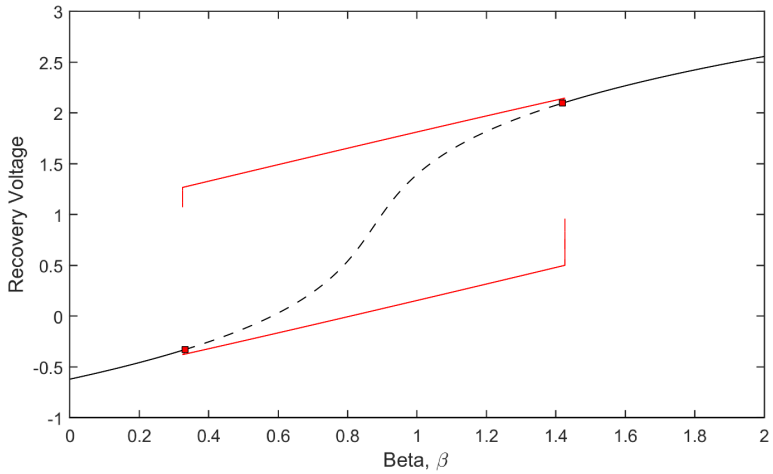

Figure 3.18: Bifurcation diagram of the FitzHugh-Nagumo model for the recovery voltage, representing the maximum/minimum experienced for the single cell model.Black solid lines indicate stable fixed points, black dashed lines indicate unstable fixed points, red solid lines indicate stable limit cycles and red squares indicate bifurcation points.

As found via the software AUTO, the FitzHugh-Nagumo model contains two Hopf bifurcations at $\beta = 0.333$ and $\beta = 1.417$. Above and below these bifurcations the solution reaches a steady state value over time. Between these two bifurcations the model oscillates in potential with an associated period detailed by Figure 3.19. Note potential unstable limit cycles near the bifurcation points on Figure 3.17 and 3.18 were omitted for clarity and readability. These bifurcations were determined to contain neglectable detail on the scale described above. For further reading a full diagnosis of these bifurcations was undertaken Kostova et al. (2004).

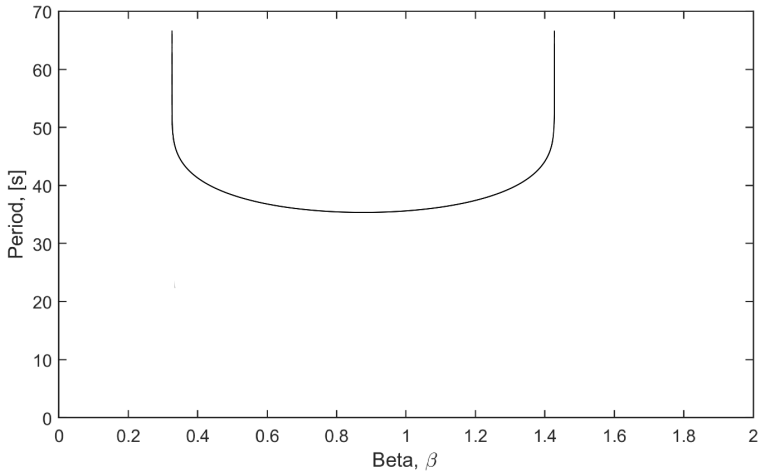

Figure 3.19: Period of oscillation for the FitzHugh-Nagumo model. Note that a period is only found when the solution oscillates (See Figure 3.18).

Figure 3.19 shows that both as β increases towards the upper bifurcation point ($\beta = 1.417$) and decreases towards the lower bifurcation point ($\beta = 0.333$) the period of oscillation increases. The period of oscillation has a minimum at approximately $\beta = 0.85$.

Note that due to the nature of the model $\beta \in [0,2]$ compared to the other models in which $\beta \in [0,1]$. Again, because the FitzHugh-Nagumo model does not aim to capture any physiological data, the values obtained for W and U are not compared to any physiological data.

3.6 The Koenigsberger model

It is arguable whether the model defined by Koenigsberger et al. (2004) meets enough of the classification of a SGOCM to be categorised as such. The model is specifically designed for the Smooth Muscle Cell (SMC) and is intricate

when compared to all of the other models considered. However, it is the simplest model formed via a combination of the Hodgkin and Huxley (1952) conductance based modelling techniques and chemical reaction based modelling techniques. Thus, the Koenigsberger model allows for additional validation of methods within this research. The model was based upon a model described by Parthimos et al. (1999) which purported to be a minimal model for describing calcium oscillations. Parthimos et al. (1999) included a term similar to the Goldbeter model where there was a calcium release from a second, independent IP_3 sensitive store. This assumption was carried into the model described by Koenigsberger et al. (2004), where the flux of calcium due to the saturation of the IP_3 receptor does not appear in either the membrane potential or the Sarcoplasmic Reticulum (SR) conservation equations.

Koenigsberger et al. (2004) defined a model to track the ionic calcium concentration in the cytosol (Z), the ionic calcium concentration in the intracellular store (Y), the Cellular Membrane Potential (V) and the Open Probability of the Potassium Channel (N). Koenigsberger et al. (2004) also included a rate of change IP_3 equation. However, this equation was independent of the other four equations. This (for a low value of their E parameter) resulted in a linear relationship between the bifurcation parameter and the IP_3 concentration and thus rate of change of IP_3 equation was deemed unnecessary in the production of oscillations. In order to keep the model comparable to that of the previously defined four models this equation has been removed and replaced with a linear relationship for the Koenigsberger model.

Koenigsberger et al. (2004) included a basic bifurcation analysis replicated for completeness within this section.

3.6.1 Koenigsberger model Equations

There are four coupled ODEs in the Koenigsberger model, Equations 3.24, 3.25, 3.26 and 3.27.

$$\frac{dZ}{dt} = J_{IP3} - J_{VOCC} + J_{Na/Ca} - J_{SRuptake} + J_{CICR} - J_{ext} + J_{Leak} \tag{3.24}$$

$$\frac{dY}{dt} = J_{SRuptake} - J_{CICR} - J_{Leak} \tag{3.25}$$

$$\frac{dV}{dt} = \gamma\left(-J_{Na/K} - J_{Cl} - 2J_{VOCC} - J_{Na/Ca} - J_{K}\right) \tag{3.26}$$

$$\frac{dN}{dt} = \lambda\left(K_{activation} - N\right) \tag{3.27}$$

Equations 3.24 and 3.25 are formed to track the calcium ion concentration movement into and out of their respective compartments. The membrane potential Equation 3.26 was developed on the basis of two techniques. First chemical reaction based modelling techniques were used to track the effect on the membrane due to the movement of each ion across the membrane. Second, the membrane potential equation also includes the conductance based modelling techniques to model the movement of chlorine and potassium ions (Equations 3.35 and 3.36). This additional detail creates a more complete picture and allows an accurate cellular membrane potential V to be calculated. All fluxes defined in Equations 3.24 to 3.27 are defined by Equations 3.28 to 3.39 and all parameters defined in all equations in this section are defined in Table 3.5.

The voltage gated calcium ion channel (the VOCC channel) across the cell membrane (Equation 3.28) appears in both the Z and the V equations. It is multiplied by two in the membrane potential equation to account for the valance

electrons yielding a positive two charge on calcium ions.

$$J_{VOCC} = G_{Ca}\frac{V - v_{Ca1}}{1 + e^{-[V - v_{Ca2}/R_{Ca}]}} \tag{3.28}$$

The flux of calcium through the sodium-calcium channel is given by Equation 3.29.

$$J_{Na/Ca} = G_{Na/Ca}\frac{Z}{Z + C_{Na/Ca}}(V - v_{Na/Ca}) \tag{3.29}$$

The flux of calcium through the Sarcoplasmic Reticulum (SR) uptake channel is given by Equation 3.30.

$$J_{SRuptake} = B\frac{Z^2}{Z^2 + C_b^2} \tag{3.30}$$

The flux of calcium through the CICR channel is given by Equation 3.31.

$$J_{CICR} = C\frac{Y^2}{Y^2 + S_c^2}\frac{Z^4}{Z^4 + C_c^4} \tag{3.31}$$

The flux of calcium ions through calcium extrusion from the cell via the ATPase exchange pump is given by Equation 3.32.

$$J_{ext} = C_2 Z\left(1 + \frac{V - v_d}{R_d}\right) \tag{3.32}$$

The flux of calcium leaked from the high concentration store into the cytosol is given by Equation 3.33.

$$J_{Leak} = LY \tag{3.33}$$

The change in membrane potential due to the $Na^+ - K^+$ - ATPase pump is given by Equation 3.34.

$$J_{Na/K} = F_{Na/K} \tag{3.34}$$

The change in membrane potential due to the chlorine channels is given by Equation 3.35.

$$J_{Cl} = G_{Cl}(V - v_{Cl}) \tag{3.35}$$

The change in membrane potential due to the extracellular efflux of potassium ions is given by Equation 3.36.

$$J_K = G_K N(V - v_k) \tag{3.36}$$

The calcium and voltage activation of the potassium ion channels is given by Equation 3.37.

$$J_{activation} = \frac{(Z + c_w)^2}{(Z + c_w)^2 + C_3 e^{(-[(V - v_{Ca3})/R_k])}} \tag{3.37}$$

The flux of calcium ions from the independent IP_3 sensitive stores is given by Equation 3.38.

$$J_{IP3} = C_4 \frac{I^2}{K_r^2 + I^2} \tag{3.38}$$

Finally, in replacement of an additional rate of change equation of IP_3 with respect to the PLC concentration, the linear relationship between the effect of IP_3 and β is given by Equation 3.39.

$$I = m_I \beta_4 + I_0 \tag{3.39}$$

Although β_4 is distinguishable different than β_i in the other models from this point forward β_4 will simply be known as β representing the bifurcation parameter. All other constants described by Equations 3.24 to 3.39 are defined in Table 3.5.

Table 3.5: Constants used in the Koenigsberger model equation set. Described by Equations 3.24 to 3.39.

Constant	Value	Units	Description
g_{Ca}	1.29×10^{-3}	$\mu M s^{-1} m V^{-1}$	Whole-cell Membrane Conductance for VOCC
v_{Ca1}	100	mV	Reversal potential Calcium for VOCC
v_{Ca2}	-24	mV	Half point of the VOCC activation sigmoid
R_{Ca}	8.5	mV	Maximum slope of the VOCC activation sigmoid
$G_{Na/Ca}$	3.16×10^{-3}	$\mu M m V^{-1} s^{-1}$	Whole cell conductance for Na^+/Ca^{2+} exchange
$c_{Na/Ca}$	0.5	μM	Half point for activation for Na^+/Ca^{2+} exchange
$v_{Na/Ca}$	-40	mV	Reversal potential for Na^+/Ca^{2+} exchange
B	2.025	$\mu M s^{-1}$	SR uptake rate constant
c_b	1	μM	Half point for SR ATPase activation sigmoid
C	55	$\mu M s^{-1}$	CICR rate constant
s_c	2	μM	Half point of CICR $[Ca^{2+}]$ efflux sigmoid
c_c	0.9	μM	Half point of CICR activation sigmoid

Table 3.5: Constants used in the Koenigsberger model equation set. Described by Equations 3.24 to 3.39.

Constant	Value	Units	Description
C_2	0.24	s^{-1}	Rate constant for $[Ca^{2+}]$ extrusion by the ATPase pump
v_d	-100	mV	Intercept of voltage dependence of extrusion ATPase pump
R_d	250	mV	Slope of voltage dependence of extrusion ATPase pump
L	0.025	s^{-1}	Leak from intracellular store rate constant
γ	1.970	$mV\mu M^{-1}$	Scaling factor relating net movement of ion fluxes to the membrane potential (inversely related to cell capacitance)
$F_{Na/K}$	0.0432	μMs^{-1}	Net whole cell flux via the $[Na^+]-[K^+]-$ ATPase pump
G_{Cl}	1.34×10^{-3}	$\mu MmV^{-1}s^{-1}$	Whole cell conductance for $[Cl^-]$ current
v_{Cl}	-25	mV	Reversal potential for $[Cl^{-1}]$ channels
G_K	4.46×10^{-3}	$\mu MmV^{-1}s^{-1}$	Whole cell conductance for $[K^+]$ efflux
v_K	-94	mV	Reversal potential for $[K^+]$

Table 3.5: Constants used in the Koenigsberger model equation set. Described by Equations 3.24 to 3.39.

Constant	Value	Units	Description
λ	45	s^{-1}	Rate constance for net K_{Ca} channel opening
c_w	0	μM	Translation factor for $[Ca^{2+}]$ dependence of K_{Ca} channel activation sigmoid
C_3	0.13	μM^2	Translation factor for membrane potential dependence of K_{Ca} channel activation sigmoid
v_{Ca3}	-27	mV	Half point for the K_{Ca} channel activation sigmoid
R_k	12	mV	Maximum slope of $[K_{Ca}]$ activation sigmoid
K_r	1	μM	Half-saturation constant for antagonist-dependent calcium entry
C_4	0.23	μM	Maximum rate of activation dependent calcium influx
m_I	-1.2	μM	Slope relationship between $[IP_3]$ and β (negative relationship)
I_0	1.7	μM	Maximum $[IP_3]$ concentration for β

3.6.2 Koenigsberger model Results

First, to get a rough idea of the oscillatory dynamics of the Koenigsberger model the ODE system described by Equations 3.24 to 3.39 was integrated over time using the ODE solver in the software MATLAB as per Section 2.3.1. One example of $\beta = 0.7$ was used to compute the integral and display the results for some time such that any effect of the initial conditions is negligible.

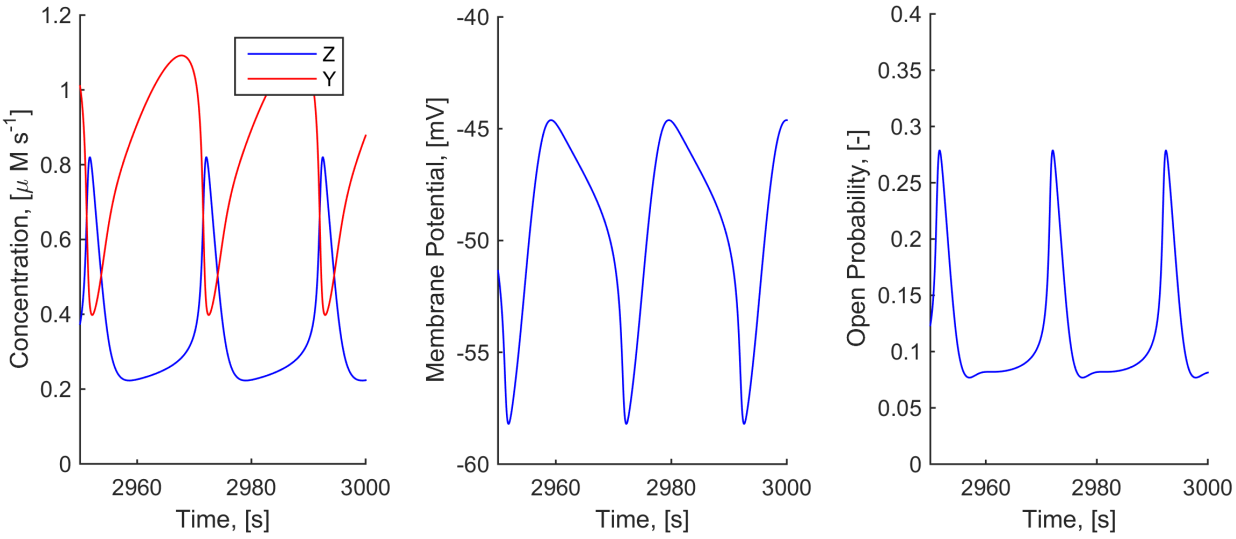

(a) Z and Y *(b) V* *(c) N*

Figure 3.20: Example oscillatory dynamics of Koenigsberger model ODEs (Equations 3.24 to 3.39) with $\beta = 0.7$.

Again, to complete the review of existing models, a complete bifurcation analysis was undertaken using the software AUTO (Section 2.4.1). The four variables in the Koenigsberger model, Z, Y, V and N, are expressed with their relationship to the bifurcation parameter β, in Figures 3.21, 3.22, 3.23 and 3.24 respectively.

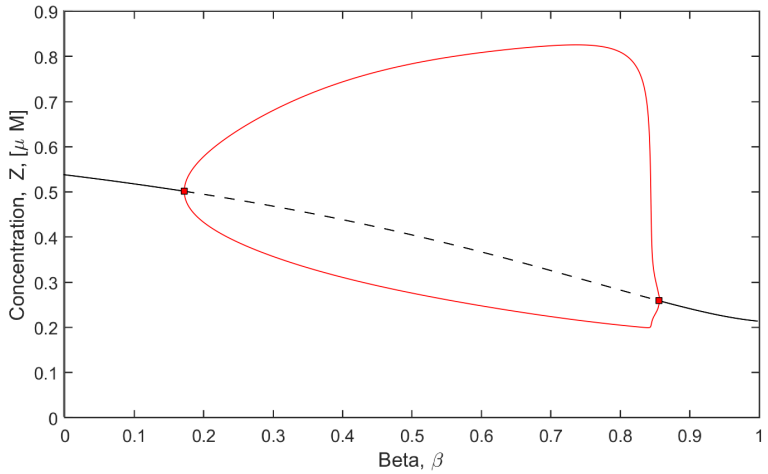

Figure 3.21: Bifurcation diagram of the Koenigsberger model for the calcium concentration in the cytosol, representing the maximum/minimum concentration experienced for the single cell model. Black solid lines are stable fixed points, black dashed lines are unstable fixed points, red lines are stable limit cycles and red squares are bifurcation points.

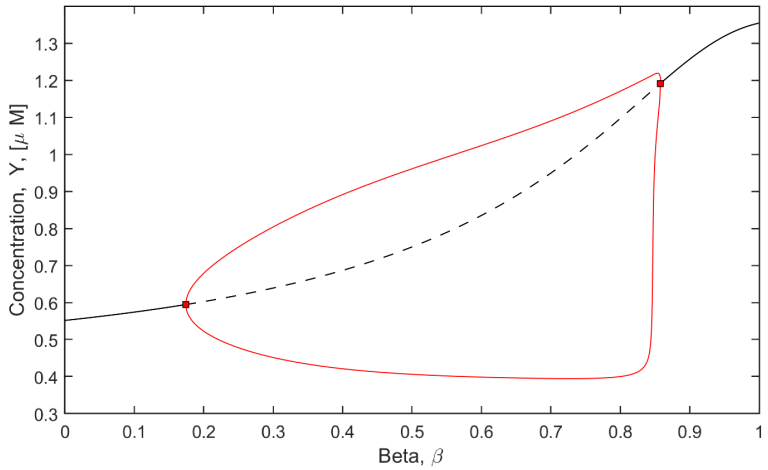

Figure 3.22: Bifurcation diagram of the Koenigsberger model for the intracellular store calcium concentration, representing the maximum/minimum concentration experienced for the single cell model. Black solid lines are stable fixed points, black dashed lines are unstable fixed points, red lines are stable limit cycles and red squares are bifurcation points.

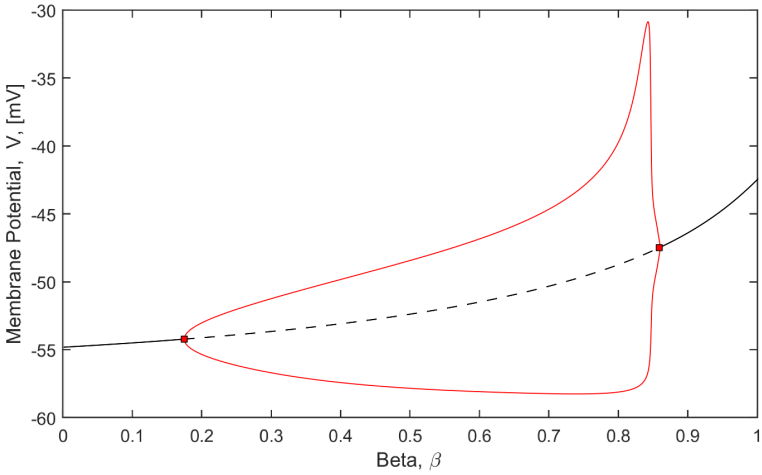

Figure 3.23: Bifurcation diagram of the Koenigsberger model for the membrane potential, representing the maximum/minimum experienced for the single cell model. Black solid lines are stable fixed points, black dashed lines are unstable fixed points, red lines are stable limit cycles and red squares are bifurcation points.

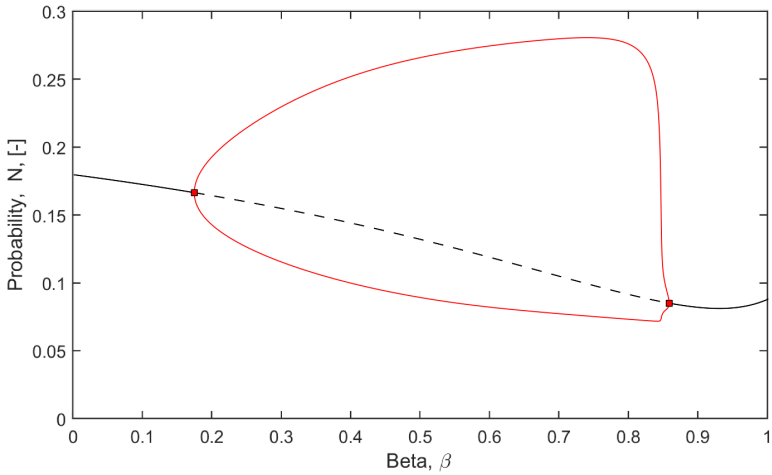

Figure 3.24: Bifurcation diagram of the Koenigsberger model for the open probability, representing the maximum/minimum experienced for the single cell model. Black solid lines indicate stable fixed points, black dashed lines indicate unstable fixed points, red lines indicate stable limit cycles and red squares indicate bifurcation points.

Continuation analysis in the software AUTO shows that the Koenigsberger model exhibited two Hopf bifurcations at $\beta = 0.174$ and $\beta = 0.857$. For the Koenigsberger model oscillations occurred for $0.174 < \beta < 0.857$. These bifurcation diagrams match those originally generated by Koenigsberger et al. (2004). These oscillations have an associated period given by Figure 3.25.

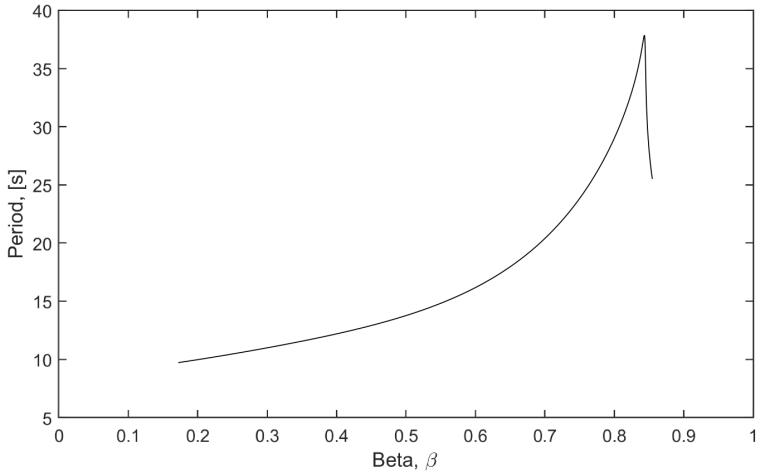

Figure 3.25: Period of oscillation for the Koenigsberger model. Note that a period is only found when the solution oscillates (See Figure 3.21).

The period of oscillation for the Koenigsberger model overall increases with increasing β. It is similar to the Goldbeter model and the Dupont model in that it increases towards the 'lower steady state Z concentration' known as the 'lower bifurcation point' ($\beta = 0.857$).

The Koenigsberger model is the most intricate, and the most physiologically accurate, model of the five previously discussed. The membrane potential (Figure 3.23) remained between $-60mV$ and $-30mV$. Although this membrane potential equation is not the complete picture of a membrane potential it is within

approximately expected values from Section 2.2.4. The calcium ion concentration in the cytosol (Figure 3.21) appears to have the opposite relationship to β than that seen in all of the other models; the calcium ion concentration decreases with increasing β. This is due to the β parameter in this model being inversely proportional to the saturation of the IP_3 receptor via the PLC concentration. As such, in comparison of like β profile, this relationship matches that described by Koenigsberger et al. (2004). The intracellular stores calcium ion concentration varies between half and 10 times the cytosolic calcium ion concentration. The only potential issue with the Koenigsberger model is the presence of a separate, infinite, IP_3 sensitive store. This assumption has propagated through many simplified cell models and is not a physiologically accurate assumption without the addition to the membrane potential. So, whilst the Koenigsberger model is a higher detail model with accurate representations, it is still not a truly physiologically accurate model in describing the cell's calcium ion concentrations.

3.7 Discussion

Five unique, yet related existing Simplified Generic Oscillatory Cell Model/s (SGOCM) have been investigated in this chapter. The first two, the Goldbeter model and the Dupont model, are similar in their expression of lumped parameter cell models and their attempt to capture the appropriate cell mechanics via chemical based modelling techniques. The Ermentrout model and the FitzHugh-Nagumo model are developed from the conductance based model presented by Hodgkin and Huxley (1952) (Section 2.2.7) that tracked changes to the membrane potential. The Ermentrout model is based on the ionic movement across the cell membrane, in comparison to the FitzHugh-Nagumo model which, attempts to be a simplified minimal mathematical model. Finally, the Koenigs-

berger model attempts to combine the two bases of knowledge to create a more physiologically accurate model of a SMC.

It can be argued the first two models (Goldbeter and Dupont) are in some cases more useful than the second two (Ermentrout and FitzHugh-Nagumo) because they keep track of the intracellular calcium ion concentration. This intracellular store contains an important CICR channel responsible for unique dynamics that is not considered by the second two models. The difference between the Goldbeter model and the Dupont model is that the Goldbeter model included a second IP_3 sensitive store whereas the Dupont model combined the two stores by creating a IP_3-sensitized CICR channel instead.

The Ermentrout model is useful because it explicitly calculates the changes in the membrane potential. In particular, the Ermentrout model involves the changes induced by the VOCC channel which has its own unique dynamics. Given that the membrane potential plays a part in the spatial diffusivity of ions it is desirable to consider this equation. The FitzHugh-Nagumo model is a minimal mathematical model to view specific dynamics and is important for comparison to toy models in later chapters (Chapter 6).

The Koenigsberger model is the most intricate model examined within this research and is barely categorised as a SGOCM due to its intricacy. It is a combination between the Goldbeter model and the Ermentrout model, including both chemical reaction based modelling techniques for the calcium ions concentration and conductance based modelling for the other unknown concentrations (K^+, Na^+ and Cl^-).

In terms of fundamental dynamics, all the models behaved the same (Figures 3.3, 3.8, 3.13, 3.17 and 3.21); for low and high bifurcation parameter values the system reached a steady state value for all time. For mid-range bifurca-

tion parameter values they experienced oscillatory behaviour with the overall period of oscillation increasing with changes in β towards the 'lower bifurcation point', except the FitzHugh-Nagumo model. The FitzHugh-Nagumo model should only be considered in one half of the bifurcation parameter region as, unlike the others, it has a minimum period in the middle of the oscillatory range ($\beta = 0.85$).

Physiologically, it is important to remember that these simplified, single cell models are chosen to look at the overall single cell dynamics. This research is not focused on obtaining a true and accurate model for the intracellular concentrations such as those described by Dormanns et al. (2015), Farr and David (2011) and Johny et al. (2015). The models described in this chapter are detailed enough to encompass the sought after oscillatory behaviour, whilst not adding unnecessary additional complexity.

3.8 Conclusion

Five simple, single cell models have been described in detail within this chapter: the Goldbeter model, the Dupont model, the Ermentrout model, the FitzHugh-Nagumo model and the Koenigsberger model. These five models have been selected as they capture Simplified Generic Oscillatory Cell Model/s (SGOCM) dynamics critical to this research. It was decided not necessary to accurately model the intracellular ionic concentrations in order to understand the oscillatory dynamics of a cell. This enables a more focused approach on the effect of diffusion on the system by removing surplus additional computation. The effect of diffusion on these models is to be discussed in the following chapters (Chapters 5, 6 and 7).

4 Model Adaptations

4.1 Introduction

As noted in Section 3, each of the five simplified models track slightly different variables. Within the options of possible variables there are some points of cross over between the models. In order to compare the different SGOCMs, similar parameters need to be considered. Table 4.1 indicates approximately what each model attempts to measure. It should be noted that this table is an approximate comparison only and the parameters are up to the interpretation of the literature. This comparison was completed with consideration to the units and rough definitions of each variable. This comparison will not consider the values of the variables found as they are not within any realistic tolerance of each other (as seen in Chapter 3).

Table 4.1: Summary of the variables found for each of the 5 SGOCMs. Where the variable options in common are the ionic calcium concentration in the cytosol (Z), the ionic calcium concentration in the intracellular store (Y), the Cellular Membrane Potential (V) and the Open Probability of the Potassium Channel (N).

	Variables *				
	Z	**Y**	**V**	**N**	**Other**
Goldbeter model	✓	✓			
Dupont model	✓	✓			
Ermentrout model	✓		✓	✓	
Koenigsberger model	✓	✓	✓	✓	
FitzHugh-Nagumo model					✓

As mentioned in Section 1.3 the single cell models will be considered in a spatial arrangement (Chapter 5). As such, there are two variables in particular that are desired to be observed, the ionic calcium concentration in the cytosol (Z) and the Cellular Membrane Potential (V), due to these two variables' effects upon the spatial dynamics. The ionic calcium concentration in the intracellular store (Y) and the Open Probability of the Potassium Channel (N) are merely intracellular facilitators to mediate the oscillatory response to a stimulus over time. The variable Z is vital as it has been identified as a primary control of the contraction and activation of SMCs surrounding the blood vessel. The Cellular Membrane Potential (V) is desired to be understood because of a novel feature within this research; Electro-Diffusion (ED). This will be detailed in Chapter 5.

Considering Table 4.1 it is clear that the Koenigsberger model does not need to be altered further as it contains all the variables of interest. Next, the Ermentrout model consists of three of the four variables excluding the ionic calcium concentration in the intracellular store (Y) and as such also does not need to be

* The comparison between these variables is up to interpretation of the literature. This comparison is focused on units and rough explanation, they may not have the exact same definitions.

modified. The FitzHugh-Nagumo model is, unfortunately, not related strongly enough to any specific physiological variables in order to be directly compared to the other models. However, the FitzHugh-Nagumo model is still included as it is the minimalist mathematical model to obtain the desired dynamics mentioned in Chapter 3.

Finally, both the Goldbeter model and the Dupont model contain only calcium ion dynamics and do not contain a Cellular Membrane Potential (V) equation. It is possible to consider the changes in the membrane potential based solely upon the calcium ion movement across the cell membrane. This chapter will discuss the addition of a membrane potential equation to both the Goldbeter model and the Dupont model, along with the benefits and downfalls of such an addition.

4.2 Method

To account for any changes in membrane potential based upon any changes in the cytosolic free calcium movement, a conversion needs to be applied. For some additional rate of change in calcium $\mathcal{L}_{AdditionalCa}$ the corresponding rate of change in membrane potential can be calculated by Equation 4.1.

$$\frac{dV}{dt}_{AdditionalCa} = \frac{1}{C_m \alpha} \mathcal{L}_{AdditionalCa} \tag{4.1}$$

where C_m is the cell membrane capacitance coefficient ($[CV^{-1}]$) and α is the same conversion coefficient found in Section 3.4 in Equation 3.21. The constants defined in this equation are found in the associated Table 3.3. Equation 4.1 is generated via the relationship ($C_m V = q$) where C_m is the capacitance and q is the charge of the ion in question.

In order to create a rate of change of membrane potential from the change in calcium dynamics for both the Goldbeter model and the Dupont model, Equation 4.1 will be combined with all currents crossing the membrane. The Dupont model will be considered first. In the Dupont model there are two lumped pathways of ions moving across the cell membrane; the flux flowing in (V_{in}) and the flux gradient release (kZ). As such, the equation defining the change in membrane potential due to ions crossing the cell membrane is defined by Equation 4.2.

$$\frac{dV}{dt}_{Dupont} = \frac{1}{C_m\alpha}(v_0 + v_1\beta - kZ) \tag{4.2}$$

The Goldbeter model on the other hand has a complication with the production of this formula. The definition of V_{in} in the Goldbeter model is a flux encompassing both ion movement across the cell membrane and the ion movement from the second store. As such, the ionic flux used to calculate the membrane potential needs to be adjusted accordingly (Equation 4.3).

$$\frac{dV}{dt}_{Goldbeter} = \frac{1}{C_m\alpha}(v_0 - kZ) \tag{4.3}$$

Due to this membrane potential equation being based upon the definition of the model it is an unbalanced equation. Given that $v_0 = 1\mu Ms^{-1}$ and $k = 10s^{-1}$, in order for the rate of change of the membrane potential to reach an equilibrium the concentration must be around $0.1\mu M$. However, by Figure 3.3 it is clear that $0.1 < Z < 1.9$ and thus the rate of change of V will always be negative. This membrane potential ODE is, thus, abandoned.

It should be kept in mind that the Dupont model's rate of change of voltage is not physically accurate in calculating the membrane potential as it only

considers the effect of calcium ion movement and not other ionic species. An important note on this type of membrane potential calculation is that, unlike in the Ermentrout model, the membrane potential can be independently calculated after the rate of change of the intracellular calcium. Thus, V has no feedback or effect upon the Z.

4.3 Results

The results within this chapter are focused on the adaptation to the models to include a membrane potential equation. As stated previously, the membrane potential can be calculated independently from the calcium ion concentration and as such those results are not reproduced within this section. For a complete review of the Dupont model see Section 3.3. The 'bifurcation diagram' of membrane potential for the Dupont model is given in Figure 4.1.

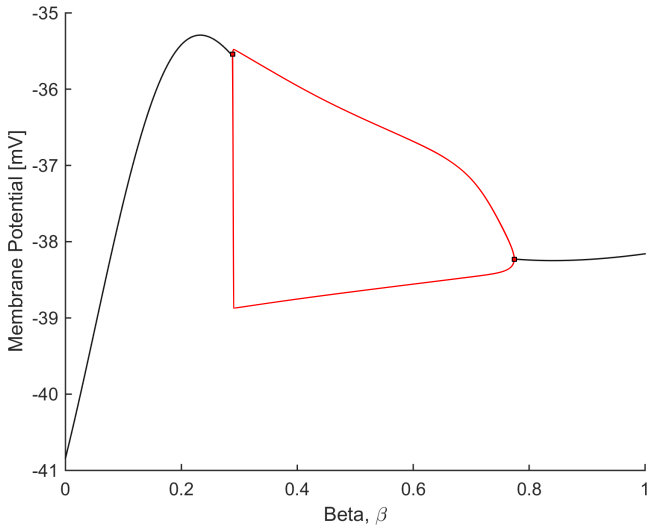

Figure 4.1: 'Bifurcation diagram' of the Dupont model for the membrane potential. Representing the maximum/minimum experienced for the single cell model when the initial membrane potential, $V_0 = -40mV$. Red is oscillatory region, black is steady state solution and red squares indicate bifurcation points.

Figure 4.1 shows the same bifurcation points as that of the Dupont model explored previously. What is important to note about Figure 4.1 is that it is not a true bifurcation diagram because it is entirely dependent on the ionic calcium concentration and thus also its initial conditions. For this reason, for a somewhat reasonable change to the membrane potential, the initial condition for the membrane potential was set to $V_0 = -40mV$.

Given that the membrane potential ODE relating the change in membrane potential to the ions crossing the cell membrane was not suitable for the Goldbeter model, this adaptation has been abandoned.

4.4 Discussion

The purpose of this chapter was to create an equation for the Cellular Membrane Potential (V) to allow comparison of more variables across multiple models. The Cellular Membrane Potential (V) is also desirable to compare and contrast additional models under Electro-Diffusion (ED) (yet to be described) in Chapter 5.

The membrane potential is able to be measured in vivo and in vitro (inside and outside their normal biological context). This ability makes the membrane potential a desirable measurement to obtain in mathematical modelling. By obtaining theoretical data for the membrane potential it can be compared to that found in experimental data. However, the membrane potential equation found in this chapter is not a true representation of the membrane potential of a cell.

The variable V found within this chapter is the effect upon the membrane potential due to the flux of calcium ions crossing the membrane. Henceforth,

this effect will be simply known as the membrane potential with knowledge that any membrane potential found within this research is not considered a true membrane potential. Figure 4.1 depicts the 'bifurcation diagram' of V for the Dupont model with the same bifurcation points from Figure 3.8 in Section 3.3. It shows that the change in membrane potential is consistent with what is expected for the flux of calcium ions (between -41 to $-35mV$ from Section 2.2.4).

The purpose of this equation is to compare future results across multiple SGOCMs. This will be used to understand the cause and effect of calcium ion concentration dynamics in spatial media (Chapter 5).

As discussed following the formation of the membrane potential ODE for the Goldbeter model (Equation 4.3) this equation is not balanced. The definition of the model described within Section 3.2 indicates that the only two fluxes cross the membrane: the constant calcium influx and the calcium efflux based upon the cytosolic calcium concentration. Unfortunately, these rates always result in a negative rate of change on membrane potential. Thus, the rate of change or membrane potential for the Goldbeter model is unstable and therefore, was abandoned.

4.5 Conclusion

This chapter discussed a model adaptation to both the Goldbeter model and the Dupont model. An equation for the effect upon the membrane potential based on the flux of calcium ions crossing the cell membrane was created. The membrane potential, within this research, is thus not the true membrane potential. The Dupont model found that the change in V for the flux of calcium ions varied between $-40mV$ and $-35mV$ for the initial condition $V_0 = -40mV$. This result is useful for the comparison to other SGOCMs but should not be compared

to the true membrane potential in experimental data. The membrane potential ODE formed for the Goldbeter model was unstable and thus abandoned.

5 Spatial Diffusion

5.1 Introduction

To introduce a spatial context to the mathematical models (described in Chapter 3) a comparison of length scales is necessary to relate, compare and contrast different constants and parameters. Here, two separate length scales are defined: the macroscale and the microscale. The microscale defines the length of a single cell including the intracellular store. The macroscale, on the other hand, defines the overall tissue length such that it contains on the order of > 100 single cells. Figure 5.1 shows the relationship of the two different scales.

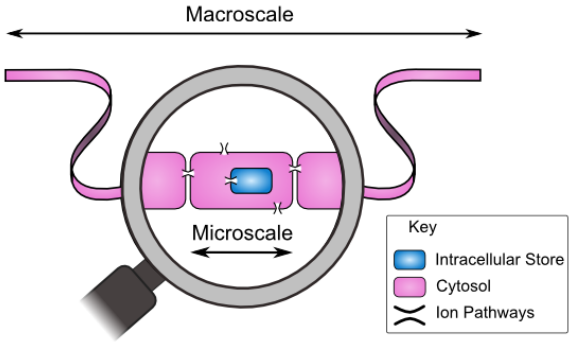

Figure 5.1: Representation of macroscale (tissue length) vs microscale (single cell length).

Cells are connected on the macroscale via diffusion of ions across neighbouring cell membranes. Physiologically, diffusion is characterised as an additional flux of an ionic concentration entering the cell through an ionic pathways (Section 1.2.3) from a neighbouring cell. In order to compute the rate of diffusion some simplifying assumptions are required. A fundamental assumption, described by Dupont et al. (2016), is that since diffusion is rapid over a short distance on the microscale local variations are smoothed out. Thus, it is only necessary to find the average or mean behaviours. This allows for averaged field equations to be derived for the larger macroscale. This is done by a process known as homogenisation (Dupont et al., 2016). As such, the use of the term 'cell' now indicates a position on a continuous spatial media and no longer a specific, defined cell.

The dynamics of a single cell with potential oscillatory behaviour have been examined a number of times. Chapter 3 investigated 5 unique and related SGOCM which examine intracellular dynamics on the microscale. However, the differences in the single cell dynamics' effect on the macroscale is still under contention. As such, the macroscale is the focus of this chapter. Specifically, what effect do the microscale's oscillatory dynamics have upon the spatially connected macroscale? This effect will be examined across the five different single cell models from Chapter 3 plus Chapter 4.

This chapter looks to introduce three things important to the spatial context: a spatially varying stimulus, Fickian Diffusion (FD) and Electro-Diffusion (ED). A spatially varying stimulus is a novel area of research and its effect on the spatially connected macroscale has not been thoroughly explored.

5.2 Method

In order to compute the dynamics of the spatially coupled macroscale system encompassing the microscale dynamics, multiple components need to be brought together. The spatial coupling methods specified in this chapter are combined with the five single cell model equation sets defined by the Goldbeter model, the Dupont model (with additions), the Ermentrout model, the FitzHugh-Nagumo model and the Koenigsberger model described in Sections 3.2, 3.3 (plus Chapter 4), 3.4, 3.5 and 3.6 respectively.

5.2.1 Reaction Diffusion Equation

In order to incorporate the diffusion of ions across cells on the macroscale, the rate of movement of ions over time must be added to the original rate of change of the ionic concentration within the cytosol in the microscale. To consider the two independent variables of the system, space (x) and time (t), the original ODE must now become a Partial Differential Equation (PDE). Equation 5.1 is known as a generic Reaction Diffusion Equation and will be built upon with two unique types of diffusion.

$$\frac{\partial \Phi}{\partial t} = \mathcal{L}_{Diffusion} + F_1(\Phi, \bar{\Psi}, t)_{Reaction} \tag{5.1}$$

and

$$\frac{\partial \bar{\Psi}}{\partial t} = F_2(\Phi, \bar{\Psi}, t)_{Reaction} \tag{5.2}$$

where Φ is the variable diffused and $\bar{\Psi}$ represents all other variables in the equation set. F_1 and F_2 are the combination of all other fluxes of ions within the cell. Additionally, if there exists a membrane potential equation this is subse-

quently altered. The membrane potential (section 2.2.4) is affected due to the diffusive movement of ions traversing the cell membrane. As the ions cross the membrane, as described in Section 4.2, the membrane potential is adjusted proportionally depending on the ions that moved, the capacitance of the cell membrane, the volume ratio between the intracellular space and the extracellular space and Faraday's constant. Using Equation 4.1 described in Chapter 4 a conversion is needed for the calcium ion movement. The resulting addition to the membrane potential equation is defined by Equation 5.3.

$$\frac{\partial V}{\partial t} = \frac{1}{C_m \alpha}(\mathcal{L}_{Diffusion}) + F_3(V, \Phi, \bar{\Psi}, t)_{Reaction} \tag{5.3}$$

where again C_m is the cell membrane capacitance coefficient ($[CV^{-1}]$), α is the same conversion coefficient found in Section 3.4, Equation 3.21, and F_3 represents all other changes to the membrane potential over time (including any capacitance conversion, C_m, to a current if applicable).

5.2.2 *Fickian Diffusion (*FD*)*

The most common type of diffusion considered is known as Fickian Diffusion. Fickian diffusion, originally described by Adolf Fick (1855), defines the spatial movement of a solute from a region of high concentration to a region of low concentration across a concentration gradient. By Fick's second law, the concentration change over time due to diffusion is defined by Equation 5.4.

$$\mathcal{L}_{FD} = \frac{\partial \Phi}{\partial t}_{FD} = \frac{\partial}{\partial x}\left(D(x)\frac{\partial \Phi}{\partial x}\right) = D\frac{\partial^2 \Phi}{\partial x^2} \tag{5.4}$$

where D is the Homogenised Macroscale Diffusion Coefficient (Section 5.2.4). The simplification in Equation 5.4 can only be made on the assumption that the

diffusion constant is not a function of the macroscale space (x), which will be discussed in Section 5.2.4. Thus, when only FD is considered, Equation 5.1 can be rewritten as Equation 5.5.

$$\frac{\partial \Phi}{\partial t} = D\frac{\partial^2 \Phi}{\partial x^2} + F_1(\Phi, \bar{\Psi}, t)_{Reaction} \tag{5.5}$$

5.2.3 Electro-Diffusion (ED)

As described by Keener and Sneyd (2009), there are two prominent methods by which an ionic concentration can diffuse. The first, described previously, is driven by concentration gradients. The second is due to an electric field. The contribution of movement attributed to the electric field is given by Planck's equation (Equation 5.6).

$$\mathbf{J} = -u\frac{z_i}{|z_i|}\Phi\frac{dV}{dx} \tag{5.6}$$

where u is the mobility of an ion, z_i is the valance of the ion, again Φ is the ion being diffused and V is the membrane potential. Following this, a relationship between the diffusion coefficient and the mobility can be found as determined by Einstein (Equation 5.7).

$$\frac{u}{|z_i|} = \frac{DF}{RT} \tag{5.7}$$

where F is Faraday's constant, R is the universal gas constant, T is the average normal body temperature in degrees Kelvin and D is the homogenised macroscale diffusion coefficient from Section 5.2.4. Given Equation 5.7's relationship and Equation 5.6, an equation for the effect of both types of diffusion can be derived (Equation 5.8).

$$\mathbf{J} = D\left(\frac{d\Phi}{dx} + \frac{z_i F}{RT}\Phi\frac{dV}{dx}\right) \tag{5.8}$$

Thus, the flux due to both types of diffusion (FD and ED) can be produced (Equation 5.9). This is known solely as Electro-Diffusion (ED) since ED is not typically found without FD.

$$\mathcal{L}_{ED} = \frac{\partial\Phi}{\partial t}_{ED} = \frac{\partial}{\partial x}\left(D(x)\left(\frac{\partial\Phi}{\partial x} + \gamma\Phi\frac{\partial V}{\partial x}\right)\right) \tag{5.9}$$

with

$$\gamma = \frac{z_{Ca}F}{RT} \tag{5.10}$$

where γ has units of $[mV^{-1}]$. Next, with the assumption that the homogenised macroscale diffusion coefficient (D) does not vary over the macroscale (Section 5.2.4) and using the product rule of differentiation it is possible to expand Equation 5.9 to become Equation 5.11.

$$\mathcal{L}_{ED} = D\left(\frac{\partial^2\Phi}{\partial x^2} + \gamma\frac{\partial\Phi}{\partial x}\frac{\partial V}{\partial x} + \gamma\Phi\frac{\partial^2 V}{\partial x^2}\right) \tag{5.11}$$

Finally, when ED is considered (including FD), Equation 5.1 can be rewritten as Equation 5.12.

$$\frac{\partial\Phi}{\partial t} = D\left(\frac{\partial^2\Phi}{\partial x^2} + \gamma\frac{\partial\Phi}{\partial x}\frac{\partial\Phi}{\partial x} + \gamma\Phi\frac{\partial^2 V}{\partial x^2}\right) + F(\Phi,\bar{\Psi},t)_{Reaction} \tag{5.12}$$

5.2.4 Homogenised Macroscale Diffusion Coefficient

When the length scale of a single cell is considerably less than the length of the macroscale, the rate of diffusion over space can be approximated by a new

homogenised macroscale diffusion coefficient, D. Dupont et al. (2016) detail a method for calculating the homogenised macroscale diffusion coefficient depending on the microscale. For a one dimensional macroscale the homogenised macroscale diffusion coefficient can be approximated as the definite integral over the length of the cell of the microscale diffusion rate, Equation 5.13.

$$\frac{1}{D} = \frac{1}{L}\int_0^L \frac{1}{D(x)}dx \tag{5.13}$$

where L is the length of a single cell and $D(x)$ is the diffusion coefficient as a function of the position within the microscale. The spatially varying diffusion coefficient can be further de-constructed into the summation of resistance through the cytosol and the cell membrane on the microscale, Equation 5.14.

$$\frac{1}{D} = \frac{1}{L}\left(\int_0^{L-\varepsilon} \frac{1}{D_e(x)}dx + \int_{L-\varepsilon}^{\varepsilon} \frac{1}{D_i(x)}dx\right) \tag{5.14}$$

where ε is twice the width of the cell membrane and $D_e(x)$ represent the diffusion coefficient of the ion through the cytosol and $D_i(x)$ represents the diffusion coefficient of the ion through the cell membrane (including via gap junctions). Next, by averaging the diffusion coefficients over the microscale (ie $D_e(x) = D_e$ and $D_i(x) = D_i$), the integrals can be evaluated, Equation 5.15.

$$\frac{1}{D} = \frac{L-\varepsilon}{L}\frac{1}{D_e} + \varepsilon\frac{1}{LD_i} \tag{5.15}$$

Considering $\varepsilon << L$, $D_i << D_e$ and when the length scale of a single cell is considerably less than the length of the macroscale the limit as $\varepsilon \to 0$ and $D_i \to 0$ can be found such that Equation 5.16 is true (Dupont et al., 2016).

$$\lim_{(\varepsilon\to 0 \text{ and } D_i\to 0)} \frac{D_i}{\varepsilon} = \mathscr{F} \tag{5.16}$$

Where $\mathscr{F}$ is the permeability coefficient of the order $\mathscr{F} \approx 10^{-6} ms^{-1}$ given by Wilkins and Sneyd (1998). Finally, the homogenised macroscale diffusion coefficient can be calculated via Equation 5.17 (Dupont et al., 2016).

$$\frac{1}{D} = \frac{1}{D_e} + \frac{1}{L\mathscr{F}} \tag{5.17}$$

where the effective diffusion coefficient of the cytosol, D_e, can be found experimentally by assuming that the analogue of Ohm's law holds (Keener and Sneyd, 2009) and is of the order $200\mu m^2 s^{-1}$. L is the length of a cell; for example, an endothelial cell is $100\mu m$ in length (from Section 1.2.1), As such, the homogenised macroscale diffusion coefficient ranges between $10^{-6} cm^2 s^{-1}$ and $10^{-5} cm^2 s^{-1}$. A middle-of-the-road first estimate of $5 \times 10^{-6} cm^2 s^{-1}$ was used for the comparison of the models within this chapter.

5.2.5 Summary of Assumptions

In order to apply the homogenisation process multiple assumptions needed to be made. Thus, for conciseness, here is a summary of the major assumptions used in this process.

- Since diffusion is rapid over a short distance on the microscale local variations in concentration are smoothed out allowing for mean or average behaviours to take precedence (Dupont et al., 2016).
- The rate of diffusion over space can be approximated by a homogenised macroscale diffusion coefficient, D.
- The homogenised macroscale diffusion coefficient (D) does not vary over the macroscale considered as it is an average.
- The length scale of a single cell is considerably less than the length of the

macroscale. Additionally, the length of the cell membrane is considerably less than the length of the cell.

- The effective diffusion coefficient, D_e, can be found experimentally by assuming that the analogue of Ohm's law holds (Keener and Sneyd, 2009).

5.2.6 Spatially Varying Stimulus

As described in Section 1.3.1, spatially varying stimuli occur within tissue modelling. In application to the mathematical models described in Chapter 3 this allows the stimulus parameter (β) to become a function of the macroscale space, ie. $\beta(x)$. This section will look exclusively at a linear relationship between β and x. This relationship was chosen as the simplest way to achieve a spatially varying stimuli and is more physiologically possible than a sudden step function (Section 1.3.1). Other options, such as a simple step function between two cells were considered, but did not yield the behaviour of interest. Note Chapter 8 will further investigate $\beta(x)$ equations with use of step and cubic functions.

5.2.7 Method of Lines (MOL)

In order to solve the PDE described by Equations 5.5 or 5.12, a numerical approximation to the partial rates of change in space is needed. Therefore, the Method of Lines (MOL) was used. The MOL is a technique for solving PDEs in which all spatial dimensions are discretised, leaving only the time variable continuous. The approximation of the MOL was first detailed by Sarmin and Chudov (1963) with more recently Hamdi et al. (2007) giving variations and updates to the method.

The process involves discretising all but one of the variables of the system. The resulting equation is able to be approximated as a system of ODEs to which

a numerical solution method with an initial value can be applied (Section 2.3). The first approximation needed is the approximation to the first partial derivative of one variable with respect to x. Using the three point average method, also known as the central difference formula, derived from the Taylor series, the approximation to the rate of change for some position x^* is defined by Equation 5.18.

$$\frac{\partial \Phi(x^*)}{\partial x} \approx \frac{\Phi(x^* + \Delta x) - \Phi(x^* - \Delta x)}{2\Delta x} + \mathcal{O}(\Delta x^2) \tag{5.18}$$

where Δx denotes the step size between approximations (detailed in Section 5.2.9), $\Phi(x^* - \Delta x)$ denotes the solution to the position before and conversely $\Phi(x^* + \Delta x)$ denotes the solution to the position after. This approximation has a second order truncation error associated with it, and as such the step size must be sufficiently small. Given that the tolerance required was set as $tol = 1 \times 10^{-6}$ as described in Section 2.3, $\Delta x \leq 1 \times 10^{-3}$ in order to obtain a second order truncation error less than $tol = 1 \times 10^{-6}$.

Similarly, one approximation to the second partial derivative of the concentration with respect to space for some position x^* can be obtained with the same three points (Equation 5.19).

$$\frac{\partial^2 \Phi(x^*)}{\partial x^2} = \frac{\Phi(x^* + \Delta x) - 2\Phi(x^*) + \Phi(x^* - \Delta x)}{\Delta x^2} + \mathcal{O}(\Delta x^2) \tag{5.19}$$

Again, since Equation 5.19 is derived from the Taylor series this leads to a second order truncation error.

5.2.8 Boundary Conditions

In order to add spatial diffusion on a One Dimension (1D) array of cells, boundary conditions need to be considered. There exist multiple boundary conditions types (and combinations) that could be employed. However, numerical cell modelling leads to two plausible boundary conditions: Zero Flux or Periodic boundary. A zero flux boundary condition states that the flux across the outer boundaries of the macroscale is zero. This is often employed in a fixed region of isolated cells or where the rate of change near the boundaries becomes sufficiently small such that it can be approximated as zero. A periodic boundary, on the other hand, is typically used when either the stimulus is a periodic function such that $\beta(x=0)=\beta(x=n)$ for some interval $x=[0,n]$ and/or in the case of a wrapped surface such as a cylinder.

For all the computed solutions within this research, unless otherwise stated, it was assumed that the rate of change near the boundaries becomes sufficiently small such that it can be approximated to zero, employing a zero flux. Physiologically, this assumption is valid for comparison to in vitro data (data collected from experiments on tissue slices outside their normal biological context) in which a zero flux boundary condition is inevitable.

The zero flux boundary condition was employed via a phantom additional 'cell' to both boundaries such that the first order flux (Equation 5.18) is equal to zero and the second order rate of change (previously Equation 5.19) can be replaced with Equation 5.20.

$$\begin{aligned} \frac{\partial^2\Phi(0)}{\partial x^2} &= \frac{2\Phi(\Delta x)-2\Phi(0)}{\Delta x^2} \\ \frac{\partial^2\Phi(n+\Delta x)}{\partial x^2} &= \frac{2\Phi(n)-2\Phi(n+\Delta x)}{\Delta x^2} \end{aligned} \tag{5.20}$$

where the interval is defined as $x = [\Delta x, n]$ such that $\Delta x << n$.

5.2.9 Simulation Tolerances

In order to ensure an accurate and reliable solution was produced, appropriate step sizes and tolerances were investigated. The tolerances specified within Section 2.3 were again applied to the system ($AbsTol = 1 \times 10^{-6}$) and in order to obtain an accuracy of this order from the second order truncation error of the MOL the spatial step was selected as $\Delta x = 1 \times 10^{-3} cm$. Next, the Courant-Friedrichs-Lewy Condition (Hersh, 2013; Hamdi et al., 2007) was considered as a necessary condition for convergence for employing a MOL approach to solving a PDE (Equation 5.21).

$$D\frac{\Delta t}{\Delta x^2} \leq C_{max} \tag{5.21}$$

where for an explicit time stepping solver $C_{max} = 1$. Given that the maximum value of the homogenised macroscale diffusion coefficient, D, under consideration is $D = 1 \times 10^{-5} cm^2 s^{-1}$ (Section 5.2.4) and the spatial step size must be $\Delta x = 10^{-3} cm$ in order to obtain the correct tolerance from Section 5.2.7, this results in $\Delta t \leq 0.1s$ for convergence. However, upon a time step investigation (not shown) it was determined that the best Δt for a combination of accuracy, detail, memory and solver time was $\Delta t = 0.001s$ for models with average periods of $0-4s$, $\Delta t = 0.01s$ for models with an average period of $4-20s$ and $\Delta t = 0.05s$ for models with an average period $\geq 20s$. The results (not shown) determined that for a change in spatial step size $\Delta x < 1 \times 10^{-3} cm$ and a change in time step size less than specified, there was no significant change in the numerical solution for all the models considered. For variations in the desired tolerances or the diffusion coefficient it is clear that the necessary restrictions on Δt and Δx can

or must change to compensate.

5.2.10 FitzHugh-Nagumo model Diffusion Variable

As mentioned in Chapter 3 Section 3.5 and again in Section 5.2.1, the FitzHugh-Nagumo model, unlike its counterparts, does not track any ionic concentrations within the cell. This is problematic in the application of an ionic concentration diffusion and given the vague definitions of the parameters within the FitzHugh-Nagumo model it can be considered unclear which parameter (W or U) should be diffused. However, given this model is simply a minimal representation of the overall oscillatory dynamics it is still desirable to compute spatial diffusion. To avoid bias on the interpretation of the parameters, FD (Equation 5.4) was computed independently for each variable: the fast rate variable (W) and the slow rate variable (U).

Computing the effect of diffusion on the FitzHugh-Nagumo model is useful in order to compare the results to similar toy models to be introduced in Chapter 6.

5.3 Results

The results that follow are spatio-temporal concentration plots of the solution to the PDE described by Equation 5.3, 5.5 and Equation 5.12. Each model will redefine the original ODE to become a set of reaction-diffusion PDE equations. For simplicity only one variable (Z) for each model is shown with the exception of the FitzHugh-Nagumo model as previously mentioned. Overlaid on each spatio-temporal concentration plot are two black horizontal lines, these lines represent the β values at which the bifurcations occur under zero diffusion. The $\beta(x)$ for all results in this section are linear relationships for simplicity, and are

kept the same for each model's diffusion types, detailed within each caption.

The displayed spatio-temporal concentration plots have varying contour scales. Each contour scale is unique to the graph being examined and indicates approximately the maximum and minimum of the variable being displayed. Although not immediately obvious the higher values (displayed by the red colour) are indeed present and typically indicate the sudden peaks in the variable being displayed. Due to this care should be taken when comparing these spatio-temporal concentration plots.

The results are grouped by model with $D = 5 \times 10^{-6} cm^2 s^{-1}$ as decided in Section 5.2.4. Table 5.1 provides a summary of the order of presentation and quick references for each of the results shown.

Table 5.1: Summary of important figures in this section. Each model is produced with either zero diffusion, FD or ED. ED is excluded from the models with no membrane potential equation.

	Zero Diffusion	**Fickian Diffusion (FD)**	**Electro-Diffusion (ED)**
Goldbeter model	5.2	5.4	
Dupont model	5.6	5.7	5.8
Ermentrout model	5.9	5.10	5.12
FitzHugh-Nagumo model- U	5.13	5.15	
FitzHugh-Nagumo model- W	5.14	5.16	
Koenigsberger model	5.17	5.18	5.19

Appendix A provides additional figures for further reference, depicting the effect of the magnitude of the diffusion constant on FD.

5.3.1 Goldbeter model Spatio-temporal Results

For completeness, the original ODE equation set from Chapter 3, Section 3.2, has been reproduced including diffusion described by Section 5.2.1 for the

Goldbeter model.

$$\frac{\partial Z}{\partial t} = \mathcal{L}_{Diffusion} + V_{in} - V_2 + V_3 + k_f Y - kZ \tag{5.22}$$

$$\frac{\partial Y}{\partial t} = V_2 - V_3 - k_f Y \tag{5.23}$$

where ionic calcium concentration in the cytosol (Z) is diffused over the macroscale. All fluxes and variables are defined in Section 3.2. Interestingly, the process of spatial diffusion for the Goldbeter model and the Dupont model was investigated by Dupont and Goldbeter (1994) (and previous work) in two spatial coordinates with a single diffusion coefficient in both directions (isotropic). An isotropic assumption, whilst easy to implement in the mathematical models, is rare in physiology, and thus a debatable choice. The results looked at the placement of stimulated 'cells' alongside non-stimulated 'cells' and the propagation of waves into the previously non-oscillatory region. This is distinctly different from the smooth gradient of a spatially varying stimulus investigated here.

Zero Diffusion

The first of the spatio-temporal results for the Goldbeter model is the system applied with the homogenised macroscale diffusion coefficient equal to zero ($D = 0$). This is also recognised as the uncoupled case and produces the behaviour dictated by the bifurcation diagram Figure 3.3. Figure 5.2 shows the concentration dynamics over time. Overlaid are black horizontal lines indicating the bifurcation points.

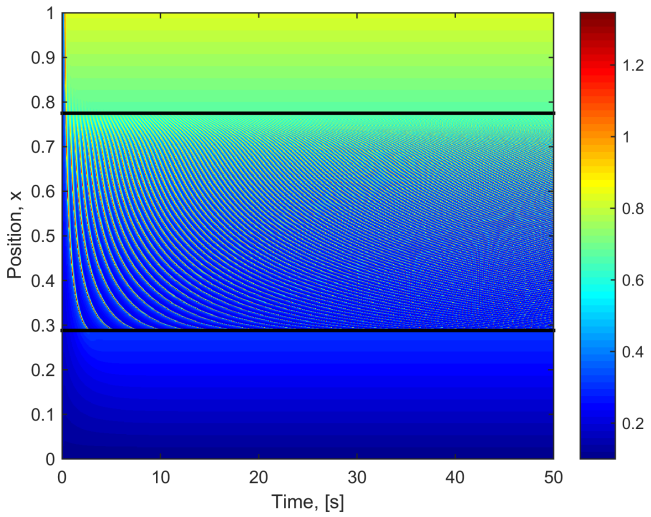

Figure 5.2: Goldbeter model: Zero Diffusion: Spatio-temporal concentration plot for the ionic calcium concentration in the cytosol (Z). The bifurcation parameter β varies linearly in space ($x = \beta$). The black lines represent the bifurcation points from Figure 3.3.

Figure 5.2 is simpler than it first appears. The apparent complexity is due to the appearance of moiré fringes. A moiré fringe in mathematics, physics, and art, is a large-scale interference pattern that can be produced when an opaque ruled pattern with transparent gaps is overlaid on another similar pattern. This visual interpretation can also be attributed to the resolution of Figure 5.2. Figure 5.3 shows a detailed zoom of the spatio-temporal solution in Figure 5.2.

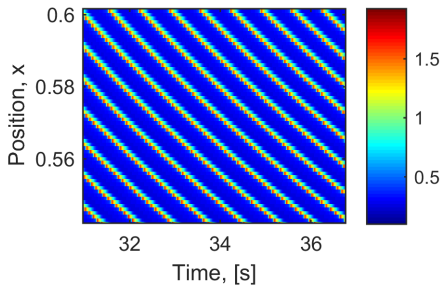

Figure 5.3: Goldbeter model: Zero Diffusion: Zoom in on Figure 5.2 to show true pattern without moiré fringes.

There does exist a variation in period over position on Figure 5.3 this is despite locally the peaks in concentration appearing evenly timed over space. This variation in period is in accordance with Figure 3.5.

*Fickian Diffusion (*FD*)*

The second spatio-temporal result for the Goldbeter model is when Fickian Diffusion (FD) is applied with $D = 5 \times 10^{-6} cm^2 s^{-1}$. The rate of change of Z due to diffusion ($\mathcal{L}_{diffusion}$) is described by Equation 5.4.

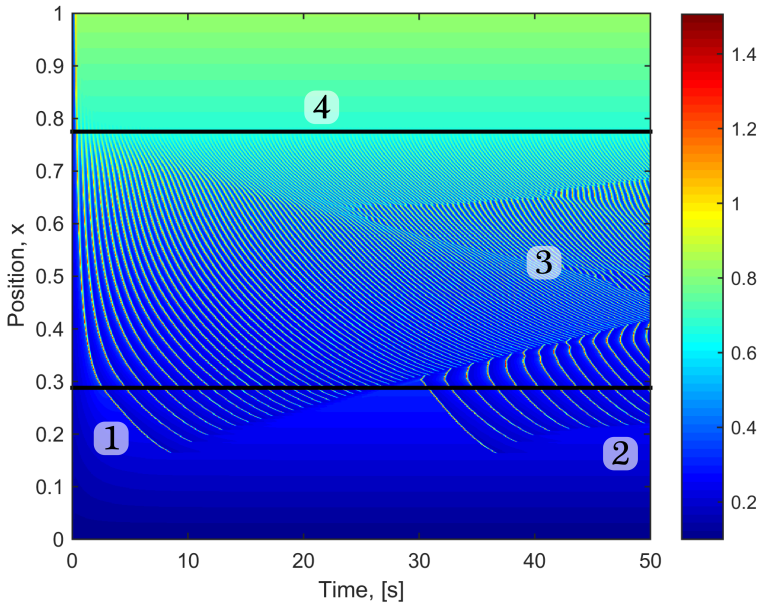

Figure 5.4: Goldbeter model: Fickian Diffusion (FD) ($D = 5 \times 10^{-6} cm^2 s^{-1}$): Space time concentration plot for the ionic calcium concentration in the cytosol (Z). The bifurcation parameter β varies linearly in space ($x = \beta$). The black lines represent the bifurcation points from Figure 3.3. Indicated are 4 areas of interest to be discussed.

Figure 5.4 shows that when 'cells' are allowed to interact with each other via Fickian Diffusion (FD) unusual patterns occur. There are four features of interest on Figure 5.4 that need discussing. First, and most importantly, is the presence of excursions. An excursion, in this context, is a peak of high concentration protruding into the previously non-oscillatory region below the lower bifurcation point (black line at $x = 0.289$). These excursions reach varying depths and appear to stop in an unidentified pattern. These excursions will be investigated further in Chapters 6-8.

Following this, there exists a subsequent pattern of excursions for time greater than ~ 30 seconds for this spatio-temporal result. The depths of these additional excursions as time passes changes unpredictably. Third, between the two bifurcation points (horizontal black lines) the spatio-temporal solution appears to be affected by interference patterns of interacting waves. Finally, the fourth important feature is the lack of excursions above the upper bifurcation point ($x = 0.775$). Above the upper bifurcation point ($x > 0.775$) the affect the initial conditions had on the solution of the Goldbeter model was minimal. On both Figure 5.2 and Figure 5.4 the concentration quickly reached an approximate steady state value for all time.

As previously mentioned, due to the Goldbeter model not containing an appropriate membrane potential equation the effects of Electro-Diffusion (ED) can not be found for this model.

Changing Diffusion Coefficient D

Figure 5.5 shows the effect of increasing the diffusion coefficient, D, on the spatio-temporal solution.

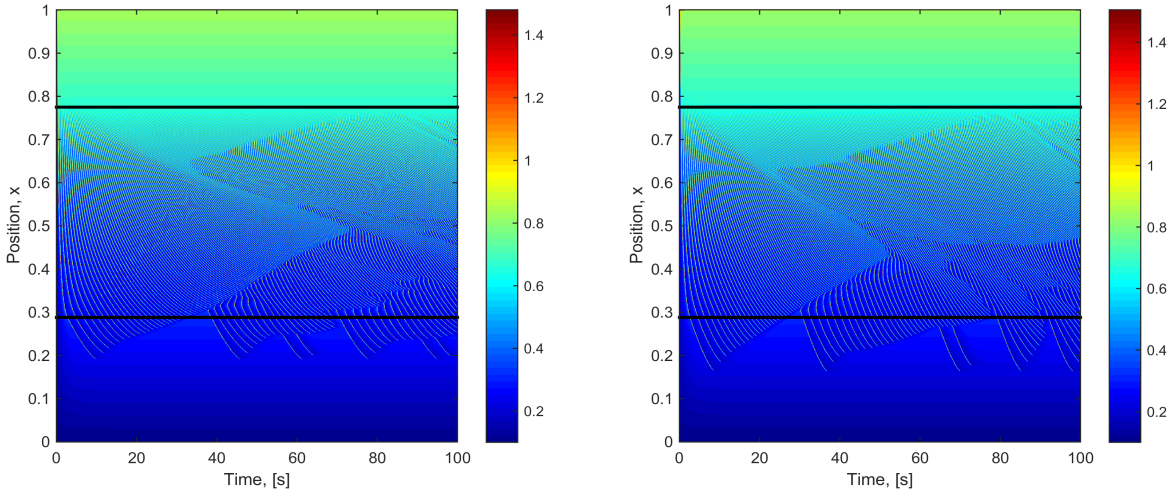

(a) $D = 2.5 \times 10^{-6}$

(b) $D = 5 \times 10^{-6}$

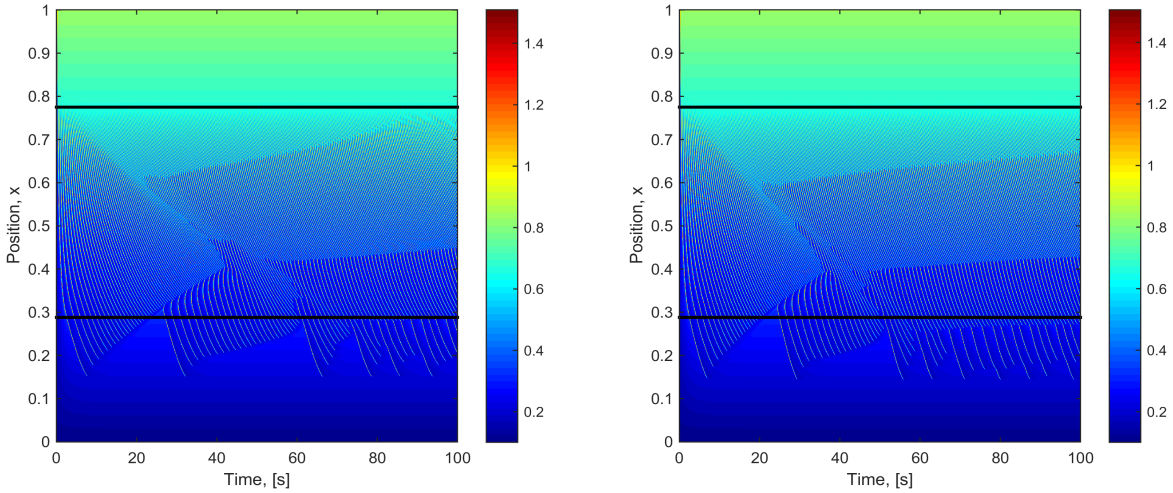

(c) $D = 7.5 \times 10^{-6}$

(d) $D = 10 \times 10^{-6}$

Figure 5.5: Spatio-temporal solutions to the Goldbeter model with increasing diffusion coefficient D $[cm^2 s^{-1}]$. The bifurcation parameter β varies linearly in space ($x = \beta$). The black lines represent the bifurcation points from Figure 3.3.

Figure 5.5 shows that all four of the previously mentioned features still occur. However, the main difference is that the time at which the second and subsequent patterns of excursions occur decreases with increasing D. As the diffusion coefficient is increased, the excursions into the previously non-oscillatory

region occur earlier and the depths reached increase. This relationship stayed the same for all other models. As such, for all other models the effect of varying D is available in Appendix A.

5.3.2 Dupont model Spatio-temporal Results

Again, for completeness the original ODE set from Chapter 3, Section 3.3, has been reproduced including diffusion described by Section 5.2.1 for the Dupont model.

$$\frac{\partial Z}{\partial t} = \mathcal{L}_{Diffusion} + V_{in} - V_2 + V_3 + k_f Y - kZ \tag{5.24}$$

$$\frac{\partial Y}{\partial t} = V_2 - V_3 - k_f Y \tag{5.25}$$

$$\frac{\partial V}{\partial t} = \frac{1}{C_m \alpha}\mathcal{L}_{Diffusion} + \frac{1}{C_m \alpha}(v_0 + v_1 \beta - kZ) \tag{5.26}$$

where ionic calcium concentration in the cytosol (Z) is diffused over the macroscale which subsequently affects the membrane potential (V). All fluxes and variables are defined in Section 3.3.

Zero Diffusion

The first of the spatio-temporal results for the Dupont model is the system applied with the homogenised macroscale diffusion coefficient equal to zero ($D = 0$). This is also recognised as the uncoupled case and produces the behaviour dictated by the bifurcation diagram in Figure 3.8. Figure 5.6 shows the concentration dynamics over time. Overlaid are black horizontal lines indicating the bifurcation points.

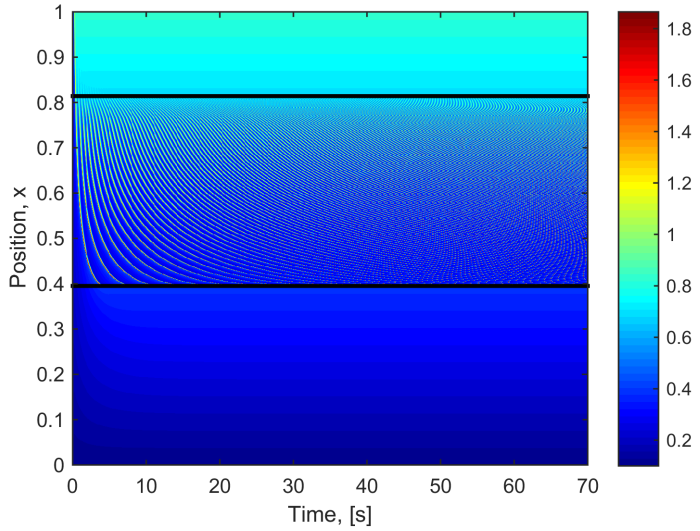

Figure 5.6: Dupont model: Zero Diffusion: Space time concentration plot for the ionic calcium concentration in the cytosol (Z). The bifurcation parameter β varies linearly in space ($x = \beta$). The black lines represent the bifurcation points from Figure 3.8.

Again, Figure 5.6 exhibits moiré fringes and as such caution needs to be taken in interpreting these figures.

Fickian Diffusion (FD)

The second spatio-temporal result of interest for the Dupont model is when Fickian Diffusion (FD) is applied with $D = 5 \times 10^{-6} cm^2 s^{-1}$. As such the rate of change of Z due to diffusion ($\mathcal{L}_{diffusion}$) is described by Equation 5.4.

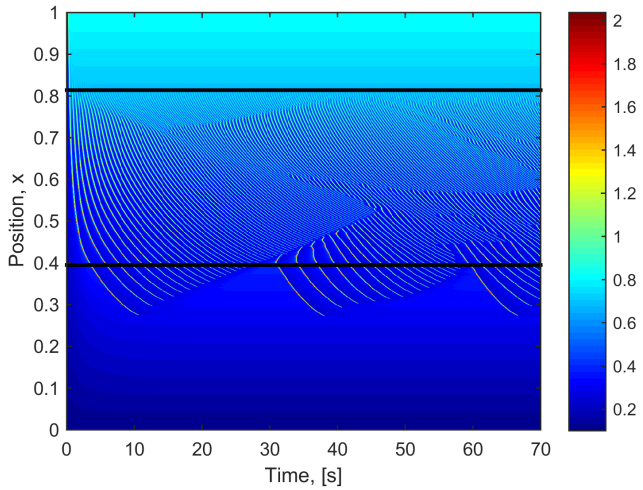

Figure 5.7: Dupont model: Fickian Diffusion (FD) ($D = 5 \times 10^{-6} cm^2 s^{-1}$): Space time concentration plot for the ionic calcium concentration in the cytosol (Z). The bifurcation parameter β varies linearly in space ($x = \beta$). The black lines represent the bifurcation points from Figure 3.8.

Figure 5.7 shows that when 'cells' are allowed to interact with each other via Fickian Diffusion (FD) unusual patterns occur. Similar to the Goldbeter model, there are four features of interest on Figure 5.7: the presence of excursions, the pattern of excursions, the lack of excursions and internal wave interference patterns.

Excursions of high concentrations appear below the bifurcation ($x = 0.395$) where previously no oscillations occurred. These excursions reach varying depths and appear to stop in an unidentified pattern. However, these excursions do not appear above the upper bifurcation point ($x = 0.814$). As time passes additional excursions occur at varying depth and frequency. Finally, between the two bifurcation points ($0.395 \leq x \leq 0.814$) the peaks in concentration appear to interact with each other other causing interference patterns.

*Electro-Diffusion (*ED*)*

The third and final spatio-temporal result for the Dupont model is when Electro-Diffusion (ED) is applied with $D = 5 \times 10^{-6} cm^2 s^{-1}$. As such, the rate of change of Z due to diffusion ($\mathcal{L}_{diffusion}$) is described by Equation 5.11.

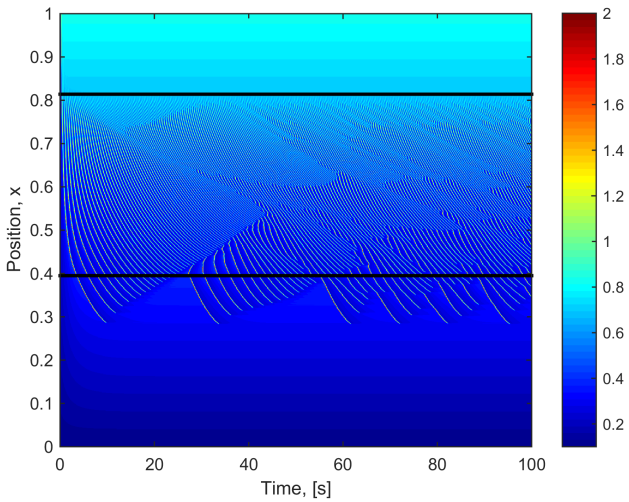

Figure 5.8: Dupont model: Electro-Diffusion (ED) ($D = 5 \times 10^{-6} cm^2 s^{-1}$): Space time concentration plot for ionic calcium concentration in the cytosol (Z). The bifurcation parameter β varies linearly in space ($x = \beta$). The black lines represent bifurcation points from Figure 3.8.

Visually, there appears very little difference between the FD results (Figure 5.7) and the ED results (Figure 5.8) when noting the similar time scales.

5.3.3 Ermentrout model Spatio-temporal Results

Again, for completeness the original ODE set from Chapter 3, Section 3.4, has been reproduced including diffusion described by Section 5.2.1 for the Ermentrout model.

$$\frac{\partial Z}{\partial t} = \mathcal{L}_{Diffusion} + (-\alpha g_{Ca} m_\infty (V - v_{Ca}) - k_{Ca} Z)\rho \tag{5.27}$$

$$\frac{\partial V}{\partial t} = \frac{1}{C_m \alpha}\mathcal{L}_{Diffusion} + \frac{1}{C_m}(-g_L(V - v_L) - g_K N(V - v_k) - g_{Ca} m_\infty (V - v_{Ca})) \tag{5.28}$$

$$\frac{\partial N}{\partial t} = \lambda_n (n_\infty - N) \tag{5.29}$$

where ionic calcium concentration in the cytosol (Z) is diffused over the macroscale, which subsequently affects the membrane potential (V). All fluxes and variables are defined in Section 3.4.

Zero Diffusion

The first of the spatio-temporal results for the Ermentrout model is the system applied with the homogenised macroscale diffusion coefficient equal to zero ($D = 0$). This is also recognised as the uncoupled case and produces the behaviour dictated by the bifurcation diagram in Figure 3.12. Figure 5.9 shows the concentration dynamics over time. Overlaid are black horizontal lines indicating the bifurcation points.

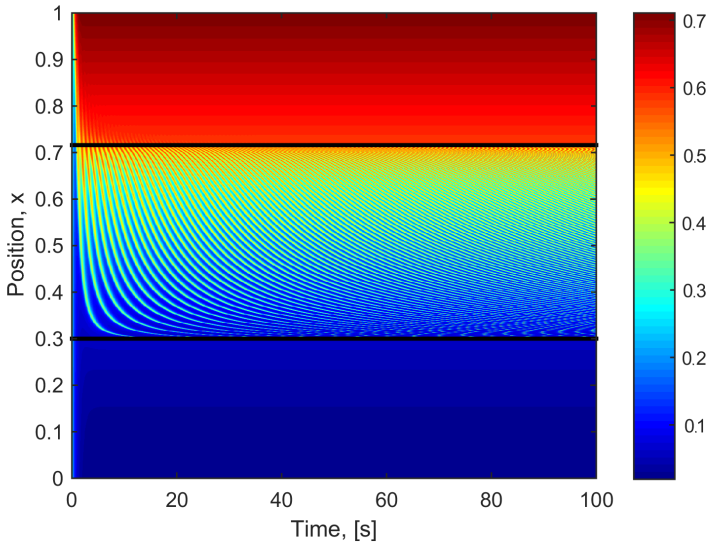

Figure 5.9: Ermentrout model: Zero Diffusion: Space time concentration plot for the ionic calcium concentration in the cytosol (Z). The bifurcation parameter β varies linearly in space ($x = \beta$). The black lines represent the bifurcation points from Figure 3.12.

Again, Figure 5.9 exhibits moiré fringes and as such caution needs to be taken in interpreting this and subsequent figures.

*Fickian Diffusion (*FD*)*

The second spatio-temporal result for the Ermentrout model is when Fickian Diffusion (FD) is applied with $D = 5 \times 10^{-6} cm^2 s^{-1}$. As such, the rate of change of Z due to diffusion ($\mathcal{L}_{diffusion}$) is described by Equation 5.4.

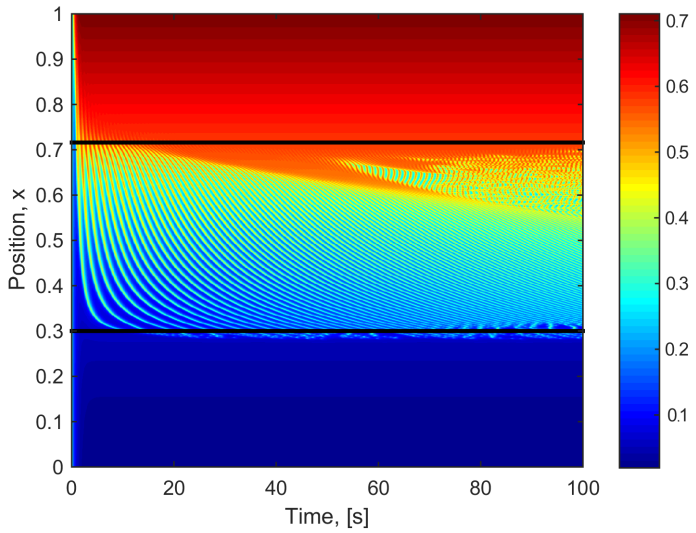

Figure 5.10: Ermentrout model: Fickian Diffusion (FD) ($D = 5 \times 10^{-6}$ $cm^2 s^{-1}$): Space time concentration plot for the ionic calcium concentration in the cytosol (Z). The bifurcation parameter β varies linearly in space ($x = \beta$). The black lines represent the bifurcation points from Figure 3.12.

Figure 5.10 appears to be distinctively different from the first two models when FD is added. Figure 5.10 does produce excursions. However, at this spatial scale it is unclear. As such, Figure 5.11 shows a zoom in on the same results around the lower bifurcation ($x = 0.299$).

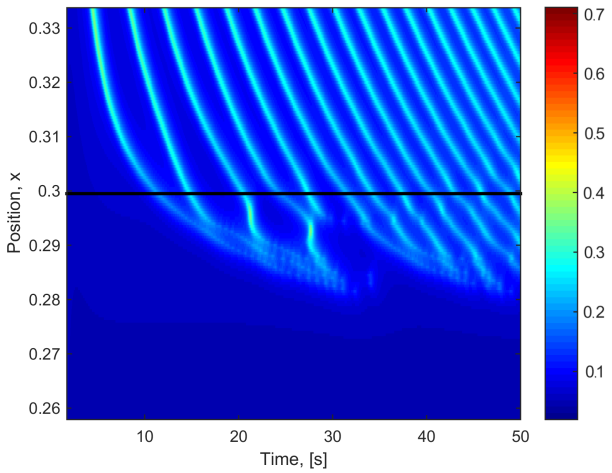

Figure 5.11: Ermentrout model: FD: Spatio-temporal concentration plot for Z. Zoom in on behaviour below the lower bifurcation point from Figure 5.10.

Figure 5.11 shows clearly the presence of excursions. However, unlike the previous models, the excursions do not exhibit distinct depths into the non-oscillatory region. Rather, the high concentration peaks blur. Similar to the previous models, Figure 5.11 shows a lack of excursions above the upper bifurcation point ($x = 0.719$) towards the lower period of oscillation.

*Electro-Diffusion (*ED*)*

The third and final spatio-temporal result for the Ermentrout model is when Electro-Diffusion (ED) is applied with $D = 5 \times 10^{-6} cm^2 s^{-1}$. As such, the rate of change of Z due to diffusion ($\mathcal{L}_{diffusion}$) is described by Equation 5.11.

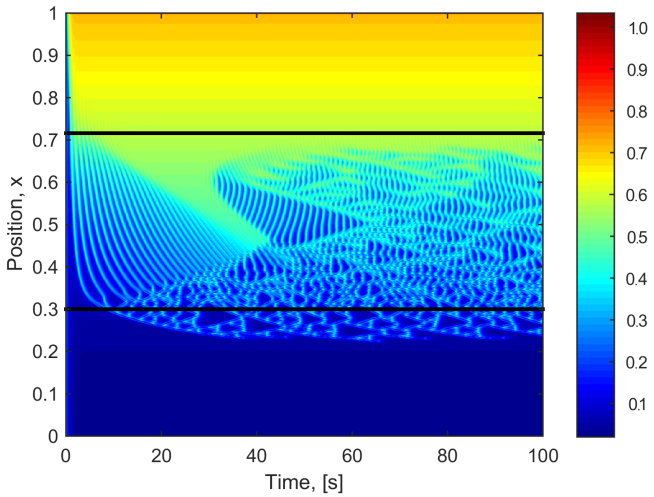

Figure 5.12: Ermentrout model: Electro-Diffusion (ED) ($D = 5 \times 10^{-6}$ $cm^2 s^{-1}$): Space time concentration plot for ionic calcium concentration in the cytosol (Z). The bifurcation parameter β varies linearly in space ($x = \beta$). The black lines represent bifurcation points from Figure 3.12.

Figure 5.12 shows that the Ermentrout model created the most interesting pattern of all the models considered when ED was introduced. Figure 5.12 has a different contour scale to Figure 5.11. This indicates that somewhere on the spatio-temporal plot the concentration peaked to a higher than previous value. The most striking difference is the presence of two directional excursions creating a triangle pattern. This pattern is exhibited both below the lower bifurcation (at $x = 0.299$) and between the bifurcations ($0.299 \leq x \leq 0.719$).

5.3.4 FitzHugh-Nagumo model Spatio-temporal Results

As said previously, the FitzHugh-Nagumo model consists of two variables that do not represent any ionic concentrations to diffuse over the macroscale. However, the FitzHugh-Nagumo model is an important minimal model exhibiting

oscillations and will be used to compare to simplified toy models in the following chapters. So, for these reasons a simple Fickian Diffusion (FD) is added to the model. To avoid bias on the interpretation of the variables, diffusion will be added to each variable separately to enable comparison. The original ODE set from Chapter 3, Section 3.5, has been reproduced in Table 5.2 to include movement of ions due to diffusion described in Section 5.2.1.

Table 5.2: Equation comparison when diffusing U vs W for the FitzHugh-Nagumo model.

U **Diffused**	W **Diffused**
$\frac{\partial W}{\partial t} = c(W - \frac{W^3}{d} - U + \beta_3 I)$	$\frac{\partial W}{\partial t} = \mathcal{L}_{Diffusion} + c(W - \frac{W^3}{d} - U + \beta_3 I)$
$\frac{\partial U}{\partial t} = \mathcal{L}_{Diffusion} + \frac{1}{\tau}(W + a - bU)$	$\frac{\partial U}{\partial t} = \frac{1}{\tau}(W + a - bU)$

where all coefficients in Table 5.2 were defined in Section 3.5. For the FitzHugh-Nagumo model the initial conditions could not be taken as approximate physiological values (Section 2.3.2) since the variables W and U do not strongly relate to any physiological quantity. Thus, the initial conditions for all space were $[W_0, U_0] = [1, -1]$.

Zero Diffusion

The first of the spatio-temporal results for the FitzHugh-Nagumo model is the system applied with the homogenised macroscale diffusion coefficient equal to zero ($D = 0$). This is also recognised as the uncoupled case and produces the behaviour dictated by the bifurcation diagrams Figures 3.17 and 3.18. Figures 5.13 and 5.14 show the variable dynamics over time. Overlaid are black horizontal lines indicating the bifurcation points.

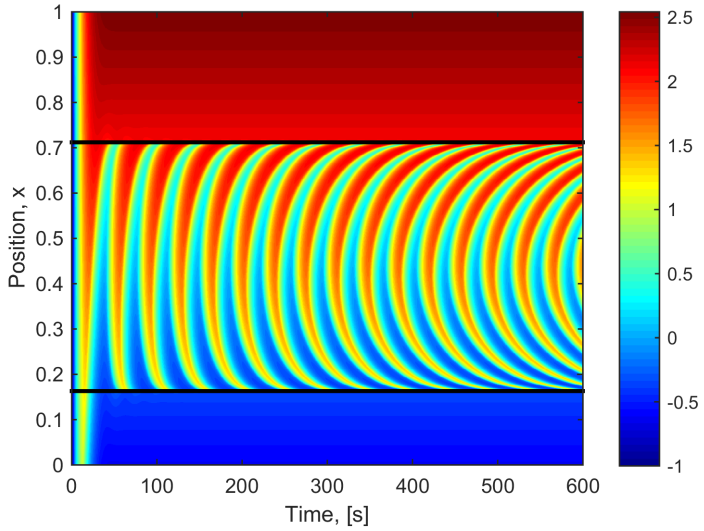

Figure 5.13: FitzHugh-Nagumo model: Zero Diffusion: Slow rate variable (U) Space time concentration plot. The bifurcation parameter β varies linearly in space ($\beta = 2x$). The black lines represent the bifurcation points from Figure 3.18

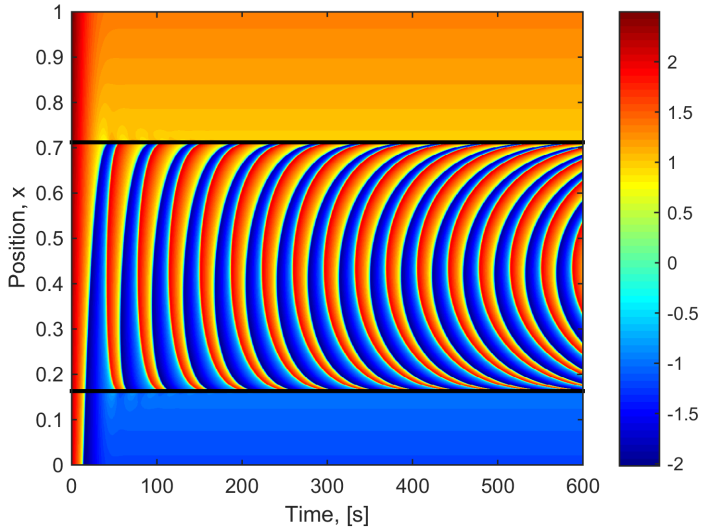

Figure 5.14: FitzHugh-Nagumo model: Zero Diffusion: Fast rate variable (W) Space time concentration plot. The bifurcation parameter β varies linearly in space ($\beta = 2x$). The black lines represent the bifurcation points from Figure 3.17.

Figure 5.13 is very similar to 5.14, as expected from their respective bifurcation diagrams being very similar also.

*Fickian Diffusion (*FD*)*

The second spatio-temporal results for the FitzHugh-Nagumo model is when Fickian Diffusion (FD) is applied with $D = 5 \times 10^{-6} cm^2 s^{-1}$. As such, movement of ions due to diffusion ($\mathcal{L}_{diffusion}$) is described by Equation 5.4. Again, two figures are presented; Figure 5.15 shows the approximation of U with U diffused and Figure 5.16 shows the approximation of W with W diffused.

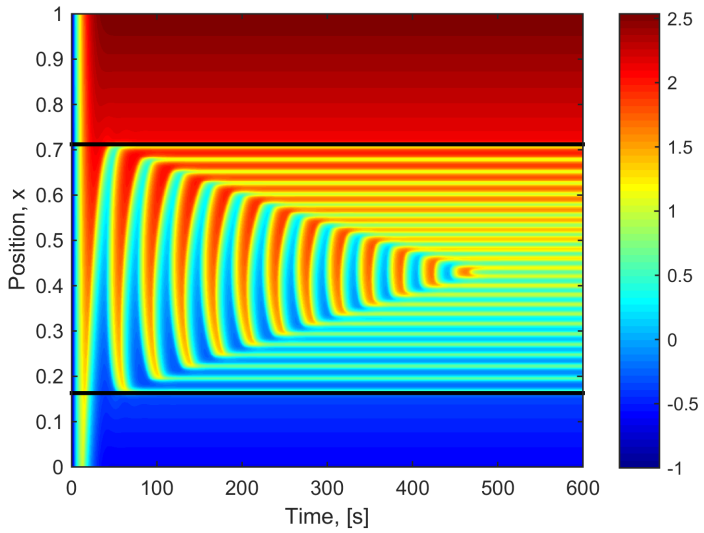

Figure 5.15: FitzHugh-Nagumo model: Fickian Diffusion (FD) ($D = 5 \times 10^{-6} cm^2 s^{-1}$): Slow rate variable ($U$) Space time concentration plot. The bifurcation parameter β varies linearly in space ($\beta = 2x$). The black lines represent the bifurcation points from Figure 3.18.

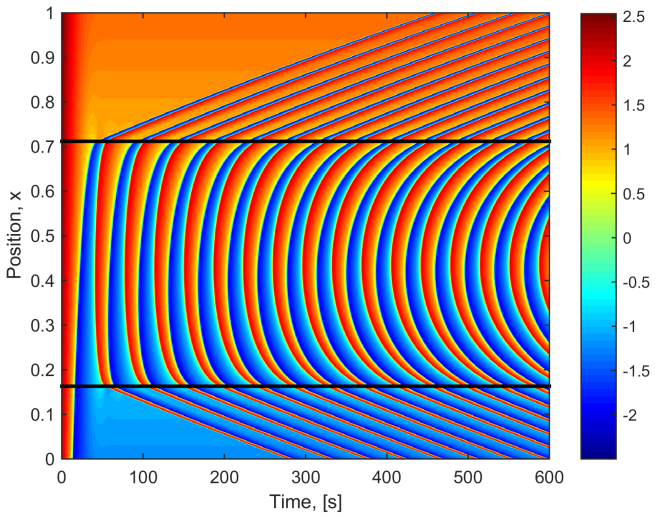

Figure 5.16: FitzHugh-Nagumo model: Fickian Diffusion (FD) ($D = 5 \times 10^{-6} cm^2 s^{-1}$): Fast rate variable ($W$) Space time concentration plot. The bifurcation parameter β varies linearly in space ($\beta = 2x$). The black lines represent the bifurcation points from Figure 3.17.

Figures 5.15 and 5.16 show two completely different results for the spatio-temporal solution to the PDE, depending on the variable diffused. On one hand, Figure 5.16 shows clear excursions of high concentration in the previously non-oscillatory region below the lower bifurcation point (at $x = 0.167$) and conversely excursions of low concentration in the previously non-oscillatory region above the upper bifurcation point (at $x = 0.709$). On the other hand, Figure 5.15 shows no evidence of excursions for all time but instead shows the high concentrations interacting between the two bifurcation points ($0.167 \leq x \leq 0.709$). This development makes the FitzHugh-Nagumo model the most useful to attempt to understand when these excursions occur and will be investigated in Chapter 6.

5.3.5 Koenigsberger model Spatio-temporal Results

Finally, the last of the five models is the Koenigsberger model. Again, for completeness the original ODE set from Chapter 3, Section 3.6, has been reproduced to include diffusion described in Section 5.2.1.

$$\frac{\partial Z}{\partial t} = \mathcal{L}_{diffusion} + J_{IP3} - J_{VOCC} + J_{Na/Ca} - J_{SRuptake} + J_{CICR} - J_{ext} + J_{Leak} \tag{5.30}$$

$$\frac{\partial Y}{\partial t} = J_{SRuptake} - J_{CICR} - J_{Leak} \tag{5.31}$$

$$\frac{\partial V}{\partial t} = \frac{1}{C_m \alpha}\mathcal{L}_{Diffusion} + \gamma\left(-J_{Na/K} - J_{Cl} - 2J_{VOCC} - J_{Na/Ca} - J_K\right) \tag{5.32}$$

$$\frac{\partial N}{\partial t} = \lambda\left(K_{activation} - N\right) \tag{5.33}$$

where ionic calcium concentration in the cytosol (Z) is diffused over the macroscale, which subsequently affects the membrane potential (V) (From Section 5.2.1). All fluxes and variables are defined in Section 3.6. In the original source of the Koenigsberger model, Koenigsberger et al. (2004), a similar diffusion term, known as a coupling flux, was investigated for a two dimensional grid of SMCs. Koenigsberger et al. (2004) looked at the coupling of ionic calcium concentration in the cytosol (Z), Cellular Membrane Potential (V), IP_3 concentration and the ability to cause "synchronization" (oscillations of similar magnitude and frequency in neighbouring cells). They concluded that "...a weak gap junctional calcium coupling can generate and desynchronize calcium oscillations". This means that a weak change in Z due to diffusion can cause excursions. They further concluded that "IP_3 diffusion does not play an important role in the achievement of synchronization", meaning that it could

not cause neighbouring cells to oscillate for reasonable parameter values in the model. They did not attempt to explain why this is the case. However, given their results it gives justification in the simplification of the model as previously described in Chapter 3, Section 3.6.

Zero Diffusion

The first of the spatio-temporal results for the Koenigsberger model is the system applied with the homogenised macroscale diffusion coefficient equal to zero ($D = 0$). This is also recognised as the uncoupled case and produces the behaviour dictated by the bifurcation diagram in Figure 3.21. Figure 5.17 shows the concentration dynamics over time. Overlaid are black horizontal lines indicating the bifurcation points.

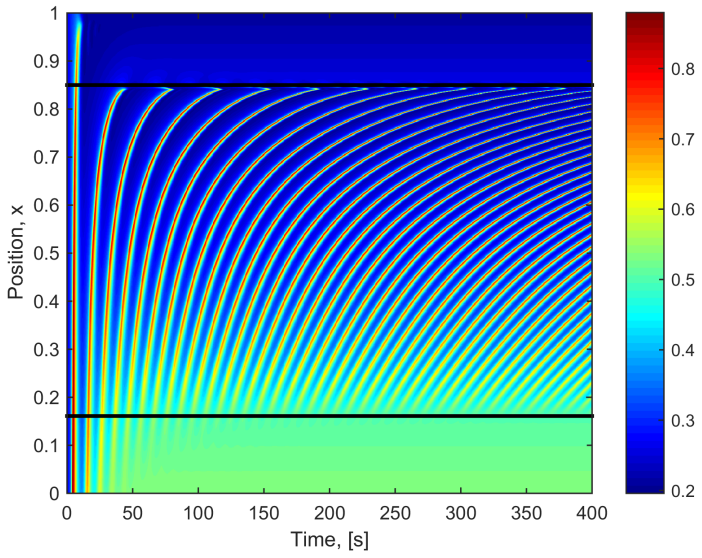

Figure 5.17: Koenigsberger model: Zero Diffusion: Space time concentration plot for the ionic calcium concentration in the cytosol (Z). The bifurcation parameter β varies linearly in space ($x = \beta$). The black lines represent the bifurcation points from Figure 3.21.

Figure 5.17 shows two important characteristics not immediately obvious in the previous models. The first is the effect of the initial conditions. The Koenigsberger model was very sensitive to the initial conditions chosen, as can be seen above and below the bifurcation points ($x \leq 0.174 \cap x \geq 0.857$). Before the system could reach an approximate the steady state above the upper bifurcation point ($x > 0.857$) it first needed to overcome the effect of the initial conditions. The second important characteristic of the Koenigsberger model, previously touched on, is the reverse β profile in comparison to the previous 5 models. While all other models on their bifurcation diagrams exhibited an increasing period of oscillation with a decreasing β and thus position, the Koenigsberger model exhibited an increasing period of oscillation with an increasing β and thus position. This is important knowledge in order to effectively compare these results across models.

*Fickian Diffusion (*FD*)*

The second spatio-temporal result for the Koenigsberger model is when Fickian Diffusion (FD) is applied with $D = 5 \times 10^{-6} cm^2 s^{-1}$. As such, the change in Z due to diffusion ($\mathcal{L}_{diffusion}$) is described by Equation 5.4.

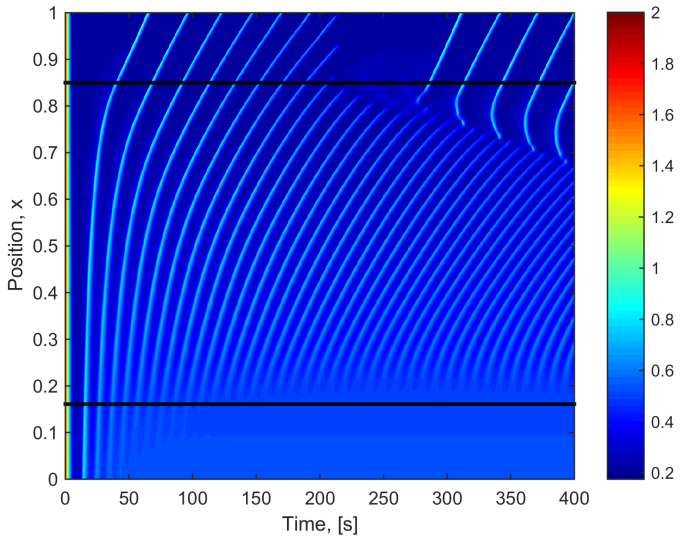

Figure 5.18: Koenigsberger model: Fickian Diffusion (FD) ($D = 5 \times 10^{-6} cm^2 s^{-1}$): Space time concentration plot for ionic calcium concentration in the cytosol (Z). The bifurcation parameter β varies linearly in space ($x = \beta$). The black lines represent bifurcation points from Figure 3.21.

Figure 5.18 shows features similar to the Goldbeter model and Dupont model. Excursions of high concentration occurred above the upper bifurcation point into the previously non-oscillatory region. The first 7 of these excursions reached full depth (to $x = 1$) whilst the 8th excursion did not. Although considered, it is not physiologically plausible to increase the β values above $x(\beta = 1) = 1$ to attempt to obtain a depth of excursions for those excursions that reached full depth. Excursions did not occur below the lower bifurcation point (at $x = 0.857$) beyond any effect of initial conditions experienced in the zero diffusion case.

*Electro-Diffusion (*ED*)*

The third and final spatio-temporal result for the Koenigsberger model is when Electro-Diffusion (ED) is applied with $D = 5 \times 10^{-6} cm^2 s^{-1}$. As such, the change in Z due to diffusion ($\mathcal{L}_{diffusion}$) is described by Equation 5.11.

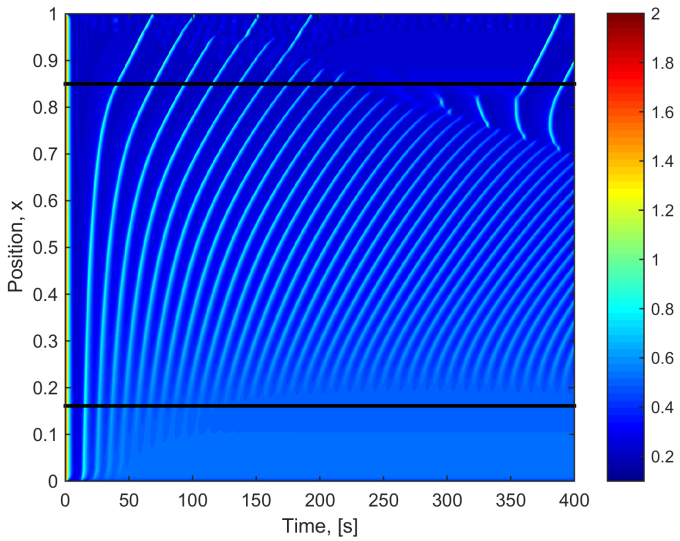

Figure 5.19: Koenigsberger model: Electro-Diffusion (ED) ($D = 5 \times 10^{-6}$ $cm^2 s^{-1}$): Space time concentration plot for ionic calcium concentration in the cytosol (Z). The bifurcation parameter β varies linearly in space ($x = \beta$). The black lines represent bifurcation points from Figure 3.21.

Figure 5.19 is visually similar to the spatio-temporal results with FD (Figure 5.18). The only minor differences were the variations in the depth of the excursions and the appearance of minor 'spotted' concentration changes ($< 5\%$) near the upper boundary at $x = 1$. When compared to the previous 4 models, the difference between FD and ED is on the same level as that of the Dupont model.

5.4 Discussion

This chapter introduced three things important to the spatial media: a spatially varying stimulus, Fickian Diffusion (FD) and Electro-Diffusion (ED). The first, a spatially varying stimulus, is critical to the results depicted within this Chapter. A gradient of stimulus over space allows the visualisation of 'waves' of high concentration peaks moving over space in time for all of the models without diffusion (figures 5.2, 5.6, 5.9, 5.13 , 5.14 and 5.17).

An important concept to note about many of the figures within this chapter is the appearance of moiré fringes (Figure 5.3). Moiré fringes are large-scale interference patterns that can be produced when an opaque ruled pattern with transparent gaps is overlaid on another similar pattern. This type of visual interference pattern can be reduced by detailed zoomed figures and/or higher resolution. As such, caution should be taken before conclusions are drawn about the figures within this chapter.

Another point of note is the effect of initial conditions on the response in the zero diffusion case. The Koenigsberger model displays the most prominent effect from the choice of initial conditions (Figure 5.17). Before reaching steady state, fleeting oscillations in the concentration occur. However, these oscillations rapidly die out and it is clear they do not start again (as expected of such a bifurcation and no spatial interaction). This behaviour can be also be seen in the subsequent spatio-temporal results for the Koenigsberger model under FD. It is important to distinguish which behaviour is attributed to the diffusion as opposed to the initial conditions.

Although all the models have varying concentration ranges and periods of oscillation they all exhibit similar properties detailed in Section 3.7: an oscilla-

tory region, preceded and followed by steady state regions. Additionally, all the models exhibit a period of oscillation which generally increases in amplitude towards the lower steady state concentration bifurcation point. For the Goldbeter model, the Dupont model and the Ermentrout model the lower concentration bifurcation point occurred at the lower of the two positions ($x = 0.289, 0.395$ and 0.299 respectively for each model). This point was labelled the 'lower bifurcation point'. For the FitzHugh-Nagumo model the period of oscillation increased in amplitude towards both bifurcation points and for the Koenigsberger model the lower concentration bifurcation point occurred at the higher position ($x = 0.857$). The Koenigsberger model's 'upside-down' behaviour was, as previously mentioned in Chapter 3, attributed to the bifurcation parameter (β) having a negative relationship in comparison to the other 4 models.

On the introduction of Fickian Diffusion (FD) combined with a spatially varying stimulus multiple interesting patterns arose. The most striking pattern was the presence of excursions of high concentrations, which penetrated the previously non-oscillatory region. This exclusively occurred in the non-oscillatory region adjacent to the 'lower bifurcation point'. The excursions reached varying depths with no easily recognisable pattern. The depths of these excursion are of great interest as the 'cells' that were previously expected to reach a steady state value no longer do so, thus altering the cells' ability to regulate the blood supply (Koenigsberger et al., 2004).

The Goldbeter model and the Dupont model appeared to exhibit visually similar patterns on a similar time scale in their responses to FD which, matched their very similar bifurcation diagrams. This further enhances the argument made by Dupont and Goldbeter (1994) that the β parameter can be added to the V_3 term (Equation 3.10) as it does not effect the overall dynamics but now can

describe a single pool cell.

The FitzHugh-Nagumo model exhibited two vastly different responses depending on whether the variable U or W was diffused. When the variable U was diffused (Figure 5.15) the waves within the oscillatory region appeared to experience destructive interference. However, when the variable W was diffused (Figure 5.16) the waves of high concentration produced excursions into the lower steady state region and the troughs produced excursions into the upper steady state region. This was the most drastic difference between any two models. It highlights an important possibility that excursions could be induced in neighbouring cells based upon a model's dynamics. This phenomenon of excursions of high concentrations entering the previously non-oscillatory region is important to be understand and there exists a desire to determine whether or not this can be controlled. This is a point of investigation that will be further explored in the following chapters.

The Ermentrout model applied with FD appears to have a compromise between the cancelling out of waves and the presence of excursions. When viewed on the correct scale, excursions were present but did not have distinct depths or clear concentration peaks. Unlike the other models, the peaks were blurred over space and time. At this stage, asides from attributing this behaviour to the different type of bifurcation point ("an undetermined saddle node infinite cycle bifurcation" compared to a Hopf bifurcation) it is still unclear as to why the Ermentrout model behaves this way.

Figure 5.5 and additionally Appendix A show the effect of a variation of different homogenised macroscale diffusion coefficients (D) for each of the 5 models. It was noted in Section 5.3.1 that by increasing the diffusion coefficient, excursions occur quicker in time. The reason for this is under investigation and

will be discussed in following chapters (Chapters 7 and 8).

Electro-Diffusion (ED) was able to be added to only three of the 5 models: the Dupont model, the Ermentrout model and the Koenigsberger model. This was due to the ED equation (Equation 5.12) requiring both an equation for the Cellular Membrane Potential (V) and the ionic calcium concentration in the cytosol (Z). On one hand, the ED results for the Dupont model and the Koenigsberger model (Figure 5.8 and 5.19) were visually similar to their results with the inclusion of FD (Figure 5.7 and 5.18). For these two models the difference between zero diffusion and FD was significantly more prominent than the difference between the different types of diffusion (FD to ED). On the other hand, when ED was applied to the Ermentrout model (Figure 5.12) the spatio-temporal solution had the largest difference between the types of diffusion of all the models explored. This suggests that the membrane potential in the Ermentrout model plays a more dominant role than it does in the first two models.

On comparison of the mathematical decomposition of the three models (to which ED was applied) the difference becomes clear. The Ermentrout model is built via conductance based modelling techniques (Section 2.2.7), for which a change in the membrane potential presumes a change in the cytosolic ionic calcium concentration. Conversely, the Dupont model is built primarily using chemical reaction based modelling techniques, with the movement of calcium dictating the change in membrane potential. The Koenigsberger model is unique in that it was developed as a compromise between the two types of models. Whilst all three exhibit the same single cell dynamics (previously mentioned) they produce different responses under a spatial stimulus with FD and ED. Since, as compared, the Koenigsberger model behaves visually similar to the Dupont model it suggests that the Koenigsberger model is influenced greater by

the chemical reaction based modelling components over the conductance based modelling components.

Although the results of the Ermentrout model are revisited in the following chapters, the results of the other two models give rise to the notion that the difference between zero diffusion and FD is far greater than the difference between FD and ED on the macroscale. As a result, FD and the resulting excursions will be the focus for the remainder of this research.

5.5 Conclusion

This chapter introduced three things important to the spatial context: a spatially varying bifurcation parameter, Fickian Diffusion (FD) and Electro-Diffusion (ED). Without any diffusion, 'waves' of high concentration were seen moving over space in time. These waves, with the addition of FD, were then seen to create excursions of high concentration over space into the previously non-oscillatory region. The high concentration excursions reached varying depths in space and time, and only appeared in the non-oscillatory region bordering the 'lower bifurcation point'.

The FitzHugh-Nagumo model exhibited interesting responses to the addition of FD. When the variable U was diffused the peaks within the oscillatory region appeared to cancel each other out and smooth the internal oscillations. However, when the variable W was diffused excursions were present in the previously non-oscillatory region. ED saw two groups of results: the Ermentrout model produced bi-directional waves compared to the Koenigsberger model and the Dupont model whose results resembled their FD counterparts. In fact, the difference between the spatio-temporal results of the Dupont model and the Koenigsberger model applied with zero diffusion vs FD was far greater

than the difference between the application of FD vs ED. As such, FD and the occurring excursions will be the focus for the remainder of this research.

6 Wave Shape Theory, Front Heavy (FH) Score: Toy Models

6.1 Introduction

The previous chapter highlighted how models that had similar dynamics on the single cell level (oscillations, bifurcations and period comparison see Chapter 3 and 5) each produced slightly different results when connected in a spatial medium and applied with Fickian Diffusion (FD). A common theme across many of the models was the presence of excursions of high concentration entering the previously non-oscillatory region. The peaks of high concentration appeared to move in space over time and reached seemingly unpredictable depths into this region. Importantly, these excursions only occurred in the previously non-oscillatory region on the macroscale space neighbouring the 'lower bifurcation point'. This chapter looks to investigate why not all of the models experienced these excursions of high concentration with the addition of FD, and proposes a new theory to aid in predicting when excursions will occur.

The FitzHugh-Nagumo model provided the most insight into when excursions of high concentration occur. When the variable U was diffused, the waves within the oscillatory region visually appeared to cancel each other out and

smooth the internal oscillations. In comparison, diffusion of the variable W resulted in waves of high concentration penetrating into the lower steady state region and the waves of the troughs penetrating the upper steady state region. The FitzHugh-Nagumo model, whilst not a cell model, offers a thus far unique example in which excursions do not occur. Understanding the difference and similarities between the FitzHugh-Nagumo model and the other cell models leads to a potential ability to control the presence of excursions.

This chapter seeks to propose and test a new theory as to when excursions of high concentration into the previously non-oscillatory region will occur. To do this first, the theory will be posed followed by an initial review. The theory will then be quantified and tested on all the models in addition to its application to three generated 'Toy Models'.

6.2 Hypothesis

The presence of excursions of high concentrations, on the addition of FD, into the previously non-oscillatory region are present under the following three criteria:

1. Within the macroscale (under no coupling) the model must experience both an oscillatory region and a non-oscillatory region (also known as a steady state region) separated by a bifurcation point.
2. The period of oscillation must change over space, such that on the macroscale (of order $1cm$) the period of oscillation must show a trend of increasing period towards the aforementioned bifurcation point. *

* Period variations contrary to this criteria are allowed on the spatial macroscale in accordance with Chapter 3.

3. The wave shape (near the bifurcation point), further detailed in the following subsection, must have a front heavy asymmetric profile.

The first criteria is the presence of two separate regions. This is necessary as without a non-oscillatory region excursions can not occur, and without an oscillatory region there are no peaks of high concentration to be diffused. The second criteria is that the period of oscillation, overall, must increase towards the transition between the two regions. As long as the period of oscillation increases overall, sudden reductions near the bifurcation point can be neglected. This is in line with the physiological models such as the Goldbeter model, the Dupont model and the Koenigsberger model.

6.2.1 Wave Shape

The wave shape of a solution is defined as one period of a steady concentration oscillation over time, for a system of ODEs, from one minimum to the next.

$$Waveshape = \Phi(\beta^*, t) \qquad \text{where} \qquad t \in [t_{min}, t_{min} + T] \tag{6.1}$$

where β^* must produce an oscillatory response, T is the period and t_{min} is the time at which the minimum occurs. Furthermore, the chosen beta value β^* and its position must be within $\sim 10\%$ of the true bifurcation value (β_B) and position (x), ie. $\{|\beta_B - \beta^*| < 0.1\beta_B\} \cap \{|x(\beta_B) - x(\beta^*)| < 0.1x(\beta_B)\}$. It is assumed that for small changes in position (and thus small changes in the β value) the shape of the oscillation will not significantly change.

$$|\Phi(\beta^* + \varepsilon, t) - \Phi(\beta^* - \varepsilon, t)| \leq tol \qquad \text{for} \qquad t \in [t_{min}, t_{min} + T] \tag{6.2}$$

The resulting wave shape can be categorised as one of three shapes: Symmetric, an Asymmetric Front Heavy (FH) wave shape or an Asymmetric Backwards Heavy (BH) wave shape. A symmetric wave shape, for example $y = sin(x)$, is an even function about its maximum. An Asymmetric Front Heavy (FH) wave shape has, about its maximum, a rapid increase in concentration followed by a slow decrease in concentration. Conversely, an Asymmetric Backwards Heavy (BH) wave shape has, about its maximum, a slow increase in concentration followed by a rapid decrease in concentration. This will be quantified further in this chapter.

6.3 *Application:* TM1, TM2

In order to fully understand why and when the excursions occur, it is necessary to understand the dynamics of the models. The physiological models introduced in Chapter 3 have set parameter values as they have been linked to experimental data. Therefore, manipulating these models would destroy the physiological comparability. To avoid this dilemma, 'Toy Models' (TM) have been created, with no physiological relevance, in order to adapt and change the parameters without implying physiological phenomena. The Toy models are initially based on the FitzHugh-Nagumo model as it is the simplest model examined that created the behaviour of interest; excursions of high concentration into the previously non-oscillatory region. The Toy models were designed in order to fulfil the following predefined criteria:

- The models must contain a bifurcation parameter which varies over the macroscale ($\beta(x)$).
- On the specific variation of β the model must transition from a steady

state solution to a periodic oscillatory solution.

- This transition for the Toy models will be a Hopf bifurcation to avoid unnecessary complexity.
- The associated period of the oscillatory region must increase over space towards the sole bifurcation point.

The purpose of the Toy models was to create an analytically solvable mathematical model in which the bare minimum components are included to produce the desired behaviour. A Hopf bifurcation, whilst not a necessary criteria, was chosen in order to have the most relevance for comparison to the majority of the other models.

Many different Toy models were investigated, each a small variation of the FitzHugh-Nagumo model. Two examples with specific parameter choices are presented in this research to highlight key findings. Of the two models, the first was designed so it does not produce excursions of high concentrations in the previously non-oscillatory region under FD and the second, conversely, was designed to exhibit excursions under FD for comparison.

The two Toy models do not attempt to model any physiological quantity and should not be applied in such a way. The Toy models were simulated by the method discussed in Chapter 5 and with a bifurcation analysis discussed in Section 2.4.1. Additionally, the bifurcation points of the toy models were found using an analytical approach. An example of this was preformed on TM2 and is found in Appendix C.

*6.3.1 Toy Model 1 (*TM1*)*

The first of the two Toy models is defined by two rates of change of the two variables Φ and Ψ (Equations 6.3 and 6.4 respectively).

$$\frac{\partial \Phi}{\partial t} = \beta\Psi - \frac{\Phi^3}{3} - \frac{\Phi^2}{2} + \mathcal{L}_{Diffusion} \tag{6.3}$$

$$\frac{\partial \Psi}{\partial t} = -(\beta\Phi + c) \tag{6.4}$$

where $\{\beta = x + 0.5\}$, $c = 1$ and Fickian Diffusion (FD) is applied to only the variable Φ as only one example is desired. For this model a Hopf bifurcation occurs when $\beta = c$ and, thus, the bifurcation will occur at $x = 0.5$. This relationship was found analytically (not included) by finding the eigenvalues of the Jacobian matrix. This was confirmed with continuous bifurcation analysis completed in Auto07p (Section 2.4.1). These parameters were chosen to obtain the desired output. Multiple options were considered but determined surplus in representing the desired behaviour.

*6.3.2 Toy Model 2 (*TM2*)*

The second of the two models, consistent with the first, is again defined by two rates of change variables Φ and Ψ (Equations 6.5 and 6.6 respectively).

$$\frac{\partial \Phi}{\partial t} = \beta\Psi - \frac{\Phi^3}{3} + \Phi + \mathcal{L}_{Diffusion} \tag{6.5}$$

$$\frac{\partial \Psi}{\partial t} = -(\beta\Phi + c) \tag{6.6}$$

where $\{\beta = 0.2x + 0.1\}$, $c = 0.2$ and, again, Fickian Diffusion (FD) is applied to only the variable Φ. Again, for this model a Hopf bifurcation occurs when $\beta = c$. This relationship was found analytically by finding the eigenvalues of the Jacobian matrix (Appendix C).

The clear difference between the two models is the term $-\frac{\Phi^2}{2}$ in TM1 compared with the simple Φ term in TM2. As Φ increases in magnitude from the

unstable fixed point, TM1 will act to reduce the rate of change of Φ quicker than TM2.

6.4 Initial Results

6.4.1 Application Results

The initial results required in this section are the bifurcation diagrams of the two Toy models, along with the associated periods of oscillation. These were created in Auto07p as detailed in Section 2.4.1. Bifurcation diagrams (Figure 6.1) and their associated periods of oscillation (Figure 6.2) are needed in order to confirm that the Toy models meet the criteria defined in Section 6.3.

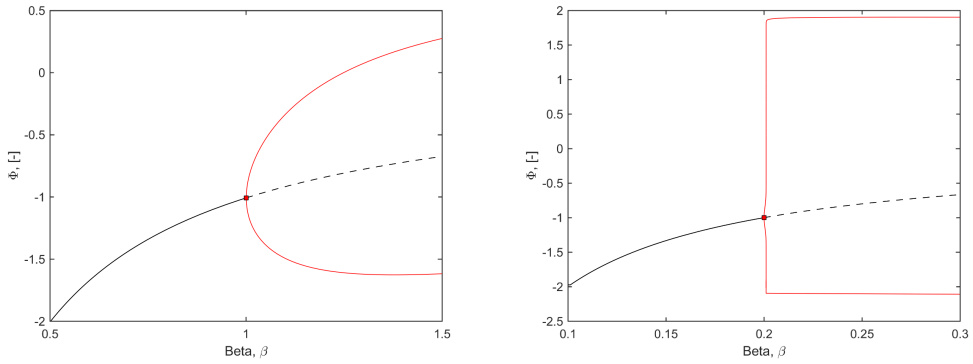

(a) TM1 *(b)* TM2

Figure 6.1: Bifurcation Diagrams of Two Toy models defined by Section 6.3.1 and 6.3.2. The bifurcation points occur at $\beta = 1$ and $\beta = 0.2$ for TM1 and TM2 respectively. Black line indicates a stable fixed point, red line indicates stable limit cycle and black dotted line indicates unstable fixed point.

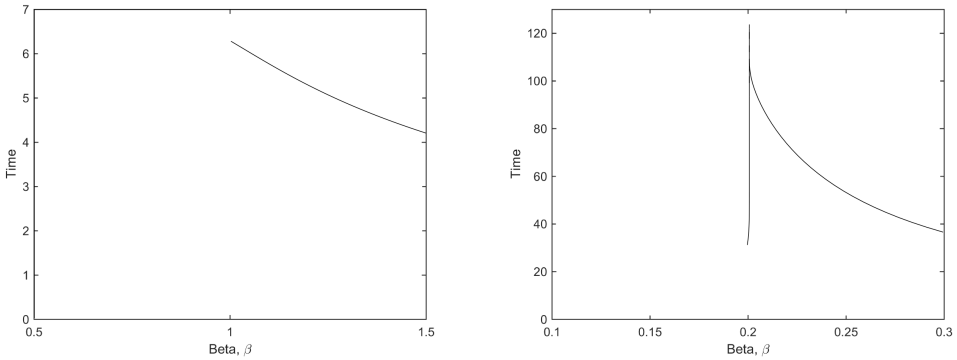

(a) TM1 *(b)* TM2

Figure 6.2: Period of oscillation for Two Toy models defined by Sections 6.3.1 and 6.3.2.

Figure 6.1 and 6.2 show that the two Toy models meet all of the specified criteria: a bifurcation parameter, a steady state region and an oscillatory region, a Hopf bifurcation (confirmed in Auto07p) and an associated period which increases towards the bifurcation point.

Next, the two Toy models were solved spatially with the bifurcation parameter varying linearly in space such that both bifurcation points occurred at $x = 0.5$. The models were solved with zero diffusion ($D = 0$) and Fickian Diffusion (FD) with $D = 5 \times 10^{-6} cm^2 s^{-1}$ and a $\beta(x)$ profile defined in their respective sections (Sections 6.3.1 and 6.3.2).

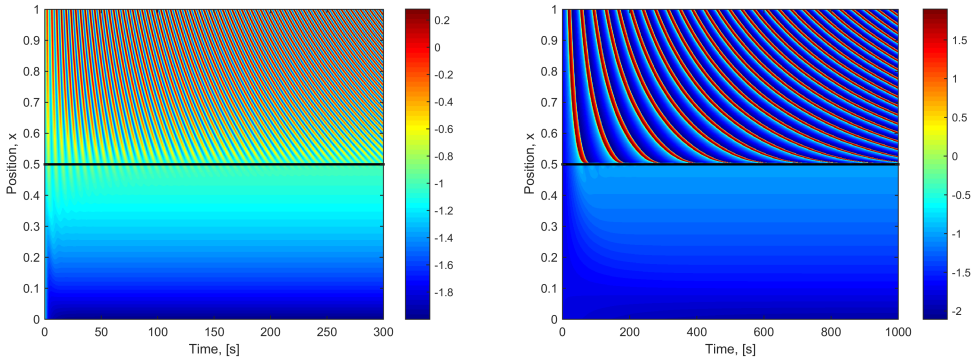

(a) TM1 Zero Diffusion *(b)* TM2 Zero Diffusion

Figure 6.3: Space time concentration plots for the two Toy models with zero diffusion ($D = 0$). Black line indicates bifurcation points. Where $x = f(\beta)$ is described in Sections 6.3.1 and 6.3.2 respectively.

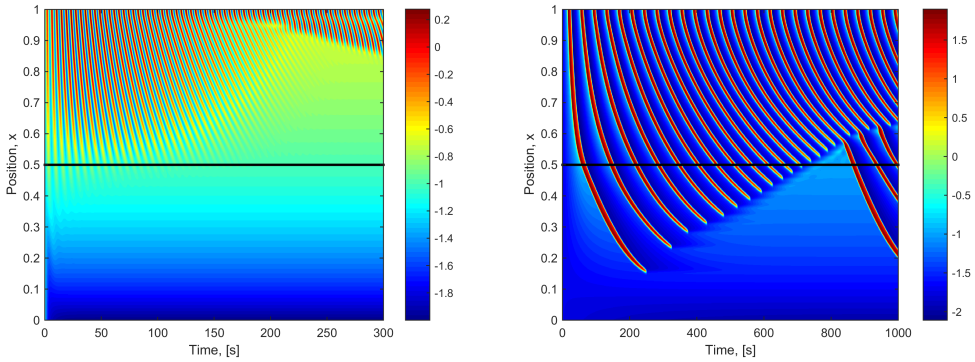

(a) TM1 Fickian Diffusion (FD) *(b)* TM2 Fickian Diffusion (FD)

Figure 6.4: Space time concentration plots for the two Toy models with Fickian Diffusion (FD) ($D = 5 \times 10^{-6} cm^2 s^{-1}$). Black line indicates bifurcation points. Where $x = f(\beta)$ is described in Sections 6.3.1 and 6.3.2 respectively.

It is clear that although both models met all the predefined criteria, (Section 6.3) when applied with FD two very different results occurred. Next, using the definition of a wave shape (Section 6.2.1) it became apparent why this is true. Figure 6.5 shows the wave shape for the two Toy models compared to itself stepped forward in time (the blue dotted line) and stepped backwards in time (the black line). The transition of 10% of the period was chosen as a visual

example. Again, it was assumed that for small changes in β this wave shape did not change significantly.

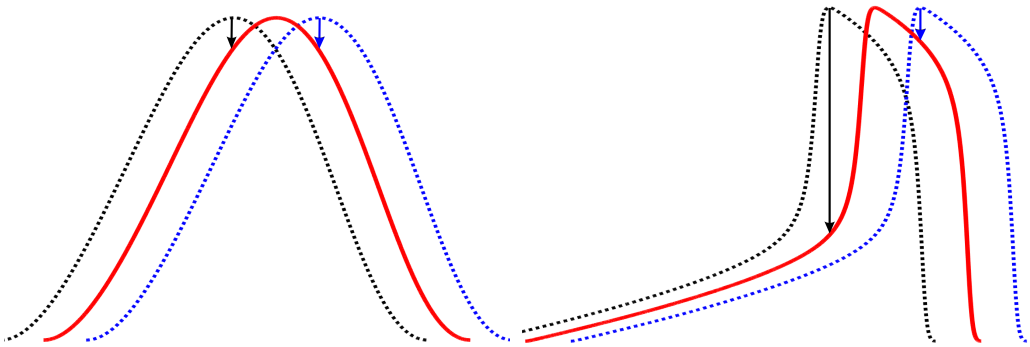

(a) Toy Model 1 (TM1) *(b)* Toy Model 2 (TM2)

Figure 6.5: Wave shape of each of the Toy models close to the bifurcation point, where the dotted black line is the red line translated in time by -10% of the period and the blue is translated forward in time 10% of the period. Arrows are added from the peak of concentration to indicate magnitude. Time is on the x axis and Φ is on the y axis. Values have been omitted to avoid confusion.

TM1 is almost symmetric about its maximum. However, TM2 has a FH asymmetric wave shape. This means TM2 has a rapid increase in concentration followed by a slow decrease in concentration immediately surrounding the maximum. Given that in space there is an increasing period of oscillation towards the bifurcation point it can be considered, as an approximation, that the black dotted line is further away from the bifurcation point in space compared to the red line. Conversely, the blue dotted line is closer to the bifurcation point in space (the next spatial position). As time increases, variations of this alignment between the three waves (percentage of period translations) will occur.

Overlaid on Figure 6.5 are two arrows from the maximum concentration of the translated wave shapes to the original. For a symmetrical wave (for example $y = sin(x)$) these two arrows, for an equal translation either side of the maximum concentration, will always be equal in magnitude. TM2, on the other hand, being

a FH asymmetrical wave shape, has unbalanced arrows such that the black arrow is greater in magnitude than the blue arrow. Should the blue arrow be greater the wave shape would be considered a Backwards Heavy (BH) asymmetrical wave shape.

Using the definition of Fickian Diffusion (FD) from Equation 5.19 the magnitude of the change in Φ due to diffusion is approximated as proportionate to three 'cells' concentration: the previous spatial position (the black dotted line), the next spatial position (the blue dotted line) and the current spatial position (the red line). When the two differences in concentration to the current position (the black arrow and the blue arrow) are unbalanced in magnitude, there exists a directional net diffusion flux. When the change in concentration from the previous position (the black arrow) outweighs (in magnitude) the change in concentration from the next position (the blue arrow) then the direction is from the previous position (black dotted line) towards the next position (blue dotted line). Thus, recalling this translation is approximating the period change, the direction of this net diffusional flux is towards the greater period of oscillation. In TM2's case this net flux, is in the direction of the larger period, which is in the direction of the bifurcation point.

6.4.2 Model Results

To translate this knowledge to all the other models, their waves shapes are depicted in Figure 6.6.

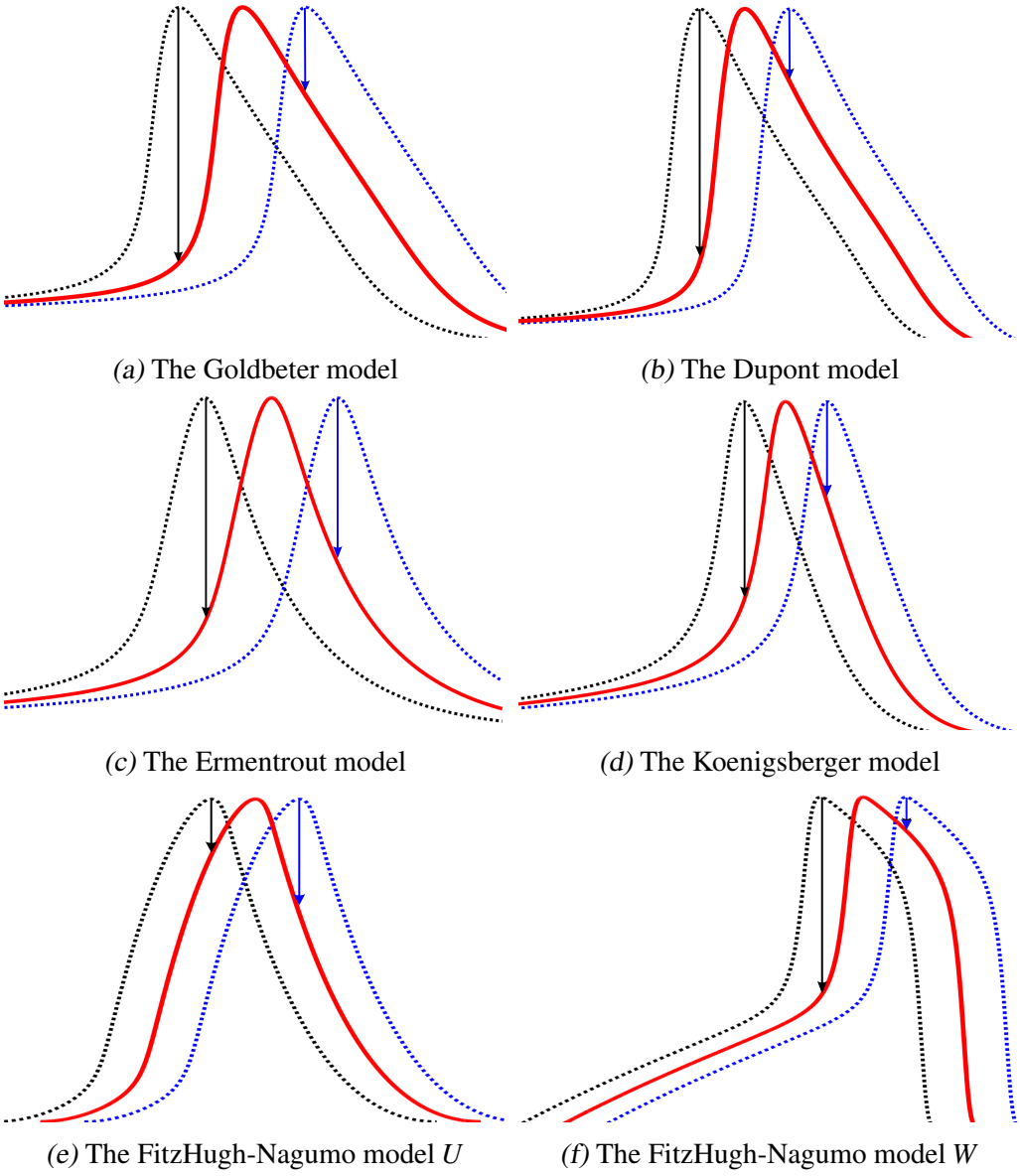

(a) The Goldbeter model

(b) The Dupont model

(c) The Ermentrout model

(d) The Koenigsberger model

(e) The FitzHugh-Nagumo model *U*

(f) The FitzHugh-Nagumo model *W*

Figure 6.6: Wave shape of each of the models close to the bifurcation point. Where the dotted black line is the red line translated in a negative fixed percentage of the period and the blue is translated forward in time the same fixed percentage of the period. Arrows are added from the peak of concentration to indicate magnitude. Time is on the x axis and Φ is on the y axis. Values have been omitted to avoid confusion.

The wave shapes within Figure 6.6 (a), (b), (c), (d) and (f) have a Front Heavy (FH) asymmetric Wave Shape in which the blue arrow is greater than the black

arrow for small shifts in the translation. The FitzHugh-Nagumo model variable U, on the other hand, produced a Backwards Heavy (BH) asymmetric Wave Shape (Figure 6.6.e). A full review of these results alongside the models that produce excursions of high concentrations into the previously non-oscillatory region is summarised in Table 6.1.

Table 6.1: Summary of results described within this chapter and Chapter 5.

	Front Heavy (FH) **Asymmetric Wave Shape**	**Excursions in Previously Non-Oscillatory Region**
Goldbeter model	✓	✓
Dupont model	✓	✓
Ermentrout model	✓	✓
FitzHugh-Nagumo model- U	X	X
FitzHugh-Nagumo model- W	✓	✓
Koenigsberger model	✓	✓
Toy Model 1 (TM1)	X	X
Toy Model 2 (TM2)	✓	✓

Note that the more FH a wave shape is does not relate to depth of excursions into the non-oscillatory region. This will be addressed in Chapter 7 and 8.

6.5 Interpretation of Results

This chapter looks to propose and test a hypothesis to predict when excursions of high concentration into the previously non-oscillatory region will occur. Thus far, the hypothesis has been posed and an initial review of the theory applied to all the models has been viewed. The hypothesis states that in order for excursions to occur under feasible D values, three criteria need to be met. First, the model must exhibit, over the macroscale, a region of non-oscillatory steady state behaviour and a region of oscillatory behaviour separated by a bifurcation point.

Second, the oscillatory region must have a period of oscillation that overall increases over space towards the mentioned bifurcation point. Finally, the wave shape (defined in Section 6.2.1) must have an asymmetric Front Heavy (FH) profile.

An asymmetric FH wave shape produces a directional net diffusion flux when aligned with two neighbouring positions of different periods. As the period of oscillation increases over the macroscale towards the aforementioned bifurcation point this net diffusion flux, for an asymmetric FH wave shape, must travel in the direction of the increasing period over space. Considering the majority of the models exhibit a period of oscillation increasing towards at least one of the bifurcation points, this net diffusion flux causes the excursions to propagate through space beyond that bifurcation point. Should the wave exhibit a Backwards Heavy (BH) wave shape the excursions were directed in the opposite direction.

A distinct correlation between a model's wave shape and whether it produces oscillations in the previously non-oscillatory region is shown in Table 6.1. In particular, TM1 exhibited a nearly symmetrical wave shape and the FitzHugh-Nagumo model variable U produced a Backwards Heavy (BH) wave shape. Both of these models did not produce excursions into the non-oscillatory region while all others did.

A FH wave shape is critical in producing excursions due to the directional net diffusion flux in the direction from the oscillatory region towards the non-oscillatory region. The shape needs to be quantified in order to accurately predict excursions. Furthermore, this quantification is important to, in future, modify the single cell dynamics such that the presence of these excursions can be controlled. This would limit which 'cells' experience sudden large spikes in

concentrations.

6.6 Quantification Method

To quantify how asymmetric FH the wave shape is, the following derivation (Equations 6.7 to 6.15) of the FH-score is needed.

Generically, for three positions, a, b and c, with concentrations, $\Phi(a)$, $\Phi(b)$ and $\Phi(c)$, a net one directional flow of Φ will occur from a to c if Equation 6.7 is true.

$$\Phi(b) - \Phi(a) < \Phi(b) - \Phi(c) \tag{6.7}$$

where $\Phi(b) > \Phi(a)$ and $\Phi(b) > \Phi(c)$. Thus,

$$\Phi(a) - \Phi(c) > 0 \tag{6.8}$$

When comparing this to the PDE system in time and space, Equation 6.8 can be rewritten to show a net one directional flow of Φ from $x + \Delta x$ to $x - \Delta x$ if Equation 6.9 is true.

$$\Phi(x + \Delta x, t) - \Phi(x - \Delta x, t) > 0 \tag{6.9}$$

where $\Phi(x + \Delta x, t)$ has a small decrease in period and $\Phi(x - \Delta x, t)$ has a small increase in period from $\Phi(x, t)$ for the described models. The following approximations (Equations 6.10 and 6.11) are made for small variations in the period for $t \in [t_{min}, t_{min} + T]$ about the maximum concentrations.

$$\Phi(x + \Delta x, t) \approxeq \Phi(x, t + \varepsilon_1) \tag{6.10}$$

$$\Phi(x - \Delta x, t) \approxeq \Phi(x, t - \varepsilon_2) \tag{6.11}$$

Figure 6.7 shows a depiction of this approximation for a simple $y = sin(x)$ wave over time.

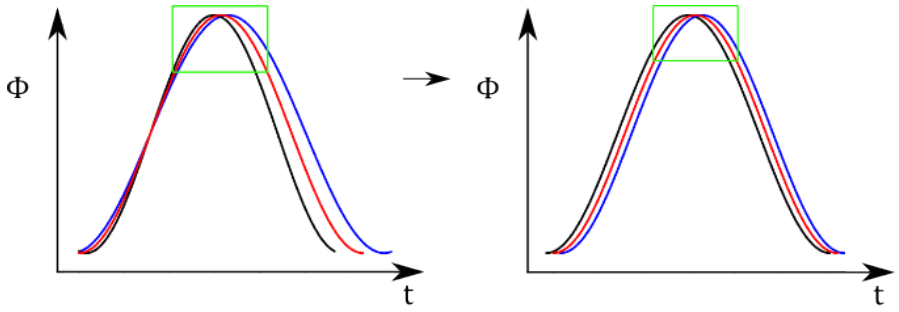

Figure 6.7: Amplified example of approximations in Equation 6.10 and 6.11. Left: three positions, $\Phi(x+\Delta x,t)$ (black) with smallest period, $\Phi(x-\Delta x,t)$ (blue) with largest period and $\Phi(x,t)$ (red). The difference is only valid for small changes in period about the maximum (green box).

Given this assumption, Equation 6.9 can be re-written as Equation 6.12.

$$\Phi(x,t+\varepsilon_1)-\Phi(x,t-\varepsilon_2)>0 \tag{6.12}$$

Next, the average value of Φ is found for changes in ε_i $(0 \leq \varepsilon \leq \Delta\varepsilon)$ about t_{max} (where t_{max} is defined as the time at which the maximum concentration occurs). This is due to the largest flux being gained about the maximum concentration.

$$\frac{1}{\Delta\varepsilon}\int_0^{\Delta\varepsilon}\Phi(x,t_{max}+\varepsilon_1)d\varepsilon_1-\frac{1}{\Delta\varepsilon}\int_{\Delta\varepsilon}^{0}\Phi(x,t_{max}-\varepsilon_2)d\varepsilon_2>0 \tag{6.13}$$

Shifting the bounds on the integral in Equation 6.13 results in Equation 6.14.

$$\frac{1}{\Delta\varepsilon}\left(\int_{t_{max}}^{t_{max}+\Delta\varepsilon}\Phi(x,t)dt-\int_{t_{max}-\Delta\varepsilon}^{t_{max}}\Phi(x,t)dt\right)>0 \tag{6.14}$$

Next, it is chosen that $t_{max} + \Delta\varepsilon = \tau$ and thus $\Delta\varepsilon = \tau - t_{max}$.

$$\frac{1}{\tau - t_{max}} \left(\int_{t_{max}}^{\tau} \Phi(x,t)dt - \int_{2t_{max}-\tau}^{t_{max}} \Phi(x,t)dt \right) > 0 \tag{6.15}$$

It was determined that in order to compare this result across multiple models, the first step in calculating the FH-score is to normalise the concentration wave, $\widetilde{\Phi}$, such that the maximum and minimum were bounded by $0 \leq \widetilde{\Phi} \leq 1$. Equation 6.16 describes this process.

$$\widetilde{\Phi} = \frac{\Phi(\Psi, t \in [0, \mathrm{T}], \beta^*) - \Phi_{min}}{\Phi_{max} - \Phi_{min}} \tag{6.16}$$

where Ψ denotes all other variables of the equation set, $t \in [0, \mathrm{T}]$ denotes one period of steady oscillation such that $\Phi(t = 0) = \Phi(T) = \Phi_{min}$ and β^* denotes the β value such that it is close to the bifurcation point yet still within the oscillatory region as previously defined. Φ_{min} and Φ_{max} denote the minimum and maximum values of Φ under consideration respectively.

Finally, the FH-score is found by calculating the area under the curve for an equal length of time preceding and following the maximum concentration, t_{max}. This calculation is described by Equation 6.17.

$$FH_{score} = \frac{1}{T} \left(\int_{t_{max}}^{\tau} \widetilde{\Phi}(\Psi, t, \beta_{wave})dt - \int_{2t_{max}-\tau}^{t_{max}} \widetilde{\Phi}(\Psi, t, \beta_{wave})dt \right) \tag{6.17}$$

where τ is the smallest of either the time at which the concentration, Φ, following the maximum, has reduced to half the maximum concentration (ie. $\widetilde{\Phi} = 0.5$) or when $2\tilde{t}_{max} - \tilde{\tau} = 0$ (where the macron indicates the normalised value over the period). Note the case of $2\tilde{t}_{max} - \tilde{\tau} = 0$ was not observed first in any of the cal-

culations completed but is included for completeness. Although other options for τ were considered, the time bound choice at half the maximum concentration (τ) was chosen after careful consideration. The full period was not a viable bound as minor increases on the minimum concentration for a large percentage of the period skewed the area calculation. The majority of the concentration movement due to diffusion occurs at the maximum concentration. The time at which the wave shape reached half the height was chosen as a trade off between incorporating more information and its affect upon diffusion.

In order to normalise the time of the wave profile, the difference in areas is divided by the period of the oscillation T. This was chosen to incorporate wave shapes with a large period (T) in comparison to the time to reach half height from the maximum ($\tau - t_{max}$). Note that given the numerical solution to Φ the integral was approximated using Simpson's rule with a fine step size to reduce the associated error. Figure 6.8 shows two pictorial examples of this calculation.

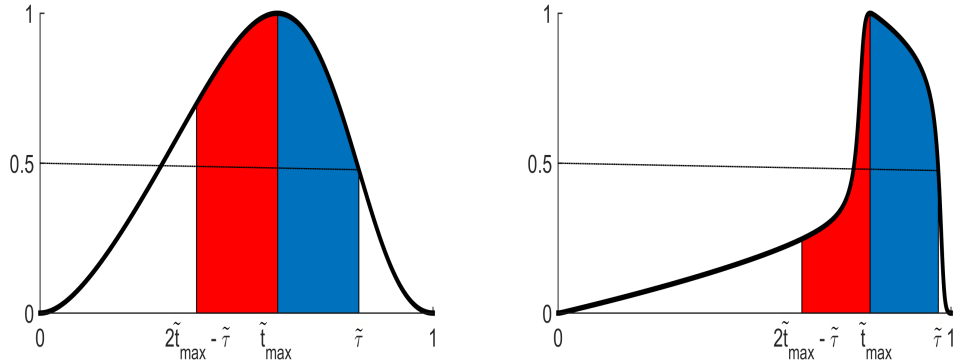

(a) BHwaveshape *(b) FHwaveshape*

Figure 6.8: Two examples of normalised wave shapes with highlighted areas. Where the FH_{score} is equal to the blue area subtract the red area. The x axis, including the bounds, is normalised time and the y axis is normalised concentration Φ.

For this calculation when the FH-score > 0 it indicates that the model will produce excursions. Conversely, a FH-score ≤ 0 indicates that no excursions will

occur. In particular, a symmetrical wave shape will obtain a FH-score $= 0$. Note that due to not all of the wave being considered, and an integral approximation being used, a non-symmetrical wave shape could, in theory, obtain a FH-score $= 0$. Whilst technically possible, this is numerically unlikely.

6.6.1 Confirmation of Approximations using Rate of Φ due to Diffusion

Equations 6.10 and 6.11 (also see Figure 6.7) introduced two approximations to derive the FH-score. These approximations were said to be true for small changes in the value of Δx about the maximum concentration. To confirm the accuracy of these approximations, the approximated rate of Φ due to diffusion can be compared to the true rate of Φ due to diffusion, $\mathcal{L}_{FD}$, from a spatio-temporal solution.

The Goldbeter model is used here as one example of the true rate of diffusion, and the approximated rate of diffusion was found given the definition of the rate of change of Φ over time due to diffusion (Equations 5.4 and 5.19).

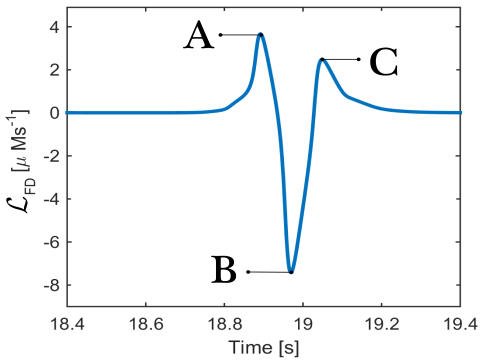

(a) True change in Z due to Diffusion, $\mathcal{L}_{FD}$

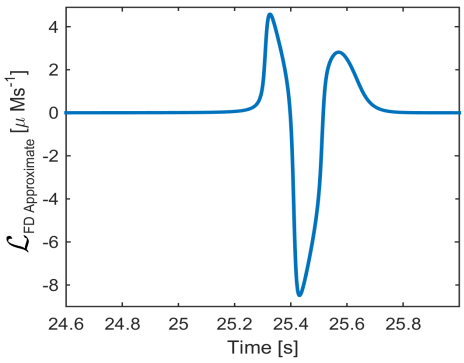

(b) Approximated: $t_{lag} = 0.1s$

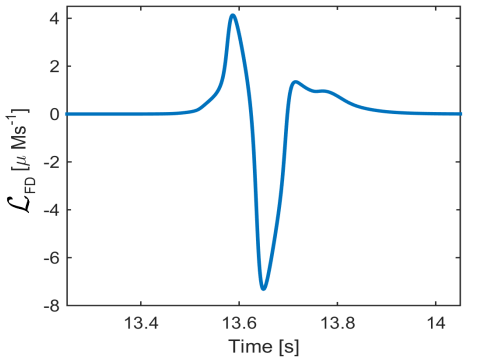

(c) True change in Z due to Diffusion, $\mathcal{L}_{FD}$

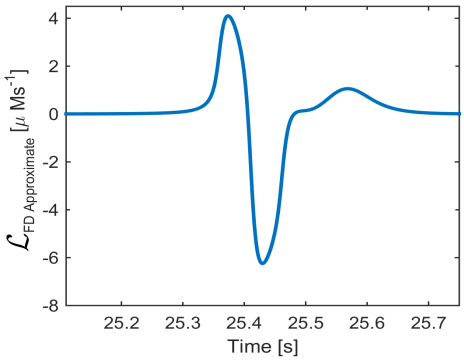

(d) Approximated: $t_{lag} = 0.05s$

Figure 6.9: Example comparison between the true rate of change of Φ over time due to diffusion (a), (c) for the Goldbeter model under FD at $x = 0.3$ compared to approximation of the rate of Φ due to diffusion (b), (d) using approximation Equations 6.10 and 6.11 to estimate the rate of Φ due to diffusion (Equations 5.4 and 5.19). Shape comparison only. Three points {A,B,C} indicated on (a) for discussion.

Figure 6.9 (a), (c) shows two true rates of change of Z over time due to diffusion for some position ($x = 0.3$) at two different points in time for two different excursions. These have been compared to two approximated rates of change of Z over time due to diffusion (Figure 6.9 (b) and (d)) from the wave shape, the two approximations, Equations 6.10 and 6.10, and the definition of the change due to diffusion from Equations 5.4 and 5.19. Figure 6.9 (b) used a time lag between the maximums of $t_{lag} = 0.1s$ and Figure 6.9 (d) used a time lag between

the maximums of $t_{lag} = 0.05s$ which showed two very similar comparisons.

Figure 6.9 (a) indicated three points, {A,B,C} for discussion. Points A and C are positive indicating the current position (x^*) is at a lower concentration than the neighbouring positions. Conversely, point B is negative indicating the current position had a greater concentration than its neighbouring positions. Importantly, point A is greater in magnitude and area bound between the curve and the x axis than B due to the FH shape of the wave. Point A can be considered the flux from the 'cell' at $\{x^* + \Delta x\}$ and Point B can be considered the flux from the 'cell' at $\{x^* - \Delta x\}$ into the current position. This confirms the net directional flux of Φ from $\{x + \Delta x\}$ to $\{x - \Delta x\}$ due to diffusion.

6.7 *Application* - TM3

In order to test the FH-score's accuracy in predicting excursions of high concentration in the previously non-oscillatory region a new third toy model is introduced. Toy Model 3 (TM3) is defined by Equations 6.18 and 6.19.

$$\frac{\partial \Phi}{\partial t} = \beta \Psi - \frac{\Phi^3}{3} + \xi \Phi + \mathcal{L}_{Diffusion} \tag{6.18}$$

$$\frac{\partial \Psi}{\partial t} = -(\beta \Phi + c) \tag{6.19}$$

where $c = 0.2$ and β is the bifurcation parameter as a function of space $\beta = 0.7x + 0.1$. TM3 is distinctly different from the other two Toy models through the addition of a new parameter $\xi \in [0.1, 1]$. As such, the bifurcation point changes with ξ such that $\beta_{Bi} = c\xi^{-0.5}$ or in terms of position $x_{Bi} = 0.7^{-1}(c\xi^{-0.5} - 0.1)$. This relationship is found via the analytical approach of finding the eigenvalues of the Jacobian matrix (not included).

The purpose of the addition of ξ is to alter the wave shape. As ξ varies ($\xi \in$

$[0.1, 1]$) the model varies from producing a BH wave shape, and thus does not create excursions, to producing a FH wave shape and thus does create excursions of high concentration into the previously non-oscillatory region.

The reason why altering ξ within TM3 creates a FH vs BH wave shape is due to the rate of change of Φ increases faster with more Φ for the larger values of ξ and for smaller values of ξ this additional rate is not enough to overcome the $\beta\Psi$ with negative values of Ψ.

6.8 Quantification Results

6.8.1 Results Application

The first results depicted in this section are a variation of the ξ parameter in TM3. For each of the four examples of ξ, a bifurcation diagram obtained via the software Auto07p (Section 2.4.1), a wave shape pictorial (Section 6.2.1) and the spatio-temporal results of the PDE system (described by Equations 6.18 and 6.19) applied with FD were generated to show the trend of increasing $\xi \in [0.1, 1]$. These results are shown in Figure 6.10.

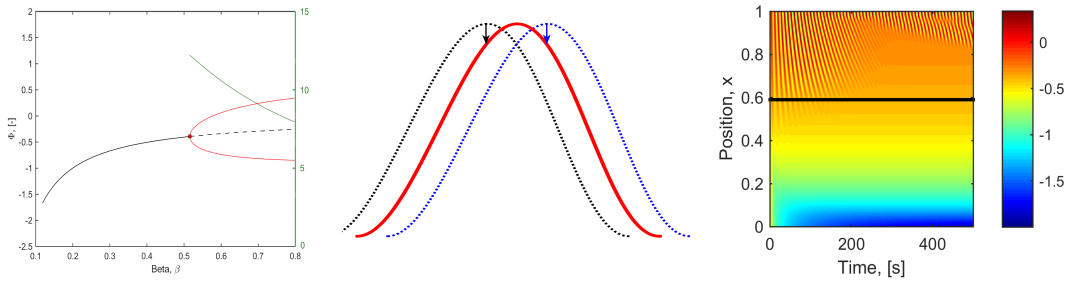

(a) $Bif : \xi = 0.15$ (b) $Waveshape : \xi = 0.15$ (c) $Solution : \xi = 0.15$

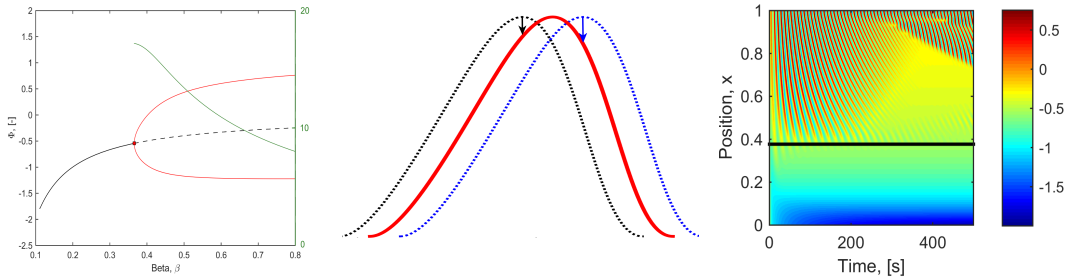

(d) $Bif : \xi = 0.3$ (e) $Waveshape : \xi = 0.3$ (f) $Solution : \xi = 0.3$

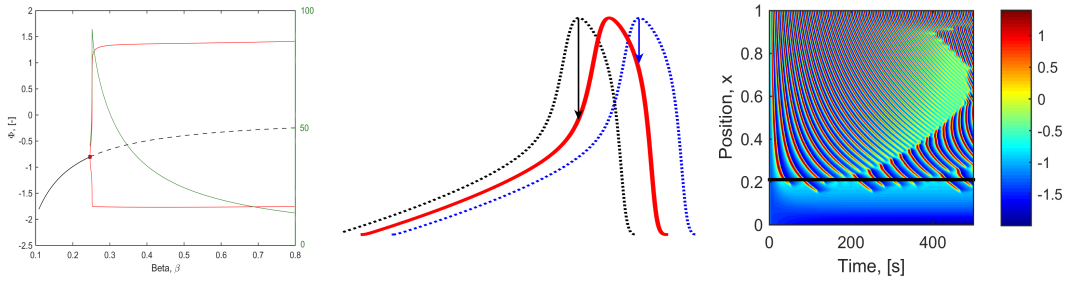

(g) $Bif : \xi = 0.65$ (h) $Waveshape : \xi = 0.65$ (i) $Solution : \xi = 0.65$

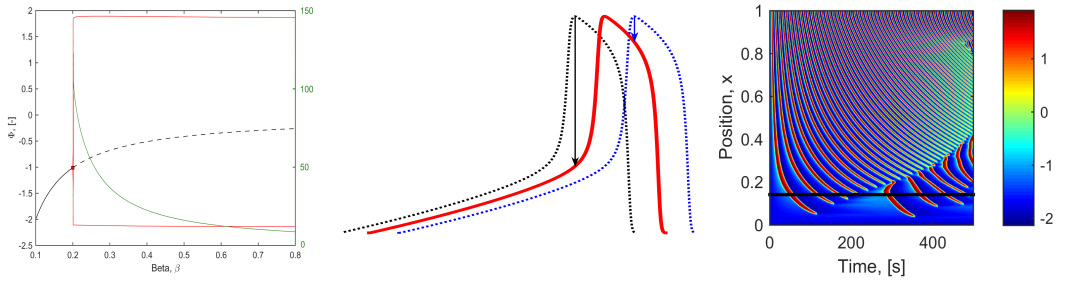

(j) $Bif : \xi = 1$ (k) $Waveshape : \xi = 1$ (l) $Solution : \xi = 1$

Figure 6.10: Four examples of varying ξ for Toy Model 3 (TM3) in which the wave shape changes from Backwards Heavy (BH) to Front Heavy (FH) producing no excursions to producing excursions. Left Hand Column: Bifurcation in red and black and period in green. Centre Column: Wave shape with shift of 10% period. Right Hand Column: Spatio-temporal Solution for FD with $D = 5 \times 10^{-6}$.

As mentioned previously, minor contradictions to the period of oscillation (in this case) increasing with decreasing position did not affect the outcome in terms of excursions. Figure 6.10 (d), (g) and (j) show the period decreasing immediately next to the bifurcation point and yet two produce excursions whilst the first does not. These results were replicated 19 times for varying ξ, and Figure 6.11 was created to demonstrate that as the FH-score transitioned across zero the model went from producing no excursions to producing excursions of high concentrations in the previously non-oscillatory region.

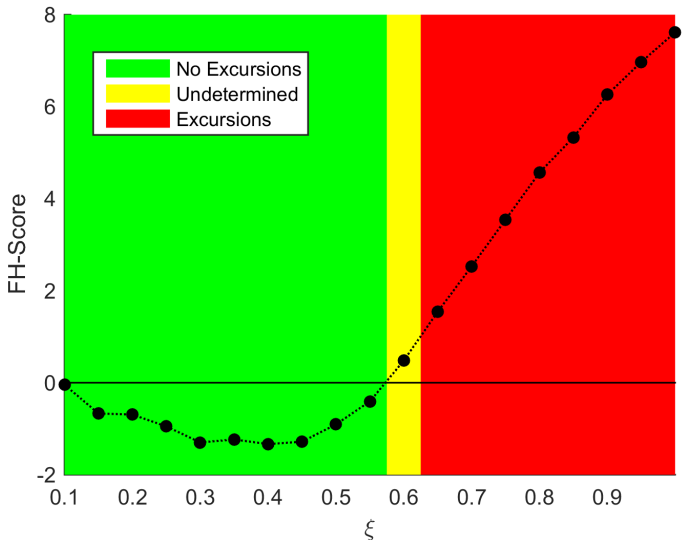

Figure 6.11: Toy Model 3 (TM3) Changing ξ and its effect on the FH-score. Background colour is determined by visual inspection where Green indicates no excursions, Red indicated excursions and yellow is undetermined.

6.8.2 Model Results

Finally for this section, a FH-score for each of the models described within this research was computed and compared against the occurrence of excursions

(Table 6.2).

Table 6.2: Summary of FH-score for all other models presented within this research.

	Front Heavy Score (FH-score)	**Excursions Occur in Non-Oscillatory Region**
Goldbeter model	1.3017	✓
Dupont model	1.6312	✓
Ermentrout model	0.3804	✓
FitzHugh-Nagumo model- U	-1.6027	X
FitzHugh-Nagumo model- W	8.2337	✓
Koenigsberger model	1.1922	✓
Toy Model 1 (TM1)	-0.5724	X
Toy Model 2 (TM2)	7.5728	✓

6.9 Discussion

The Front Heavy Score (FH-score) is a way of quantifying how asymmetric and how front heavy a wave shape is. The wave shape of an ODE(β, t) is here defined as one period of oscillation in a variable over time from one minimum to the next. The wave shape is found for the variable that is being diffused over space given a bifurcation parameter near a bifurcation point of interest. This analysis only considered excursions beyond the "lower bifurcation point".

Table 6.1 shows that front heavy waves consistently result in excursions of high concentration in the previously non-oscillatory region. The 'front heaviness' of the wave shape was further quantified as a FH-score. The FH-score was derived using an axiomatic argument. This gives validity to its ability to predict excursions into the previously non-oscillatory region.

To further validate the quantified hypothesis an additional Toy model (Toy Model 3 (TM3)) was used. TM3 allows the model to change from a BH wave-

shape to a FH wave shape as the parameter ξ is changed between 0.1 and 1. Hence, the model transitioned from one that exhibited no excursions into the non-oscillatory region to one that did exhibit excursions into the non-oscillatory region. The established physiological models must retain their parameter values to remain meaningful. Hence, they do not allow modulation of parameters to enable transitions from positive to negative FH-score. In contrast, the lack of physiological meaning of TM3 allowed for a direct comparison between the excursions and the FH-score.

Figure 6.10 showed 4 examples of TM3; two that did not penetrate the non-oscillatory region ($\xi = 0.15$ and $\xi = 0.3$) and two which did ($\xi = 0.65$ and $\xi = 1$). These were chosen to represent the range of wave shapes that the model could produce. Additionally, Figure 6.11 shows the relationship between the parameter ξ and the calculated FH-score. When $\xi = 0.6$ the excursions were so small that upon first visual inspection it was unclear if the concentration changes were due to numerical error, smoothing, initial conditions or true excursions predicted by the FH-score of the wave. Given that FH-score$(\xi = 0.6) = 0.48$ is positive despite this being small compared to other FH-scores for the same model, the hypothesis predicted that excursions would take place. Detailed visual inspection of the non-oscillatory region for $\xi = 0.6$ indicated small excursions did in fact occur. This confirms the robustness of the FH-score as a prediction technique as it was able to accurately predict borderline cases.

Table 6.2 shows the computed FH-score of the physiological models and the two Toy models. The Goldbeter model, the Dupont model and the Koenigsberger model have very similar FH-scores. This attempts to explain why they produced similar spatio-temporal results as FD was applied. The FitzHugh-Nagumo model variable W and TM2 have large FH-scores which also cor-

responds to excursions in both cases. Interestingly, while TM1 visually appeared to be a symmetrical wave shape, on closer inspection and calculation of the FH-score it was a Backwards Heavy (BH) wave shape as indicated by a FH-score $= -0.5724$. This indicates the directional net flux was directed internally into the oscillatory region which explains the cancellation of waves seen in the spatio-temporal solution (Figure 5.15).

Finally, the Ermentrout model has a comparably low FH-score $= 0.3804$, which corresponded to small excursions into the non-oscillatory region (Figure 5.10). This could be compared to TM3 at $\xi = 0.6$, where the excursions did in fact occur but were not large. It is important to note that the FH-score is not an indication of excursion depth as this was different for each model and changed over time. The depth of excursions will be further investigated in following chapters (Chapters 7 and 8).

The hypothesis presented at the beginning of this chapter has been shown to correctly predict excursions across many unique ODE equation sets. An axiomatic argument was given to the derivation of the FH-score to increase validity. Although the theory can not be proven without a limitless exhaustive search of all possible models, the current evidence gives support to the hypothesis. The tests the hypothesis has been put through give strong evidence to the validity of the theory and thus, at this point in time, it can be assumed to hold true for all cases.

Being able to quantify whether or not excursions will occur based upon the dynamics of the single cell alone is a significant and apparently novel achievement. This allows prediction of when waves will be seen travelling in the tissue media. The ability to quantify the wave shape allows for an aim to modify the single cell dynamics such that this wave movement will not occur in the sur-

rounding cells.

6.10 Conclusion

This chapter proposed a hypothesis that on the satisfaction of three criteria excursions of high concentration would be present in the previously non-oscillatory region. First, on varying bifurcation parameter a region of steady state solution and a region of periodic oscillatory solution over time separated by a bifurcation point would exist. Next, the period of oscillation would increase over space towards the 'lower bifurcation point'. Finally, the wave shape of the oscillations near the bifurcation point must be an asymmetric Front Heavy (FH) wave shape.

A FH wave shape is critical in producing excursions due to an unbalanced net diffusive flux over space in the direction from the oscillatory region towards the non-oscillatory region. The FH-score was derived using an axiomatic argument to calculate a net directional flux of ions. This number relates directly to the presence of excursions into the previously non-oscillatory region on the application of FD. A positive FH-score indicates excursions compared to a FH-score less than or equal to zero which indicates no excursions occurred (in connection to the 3 criteria).

TM3, with a parameter ξ, was used to show a direct comparison between the excursions and the FH-score, proving its hypothesised relationship. What is important to note about the FH-score is that it is not an indication of excursion depth. As such, this will be further investigated in the following chapters.

Finally, the ability to quantify whether or not excursions will occur based upon the dynamics of the single cell alone is a significant achievement. It allows predictions for larger scale models to be made and, importantly, can be used as

an aim to modify the single cell dynamics such that this wave movement in tissue media will or will not occur in the surrounding cells.

7 Excitability (E) Profile and Depth of Excursions

7.1 Introduction

The previous chapter (Chapter 6) discussed when excursions of high concentration would be predicted in the non-oscillatory region. Two criteria were determined for the presence of excursions: a period of oscillation generally increasing over space towards the 'lower bifurcation point' and an asymmetric FH wave shape near the bifurcation point. In particular, the FH-score needed to be greater than zero for excursions to occur.

Unfortunately, the FH-score does not create a complete picture of when, and how far, the excursions would go into the non-oscillatory region. The pattern of the excursions is also dependent on the $\beta(x)$ profile, which thus far has only been a linear relationship. There exist particular $\beta(x)$ profiles that suppressed excursions even though the linear $\beta(x)$ profile produced excursions. An example of this is available for the Dupont model in Appendix B.

This chapter looks closely at the previously non-oscillatory region and investigates how the 'cells' react under applied changes. This reaction is then related to the depth of excursions in the spatio-temporal solutions under FD to form

relationships between the diffusion coefficient and the depth of excursions.

7.2 Excitability (E) Method

As mentioned, this section looks exclusively at the previously non-oscillatory region of all the models. In particular, this chapter looks at the β values beyond the 'lower bifurcation point' which experienced excursions on the addition of FD (Chapter 5). The β values considered, thus, all produced a steady state solution over time.

To understand the response dynamics of the system, it can be useful to look at an example of a direction field of a model. For models with more than two variables a direction field is difficult to interpret. As such, one example of the Dupont model with only two variables will be displayed here. The direction field was obtained using software program MAPLE for the two variable Dupont model to be used as a simplified example.

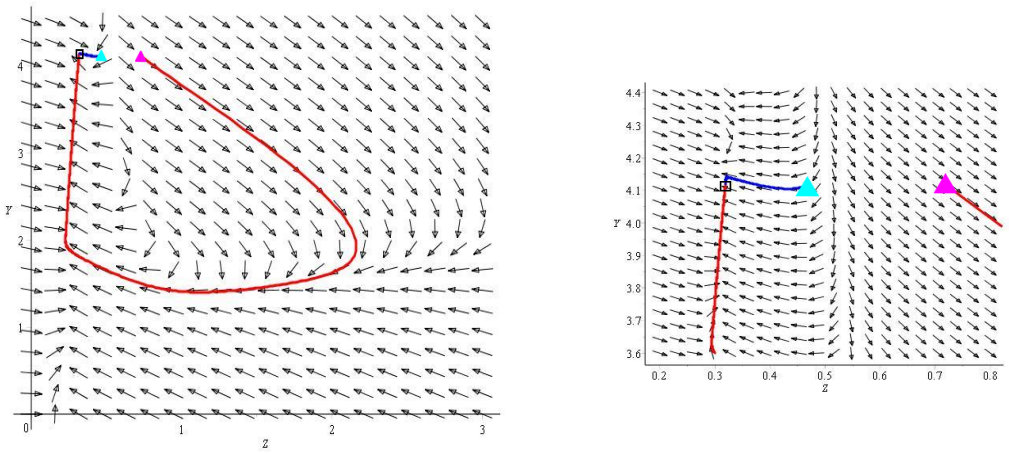

(a) Full Direction Field *(b)* Detailed View

Figure 7.1: Example of a direction field for Dupont model two variable system (Z and Y) and $\beta = 0.3$. Red and blue lines show two different initial conditions (pink and aqua triangles) paths of solutions to the steady state solution (where they meet, black hollow square). Created via software package Maple.

Figure 7.1 shows that depending on the initial conditions (the pink and aqua triangles) the path the system takes (the red vs blue line) in order to reach the steady state solution (the black square) can be very different. Figure 7.1 shows two unique paths to the steady state solution: one direct path (the blue path) and one indirect path (the red path). The red path must first increase the cytosolic calcium ion concentration (Z) before it can return to the low steady state solution. This increase in concentration will be known as an excitement to the system. The difference in Z between the steady state solution and the initial conditions will be henceforth known as a Perturbation (P) to the system.

Figure 7.2 shows a time dependent representation of this excitement given two perturbations (note the different vertical scales). Again, the Dupont model with a chosen β value is used as an example. The blue path on Figure 7.1 relates to Figure 7.2 (a) and the red path on Figure 7.1 relates to Figure 7.2 (b).

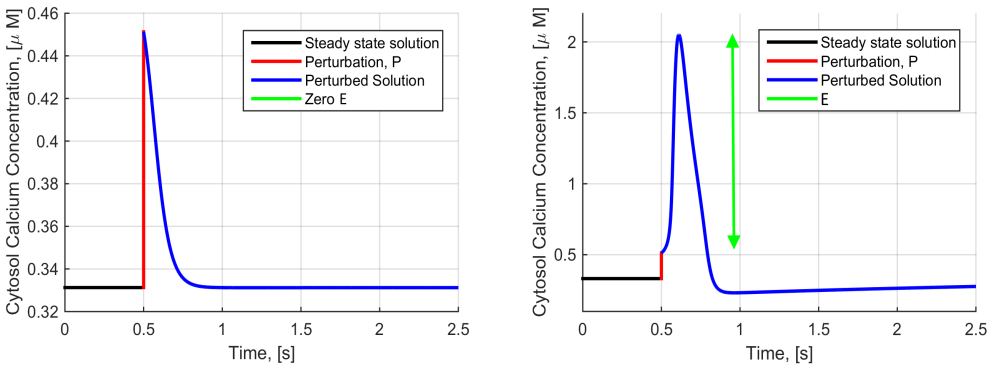

(a) $E = 0$ resulting from a small perturbation ($P = 0.12$). Matching blue path on Figure 7.1

(b) $E > 0$ resulting from a large perturbation ($P = 0.18$). Matching red path on Figure 7.1

Figure 7.2: Pictorial indicating a systems response and the new E value given a perturbation (P) and a β value. (Reaction of Dupont model $\beta = 0.3$) of which only (b) was excited. Note the different vertical scales.

Similar to Figure 7.1, Figure 7.2 depicts one path that is excited (b) and one path that is not excited (a) based on the perturbation given (note the different

vertical scales). Indicated on Figure 7.2 are 4 important properties. First, the steady state solution in black that the system will return to given enough time. Second, the perturbation, P, above the steady state solution. Third, the system's response to the perturbation to return to the steady state value, and finally a new variable E which denotes the maximum change in the perturbed variable above the steady state solution and the perturbation over time. Figure 7.2 (a) did not 'excite', thus it has an $E = 0$. The new variable $E(\beta, P)$ is a function of the model, the β value and the perturbation P.

On Figure 7.1 it is clear that between the initiation of the red and blue paths there exists some critical perturbation P such that the response must change between the non-excited path (Figure 7.2.a) and the excited path (Figure 7.2.b).

An Excitability Profile (E-Profile) can be created for each model, for variations of β and a variety of perturbations. The E-Profile takes a range of perturbations, P, for each value of β and finds the amount, E, the 'cell' is excited by, $E(\beta, P)$. Mathematically, first, let Φ_r be the response to the system of ODEs defining the model as a function of the initial conditions, time and the β value (Equation 7.1).

$$\Phi_r(\beta, P, t) = \Phi\Big(\{\Phi_0(P), \bar{\Psi}_{ss}\}, \beta, t \in [0, t_{ss}]\Big) \tag{7.1}$$

where t_{ss} is the time the solution takes to reach the steady state solution. The difference between Φ_r and any normal solution over time is the dependence on the specific initial conditions ($\{\Phi_0(P), \bar{\Psi}_{ss}\}$). The initial condition of Φ is a function of the perturbation and is equal to $\Phi_0(P) = \Phi_{ss}(\beta) + P$. The initial conditions of all other variables denoted by $\bar{\Psi}$ are the steady state values of the variables for the considered β (note that the subscript of ss indicates the steady state solution of the given β value).

Finally, Equation 7.2 mathematically describes the formation of the Excitability Profile (E-Profile) with units the same as $[\Phi]$.

$$E(\beta,P) = \max_{0\leq t\leq t_{ss}} \left(\Phi_r(\beta,P,t) \right) - P - \Phi_{SS}(\beta) \tag{7.2}$$

What is important to note is that the values of E are not comparable across different models unless the models are of similar concentrations. E has the same units as P and Φ.

7.2.1 How E Relates to Spatial Diffusion

In order to connect the E-Profile to the case of coupled cells via diffusion, it is important to remember the definition of J_{FD} (Equation 5.4). When a neighbouring 'cell' exhibits a high concentration of the variable being diffused, a movement of concentration occurs as a small, near instantaneous, addition to the neighbouring 'cell'. The addition from the 'cell' of higher concentration can be translated to the perturbation of the E-Profile method. Thus, if the addition is small the system will rapidly act to reduced this (non-excited). Alternatively, if the addition is of a sufficient size it will act to excite the cell and cause a sudden large increase in the concentration (Figure 7.2.b). This then creates an environment for the next 'cell' in the sequence to also excite. Succinctly, the process of diffusion can be considered as a quick addition of concentration to a cell that can either be quickly depleted or produce an excited response, and thus create excursions.

7.2.2 Perturbations, P

The perturbations for each model were chosen as a range of values between 0 and a proportion of the maximum change in concentration of the oscillations of

each model. Importantly, again, this is not comparable across models as most of the models have very different ODE behaviour.

7.2.3 Models With Membrane Potential Equations

The Ermentrout model and the Koenigsberger model both are the only two models to contain integrated membrane potential equations. These add an additional complexity to the possible perturbations. Given that an addition of concentration via diffusion must cross the membrane it must therefore affect the membrane potential (Equation 5.3, Section 2.1.3). For these two models there are two options of perturbations that can be added: a perturbation to the ionic calcium concentration in the cytosol (Z) called P_Z and a perturbation of the Cellular Membrane Potential (V) called P_V. Keeping in mind that the change in Z (occurring across the membrane) affects the membrane potential. Equation 7.3 can be used to relate the two types of perturbations.

$$P_{V(Z)} = \frac{1}{C_m \alpha} P_Z \approx 6.4 P_Z \tag{7.3}$$

Equation 7.3 is created via first converting the ionic calcium concentration to an electrical charge. Equation 7.4 details its creation.

$$V = \frac{q}{C_m} \quad and \quad q\left(\left[Ca^{2+}\right]\right) = \frac{Z}{\alpha} \tag{7.4}$$

where V is the voltage, C_m is the capacitance and q is the charge. α is a function of Faraday's constant, the volume and the valance of the ion. α has been previously defined in Chapter 3, Section 3.4, Equation 3.21.

7.2.4 *Previous Literature*

Ermentrout and Rinzel (1996) detail a similar comparatively incomplete understanding of excitements to an ODE with a steady state solution. Ermentrout and Rinzel (1996) called the spikes, depending on the change from steady state "oscillations with zero frequency". Ermentrout and Rinzel (1996) did not elaborate on this phenomenon any further than to show their existence and an example on the phase plane (similar to the direction field in Figure 7.1).

In fact, many sources have noted the occurrence of a threshold before excitation on the phase plane (Ermentrout and Rinzel (1996), Doi et al. (2010), Holloway and Richardson (2008), Hilborn et al. (2012), Bartocci et al. (2008), Zhao and Gu (2017), Drion et al. (2012) and Gerstner et al. (2014) to name a few). However, none of the viewed literature created a continuous picture (an E-Profile) over varying β and varying perturbations to attempt to understand any relationship between these variables. Furthermore, none of the viewed literature then attempted to compare this to the patterns on the spatio-temporal solution with diffusion.

7.3 E-Profile *Results*

The first results in this chapter are E-Profiles for each model. The vertical axis represents the β values that under no coupling ($D = 0$) result in the system reaching a steady state after some time. The horizontal axis indicates the perturbations applied (P) to find the excitability (contour scale) using Equation 7.2. No colour represents an $E = 0$, thus the model is not excitable for the (β, P) combination. The results in this section will be broken up into similar pairs for easy comparison, noting that the E values are not comparable across models. Quick

reference links to each model's respective bifurcation diagrams, spatio-temporal solutions with FD and also their wave shapes have been included within each caption.

First, the E-Profiles are displayed for the Goldbeter model and the Dupont model.

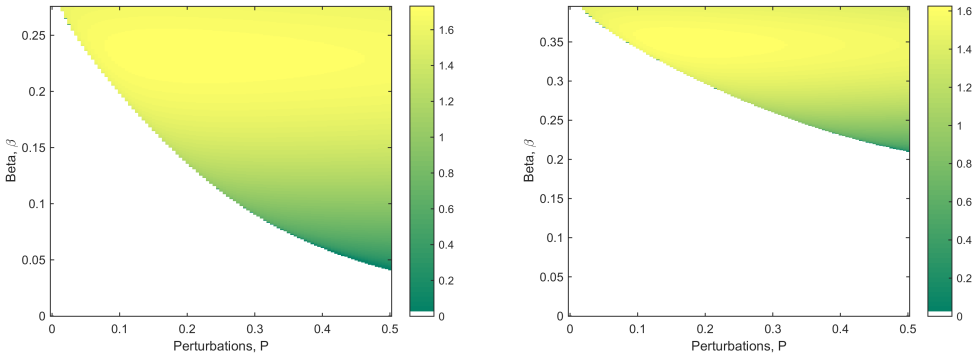

(a) The Goldbeter model *(b)* The Dupont model

Figure 7.3: E-Profile for the excitability of the ionic calcium concentration in the cytosol (Z) given a small perturbation to Z (Equation 7.2). With bifurcations of Figures 3.3 and 3.8 respectively. Spatio-temporal solutions with FD Figures 5.4 and 5.7 respectively and wave shapes of Figure 6.6 (a) and (b) respectively.

Figure 7.3 shows that as beta, β, decreases from the 'lower bifurcation point' ($\beta = 0.289$ for the Goldbeter model and $\beta = 0.395$ for the Dupont model) an increasingly higher value of P is necessary to obtain an $E > 0$. This indicates that as the β value increases from the bifurcation point, without any additional external addition of Z, the propagating wave will die out because it will eventually not pass the critical perturbation to the next 'cell'.

Next is the comparison of the two toy models from Chapter 6, of which Toy Model 1 (TM1) did not produce excursions and Toy Model 2 (TM2) did produce excursions.

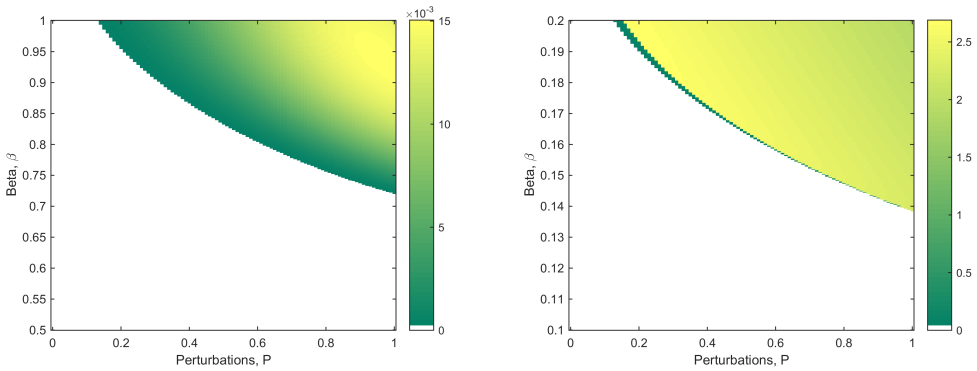

(a) Toy Model 1 (TM1) *(b)* Toy Model 2 (TM2)

Figure 7.4: E-Profile for the excitability of Φ given a small perturbation to Φ (Equation 7.2). With bifurcations of Figure 6.1 (a) and (b) respectively. Spatio-temporal solutions with FD Figure 6.4 (a) and (b) respectively and wave shapes of Figure 6.5 (a) and (b) respectively. Note E values are not comparable across models.

Figure 7.4 showed a visually very similar E-Profile to Figure 7.3 with the same decreasing β from the 'lower bifurcation points' ($\beta = 1$ for TM1 and $\beta = 0.2$ for TM2). This indicates that the E-Profile is not the sole determining factor for excursions. Rather the existence of excursions is still dependent on the FH-score of the wave shape from Chapter 6. Figure 7.4 (b) in particular displays an important note about uncertainty. The cut off criteria to display a white area on the E-Profile ($E = 0$) was 1.56% of the maximum E on that E-Profile. This cut off criteria on Figure 7.4 (b) appears not sufficient as it missed a few points displayed by a dark green line of low E values. The points of low E values above the cut off criteria could be attributed to noise of the process and are not critical to the interpretation of the E-Profile. (This also occurs on Figures 7.5 (b), 7.6 (a) and 7.6 (b))

Next, Figure 7.5 compares the excitability of the FitzHugh-Nagumo model when either U or W is perturbed.

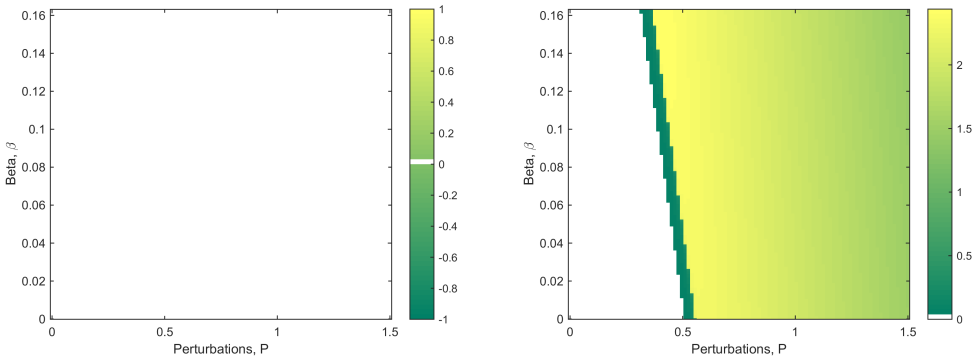

(a) Perturbations to U *(b)* Perturbations to W

Figure 7.5: FitzHugh-Nagumo model E-Profile for the excitability of U and W given a small perturbation to U and W respectively (Equation 7.2). With bifurcations of Figures 3.18 and 3.17 respectively. Spatio-temporal solutions with FD Figures 5.15 and 5.16 respectively and wave shapes of Figure 6.6 (e) and (f) respectively.

Figure 7.5 shows that, no matter the perturbation to U the system will not excite. This suggests that even if the wave shape of the FitzHugh-Nagumo model variable U was converted to a FH-score > 0 the system would still not produce excursions. Figure 7.5 (b), on the other hand, shows that once a system starts an excursion in time, that excursion is likely to reach the 'full depth' to $\beta = 0$. This is because the critical threshold (to obtain an $E > 0$) only changes between 0.3 to 0.5 over the considered β values.

7.3.1 With Membrane Potential Equations

Next, the Koenigsberger model and the Ermentrout model also contain integrated membrane potential equations. This means that a small perturbation can be made to either the ionic calcium concentration in the cytosol (Z) or the Cellular Membrane Potential (V). The first of the two to be examined is the Koenigsberger model (Figure 7.6).

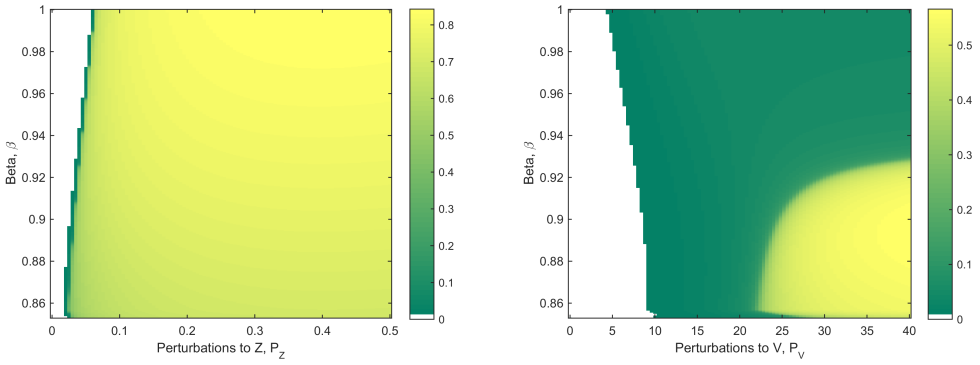

(a) Perturbations to Z *(b)* Perturbations to V

Figure 7.6*:* Koenigsberger model E-Profile for the excitability of Z given a small perturbation to Z and V respectively (Equation 7.2). With bifurcations of Figures 3.21 and 3.23. A spatio-temporal solutions with FD Figure 5.18 and a wave shape of Figure 6.6 (d). Importantly, the bifurcation point occurs at the bottom, ie $\beta = 0.857$.

Importantly, the Koenigsberger model, unlike the other models, has its 'lower bifurcation point' at the bottom of the E-Profile at $\beta = 0.857$. From Figure 7.6 (a) and (b) it is clear that Z is the main component in the propagation of excursions, as in order for the membrane potential to contribute significantly it requires a $P_V > 20mV$. Figure 7.6 (a) has an E-Profile visually similar to the FitzHugh-Nagumo model W E-Profile, meaning it is likely that most excursions will traverse the entire previously non-oscillatory region.

Finally, the E-Profile is viewed for the Ermentrout model as a function of the perturbation, P, and the β value.

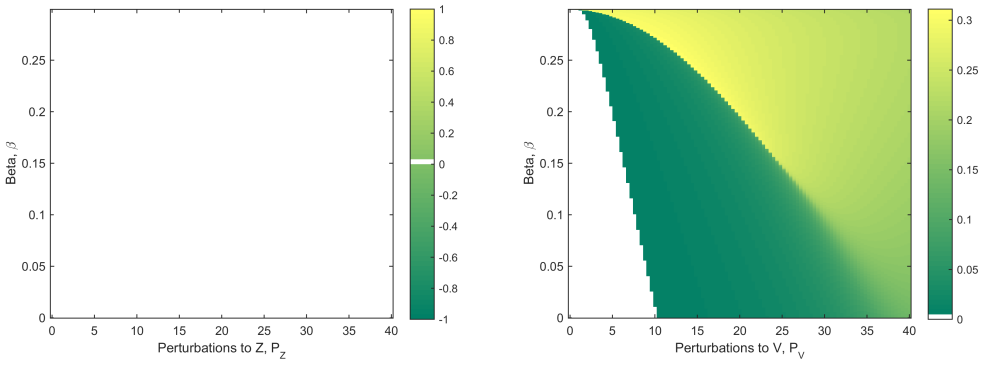

(a) Perturbations to Z *(b)* Perturbations to V

Figure 7.7*:* Ermentrout model E-Profile for the excitability of Z given a small perturbation to Z and V respectively (Equation 7.2). With bifurcations of Figures 3.12 and 3.13. A spatio-temporal solutions with FD Figure 5.10 and a wave shape of Figure 6.6 (e).

Figure 7.7 (a) shows that no matter the perturbation to the ionic calcium concentration in the cytosol (Z) the system will not excite. However, for additions to the membrane potential, P_V the system will excite. This explains why on the small addition of V from Fickian Diffusion (FD) the excursions did not go very far into the previously non-oscillatory region. In comparison on the larger addition of V from Electro-Diffusion (ED) the resulting excursions achieved greater depths.

7.4 E-Profile *Summary*

Figure 7.1 shows an example of a direction field for the two variable system given the initial conditions. Overlaid on this image are two possible paths the system can take to the steady state solution based on the initial conditions. This is related to two time dependent solutions shown by Figure 7.2 (a) and (b). They show that under a small perturbation to the steady state solution, the system either acts to quickly diminish the concentration or the system is excited before

returning to the steady state solution. This rise in concentration above the perturbation was named the Excitability (E) and is a function of the model, the bifurcation parameter (β) and the perturbation (P) added to the system. The introduced tool, the E-Profile, combines this knowledge to aid in the understanding of the model dynamics.

The excitability of the system was related to the flux of ions across space via diffusion. When a neighbouring 'cell' exhibits a high concentration of the variable being diffused, a fraction of this is then passed via diffusion to the next 'cell'. This addition is translated to the perturbation of the E-Profile. When the perturbation is small, the system rapidly acts to reduce this back to the equilibrium point. Alternatively, if the perturbation is of a sufficient size, it will act to excite the 'cell' and cause a sudden large increase in the concentration (see Figure 7.2.b). This phenomena is critical to wave propagation over the previously non-oscillatory region.

Figures 7.3 and 7.4 (the Goldbeter model, the Dupont model, TM1 and TM2) show that as beta decreases from its respective bifurcation points, an increasingly higher value of P is necessary to obtain an $E > 0$. This infers that for these models a travelling excursion will eventually not pass on a perturbation to the next 'cell' via diffusion that is sufficient to overcome the critical perturbation required, and thus the excursion will die out.

Figure 7.4 (a) indicates that the E-Profile is not the sole determining factor of excursions, but rather that this is still dependent on the FH-score from Chapter 6. Excursions did not occur for TM1 (Chapter 5) even though the E-Profile was comparable in shape to the other models. This suggests that excursions are possible only if the diffusion term evaluated at the boundary of the non-oscillatory region is large enough to start in the excitable region of the E-Profile

($E > 0$). Note the magnitude of the E-Profile is not comparable across models.

The FitzHugh-Nagumo model U E-Profile and the Ermentrout model Z E-Profile showed that, no matter the perturbation to U or Z respectively, the system would not excite. This suggests that for the FitzHugh-Nagumo model U, even if the wave shape was converted to a FH-score > 0, the system would still not produce excursions. The FitzHugh-Nagumo model W, on the other hand, indicated once the system starts an excursion in time, it is probable that the excursion will reach the 'full depth'.

The models which contain both an equation for the ionic calcium concentration in the cytosol (Z) and the Cellular Membrane Potential (V) created interesting and informative E-Profiles. For the Koenigsberger model and the Ermentrout model, it was necessary to look at the effect that a small change to Z and V could have given that FD was added to both of these rates of change. For the Koenigsberger model, Figure 7.6, it was clear that Z played a more influential role in the excitement of the system than V. In order for the membrane potential to contribute significantly it required a $P_V > 20mV$.

In comparison, the Ermentrout model (Figure 7.7) could not instigate an excitement no matter the perturbation to Z. The small perturbations in V (P_V) were more influential in the excitement of the system. The Ermentrout model E-Profiles explain why on the small addition from FD the excursions were small but on the larger addition from ED the excursions reached far greater depths. The Excitability (E) detailed here only considered a maximum method (Equation 7.2). It is possible that, particularly for the Ermentrout model, an additional minimum method of excitability may be needed in order to further understand the bidirectional waves.

Thus far, the E-Profile shed light on how the 'cells' in the previously non-

oscillatory region were affected by small perturbations from their steady state values. This excitement can be related to the depth of excursions into the non-oscillatory region, where the depth is the distance (x) from the bifurcation point into the non-oscillatory region to where the high concentration excursion reduces below some critical concentration. The depth an excursion reaches changes with predominately 4 things: different models, different diffusion constants, different $\beta(x)$ profiles and, needless to say, over time. In order to analyse different $\beta(x)$ profiles, the relationship between the depth, the diffusion constant and time for each model will be investigated.

7.5 Relationship between Excitability Profile and Depth

7.5.1 Wave Front Number ($\bar{\imath}$)

First, a new definition is used for the peaks in concentration in order to understand the effect on the excursions over time. The Wave Front Number ($\bar{\imath}$) indicates the integer number in order of occurrence in time of the local maximum in concentration $\Phi(x)$. This number is not found beyond the initial response behaviour where multiple wave fronts are seen to interact. Figure 7.8 gives an example of the $\bar{\imath} = \{1,2,3\}$.

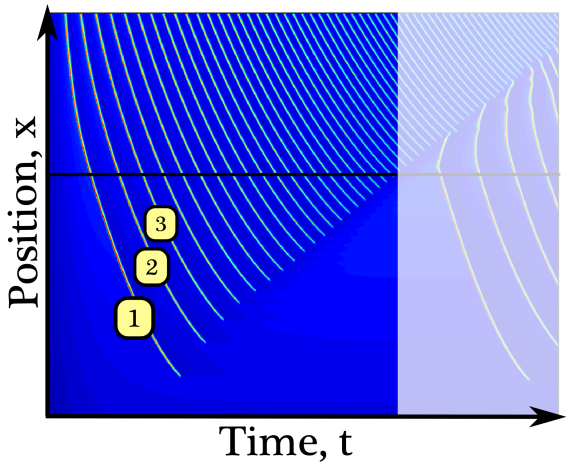

Figure 7.8: Example spatio-temporal solution with first 3 wave fronts, $\bar{\imath} = \{1,2,3\}$, indicated. Lightened section shows end of $\bar{\imath}$ used. Blue represents low concentration and light/red indicates a high concentration. The black horizontal line indicates a zero diffusion bifurcation point ('lower bifurcation point').

7.5.2 Models Under Consideration

Between Chapter 6 and the E-Profile it is apparent that not all the models examined within this research behave the same. This section is only capable of investigating the following models: the Goldbeter model, the Dupont model, Toy Model 2 (TM2), the FitzHugh-Nagumo model with W diffused and the Koenigsberger model. The remaining 4 models were excluded due to two criteria. First, in order to investigate the depth of excursions the model must first create excursions. This criteria excluded Toy Model 1 (TM1), the FitzHugh-Nagumo model when U was diffused and specific ξ values for Toy Model 3 (TM3). The second criteria in order to investigate the depth of excursions was that the spatio-temporal solution needed to have a definite depth of excursion for them to be quantified accurately. Unfortunately, given that the Ermentrout model did not

have clearly defined excursion depth it could also not be investigated in this way.

7.5.3 Actual Depth Measurement and Bifurcation Parameter

To obtain a relationship between depth, diffusion, Excitability (E) and $\bar{\iota}$ first some data on the actual depth is needed to be produced. All the models in this section were given $\beta(x)$ profiles to first satisfy the following criteria for easy comparison:

- The 'lower bifurcation point' occurred at $x = 0.5$. ie $\beta(x = 0.5) = \beta_B$.
  - For positions $0 < x < 0.5$ the system under no coupling (ie. $D = 0$) would produce a steady state solution.
  - For positions $0.5 < x < 1$ the system under no coupling (ie. $D = 0$) would produce periodic stable oscillations.
- In the oscillatory region, under no coupling (ie. $D = 0$), the period of oscillation would overall* increase with decreasing x.

Finally, for simplicity only, the $\beta(x)$ function will remain linear. Excursions will thus only occur within the region $0 < x < 0.5$. The solution to the PDE equation set for each model will be computed with multiple different diffusion coefficients between $1 \times 10^{-6} \leq D \leq 10 \times 10^{-6}$ and the actual depth of the first 10 excursions (if available) will be recorded. The actual depth of excursion will be between $0 \leq Depth \leq 0.5$ where $Depth = 0.5$ indicates it did not produce an excursion and $Depth = 0$ indicates the excursion reached maximum depth possible for this specific $\beta(x)$.

The actual depth $x_d(t)$ was found via a stepping method in space x, post-simulation, relying on the period of oscillation increasing with decreasing posi-

* Minor variations acceptable in accordance with the results in Chapter 3.

tion. Thus, the time at which the maximum concentration was reached increased with decreasing position (x) for each $\bar{\iota}$ (Equation 7.5 must be true).

$$\text{If} \quad \frac{d\Phi(x_i,t_i)}{dt} = 0 \quad \text{then there exists} \quad \frac{d\Phi(x_i-\Delta x,t_i+\varepsilon t)}{dt} = 0 \tag{7.5}$$

where for some position on the spatio-temporal solution (x_i,t_i) a maximum occurs and thus for a small change in position (Δx), there exists a small change in time (εt) such that another maximum occurs. The stepping process stops when the maximum concentration reduces below 10% of the maximum change in concentration for the entire solution. Explicitly, $\Phi_{i+1} < 0.1\left(\Phi_{max} - \Phi_{min}\right) + \Phi_{min} = Tol_C$. Figure 7.9 describes this stepping process to find the actual depth.

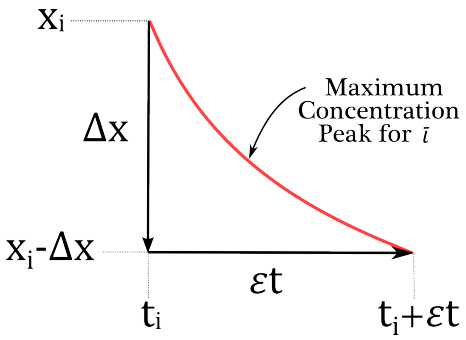

Figure 7.9: Stepping process representation to find actual depth of excursion. For a small spatial step (Δx), it is expected that a maximum ($d\Phi/dt = 0$, red line) will occur within some small time (εt) in the future. This process stops when either $\varepsilon t > 0.5T$ (half the period) or when $\Phi < Tol_C$.

Additionally, this depth was confirmed by visual inspection.

7.5.4 Excitability Profile to Depth

The E-Profile describes the maximum concentration that a system can be excited to above the perturbation (P) and the steady state value (Φ_{ss}). On the application

of Fickian Diffusion (FD) approximately some fraction (f_1) of this maximum change in concentration will be passed to the neighbouring positions. This gives way to an iterative process to replicate the diffusive process discretely without simulating the solution to the PDE sets. The E-Path iterative process is described by Equation 7.6.

$$P(x_i - \Delta x) = \left(E\left(\beta(x_i), P(x_i)\right) + P(x_i) \right) \times f_1 \tag{7.6}$$

where for some position, x_i, below the 'lower bifurcation point' the next position can be described as $x_{i+1} = x_i - \Delta x$. The initial perturbation P_0 is defined for each model. Equation 7.6 is dimensionally correct as previously noted (for $\Phi = [\mu M]$): E is of units $[\mu M]$, P is also of units $[\mu M]$ and f_1 is dimensionless [-].

The process stops when $E\left(\beta_i, P_i\right) = 0$, as then the perturbation can no longer sustain an excited state in the next 'cell' and thus the excursion will stop. The depth at the end of the E-Path is also known as the predicted depth. To view the path the wave takes on the E-Profile, for future chapters, the E-Profile can be reordered to match the new $\beta(x)$ profile. However, as previously stated, this chapter will look exclusively at a linear profile.

7.5.5 The Significance of f_1

f_1, depicted in Equation 7.6, describes some fraction of the maximum concentration of the previous position, above the steady state value, that is passed to the next position. Thus, f_1 is a function of the dynamics of a particular model, and is a representation of the process of diffusion (see Section 7.7) but it is not a continuous approach. This fraction is a function of four components. First, f_1 is dependent on the model used and its associated dynamics. Second f_1 is dependent on the diffusion coefficient (D), as mentioned in Chapter 5, as the

diffusion coefficient increases the depth of the excursions also increases. Third, f_1 is dependent on the recovery time of the model; following a change in concentration of an otherwise non-oscillatory 'cell' the solution, $\Phi(t)$, must return back to the steady state value. If this time is greater than the period of oscillation it is possible that the small addition of concentration (P) from diffusion will no longer excite the 'cell'. Finally, f_1 is dependent on the alignment of the wave profiles, also known as phase lag, described in Chapter 6. Between two positions of varying periods it is expected that the peaks of the concentration will vary in and out of alignment due to the phase lag. Thus, the phase lag creates a variation in the fraction f_1 that can be passed to the next position.

Due to the third and fourth components both being a function of time, they can be combined into their effect on the Wave Front Number ($\bar{\iota}$). This reduces f_1 to a function of three components: the model, the diffusion coefficient and the Wave Front Number ($\bar{\iota}$). This relationship will be further investigated for each model.

7.5.6 Curve Fit Analysis

In order to obtain relationships between the dependent variable based on the independent variables, curve fit analysis is necessary. The independent variables within this chapter include the previously mentioned Wave Front Number ($\bar{\iota}$) and the diffusion coefficient, D, as these values dictate different properties of the spatio-temporal solution under the applied Fickian Diffusion (FD). The dependent variable will be considered to be the depth an excursion reaches into the previously non-oscillatory region. From the relationship generated via the E-Path, the dependent depth can subsequently be considered as the f_1 value in order to obtain the correct depth of the excursion.

Curve fit analysis is the process of finding the line of best fit relating the independent variable/s to the dependent variable/s. This is done through trial of common regression line equations that best fit the produced data. The fit was determined to be a good fit if the Linear Coefficient of Determination, $r^2 \in [0,1]$ (Section 7.5.7) obtained a high value (ie close to 1). The larger the fraction of variation in the dependent variable (r^2) that is 'explained by' the variation in independent variable the better the correlation is said to be.

7.5.7 Linear Coefficient of Determination, r^2

The Linear Coefficient of Determination (r^2) is the proportion of the variance in the dependent variable that is predictable from the independent variable (the predictor) for specifically a linear relationship. The degree of linear correlation measures the distance between a fitted line on a graph and all the data points that are scattered around the graph. The variability of the data can be measured using a 'sum of the squares' formula. First, the sum of squares of the residuals (Equation 7.7) is found which measures the discrepancy between the data and an estimation model.

$$SS_{res} = \sum_{i=1}^{n} (y_i - \hat{y}_i)^2 \tag{7.7}$$

where n indicates the number of data points, y_i is the actual data point collected (in this case the depth collected via the spatio-temporal solution) and $\hat{y}_i$ is the calculated value from the line of best fit. Next, the maximum squared difference from the horizontal averaged line, 'the total sum of squares', needs to be found (Equation 7.8).

$$SS_{tot} = \sum_{i=1}^{n} (y_i - \bar{y})^2 \tag{7.8}$$

where again n and y_i are as above and $\bar{y}$ denotes the mean or average value of the data set. Finally, the linear coefficient of determination, r^2, can be found as a fraction of the sum of the squares of the residuals (Equation 7.7) to the total sum of the squares (Equation 7.8), described by Equation 7.9.

$$r^2 = 1 - \frac{S_{res}}{SS_{tot}} \tag{7.9}$$

Since r^2 is a proportion, it is always a number between 0 and 1 ($r^2 \in [0,1]$). If $r^2 = 1$, all of the data points fall perfectly on the regression line, thus the predictor accounts for all of the variation in y. Conversely, if $r^2 = 0$ the estimated regression line is perfectly horizontal and, thus, the predictor accounts for none of the variation in y.

7.6 Results

7.6.1 The Goldbeter model

The first model under consideration is the Goldbeter model. In order to understand the potential fractions, f_1, of concentration that could be passed to the neighbouring position the E-Path iterative method described by Equation 7.6 was computed for a range of f_1 values. Figure 7.10 depicts the relationship for the Goldbeter model between the depth reached and the given f_1, whereby no computations involving PDEs were done.

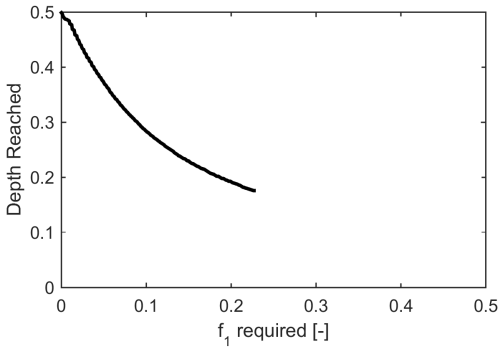

Figure 7.10: f_1 required to reach the associated depth of excursion for the Goldbeter model. Using the E-Profile (Figure 7.3.a) and the iterative E-Path (Section 7.5.4) method only (No PDEs were solved).

For Figure 7.10, an $f_1 > 0.24$ required a larger perturbation than chosen for the E-Profile (Figure 7.3.a) so is thus not depicted. Figure 7.10 shows that in order to reach a greater depth, a larger fractional amount, f_1, is required.

Next, the actual excursion depth was recorded for each spatio-temporal solution of the PDE set (Equations 5.22 and 5.23) with varying diffusion. The actual depth data was then combined with Figure 7.10 producing data of the f_1 required in order to reach the correct depth. This required f_1 data for $\bar{\iota} = 1$ and varying diffusion is plotted in Figure 7.11 (a), and the required f_1 data varying the Wave Front Number ($\bar{\iota}$) (for fixed diffusion constants) is plotted in Figure 7.11 (b).

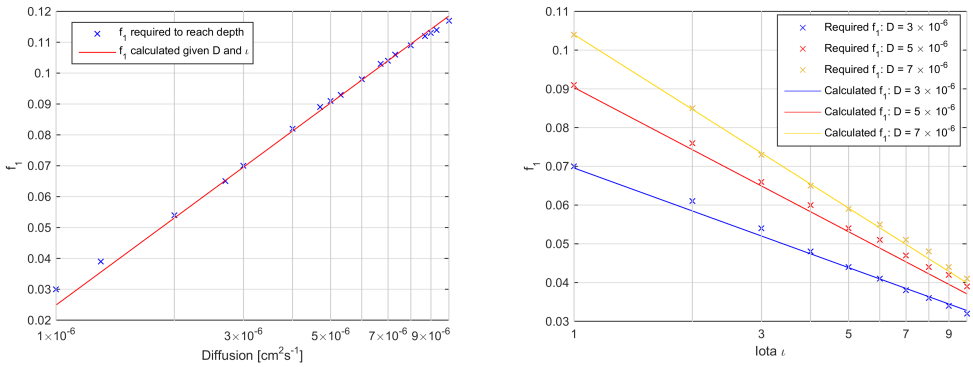

(a) Varying Diffusion ($\bar{\iota} = 1$) *(b)* Varying Wave Front Number ($\bar{\iota}$)

Figure 7.11: Relationship of f_1 for the Goldbeter model where the data points are taken from the solutions to the PDE with linear $\beta(x)$ and are overlaid with lines of best fit. Note the horizontal log scale on both figures.

Figure 7.11 (a) shows a clear natural logarithmic relationship between the diffusion coefficient and the necessary f_1 in order to reach the associated depth for the first wave front number ($\bar{\iota} = 1$). Figure 7.11 (b) also shows clear negative natural logarithmic relationships between the wave front number $\bar{\iota}$ and the necessary f_1 for each diffusion coefficient.

Thus, overlaid on Figure 7.11 is the line of best fit. This was found through curve fitting analysis as per Section 7.5.6. This relationship is a function of the diffusion coefficient and the wave front number. Specifically, this relationship was found to be Equation 7.10. Equation 7.10 is a rearrangement of a linear equation using the natural log rules.

$$f_1(D,\bar{\iota}) = ln\left(\omega_1 D^{\theta_1}\right) + \left(ln\left(\omega_2 D^{\theta_2}\right)\right) ln(\bar{\iota}) \tag{7.10}$$

Importantly, Equation 7.10 shows that when $\bar{\iota} = 1$, $f_1 = ln\left(\omega_1 D^{\theta_1}\right)$ only. The four constants $(\omega_1, \theta_1, \omega_2, \theta_2)$ have been curve fit for the Goldbeter model using a least squares approximation on these linear relationships where θ_i is dimen-

sionless and ω_i has units $[cm^{-2\theta_i} s^{\theta_i}]$. These four constants were found and are listed in Table 7.1.

Table 7.1: Four constants $(\omega_1, \theta_1, \omega_2, \theta_2)$ required for Equation 7.10 and Figure 7.11, found by curve fit for the Goldbeter model.

Parameters	ω_1	θ_1	ω_2	θ_2
Fitted Value	1.798	0.0407	0.812	-0.0151

A linear equation was fit to the data in Figure 7.11 (a) and the linear coefficient of determination was found to be $r^2 = 0.9936$, indicating that 99.4% of the variation in f_1, due to D, is accounted for by the prediction Equation 7.10. Additionally, a linear equation was fit to the data in Figure 7.11 (b) and the linear coefficient of determination was found to be $r^2 \in [0.9875 - 0.9991]$ depending on the diffusion coefficient, D, indicating that at least 98.8% of the variation in f_1, due to $\bar{\iota}$, is accounted for by the prediction Equation 7.10. Thus, overall 98.8% of the total variation in f_1 is explained by the full Equation 7.10, therefore providing strength to the 'goodness of fit' of the equation.

What is important to note about this relationship is that in order to obtain the four constants $(\omega_1, \theta_1, \omega_2, \theta_2)$ technically only two spatio-temporal solutions with FD need to be simulated. This would introduce a trade off between the simulation time and stability of the constants for extrapolation or experimental constraints.

In theory the E-Profile can be found via experimentation. This could lead to experimental relationships between the diffusion coefficient, the excursion depth, and the Wave Front Number $(\bar{\iota})$. These relationships are critical to understanding the dominant dynamics of the single cell necessary in predicting intercellular ionic concentrations. Through application of such relationships to experimental data, it is possible new connections could be made. How this rela-

tionship will be utilised in experimentation is yet to be understood.

7.6.2 The Dupont model

The same process from the Goldbeter model was repeated for the Dupont model. Again, Equation 7.6 was used to generate the E-Path (Section 7.5.4) for a range of f_1 values and the depth reached was recorded. Figure 7.12 shows the relationship for the Dupont model between the depth reached and the given f_1 whereby no computations involving PDEs were done.

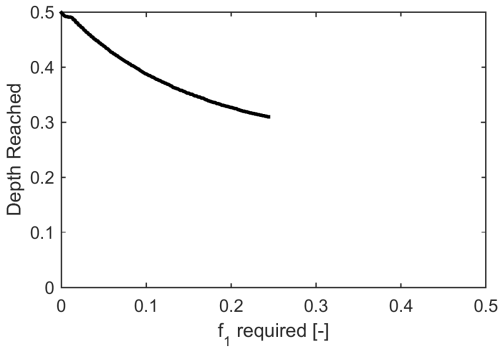

Figure 7.12: f_1 required to reach the associated depth of excursion for the Dupont model. Using the E-Profile (Figure 7.3.b) and the iterative E-Path (Section 7.5.4) method only (No PDEs were solved).

For Figure 7.12, an $f_1 > 0.25$ required a larger perturbation than chosen for the E-Profile (Figure 7.3.b) so is thus not depicted. Figure 7.12 shows that in order to reach a greater depth a larger fractional amount, f_1, is required.

Next, for each spatio-temporal solution of the PDE set (Equations 5.24 to 5.26) with varying diffusion the actual depth was recorded. The actual depth data was then combined with Figure 7.12 to produce data on the f_1 required in order to reach the correct depth. This required f_1 data for fixed $\bar{\iota} = 1$ varying

diffusion is plotted in Figure 7.13 (a) and the required f_1 data varying the Wave Front Number ($\bar{\iota}$) (for fixed diffusion coefficient) is plotted in Figure 7.13 (b).

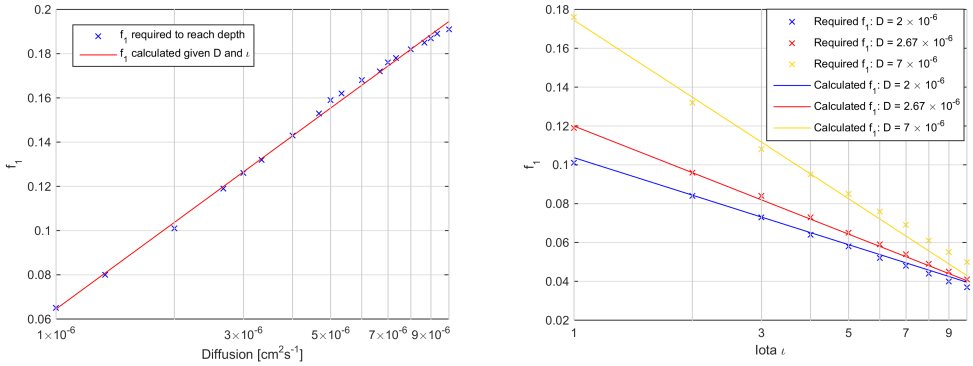

(a) Varying Diffusion ($\bar{\iota} = 1$) *(b)* Varying Wave Front Number ($\bar{\iota}$)

Figure 7.13: Relationship of f_1 for the Dupont model where the data points are taken from the solutions to the PDE with linear $\beta(x)$ and are overlaid with lines of best fit. Note the horizontal log scale of both figures.

Similar to Figure 7.11, Figure 7.13 (a) shows a clear natural logarithmic relationship between the diffusion coefficient and the necessary f_1 in order to reach the associated depth for the first wave front number ($\bar{\iota} = 1$). Figure 7.13 (b) also shows clear negative natural logarithmic relationships between the wave front number $\bar{\iota}$ and the necessary f_1 for each diffusion coefficient.

Thus, through curve fitting analysis (Section 7.5.6), overlaid on Figure 7.13 is the line of best fit found which can be calculated as a function of the diffusion coefficient and the wave front number. Notably, Equation 7.11 is the same as that for the Goldbeter model (Equation 7.10).

$$f_1(D,\bar{\iota}) = ln\left(\omega_1 D^{\theta_1}\right) + \left(ln\left(\omega_2 D^{\theta_2}\right)\right) ln(\bar{\iota}) \tag{7.11}$$

Importantly, again Equation 7.11 shows that when $\bar{\iota} = 1$, $f_1 = ln\left(\omega_1 D^{\theta_1}\right)$ only. The four constants $(\omega_1, \theta_1, \omega_2, \theta_2)$ have been curve fit for the Dupont model

using a least squares approximation on the same linear relationships from the Goldbeter model. Again, θ_i is dimensionless and ω_i has units $[cm^{-2\theta_i}s^{\theta_i}]$. These four constants were found and are detailed in Table 7.2.

Table 7.2: Four constants $(\omega_1, \theta_1, \omega_2, \theta_2)$ required for Equation 7.11, found by curve fit for the Dupont model.

Parameters	ω_1	θ_1	ω_2	θ_2
Fitted Value	2.3274	0.0565	0.7172	-0.0232

Again, a linear equation was fit to the data in Figure 7.13 (a) and the linear coefficient of determination was found to be $r^2 = 0.9953$, indicating that 99.5% of the variation in f_1, due to D, is accounted for by the prediction Equation 7.10. Additionally, a linear equation was fit to the data in Figure 7.13 (b) and the linear coefficient of determination was found to be $r^2 \in [0.9666 - 0.9995]$ depending on the diffusion coefficient, D, indicating that at least 96.6% of the variation in f_1, due to $\bar{\iota}$, is accounted for by the prediction Equation 7.10. Thus, overall 96.6% of the total variation in f_1 is explained by the full Equation 7.10, therefore providing strength to the 'goodness of fit' of the equation.

*7.6.3 The Toy Model 2 (*TM2*)*

The same process from the Goldbeter model and the Dupont model was repeated for TM2. Again, Equation 7.6 was used to generate the E-Path (Section 7.5.4) for a range of f_1 values and the depth reached was recorded. Figure 7.14 shows the relationship for TM2 between the depth reached and the given f_1, whereby no computations involving PDEs were done.

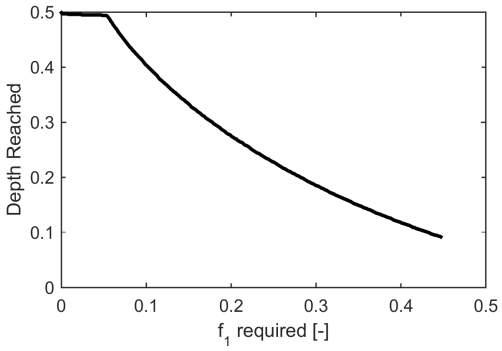

Figure 7.14: f_1 required to reach the associated depth of excursion for TM2. Using the E-Profile (Figure 7.4.b) and the iterative E-Path (Section 7.5.4) method only (No PDEs were solved).

For Figure 7.14, an $f_1 > 0.45$ required a larger perturbation than chosen for the E-Profile (Figure 7.4.b) so is thus not depicted. Figure 7.14 shows that in order to reach a greater depth, a larger fractional amount, f_1, is required.

Next, for each spatio-temporal solution of the PDE equation set (Equations 6.3 and 6.4) with varying diffusion the actual depth was recorded. The actual depth data was then combined with Figure 7.14 to produce data on the f_1 required in order to reach the correct depth. This required f_1 data for fixed $\bar{\iota} = 1$ varying diffusion is plotted in Figure 7.15 (a) and the required f_1 data varying the Wave Front Number ($\bar{\iota}$) (for fixed diffusion coefficients) is plotted in Figure 7.15 (b).

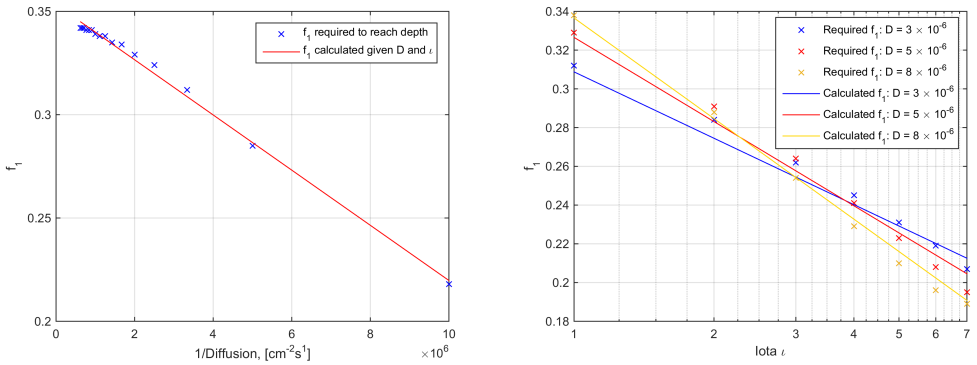

(a) Varying Diffusion ($\bar{\iota} = 1$) *(b)* Varying Wave Front Number ($\bar{\iota}$)

Figure 7.15: Relationship of f_1 for Toy Model 2 (TM2) where the data points are taken from the solutions to the PDE with linear $\beta(x)$ and are overlaid with lines of best fit. Note the horizontal log scale of (b).

Unlike the Goldbeter model or the Dupont model, Figure 7.15 (a), shows an inverse $(1/D)$ relationship between the diffusion coefficient and the necessary f_1 in order to reach the associated depth for the first wave front number ($\bar{\iota} = 1$). Figure 7.15 (b) also shows negative natural logarithmic relationships between the wave front number $\bar{\iota}$ and the necessary f_1 for each diffusion coefficient.

Thus, through curve fitting analysis (Section 7.5.6), overlaid on Figure 7.15 is the line of best fit found which can be calculated as a function of the diffusion coefficient and the wave front number. Specifically, this relationship was found to match Equation 7.12.

$$f_1(D,\bar{\iota}) = \left(\frac{1}{\omega_1 D} + \theta_1\right) + \left(ln\left(\omega_2 D^{\theta_2}\right)\right) ln(\bar{\iota}) \tag{7.12}$$

Importantly, Equation 7.12 shows that when $\bar{\iota} = 1$, $f_1 = 1/(\omega_1 D) + \theta_1$ only. The four constants $(\omega_1, \theta_1, \omega_2, \theta_2)$ have been curve fit for TM2 using a least squares approximation on the linear relationships. θ_i is dimensionless and ω_1 has units $[cm^{-2}s]$ whilst ω_2 has units $[cm^{-2\theta_2}s^{\theta_2}]$. These four constants were found and

are listed in Table 7.3.

Table 7.3: Four constants $(\omega_1, \theta_1, \omega_2, \theta_2)$ required for Equation 7.12, found by curve fit for Toy Model 2 (TM2).

Parameters	ω_1	θ_1	ω_2	θ_2
Fitted Value	-7.429×10^7	0.3532	0.6426	-0.0262

Due to the form of Equation 7.12, in comparison to the previous two models ω_1 has a considerably bigger magnitude in order to cancel out the small diffusion coefficient.

Again, a linear equation was fit to the data in Figure 7.15 (a) and the linear coefficient of determination was found to be $r^2 = 0.9953$, indicating that 99.5% of the variation in f_1, due to D, is accounted for by the prediction Equation 7.12. Additionally, a linear equation was fit to the data in Figure 7.15 (b) and the linear coefficient of determination was found to be $r^2 \in [0.976 - 0.994]$ depending on the diffusion coefficient, D, indicating that at least 97.6% of the variation in f_1, due to $\bar{\imath}$, is accounted for by the prediction Equation 7.12. Thus, overall 97.6% of the total variation in f_1 is explained by the full Equation 7.12, therefore providing strength to the 'goodness of fit' of the equation.

The inverse relationship for TM2 was unique to this model and whilst obtaining a high r^2 value, visually it does not appear to be a perfect fit. On closer inspection with the raw spatio-temporal solutions it appears that this relationship may be an artefact of the initial conditions. Given that the initial conditions are kept the same across all the simulations of TM2 this relationship will hold true within this research. Caution should be taken on the application of this relationship under alternative initial conditions.

7.6.4 The FitzHugh-Nagumo model W

The next of the models was the FitzHugh-Nagumo model with W diffused. Again, using Equation 7.6 from Section 7.5.4 the E-Path was produced for a range of f_1 values and the depth reached was recorded. Figure 7.16 shows the relationship between f_1 and the depth reached.

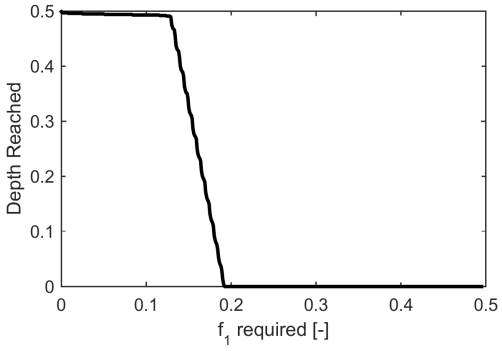

Figure 7.16: f_1 required to reach the associated depth of excursion for the FitzHugh-Nagumo model W. Using the E-Profile (Figure 7.5.b) and the iterative E-Path (Section 7.5.4) method only (No PDEs were solved).

The relationship in Figure 7.16 matches the related E-Profile from Chapter 7 (Figure 7.5.b). Figure 7.16 shows that for low f_1 the E-Path falls solely in the non-excitable region on Figure 7.5 (b) and for high f_1 the E-Path travels only in the excitable region which has a relatively constant E on Figure 7.5 (b). Finally, for a small range of moderate f_1 values the E-Path changes from the excitable region to non-excitable region which matches the cut off between $0.3 \lesssim P \lesssim 0.5$ on Figure 7.5 (b).

This relationship introduces a new problem. For all wave numbers and for all diffusion coefficients within the acceptable range, the depth reached is always

0, thus it always reaches the maximum distance. This indicates that for all reasonable D and $\bar{\iota}$ f_1 must be greater than 0.19 thus, no other relationships can be explored for this model by varying D or $\bar{\iota}$.

7.6.5 The Koenigsberger model

The final model considered is the Koenigsberger model. Again, using Equation 7.6 (Section 7.5.4) the E-Path was produced for a range of f_1 values and the depth reached was recorded. Figure 7.17 shows the relationship between f_1 and the depth reached (no PDEs were solved in order to produce this).

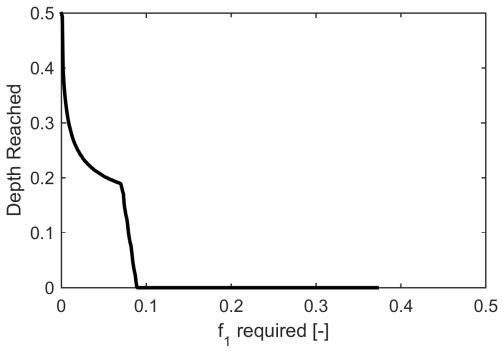

Figure 7.17: f_1 required to reach the associated depth of excursion for the Koenigsberger model. Using the E-Profile (Figure 7.6.a) and the iterative E-Path (Section 7.5.4) method only (No PDEs were solved).

The Koenigsberger model behaves somewhat similar to the FitzHugh-Nagumo model in that for an $f_1 > 0.92$ the model will exhibit excursions that will always reach the full depth ($x_d = 0$). This matches the associated E-Profile from Chapter 7 (Figure 7.6.a), which also visually resembled the FitzHugh-Nagumo model variable W.

The first waves for all diffusion coefficients within the acceptable range for the Koenigsberger model, also exhibited excursions that reached the maximum depth ($x_d = 0$). This made determining the relationship with the diffusion more difficult. Although, from $\bar{\iota} = 5$ to 10 the model did not appear to reach the full depth, indicating that $f_1 < 0.92$, there was insufficient data in order to produce a further relationship between f_1 and diffusion or $\bar{\iota}$.

7.7 f_1 Relationship to Diffusion

The fit of the natural logarithmic relationship presented an interesting development and can be connected to the dynamics of the change in Φ over time due to diffusion. First, recall the definition of Fickian Diffusion (FD), Equation 5.4, repeated here for convenience.

$$\mathcal{L}_{FD} = \frac{\partial \Phi}{\partial t} = D\frac{\partial^2 \Phi}{\partial x^2} \tag{5.4}$$

There exists a recognised solution to Equation 5.4 for $\Phi(x^*,t^*)$ under specific circumstances. The concentration at some position after some time for a large constant concentration (Φ_a) at $x^* = 0$ diffusing into a median ($x^* > 0$) with some smaller initial concentration Φ_b can be described by Equation 7.13 (Serrano-López et al., 2013; Crank, 1975).

$$\Phi(x^*,t^*) = \Phi_b + (\Phi_a - \Phi_b)\text{erfc}\left(\frac{x^*}{\sqrt{4t^*D}}\right) \tag{7.13}$$

where x^* is the considered position, t^* is the considered time and erfc is the complementary error function described by Equation 7.14.

$$\text{erfc}(a) = \frac{2}{\sqrt{\pi}} \int_a^{\infty} e^{-u^2} du \tag{7.14}$$

where the integral in Equation 7.14 can not be found analytically. To compare Equation 7.13 to the f_1 function x^* is related to Δx and t^* is some time constant, t_c, for the length of time a peak in concentration has to diffuse before it is reduced back to steady state by the system. Thus, Equation 7.13 can be rewritten as Equation 7.15.

$$\Phi(\Delta x, t_c) - \Phi_b = (\Phi_a - \Phi_b)\text{erfc}\left(\frac{\Delta x}{\sqrt{4t_c D}}\right) \tag{7.15}$$

Under the definition of E, $\Phi(\Delta x, t)$ is the lower concentration plus some addition $(P^* + \Phi_{ss})$ and the high constant concentration can be written as $E + P + \Phi_{ss}$. Equation 7.16 details these definitions.

$$\begin{aligned} \Phi(\Delta x, t) &= P(x_i - \Delta x) + \Phi_{ss} \\ \Phi_a &= E\Big(\beta(x_i), P(x_i)\Big) + P(x_i) + \Phi_{ss} \\ \Phi_b &= \Phi_{ss} \end{aligned} \tag{7.16}$$

Finally, Equation 7.17 defines the relationship between the perturbation $P(x_i - \Delta x)$ for the next spatial position and after some time t_c, assuming negligible difference between the two positions' steady state values.

$$P(x_i - \Delta x) = \Big(E\Big(\beta(x_i), P(x_i)\Big) + P(x_i)\Big)\text{erfc}\left(\frac{\Delta x}{\sqrt{4t_c D}}\right) \tag{7.17}$$

In comparison to the E-Path Equation 7.6 it follows that f_1 can be loosely compared to the erfc function of $\Delta x/\sqrt{4t_c D}$. This relationship confirms the forma-

tion of the E-Path method. This relationship does indicates why the f_1 function has a natural logarithmic relationship since the erfc function can be approximation using a $ln(a)$ relationship (Harris, 2014). However, Equation 7.17 can not be used as the f_1 function due to three issues. First, the erfc function can not be found analytically, which reduces the applicability or usefulness of its relationship. Second, the assumption that the concentration in the previous position stays constant and high is not mathematically viable. Lastly, but arguably the most important the time the concentration has to diffuse, t_c, to the next position is unknown.

7.8 Discussion

This chapter created a relationship between the depth of the excursions into the non-oscillatory region and the diffusion constant combined with the Wave Front Number ($\bar{\iota}$). This was done via a combination of a new E-Profile tool and the matching iterative E-Path process. The movement of ions due to diffusion was approximated as some fraction (f_1) of the maximum concentration above the steady state value ($E+P$) that is passed from one position to the next. This fraction either excites the next 'cell' ($E>0$) or it does not excite and thus the excursion stops ($E=0$). This was then related to data obtained about the actual depth of excursions given a range of diffusion constants (D). It was noted that for the Goldbeter model, the Dupont model and TM2 that as $\beta(x)$ decreased a larger perturbation was required to obtain an $E>0$, which indicated the excursions were destined to stop.

The E-Profile determined that in order to predict excursions a combination of both the Front Heavy Score (FH-score) (Chapter 6) and the E-Profile are necessary. Individually, under certain criteria, the two indicators would not be

able to predict when excursions would occur.

It was shown for the Ermentrout model that small perturbations in V (P_V) were solely responsible for the excitement of the system. On inspection of the E-Profile it is clear that low P_V values obtained via FD would not create excursions of great depth in comparison to the larger P_V values due to ED. It was suggested that the Ermentrout model could benefit from an additional minimum based excitability to further understand the bidirectional waves.

From the E-Profile and the E-Path mathematical relationships were found for the fractional amount, f_1 as a function of D and $\bar{\imath}$ for the Goldbeter model, the Dupont model and Toy Model 2 (TM2). This relationship was not able to be found for the other models as the excursions all reached the full depth possible. The mathematical f_1 relationships were determined to account for at minimum 97.6% (from the linear coefficient of determination (r^2) value) of the variation in the data collected from the spatio-temporal solutions and thus were determined a good linear fit. This was further confirmed by the comparison to the erfc function, which can be approximated as a natural logarithmic function under certain conditions.

The Goldbeter model and the Dupont model exhibited the same mathematical relationship for f_1 as a function of D and $\bar{\imath}$. For the first excursion, they both had a natural logarithmic relationship between f_1 and the diffusion coefficient. TM2, on the other hand, displayed an inverse relationship between f_1 and D. This relationship is unique to TM2 and was connected to the initial conditions of the model.

The FitzHugh-Nagumo model with W diffused and the Koenigsberger model could not find reliable mathematical relationships because for all reasonable diffusion coefficients the models produced excursions to the maximum depth for

the first excursion ($\bar{\iota} = 1$). However, they did both indicate that for an $f_1 > 0.19$ and $f_1 > 0.92$ the FitzHugh-Nagumo model and the Koenigsberger model respectively would reach the full depth, which matches their respective E-Profiles. This highlights an important difference of the Koenigsberger model and should be investigated under an experimental setting to determine the actual physiological response.

A mathematical relationship between the ODE system solution and the depth of excursions under spatio-temporal simulations with FD is important for three follow up abilities. First, given a system you are able to change the diffusion coefficient, Wave Front Number ($\bar{\iota}$), or the β to x function and without recomputing the PDE you could predict the depth of excursions. Second, in addition to the depth you could also predict the maximum height of the concentration wave. Thirdly, the reverse would be true. Given the spatio-temporal solution with FD it is possible to predict the diffusion coefficient. The following chapter (Chapter 8) looks into the prediction of these three things.

7.9 Conclusion

This chapter introduced a new tool (the E-Profile) to aid in the understanding of the spatio-temporal dynamics of an oscillatory cell model. From this, mathematical relationships were created between the depth of excursions into the non-oscillatory region and the diffusion constant combined with the Wave Front Number ($\bar{\iota}$) for three of the models. The Goldbeter model and the Dupont model shared the same mathematical relationship whilst TM2 had a very similar relationship. The process required the developed E-Profile tool that related the perturbation from steady state solution to the Excitability (E) of the system. The FitzHugh-Nagumo model (with the variable W diffused) and the Koenigs-

berger model were not able to have relationships formulated as the majority of the excursions reached the maximum depth. The mathematical relationships are important for follow up predictions to be discussed in Chapter 8.

8 Predictions of Depth, Concentration and D using Excitability Profile

8.1 Introduction

This chapter investigates a prediction method for the depth and maximum concentration of the excursions into the non-oscillatory region. The prediction method is based upon the E-Path introduced in Chapter 7, Equation 7.6. The E-Path is overlaid onto the Excitability Profile (E-Profile) and utilises the relationships between f_1 and the diffusion coefficient for each model.

The E-Profile determined the perturbation required in order to excite a 'cell' from the steady state value to a higher concentration before returning back to the steady state value. The process of diffusion was approximated as a discontinuous fractional amount (f_1) of the maximum concentration of a wave transferred to a neighbouring 'cell'. f_1 was determined to be a function of four components: model dynamics, diffusion coefficient (D), the recovery time and the alignment of the wave profiles. Curve fit equations were developed for $f_1(D, \bar{\imath})$ to reach the required depth of excursions for the Goldbeter model, the Dupont model and Toy Model 2 (TM2).

The f_1 equation was able to be found using only two spatio-temporal solu-

tions to the PDE sets. For now, this relationship will greatly reduce the computation time of larger, more intricate, NVU models by reducing the need for further solutions. In future, it is desired that the f_1 parameters are related to the single cell dynamics alone or potentially experimental findings thus eliminating the need to solve a PDE set entirely.

This chapter looks to predict three things using the f_1 relationship, $\beta(x)$, the E-Profile and the E-Path from Chapter 7:

1. Predict the depth of excursions given the diffusion coefficient (D) and the Wave Front Number ($\bar{\iota}$).

2. Predict the maximum concentration of the excursions over position given D and $\bar{\iota}$.

3. Predict the diffusion coefficient given a spatio-temporal solution.

Each of these prediction methods will be discussed in detail in this chapter before utilising some examples for the Goldbeter model, the Dupont model and Toy Model 2 (TM2).

8.2 Method

8.2.1 Depth Prediction

In order to predict the depth of excursions into the non-oscillatory region the E-Path process described in Chapter 7 is used. This process is defined by the iterative use of Equation 7.6, repeated here.

$$P(x_i - \Delta x) = \Big(E\Big(\beta(x_i), P(x_i)\Big) + P_i \Big) \times f_1 \tag{7.6}$$

where $E(\beta,P)$ and $f_1(D,\bar{\iota})$ were found for the Goldbeter model, the Dupont model and TM2 in Chapter 7. f_1 is described by Equations 7.10 7.11 and 7.12 with the associated parameters in Tables 7.1 7.2 and 7.3 for the three models, respectively.

For different $\beta(x)$ profiles the iterative process stays the same with a simple reordering/interpolation of the E-Profile(β,P) to give E-Profile$(x(\beta),P)$. Importantly, this reordering/interpolation means that the E-Profile(β,P) only needs to be found once no matter the change in $\beta(x)$.

8.2.2 Concentration Prediction

First, in order to convert the E-Path from the E-Profile into a concentration, the definition of Excitability (E) must be recalled from Equation 7.2, repeated here.

$$E(\beta,P) = \max\left(\Phi_{response}(\beta,P)\right) - P - \Phi_{SS}(\beta) \tag{7.2}$$

From this an equation can be derived (Equation 8.1) to find the maximum concentration of the given excursion.

$$max\left(\Phi(\bar{\iota})_{predicted}\right) = \bar{E}(\beta,P)_{\bar{\iota}} + \bar{P}_{\bar{\iota}} + \bar{\Phi}_{SS}(\beta) \tag{8.1}$$

where the added macron indicates a vector and is found using the E-Path (Equation 7.6) for each Wave Front Number ($\bar{\iota}$). Equation 8.1 is then compared to the actual maximum concentration of the excursion ($\bar{\iota}$) under consideration.

8.2.3 Diffusion Prediction

To predict the diffusion coefficient (D), the process is reversed. Given a spatio-temporal solution for a randomised diffusion coefficient the diffusion coefficient

can be predicted using the f_1 relationship. First, the depth of the first excursion from the spatio-temporal solution is recorded. Next, f_1 can be found using an interpolation of the figures in Chapter 7 relating the depth to the fractional amount f_1 (Figures 7.10, 7.12 and 7.14 for the Goldbeter model, the Dupont model and TM2 respectively). Finally, the equation for f_1 can be used to calculate the predicted diffusion coefficient.

This process to predict the diffusion coefficient will be repeated for 100 randomly selected diffusion coefficients for the Goldbeter model. Equation 8.2 depicts a rearrangement of the f_1 function for the model in order to predict the diffusion coefficient.

$$D = \left(\frac{1}{\omega_1} e^{f_1} \right)^{\frac{1}{\theta_1}} \tag{8.2}$$

8.2.4 Error

To evaluate the accuracy of the aforementioned prediction methods a percentage error was implemented between the true and the predicted results. For the depth of the excursions the percentage error is defined by equation 8.3.

$$Error = \frac{x_{DepthTrue} - x_{DepthPredicted}}{L} \times 100\% \tag{8.3}$$

where L is the characteristic length ($L = 1cm$). For the percentage error of the Excitability (E), and the diffusion coefficient, Equation 8.4 was used.

$$Error = \frac{True - Predicted}{True} \times 100\% \tag{8.4}$$

8.3 Results

The results in this chapter are divided into each of the three considered models: the Goldbeter model, the Dupont model and TM2. For each of these models four $\beta(x)$ profiles will be considered to determine the limitations of the prediction method. Each of the $\beta(x)$ profiles will maintain a linear function within the oscillatory region for $x > 0.5$ to maintain an increasing period of oscillation as x decreases.

The depth of the excursions will be recorded and predicted for each β profile and for $\bar{\iota} = 1, 2, 3$. For the linear $\beta(x)$ profile and $\bar{\iota} = 1$ the predicted maximum concentration of the excursion over position is investigated. Finally, the error associated in predicting the diffusion coefficient will be displayed for the Goldbeter model only as all the models produced similar results.

8.3.1 Goldbeter model

Example 1- Depth

The first chosen $\beta(x)$ profile to display is the linear function. Figure 8.1 (a) shows the spatio-temporal solution to the PDE with the actual depths indicated alongside the E-Profile and the predicted depths of excursions on Figure 8.1 (b). The predicted depths were found using the E-Path iterative formula (Equation 7.6) and the f_1 for the Goldbeter model given by Equation 7.10 from Chapter 7.

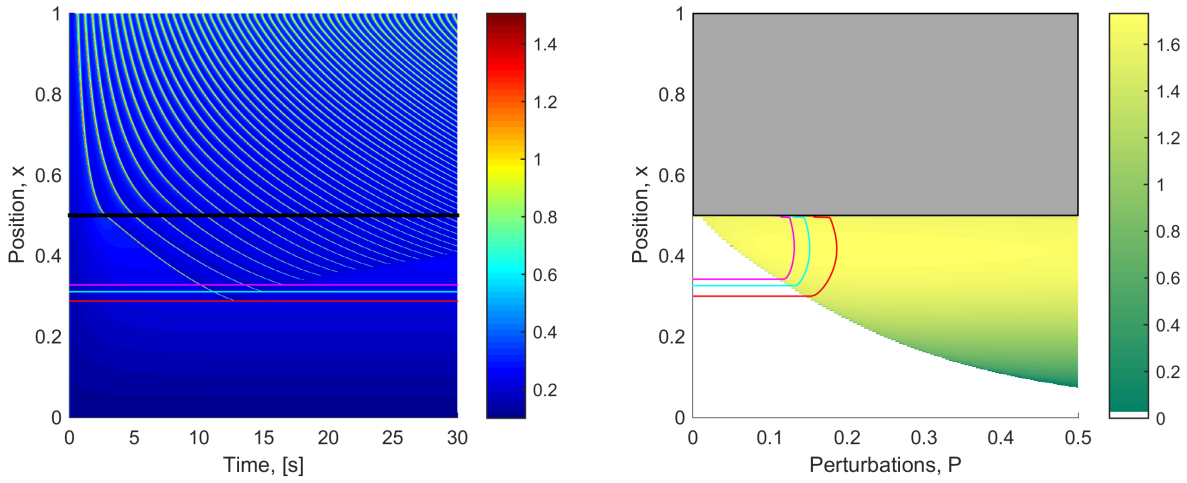

(a) Spatio-temporal solution *(b)* E-Profile with 3 E-Paths

Figure 8.1: Example 1: Goldbeter model: Linear β profile ($\beta = 2\beta_{Bi}x$) with $D = 5 \times 10^{-6} cm^2 s^{-1}$. (a) shows the associated spatio-temporal solution to the PDE (Section 5.3.1). (b) shows the E-Profile where the grey area indicated no possible E due to the oscillatory region. White indicates $E = 0$. Overlaid are the first three $\bar{\imath}$ (red, teal and magenta respectively) and their associated depths and predictions using Section 8.2.1.

Figure 8.1 shows that the actual excursion depths on the spatio-temporal solution reach the same depth as predicted by the E-Path method. This prediction method was carried out in excess of 10 times with varying diffusion coefficients and the depth was predicted for the first 10 Wave Front Number ($\bar{\imath}$)s. This resulted in a maximum depth prediction error of $\pm 0.8\%$ (using Equation 8.3).

Example 1- Concentration

Given $\bar{\imath} = 1$ for the first linear $\beta(x)$, the E-Path can be translated into a predicted concentration using Equation 8.1. The maximum concentration over space is found using the contour scale on the E-Profile (Figure 8.1) combined with the perturbation, P, and is given in Figure 8.2.

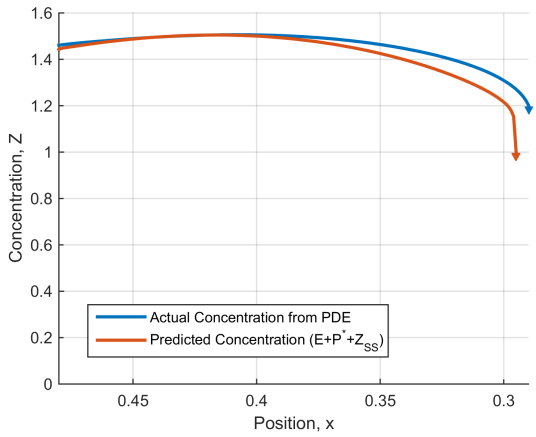

Figure 8.2: Concentration comparison: Goldbeter model: ($\bar{\iota} = 1$, $D = 5 \times 10^{-6} cm^2 s^{-1}$) shows in blue the true maximum concentration over position vs the red which is predicted using Equation 8.1.

Figure 8.2 shows the maximum concentration prediction and the actual maximum concentration are visually similar on this scale. However, it is clear the predicted maximum concentration is not accurate enough to make further recommendations as the end of the excursion had a large accumulated error. The final depth does reach the same value within the $\pm 0.8\%$ mentioned previously. The different concentration cut off points near the end of the wave ($x \approx 0.35$) is attributed to the two methods different end criteria.

Example 2 and 3

Example $\beta(x)$ profiles 2 and 3 are of similar nature; they both consist of step functions. β Profile 2 (Figure 8.3.a) steps near the β value that for a linear β profile from Example 1 the excursion would be expected to stop. β Profile 3 (Figure 8.3.b) is another simple stepped function to attempt to amplify any issues.

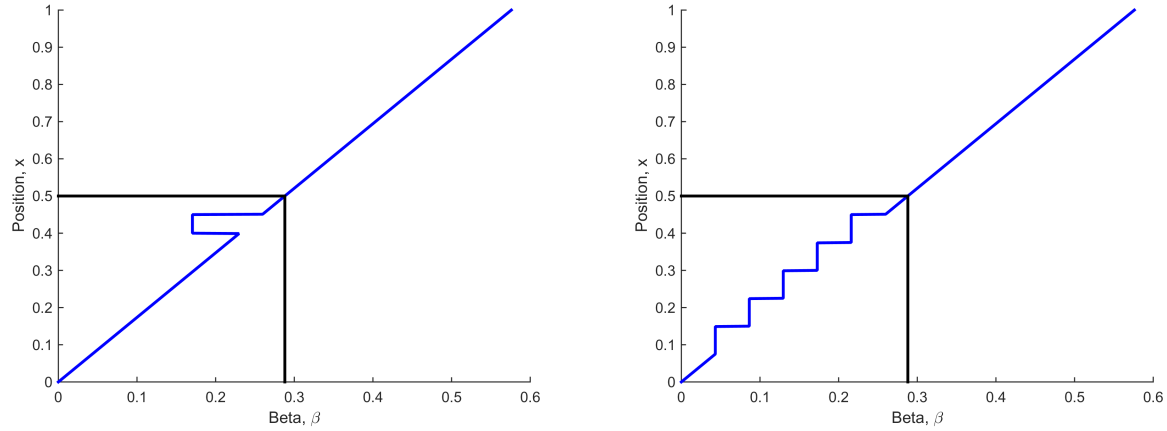

(a) Step $\beta(x)$ Profile 2 *(b)* Step $\beta(x)$ Profile 3

Figure 8.3: Example 2 and 3 step $\beta(x)$ profiles for the Goldbeter model. Corresponding to Figure 8.4. Black line indicates bifurcation point.

The spatio-temporal solutions under FD for the two $\beta(x)$ profiles depicted in Figure 8.3 are displayed in Figure 8.4 (a) and (c). The corresponding predictions using the E-Path method on the E-Profile are also given in Figure 8.4 (b) and (d) respectively for comparison.

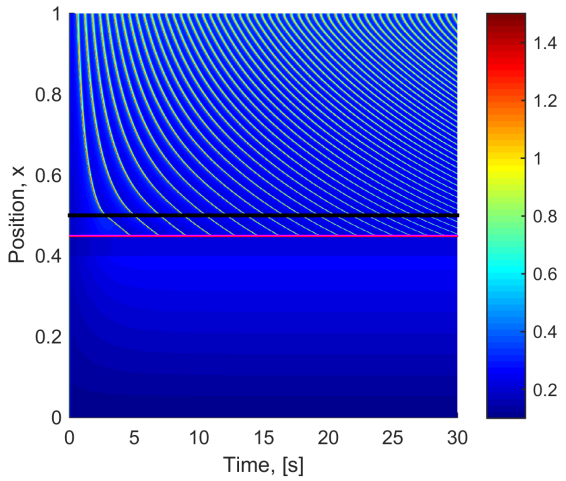

(a) Example 2: Spatio-temporal solution

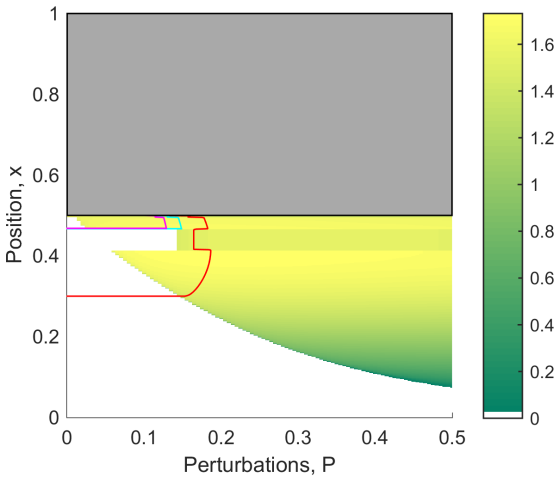

(b) Example 2: E-Profile with 3 E-Paths

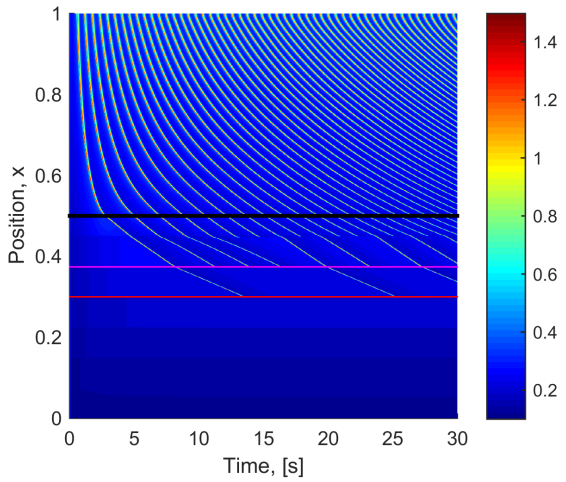

(c) Example 3: Spatio-temporal solution

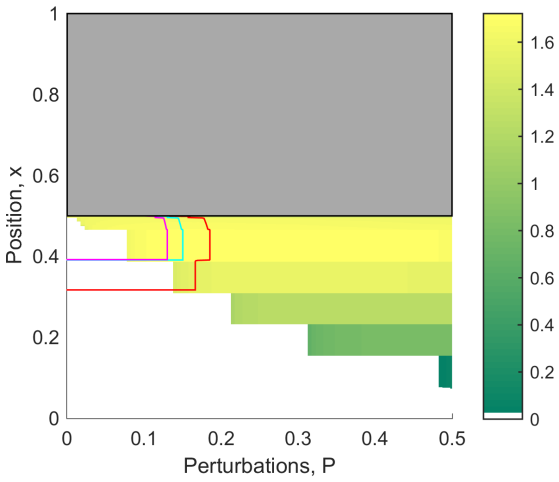

(d) Example 3: E-Profile with 3 E-Paths

Figure 8.4: Example 2 and 3: Goldbeter model: Step β profile (Section 5.3.1) with $D = 5 \times 10^{-6} cm^2 s^{-1}$. (a) shows the associated spatio-temporal solution to the PDE (Figure 5.4). (b) shows the E-Profile where the grey area indicated no possible E due to the oscillatory region. White indicates $E = 0$. Overlaid are the first three $\bar{\iota}$ (red, teal and magenta respectively) and their associated depths and predictions using Section 8.2.1. Note teal and magenta lines ($\bar{\iota} = \{2,3\}$) overlap.

Figure 8.4 (b) predicted that the excursion would reach a depth of approximately 0.31. However, the spatio-temporal solution showed that the excursion stopped as soon as the β value stepped to $\beta = 0.170$. This highlights the first case in

which the prediction method E-Path does not work. On closer examination of the positions $x = 0.4$ to $x = 0.45$ a development was made. The time dependent solution for $x = 0.4$ to $x = 0.45$ had not reached steady state prior to the interaction of the first excursion. At $t = 4.30$, just prior to any interaction of the excursion, $Z = 0.2110\mu M$. However, the steady state value for $\beta = 0.170$ is $Z = 0.2245\mu M$, a difference of $0.014\mu M$. This reduction in the steady state value would effectively reduce the perturbation applied for this step in space and thus shift the E-Path into the non-excitable ($E = 0$) region.

All other predicted excursion depths in Figure 8.4 reached the same depth as the actual spatio-temporal solution.

Example 4

The β profile chosen for the fourth example is a unique example to understand the interaction of excursions. Example 4's β profile consists of two components, a linear component for $x > 0.5$ to produce a decreasing period with increasing x, and a cubic function which transitions back into the oscillatory region, forcing excursion interactions. The $\beta(x)$ profile is detailed by Equation 8.5 and additionally in Figure 8.5.

$$\beta(x) = \begin{cases} 28.465x^3 - 24.165x^2 + 5.54x & x < 0.5 \\ 2\beta_B x & x \geq 0.5 \end{cases} \tag{8.5}$$

where the bifurcation point occurs at $\beta_{Bi} = 0.288$ for the Goldbeter model.

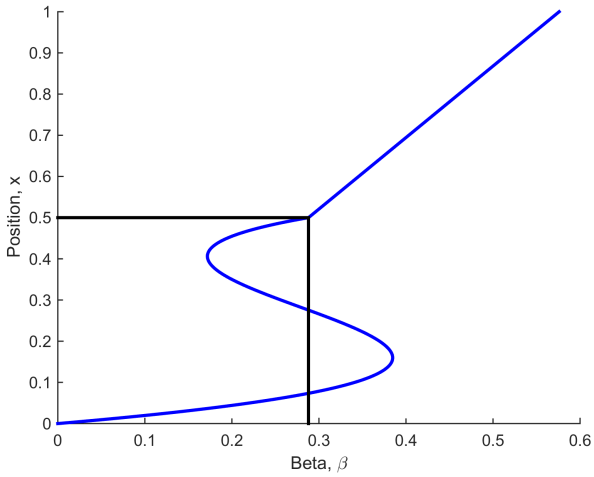

Figure 8.5: Example 4: $\beta(x)$ cubic profile function for the Goldbeter model, with position on the y-axis to match the spatio-temporal solution. Black line indicates bifurcation point. Corresponds to Figure 8.6.

Given the $\beta(x)$ profile detailed by Equation 8.5 and Figure 8.5, the spatio-temporal solution and additional E-Profile with the E-Path method predicting the depth of excursions is detailed in Figure 8.6.

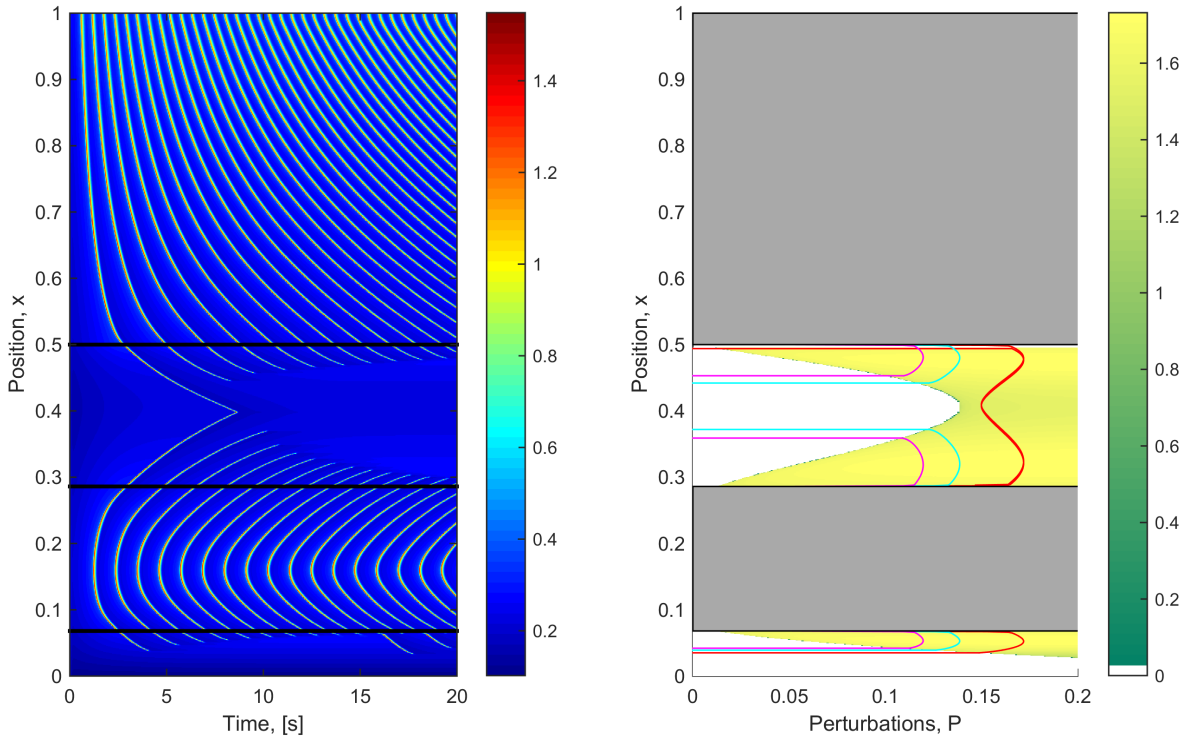

(a) Spatio-temporal solution

(b) E-Profile with 3 E-Paths

Figure 8.6: Example 4: Goldbeter model: Cubic β profile (Section 5.3.1) with $D = 5 \times 10^{-6} cm^2 s^{-1}$. (a) shows the associated spatio-temporal solution to the PDE (Figure 5.4). (b) shows the E-Profile where the grey area indicated no possible E due to the oscillatory region. White indicates $E = 0$. Overlaid are the first three $\bar{\imath}$ (red, teal and magenta respectively) and their associated depths and predictions using Section 8.2.1.

Figure 8.6 shows that the first excursion ($\bar{\imath} = 1$) initiated from $x = 0.5$ and from $x = 0.275$ interact with each other. Furthermore, the following excursions and E-Paths do not interact with each other. This shows the robustness of the E-Path method in predicting excursion with unusual β profiles.

8.3.2 Diffusion Coefficient Prediction

For the prediction of the diffusion coefficient, D, the PDE solution for the Goldbeter model was evaluated with a randomised diffusion value 100 times. Then, via the process described in Section 8.2.3, the diffusion coefficient was able to be predicted. Table 8.1 shows five examples of this process with a range of percentage errors.

Table 8.1: Process for predicting the diffusion coefficient using 5 randomised examples.

Example Number	**Actual D (2dp)**	**Depth Achieved**	**f_1 Required**	**Predicted D (2dp)**	**Error**
1	9.61×10^{-6}	0.255	0.116	9.40×10^{-6}	2.24%
2	5.37×10^{-6}	0.283	0.094	5.47×10^{-6}	-1.92%
3	8.20×10^{-6}	0.262	0.110	8.11×10^{-6}	1.13%
4	2.28×10^{-6}	0.343	0.059	2.31×10^{-6}	-1.66%
5	4.80×10^{-6}	0.290	0.090	4.96×10^{-6}	-3.40%

Over the sample of 100 randomised diffusion coefficients the percentage error between the true diffusion coefficients and the actual diffusion coefficients were recorded and are shown in Figure 8.7.

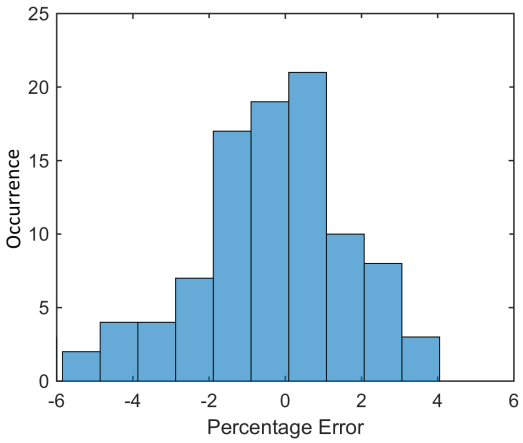

Figure 8.7: Frequency of percentage error when predicting the diffusion coefficient for a sample of 100 randomised diffusion coefficients for the Goldbeter model with a linear $\beta(x)$. Diffusion Coefficient found via Section 8.2.3. Error found by Equation 8.4.

Figure 8.7 shows a distribution of errors about zero up to $\pm 6\%$ error in predicting the diffusion coefficient.

8.3.3 Dupont model

Example 1 - Depth

Again, for the Dupont model the first chosen $\beta(x)$ profile is a linear relationship. Figure 8.8 shows the spatio-temporal solution to the PDE with the actual depths indicated alongside the E-Profile and the predicted E-Paths producing predicted depths of excursions. This was done via the iterative formula given by Equation 7.2 with the associated f_1 for the Dupont model given by Equation 7.11.

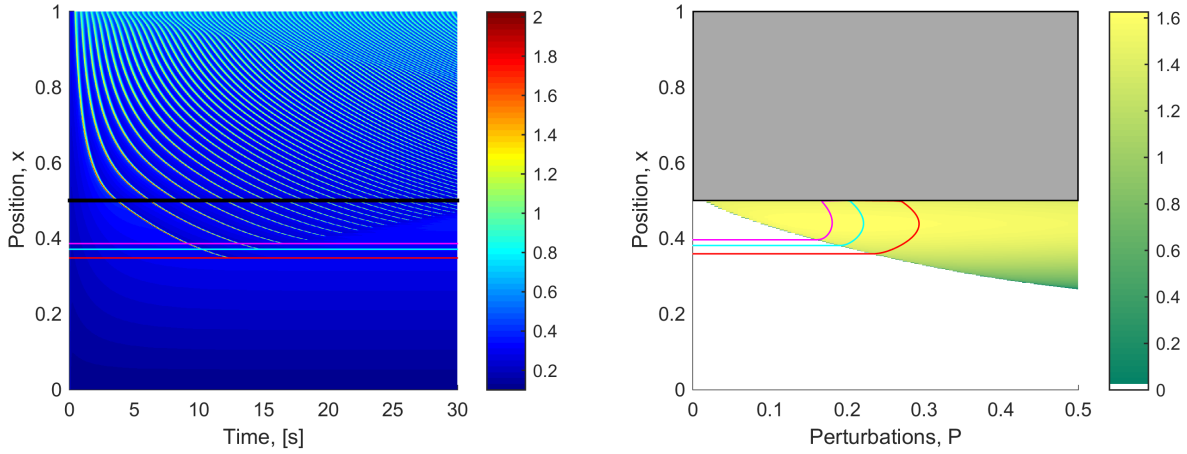

(a) Spatio-temporal solution *(b)* E-Profile with 3 E-Paths

Figure 8.8: Example 1: Dupont model: Linear β profile ($\beta = 2\beta_{Bi}x$) with $D = 5 \times 10^{-6} cm^2 s^{-1}$. (a) shows the associated spatio-temporal solution to the PDE (Section 5.3.2). (b) shows the E-Profile where the grey area indicated no possible E due to the oscillatory region. White indicates $E = 0$. Overlaid are the first three $\bar{\iota}$ (red, teal and magenta respectively) and their associated depths and predictions using Section 8.2.1.

Figure 8.8 shows that the actual depths on the spatio-temporal solution reach the same depths as predicted via the E-Path method. This prediction method was carried out in excess of 10 times with varying diffusion coefficients and the depth was predicted for the first 10 wave front numbers. This resulted in a maximum depth prediction error of $\pm 1.1\%$.

Example 1- Concentration

Given $\bar{\iota} = 1$ for the first linear $\beta(x)$ the E-Path can be translated into a predicted concentration using Equation 8.1. The maximum concentration over space is found using the contour scale on the E-Profile (Figure 8.8) combined with the perturbation, P, and is given in Figure 8.9.

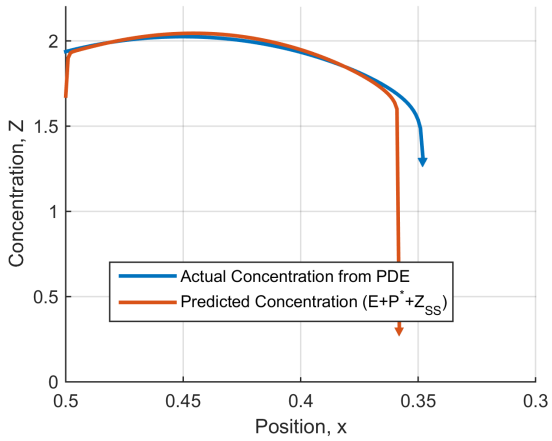

Figure 8.9: Concentration comparison: Dupont model: ($\bar{t} = 1, D = 5 \times 10^{-6}$ $cm^2 s^{-1}$) shows in blue the true maximum concentration over position vs the red which is predicted using Equation 8.1.

Figure 8.9 shows that for this model the maximum concentration predictions and the actual maximum concentrations are visually similar on this scale. The end of the predicted concentration does stop earlier in position than the actual but final depth reached is still within the $\pm 1.1\%$ mentioned previously.

Example 2 and 3

Again, $\beta(x)$ example profiles 2 and 3 are of similar nature as they both consist of step functions. β Profile 2 (Figure 8.10.a) steps very near to the β value that for a linear β profile from Example 1 the excursion would be expected to stop. β Profile 3 (Figure 8.10.b) is another simple stepped function to attempt to amplify any issues.

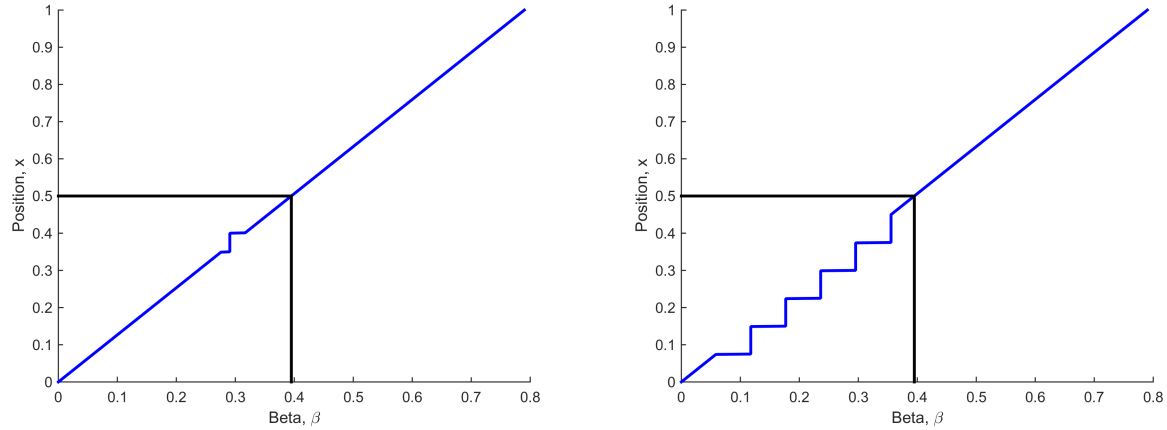

(a) β Profile 1 *(b)* β Profile 1

Figure 8.10: Example 2 and 3 step $\beta(x)$ profiles for the Dupont model. Corresponding to Figure 8.11. Black line indicates bifurcation point.

The spatio-temporal solutions under FD for the two $\beta(x)$ profiles depicted in Figure 8.10 are displayed in Figure 8.11 (a) and (c). The corresponding predictions using the E-Path method on the E-Profile are also given in Figure 8.11 (b) and (d) respectively for comparison.

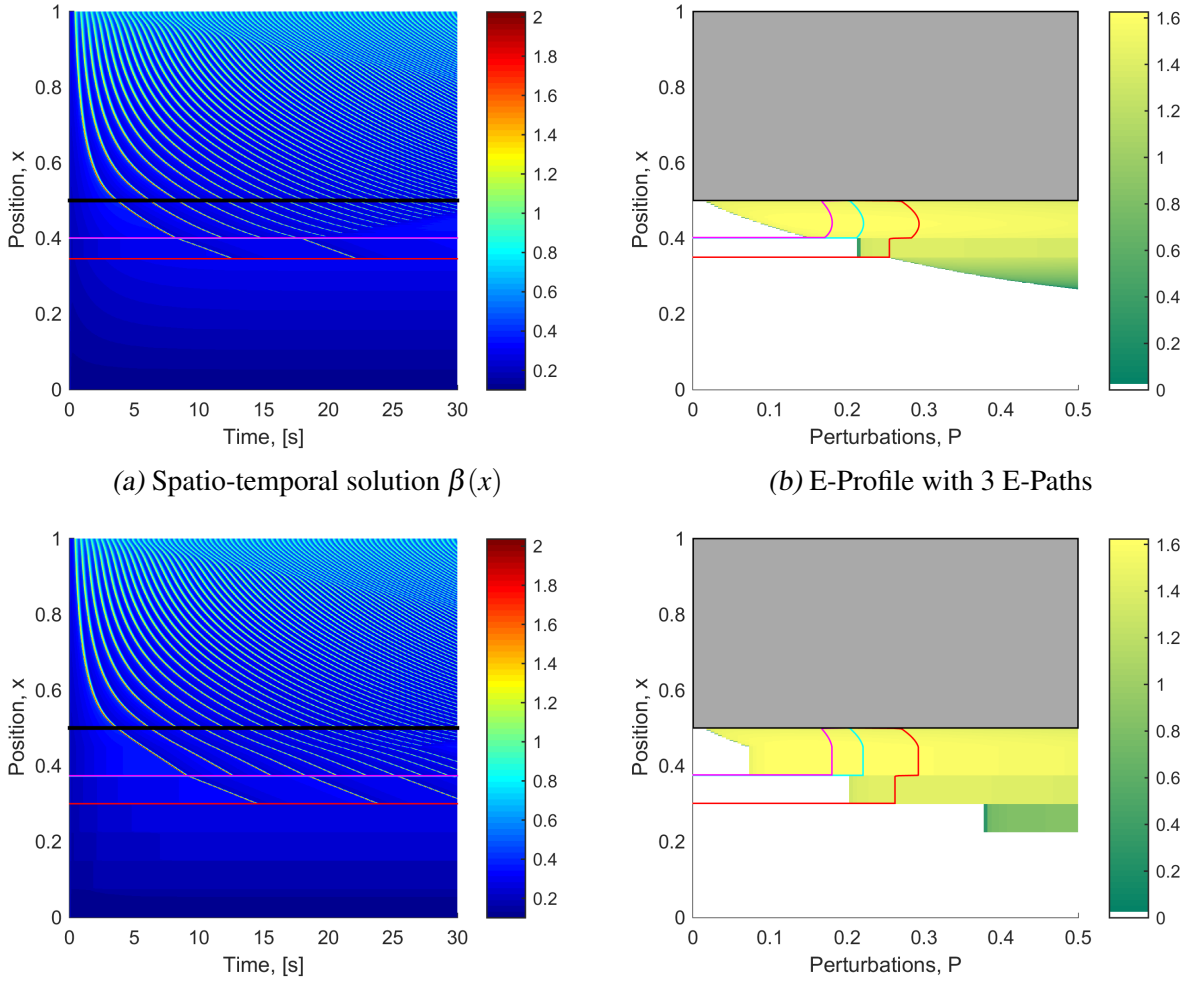

(a) Spatio-temporal solution $\beta(x)$

(b) E-Profile with 3 E-Paths

(c) Spatio-temporal solution

(d) E-Profile with 3 E-Paths

Figure 8.11: Example 2 and 3: Dupont model: Step β profile (Figure 8.10) with $D = 5 \times 10^{-6} cm^2 s^{-1}$. (a) shows the associated spatio-temporal solution to the PDE (Section 5.3.2). (b) shows the E-Profile where the grey area indicated no possible E due to the oscillatory region. White indicates $E = 0$. Overlaid are the first three $\bar{\iota}$ (red, teal and magenta respectively) and their associated depths and predictions using Section 8.2.1.

Both β profile 2 and 3 accurately predicted the depths of the excursions. Unlike the Goldbeter model, the PDE solution was able to reach steady state before the interaction of the excursions.

Example 4

Similar to the Goldbeter model, the final displayed β profile was chosen as a unique example to understand the interaction of excursions. Example 4's β profile consists of two components: a linear component for $x > 0.5$ to produce a decreasing period with increasing x, and a cubic function which transitions back into the oscillatory region forcing excursion interactions. The $\beta(x)$ profile is detailed by Equation 8.6 and additionally in Figure 8.12.

$$\beta(x) = \begin{cases} 28.27x^3 - 24.76x^2 + 6.10x & x < 0.5 \\ 2\beta_{Bi}x & x \geq 0.5 \end{cases} \tag{8.6}$$

where the bifurcation point occurs at $\beta_{Bi} = 0.395$ for the Goldbeter model.

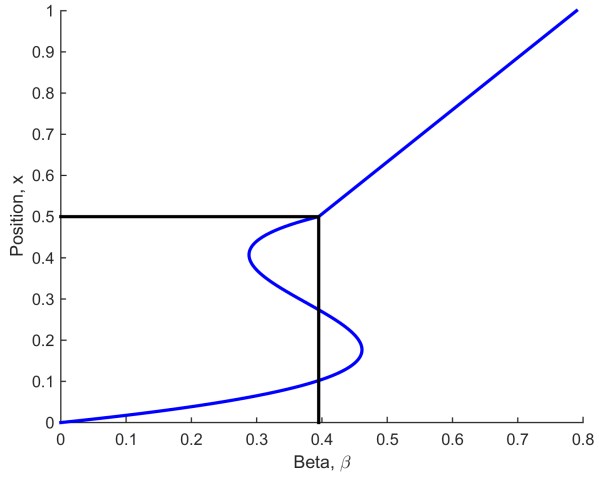

Figure 8.12: Example 4: $\beta(x)$ cubic profile function for the Dupont model. With position on the y-axis to match the spatio-temporal solution. Black line indicates bifurcation point. Corresponds to Figure 8.13.

Given the $\beta(x)$ profile detailed by Equation 8.6 and Figure 8.12, the spatio-temporal solution and additional E-Profile with the E-Path method predicting

the depth of excursions is detailed in Figure 8.13.

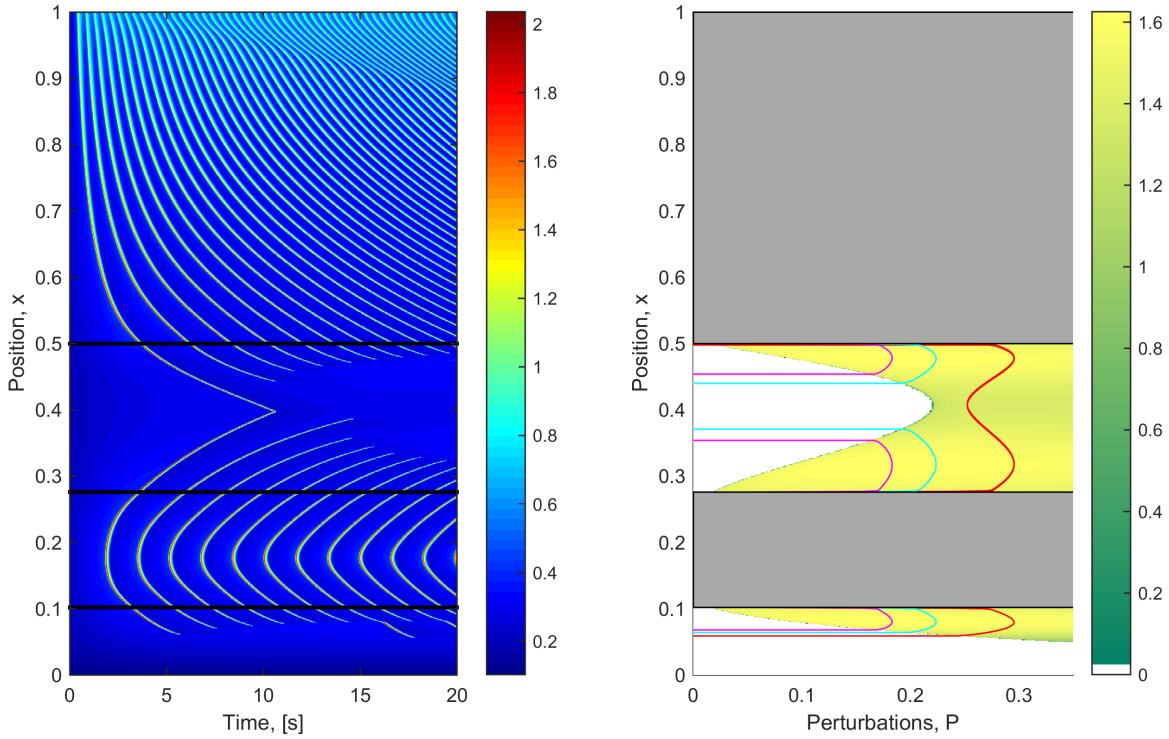

(a) Spatio-temporal solution *(b)* E-Profile with 3 E-Paths

Figure 8.13: Example 4: Dupont model: Cubic β profile (Figure 8.12) with $D = 5 \times 10^{-6} cm^2 s^{-1}$. (a) shows the associated spatio-temporal solution to the PDE (Section 5.3.2). (b) shows the E-Profile where the grey area indicated no possible E due to the oscillatory region. White indicates $E = 0$. Overlaid are the first three $\bar{\iota}$ (red, teal and magenta respectively) and their associated depths and predictions using Section 8.2.1.

Figure 8.13 shows that for the first excursion $\bar{\iota} = 1$ the excursion from $x = 0.5$ interacts with the excursion from $x = 0.275$. Furthermore, the following excursions and E-Paths do not interact with each other. The depth error was seen to increase for this β profile for increasing $\bar{\iota}$. This suggests that rapid β changes like observed here can negatively effect the accuracy of the depth prediction method.

8.3.4 TM2

Example 1 - Depth

Again, the first chosen $\beta(x)$ profile to display is the linear relationship. Figure 8.14 shows the spatio-temporal solution to the PDE with the actual depths indicated alongside the E-Profile with the predicted E-Paths producing predicted depths of excursions. This was done via the iterative formula given by Equation 7.2 with the associated f_1 for TM2 given by Equation 7.12.

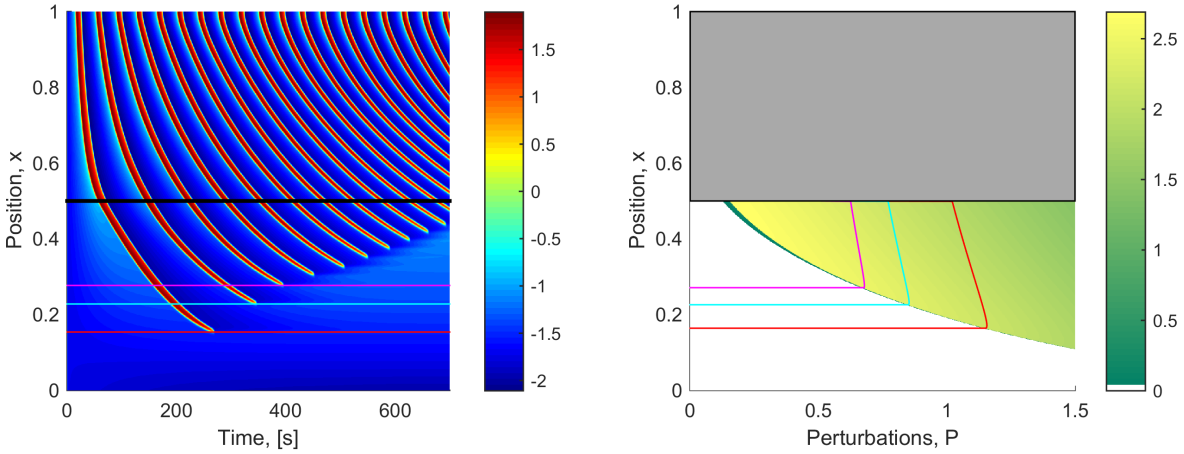

(a) Spatio-temporal solution *(b)* E-Profile with 3 E-Paths

Figure 8.14: Example 1: TM2: Linear β profile ($\beta = 0.2x + 0.1$) with $D = 5 \times 10^{-6} cm^2 s^{-1}$. (a) shows the associated spatio-temporal solution to the PDE (Section 6.3.2). (b) shows the E-Profile where the grey area indicated no possible E due to the oscillatory region. White indicates $E = 0$. Overlaid are the first three $\bar{t}$ (red, teal and magenta respectively) and their associated depths and predictions using Section 8.2.1.

Figure 8.14 shows that the actual depths on the spatio-temporal solution reach the same depths as predicted via the E-Path method. This prediction method was carried out in excess of 10 times with varying diffusion coefficients and the depth was predicted for the first 10 $\bar{t}$s. This resulted in a maximum depth prediction error of $\pm 1.0\%$.

Example 1- Concentration

Given $\bar{\iota} = 1$ for the first linear $\beta(x)$ the E-Path can be translated into a predicted concentration using Equation 8.1. The maximum concentration over space is found using the contour scale on the E-Profile (Figure 8.14) combined with the perturbation, P, and is given in Figure 8.15.

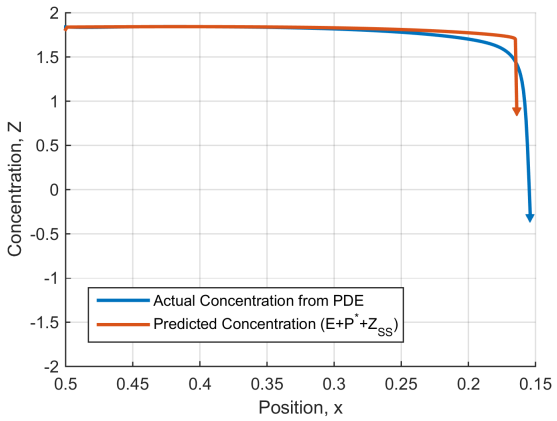

Figure 8.15: Concentration comparison: TM2: ($\bar{\iota} = 1$, $D = 5 \times 10^{-6}$ $cm^2 s^{-1}$). In blue the true maximum concentration over position vs the red which is predicted using Equation 8.1.

Figure 8.15 (a) shows the two concentrations overlapping on this scale until approximately $x = 0.25$. Then, the two concentrations deviate until the excursion ends. The vertical scale on Figure 8.15 matches the maximum/minimum concentrations from Figure 8.14 (a).

Example 2 and 3

Again, $\beta(x)$ example profiles 2 and 3 are of similar nature as they both consist of step functions. β Profile 2 (Figure 8.16.a) steps near to the β value that for the linear β profile from Example 1 the excursion would be expected to stop

at. β Profile 3 (Figure 8.16.b) is another simple stepped function to attempt to amplify any issues.

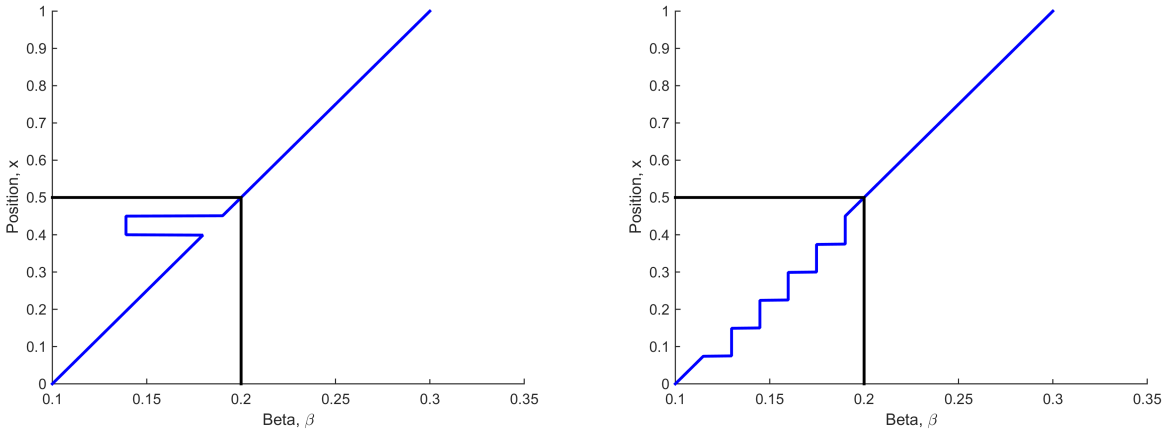

(a) β Profile 2 *(b)* β Profile 3

Figure 8.16*:* Example 2 and 3 step $\beta(x)$ profiles for TM2. Corresponding to Figure 8.17. Black line indicates bifurcation point.

The spatio-temporal solutions under FD for the two $\beta(x)$ profiles depicted in Figure 8.16 are displayed in Figure 8.17 (a) and (c). The corresponding predictions using the E-Path method on the E-Profile are also given in Figure 8.17 (b) and (d) respectively for comparison.

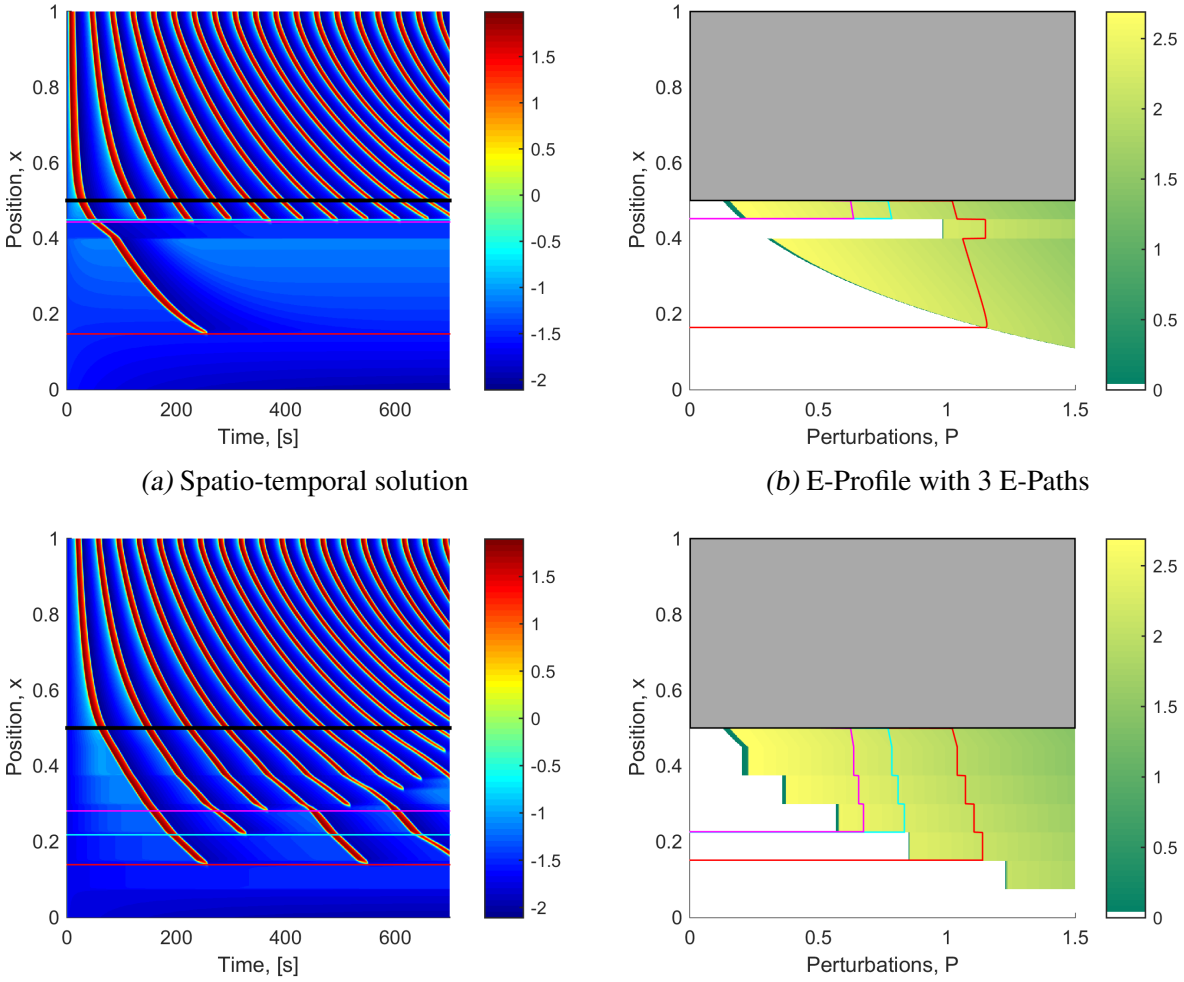

(a) Spatio-temporal solution

(b) E-Profile with 3 E-Paths

(c) Spatio-temporal solution

(d) E-Profile with 3 E-Paths

Figure 8.17: Example 2 and 3: TM2: Step β profile (Figure 8.16) with $D = 5 \times 10^{-6} cm^2 s^{-1}$. (a) shows the associated spatio-temporal solution to the PDE (Section 6.3.2). (b) shows the E-Profile where the grey area indicated no possible E due to the oscillatory region. White indicates $E = 0$. Overlaid are the first three $\bar{t}$ (red, teal and magenta respectively) and their associated depths and predictions using Section 8.2.1.

Figure 8.17 β profile 2 spatio-temporal solution (a) was able to predict the depth of the excursion to within $\pm 1.0\%$ of each other. However, Figure 8.17 (c-d) with β profile 3 produced an error in the depth prediction. For this situation a small change in the f_1 value switched the E-Path from stopping at the correct depth to

continuing. This highlights a need for the β profile to not change suddenly, as a small error in the choice of f_1 can be detrimental to the depth prediction.

Example 4

Finally, again similar to the Goldbeter model and the Dupont model, the displayed β profile chosen is a unique example to understand the interaction of excursions. Example 4's β profile consists of two components, a linear component for $x > 0.5$ to produce a decreasing period with increasing x, and a cubic function which transitions back into the oscillatory region forcing excursion interactions. The $\beta(x)$ profile is detailed by Equation 8.7 and additionally in Figure 8.18.

$$\beta(x) = \begin{cases} 12.83x^3 - 10.49x^2 + 2.24x + 0.1 & x < 0.5 \\ 0.2x + 0.1 & x \geq 0.5 \end{cases} \tag{8.7}$$

where the bifurcation point occurs at $\beta_{Bi} = 0.2$ for TM2.

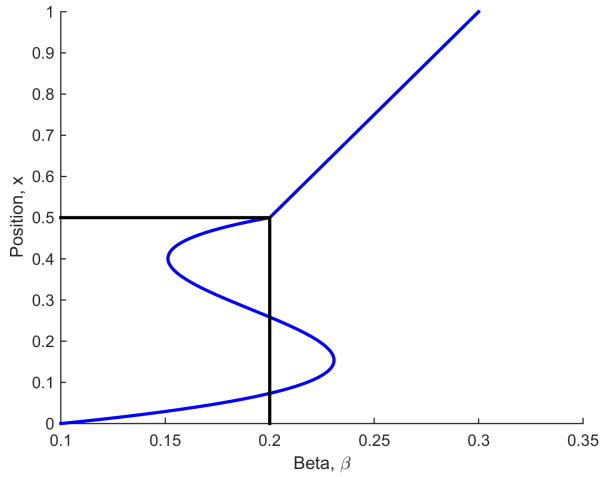

Figure 8.18: Example 4: $\beta(x)$ cubic profile function for TM2. With position on the y-axis to match the spatio-temporal solution. Black line indicates bifurcation point. Corresponds to Figure 8.19.

Given the $\beta(x)$ profile detailed by Equation 8.7 and Figure 8.18, the spatio-temporal solution and additional E-Profile with the E-Path method predicting the depth of excursions is detailed in Figure 8.19.

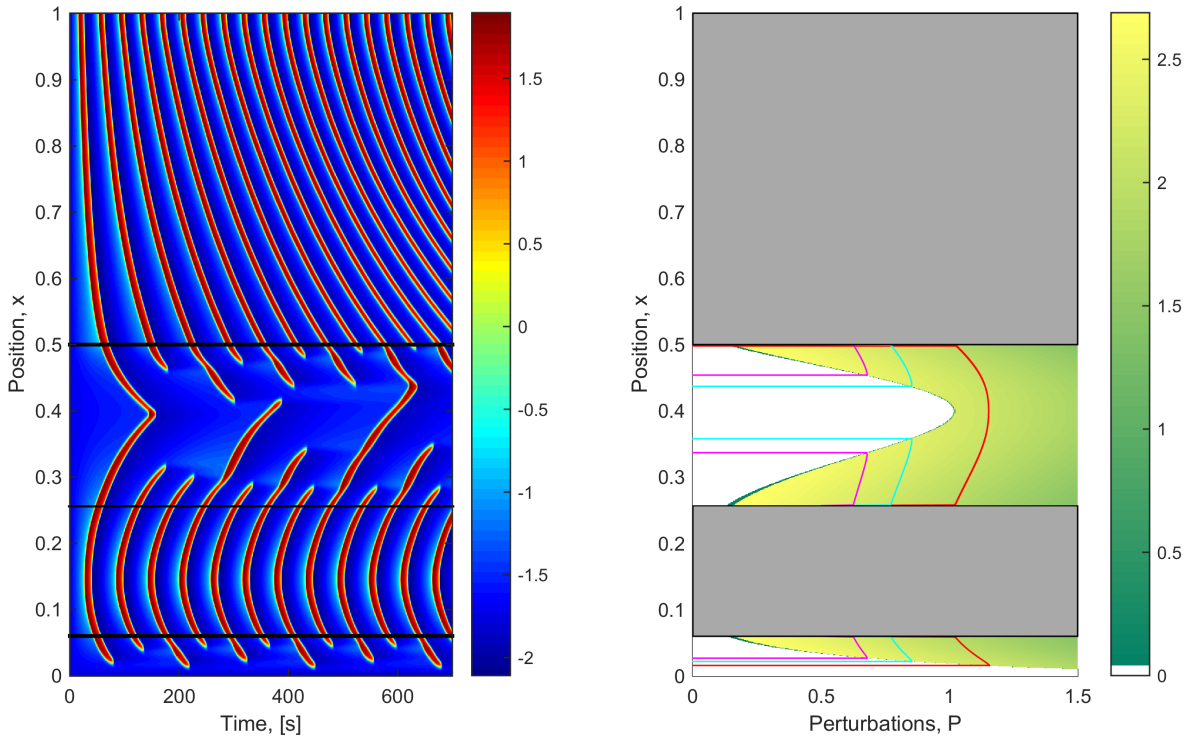

(a) Spatio-temporal solution *(b)* E-Profile with 3 E-Paths

Figure 8.19: Example 4: TM2: Cubic β profile (Figure 8.18) with $D = 5 \times 10^{-6} cm^2 s^{-1}$. (a) shows the associated spatio-temporal solution to the PDE (Section 6.3.2). (b) shows the E-Profile where the grey area indicated no possible E due to the oscillatory region. White indicates $E = 0$. Overlaid are the first three $\bar{\iota}$ (red, teal and magenta respectively) and their associated depths and predictions using Section 8.2.1.

Figure 8.19 shows clearly the interaction of the two excursions from $x = 0.5$ and $x = 0.259$ on both the spatio-temporal solution and the E-Profile. For $\bar{\iota} > 1$, similar to the Dupont model results, the prediction method is less reliable with a

greater error in depth prediction, indicating rapid changes in β negatively affect the prediction (E-Path) method.

8.4 Discussion

This chapter utilised the E-Path, described in Chapter 7, to predict three things: the depth of excursions, the maximum concentration of the excursions and the diffusion coefficient. Four examples of different $\beta(x)$ profiles that highlight different aspects of the process's reliability were explored in this chapter: one linear function, two step functions and a cubic function. The prediction method was accurate and reliable. In particular, for cases tested (excluding the extreme step $\beta(x)$ cases), the depth was accurate to a maximum spatial error of 1.1% and the diffusion coefficient was predicted with standard deviation of 1.85%.

The fourth example $\beta(x)$ profile (Figures 8.6, 8.13 and 8.19), perfectly described the interactions of excursions in the non-oscillatory region from two sources of initiation. This confirmed the robustness of the E-Path prediction method on the macroscale. Furthermore, the E-Profile only needs to be found once for any rearrangement of the $\beta(x)$ profile. This reduces re-computations and adds to the applicability of the method as the specific $\beta(x)$ profile does not need to be known at the start.

The depth prediction was accurate and reliable with the exception of three out of 36 cases due to the harsh $\beta(x)$ profiles used to exaggerate any downfalls. First, for the Goldbeter model Figure 8.4 (a-b) the excursion was predicted to reach a depth greater than the spatio-temporal solution showed. This occurred due to the concentration not yet having reached steady state, which reduced the effective perturbation enough to give an $E = 0$. This highlighted the influence of the recovery period (time to reach steady state) on the depth of excursions. The

second instance was in TM2 Figure 8.17 (c-d). The excursion was predicted to reach a depth greater than the spatio-temporal solution showed. The small error in the choice of f_1 was amplified by the sudden stepped change in the β profile and, thus, the sudden change in the E-Profile. Finally, the third instance was when the fourth β profile was used. Although the interaction of the opposing direction excursions (for $\bar{\imath} = 1$) was able to be predicted, subsequent depths (for $\bar{\imath} > 1$) reached obtained increasing error. It was determined that this was due to the rapid changes in the $\beta(x)$ profile predicting excursions of increasing error.

All of these exceptions only failed because of harsh $\beta(x)$ profiles were used to amplify any minor errors. These sudden changes in the $\beta(x)$ profiles are not expected in physiology (Section 1.3.1) and were only used to put the prediction method under extreme tests. The difficulty of the tests shows the reliability of the method to perform under difficult circumstances.

The second prediction investigated was the maximum concentration of the excursions over position. The maximum concentration prediction was found to be visually a rough estimate but deviated by an accumulated of error. The major cause was attributed to multiple combinations of E and P such that $E+P$ resulted in the same value on the E-Profile. Therefore caution is advised for use of the concentration approximation in further calculations. This prediction is, in fact, not a disadvantage of the E-Path method but rather a confirmation that the E-Path is approximating the right process.

It should be noted that the E-Path method is a discrete numerical approximation. The method is a numerical process as opposed to an analytical one, and a discrete method as opposed to a continuous approximation. The process is classed as discrete because it finds a perturbation (P) and passes it to the next position as opposed to Equation 5.4 which is continuous. Understanding these

differences allows for the best application of the E-Path process.

Finally, the diffusion coefficient could be predicted given a spatio-temporal solution and knowing the single cell dynamics. It was determined through a sample size of 100 randomly selected diffusion coefficients that it could be predicted to within $\pm 6\%$. This was displayed in Figure 8.7, which was computed for the Goldbeter model as an example. This relationship could be used to estimate the homogenised macroscale diffusion coefficient in an experimental application.

The main disadvantage to these predictions is the reliance on the f_1 function generated in Chapter 7. To generate the f_1 function, at least two solutions of the PDE set need to be computed. However, despite this disadvantage, the prediction method would drastically reduce the re-computation time for varying parameters. In particular, this methodology could eliminate the need to re-compute larger and more intricate NVU models for variations of the diffusion coefficient or $\beta(x)$ profiles. It may be possible to analytically link the f_1 equation and parameters to the single cell dynamics alone. Such a development would eliminate the need to solve the computationally expensive PDE set entirely.

8.5 Conclusion

This chapter investigated the prediction of three things: the depth of excursions, the maximum concentration over space of the excursions and the homogenised macroscale diffusion coefficient. The depth of the excursions, given the single cell dynamics and f_1, was found to be accurate to within $\pm 1.1\%$. This was determined to be a reliable prediction and useful in quantifying the area of 'cells' affected by oscillating concentrations. It was suggested for reliable predictions

that the $\beta(x)$ profile be limited in its gradient over the macroscale. The prediction method accurately predicted when excursions, initiated from different positions, would interact with each other over the macroscale. The maximum concentration over space was found to be a rough estimate, but not accurate enough for further calculations. This was attributed to instability in the E-Path where small changes in E resulted in significant changes in P. Finally, the diffusion coefficient could be predicted to within $\pm 6\%$ given the single cell dynamics, the f_1 relationship and a spatio-temporal solution to the PDE.

9 Concluding Remarks

9.1 Review

This research took 5 mathematical oscillatory models to compare and contrast. The models chosen were the Goldbeter model from Goldbeter et al. (1990), the Dupont model from Dupont and Goldbeter (1993), the Ermentrout model from Gonzalez-Fernandez and Ermentrout (1994), the FitzHugh-Nagumo model from FitzHugh (1961) and the Koenigsberger model from Koenigsberger et al. (2004). Asides from the FitzHugh-Nagumo model and the Koenigsberger model all the criteria to categorise the models as a SGOCM were met.

The FitzHugh-Nagumo model fits all the criteria, except it was originally designed to match the dynamics of a squid axon and not a cell. The model was still chosen since it not only created the right environment for a travelling wave by exhibiting oscillations over time, but also led the way in understanding when excursions of high concentration in the previously non-oscillatory region occurred. The Koenigsberger model was the most intricate of the 5 models because it was specifically designed for a SMC. However, the Koenigsberger model was still chosen because it was one of the simplest models to incorpo-

rate both conductance based modelling techniques and chemical reaction based modelling techniques (see Section 2.2.7).

This research sought to investigate the differences in the dynamics of these 5 SGOCMs and their effect upon the spatial arrangement with the addition of FD. The first comparisons made were done by their respective bifurcation diagrams using the continuation software AUTO. It was determined that all the models exhibited similar criteria:

- All the models produced an oscillatory region surrounded by two non-oscillatory regions on a variation of the bifurcation parameter.
- There existed two bifurcation points noted as the transition between the types of regions.
- The oscillatory region exhibited a period of oscillation which generally increased, over the bifurcation parameter, towards at least one of the bifurcation points. This bifurcation point was also labelled the 'lower bifurcation point' as it exhibited the lowest ionic calcium concentration in the cytosol (Z).
- This analysis additionally found that, excluding the lower bifurcation point of the Ermentrout model, all the bifurcations were Hopf bifurcations.

This basic comparison was necessary to compare multiple oscillatory models attempting to model similar components with often only minor mathematical differences. These models were compared by their core dynamics rather than a comparison for their accuracy in determining the ionic concentrations or accurate membrane potentials as this varies across cell types. This was useful to

compare reaction based modelling techniques against conductance based modelling techniques to model an oscillation over time.

The only disadvantages of this comparison was the selection of only 5 such models. There exist multiple more simple, and more intricate, mathematical models (some previously mentioned in Chapter 5) which exhibit oscillations that could yield vastly different results.

The comparisons within this research are extremely useful as they have all been carried out without bias in a consistent way. This allows for a quick detailed comparison between these oscillatory models to determine the best choice of model for the desired application and dynamics. Without this comparison the later results within this research could not have been found.

9.2 Wave Shape Theory

This research proposed a hypothesis that the wave shape of an ODE determines the presence of excursions. The wave shape was defined in Chapter 6 as one oscillation over time of the variable being diffused (near the bifurcation point where excursions would occur). This was related to the directional net flux of the ions in space because of the offset created by changing the period of oscillation. For excursions to occur the wave shape was required to be a Front Heavy (FH) asymmetric profile.

The FH asymmetric wave shape was further quantified as a FH-score. The quantification was found via an axiomatic argument that gave appropriate representations of the change in Φ over time due to diffusion. The FH-score was then tested against the full range of SGOCMs and, additionally, three toy models that were designed to exhibit specific behaviour. Since the hypothesis was shown to hold true for all applied cases and the FH-score was derived via a mathematical

approximation process, the hypothesis was labelled a theory.

The only perceived disadvantage to this theory is the dependence on the spatial stimulus function and the Excitability (E) of the neighbouring cells (Chapters 7 and 8). Thus, the theory must be used in combination with the E-Profile research completed in these chapters.

The theory proposed within this research is important as it allows the prediction of when excursions of high concentration in the previously non-oscillatory region will occur. The theory allows for an aim to modify the single cell dynamics of a region in order to either exhibit or repress excursions in the surrounding cells. This theory could, therefore, be applied to virtual mathematical models altering the dynamics of the ionic pathways, which could in turn also be applied to experimental models exhibiting this phenomena.

9.3 Excitability

Chapters 7 and 8 created and utilised a tool known as an Excitability Profile (E-Profile). The E-Profile determined a cell's potential Excitability (E) given the applied stimulus and the applied perturbation of the variable from its steady state value. Thus, the E-Profile was only generated for normally steady state solutions. Following this an E-Path was related to the depth of excursions and then in reverse utilised to predict the diffusion coefficient (given the single cell dynamics, f_1 and a spatio-temporal solution), or the depth and maximum concentration of the excursions (given the single cell dynamics, f_1 and the Wave Front Number ($\bar{\iota}$)).

It was found that the E-Profile alone explains how the excursions can propagate over space and why they are seen to stop at varying depths. The depth predictions were shown to be accurate to $\pm 1.1\%$ of the considered macroscale

length and the diffusion coefficient was able to be predicted accurately with a standard deviation of 1.8% of the true diffusion coefficient across a sample of 100 randomised diffusion coefficients. Additionally, the prediction of the maximum concentration over space was able to be given as a rough approximation.

A disadvantage to these predictions was the reliance on the f_1 function generated in Chapter 7. At least two solutions of the PDE equation set need to be computed to generate the f_1 function. However, despite this disadvantage, the prediction method would drastically reduce the re-computation time for varying parameters. In particular, this methodology could eliminate the need to re-compute larger and more intricate NVU models for variations of the diffusion coefficient or $\beta(x)$ profiles. It may be possible to analytically link the f_1 equation and parameters to the single cell dynamics alone (Section 7.7). Such a development would eliminate the need to solve the computationally expensive PDE equation set entirely.

The E-Profile tool was unseen in viewed previous literature. It allowed for a relationship between the bifurcation parameter (β), the added perturbation from steady state and the system's ability to excite before returning back to the steady state value. This tool can be utilised further in the understanding of oscillatory models and their willingness to be excited. Additionally, it gives the ability to predict the spatial behaviour of a system given the more easily obtainable single cell dynamics alone.

9.4 Future Work

As with any research, the journey is never over. As long as there are unanswered questions, research is never complete but rather can be rounded off into stages. Given the insights, tools and methods developed within this research there exist

unanswered question that could be developed upon further in future work. This future work can be separated into the two main outcomes of this research: The wave shape theory and the excitability research.

First, the wave shape theory, thus far, holds true for all tested cases. However, more research is desirable to solidify this theory.

- To further solidify the theory a more diverse range of mathematical models could be used. For example, the theory could be tested on more physiological models such as the the SMC model developed by Johny et al. (2015). Alternatively, the theory could be applied to larger NVU models of multiple cells such as by Farr and David (2011) or Dormanns et al. (2015). The application of more models would result in one of two outcomes: either the theory does not work which would be an area of investigation in itself, or the theory holds true and no additional information is obtained.

- It was mentioned within the research that the wave shape theory with the FH-score could be used as a target to modify the single cell dynamics in order to exhibit or repress the presence of excursions. This aim could be applied to the more physiological models, in particular, the chemical reaction based mathematical models (such as the Dupont model or the Koenigsberger model) to modify specific channel's reactions with the aim of suppressing excursions of high concentration into the previously non-oscillatory region.

- Following a successful adaptation of such a model this theory could be applied to an experimental application, in which these excursions are present, and attempt to suppress this behaviour.

Second, whilst the excitability research developed a new tool for understanding excursion propagation in a spatial medium, it could use additional research.

- The first investigation that follows the Excitability Path (E-Path) research would be to reformulate the f_1 equation. It is suggested that the f_1 equation be a function of percentage wave alignment or refractory period instead of the Wave Front Number ($\bar{\imath}$) to increase applicability of the equation. This process may not be easily obtainable given the relationship to the diffusion described.

- Following this, it would be useful if the constants described within the f_1 function were related to the original dynamics, thus eliminating the need to compute the PDE entirely. This connection, based upon no easily obtainable relationship, is expected by the author to not be straight forward and intricate in nature.

- Although the excitability method shows great promise in determining the depths of excursions on a 1D array of 'cells' this has yet to been converted into the more physiological 2D or 3D arrangement. This conversion would depend heavily on the connectivity between 'cells', their spatial arrangement, the stimuli function over space and the spatial assumptions made regarding the diffusion coefficient.

- Finally, it is desired that the excitability profile be externally confirmed via experimentation. Given that the E-Profile was proven integral to the propagation of waves, knowing the exact dynamics of cells under applied perturbations could lead significant advances in understanding of wave propagation. This would also indicate the most appropriate current physiological model.

Appendices

A Effect of Diffusion Rate

A.1 Goldbeter model

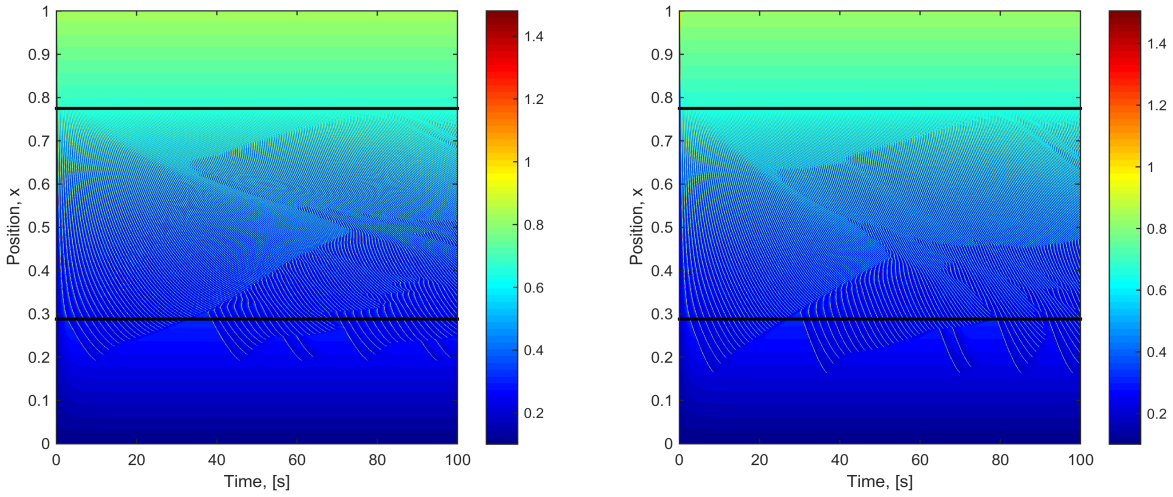

(a) $D = 2.5 \times 10^{-6}$

(b) $D = 5 \times 10^{-6}$

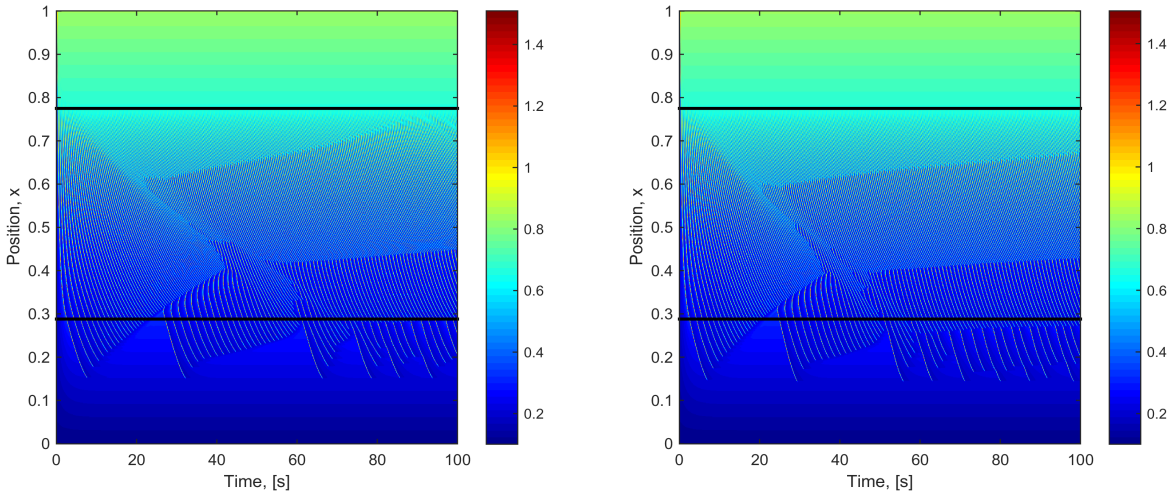

(c) $D = 7.5 \times 10^{-6}$

(d) $D = 10 \times 10^{-6}$

Figure A.1: Spatio-temporal solution to the Goldbeter model with increasing diffusion coefficient D $[cm^2 s^{-1}]$.

A.2 Dupont model

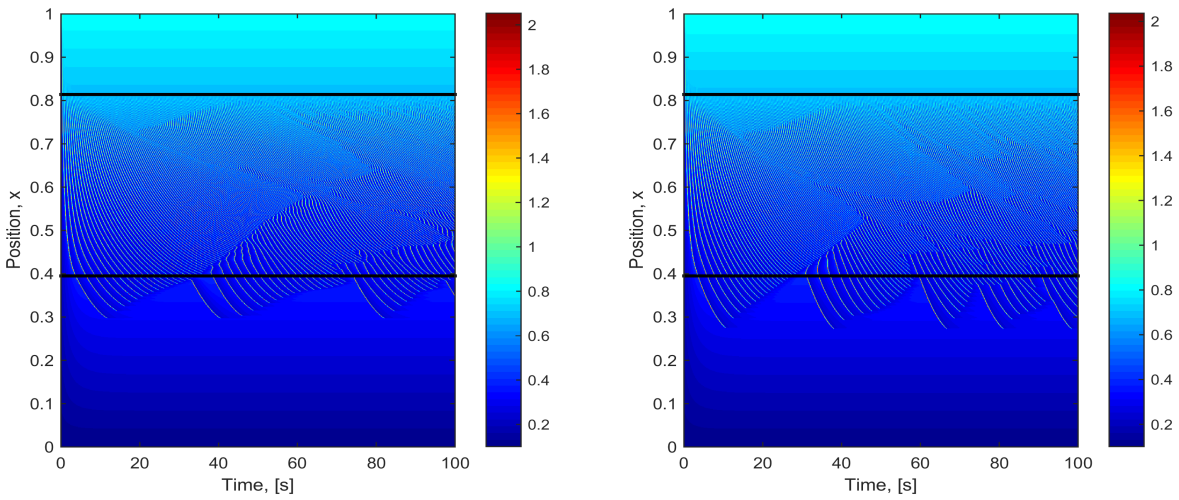

(a) $D = 2.5 \times 10^{-6}$ (b) $D = 5 \times 10^{-6}$

(c) $D = 7.5 \times 10^{-6}$ (d) $D = 10 \times 10^{-6}$

Figure A.2: Spatio-temporal solution to the Dupont model with increasing diffusion coefficient D $[cm^2 s^{-1}]$.

A.3 Ermentrout model

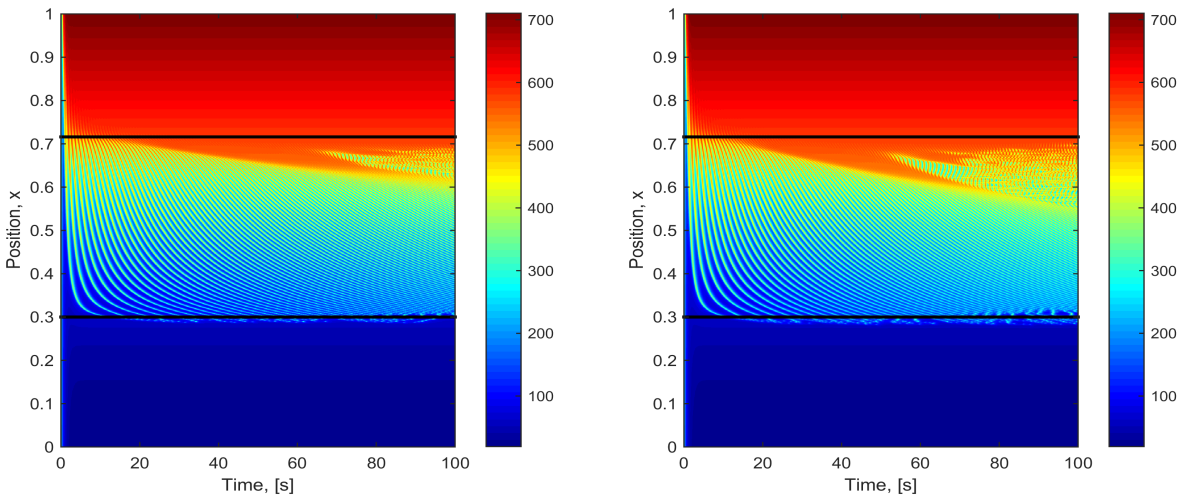

(a) $D = 2.5 \times 10^{-6}$ (b) $D = 5 \times 10^{-6}$

(c) $D = 7.5 \times 10^{-6}$ (d) $D = 10 \times 10^{-6}$

Figure A.3: Spatio-temporal solution to the Ermentrout model with increasing diffusion coefficient D $[cm^2 s^{-1}]$.

A.4 FitzHugh-Nagumo model- W

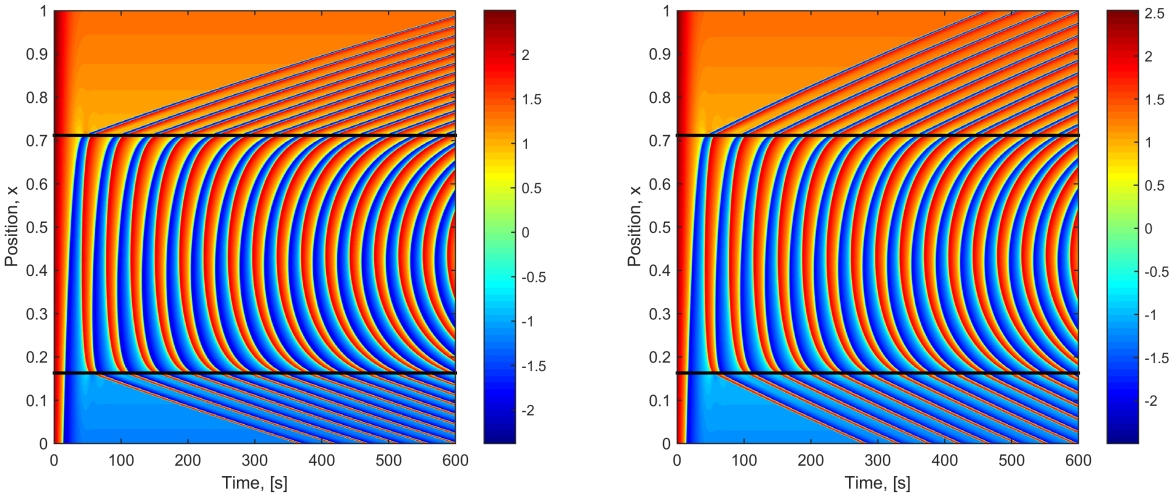

(a) $D = 2.5 \times 10^{-6}$

(b) $D = 5 \times 10^{-6}$

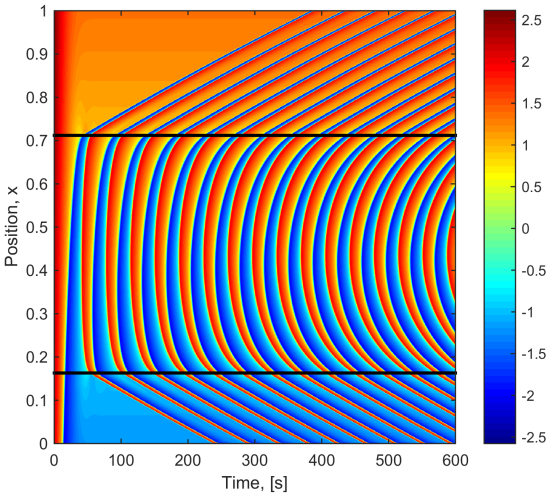

(c) $D = 7.5 \times 10^{-6}$

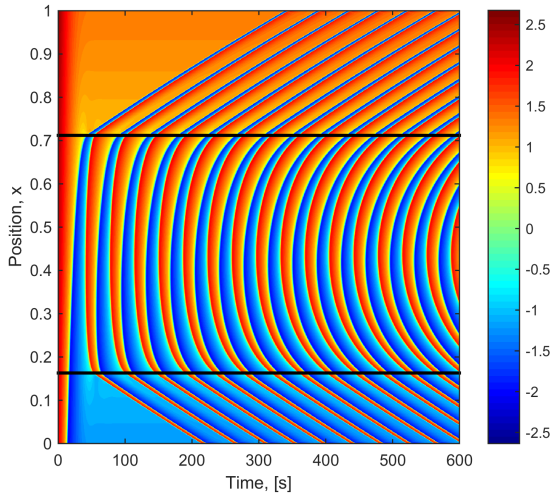

(d) $D = 10 \times 10^{-6}$

Figure A.4: Spatio-temporal solution to the FitzHugh-Nagumo model with increasing diffusion coefficient D [$cm^2 s^{-1}$].

A.5 FitzHugh-Nagumo model- U

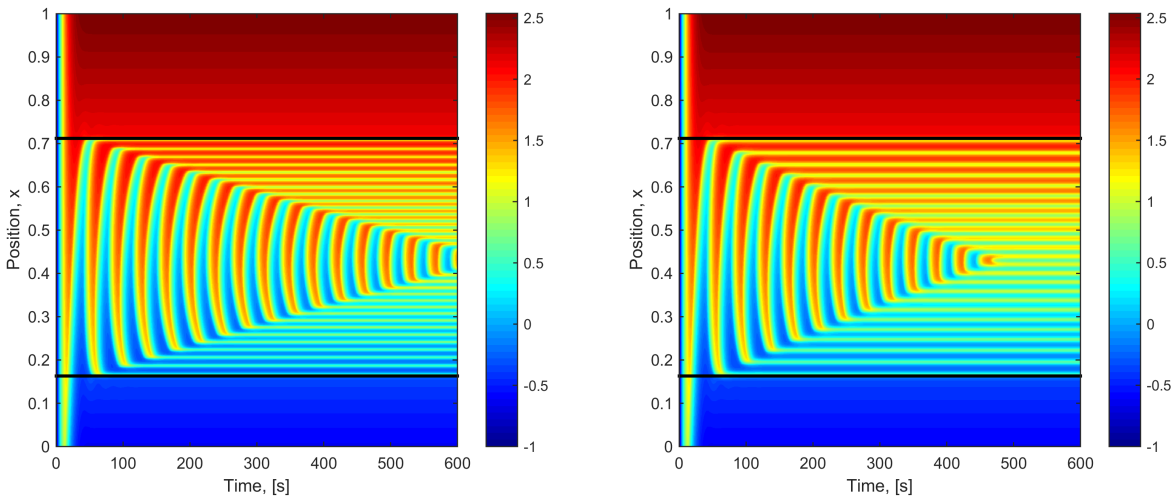

(a) $D = 2.5 \times 10^{-6}$

(b) $D = 5 \times 10^{-6}$

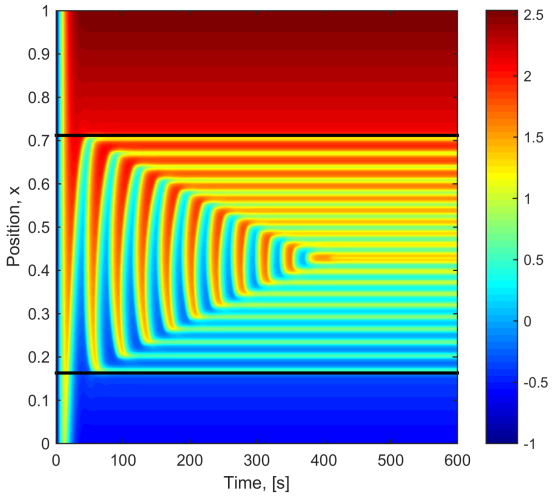

(c) $D = 7.5 \times 10^{-6}$

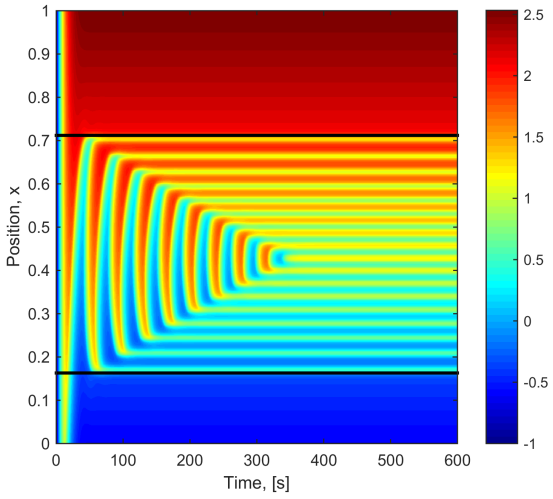

(d) $D = 10 \times 10^{-6}$

Figure A.5: Spatio-temporal solution to the FitzHugh-Nagumo model with increasing diffusion coefficient D $[cm^2 s^{-1}]$.

A.6 Koenigsberger model

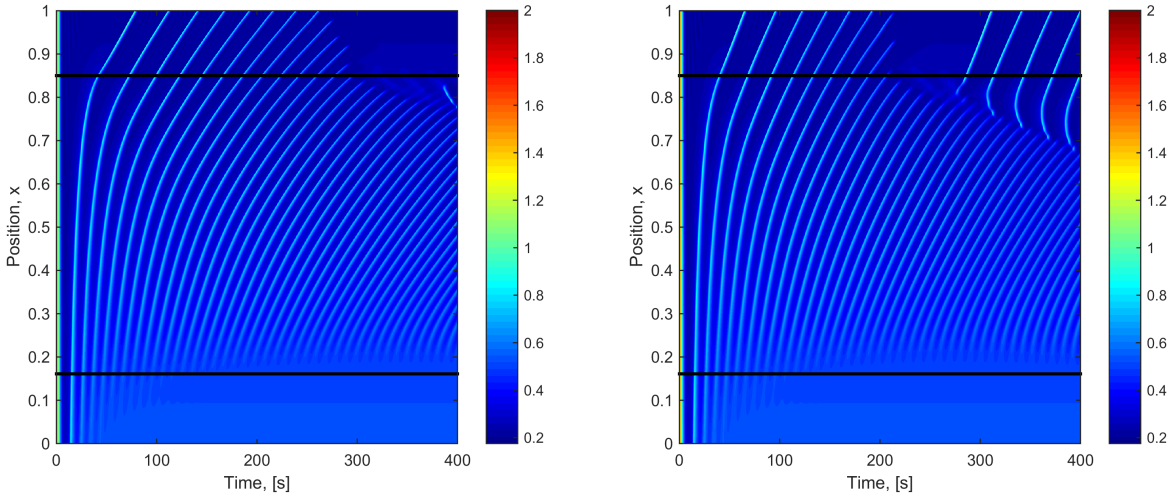

(a) $D = 2.5 \times 10^{-6}$ (b) $D = 5 \times 10^{-6}$

(c) $D = 7.5 \times 10^{-6}$ (d) $D = 10 \times 10^{-6}$

Figure A.6: Spatio-temporal solution to the Koenigsberger model with increasing diffusion coefficient D $[cm^2 s^{-1}]$.

B Example Importance of β Profile

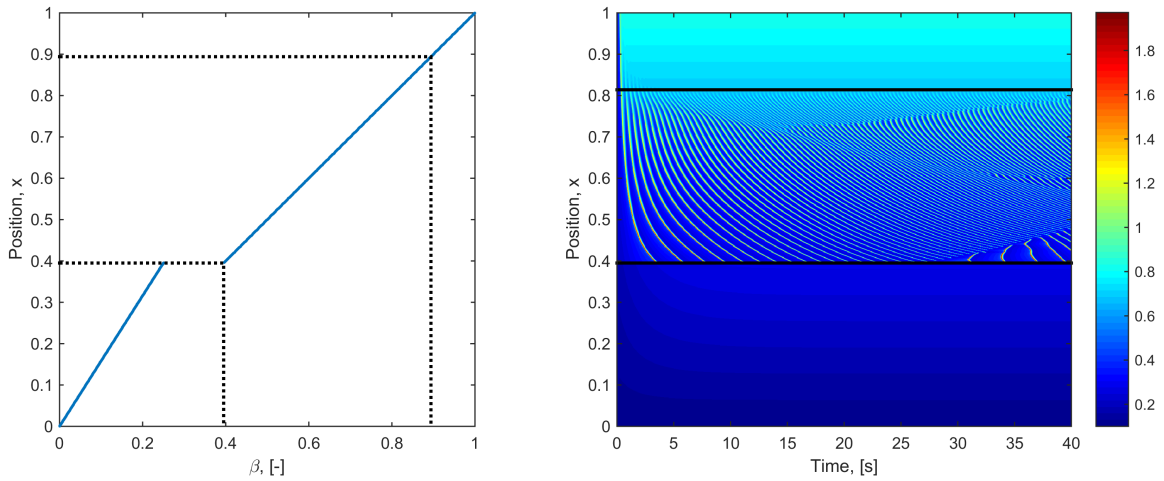

(a) $\beta(x)$ *(b)* Spatio-temporal solution

Figure B.1: Example showing importance of the $\beta(x)$ on excursions over space and time. Where the solid black line indicates the zero diffusion bifurcation point for the Dupont model and (b) shows that for this β profile no excursions occur in the previously non-oscillatory region.

C Stability Analytical Solution

Here described is the analytical analysis of the eigenvalues to determine the bifurcation points for Toy Model 2 (TM2) only. TM1 and TM3 have a similar analysis to TM2 and thus have been omitted. The process for these Toy models can be broken down into three phases: finding eigenvalues, removing impossible options and finding the transition (bifurcation point). The process of finding eigenvalues to determine stability is well documented, Roussel (2005) give one such explanation.

C.1 Finding Eigenvalues

For readability the equation set for TM2 is repeated here.

$$\frac{d\Phi}{dt} = \beta\Psi - \frac{\Phi^3}{3} + \Phi \quad \text{and} \quad \frac{d\Psi}{dt} = -(\beta\Phi + c) \tag{C.1}$$

First the fixed points are determined by setting the ODEs equal to zero.

$$0 = \beta\Psi - \frac{\Phi^3}{3} + \Phi \quad \text{and} \quad 0 = -(\beta\Phi + c) \tag{C.2}$$

Thus,

$$\Psi = \frac{1}{\beta}\left(\frac{\Phi^3}{3} - \Phi\right) \quad \text{and} \quad \Phi = -\frac{c}{\beta} \tag{C.3}$$

Next, the Jacobian matrix is found using Equation C.1.

$$\mathrm{J} = \begin{bmatrix} -\Phi^2 + 1 & \beta \\ -\beta & 0 \end{bmatrix} \tag{C.4}$$

The Jacobian matrix is then utilised to find the eigenvalues via Equation C.5.

$$Det(\lambda \mathrm{I} - \mathrm{J}) = 0 \tag{C.5}$$

$$Det \begin{bmatrix} \lambda + \Phi^2 - 1 & -\beta \\ \beta & \lambda \end{bmatrix} = 0 \tag{C.6}$$

Thus,

$$\lambda^2 + \lambda\left(\Phi^2 - 1\right) + \beta^2 = 0 \tag{C.7}$$

Using the quadratic formula the eigenvalues can be defined by Equation C.8

$$\lambda = \frac{-\left(\Phi^2 - 1\right) \pm \sqrt{\left(\Phi^2 - 1\right)^2 - 4\beta^2}}{2} = \frac{T \pm \sqrt{\Delta}}{2} \tag{C.8}$$

Therefore, the eigenvalues about the fixed point using Equation C.3 and Equation C.8 are defined by Equation C.9.

$$\lambda = \frac{-\left(\frac{c^2}{\beta^2} - 1\right) \pm \sqrt{\left(\frac{c^2}{\beta^2} - 1\right)^2 - 4\beta^2}}{2} = \frac{T \pm \sqrt{\Delta}}{2} \tag{C.9}$$

For a system of two variables the stability is directly related to the Trace (T) and the discriminant (Δ) from Equation C.9. This relationship is depicted in Figure C.1.

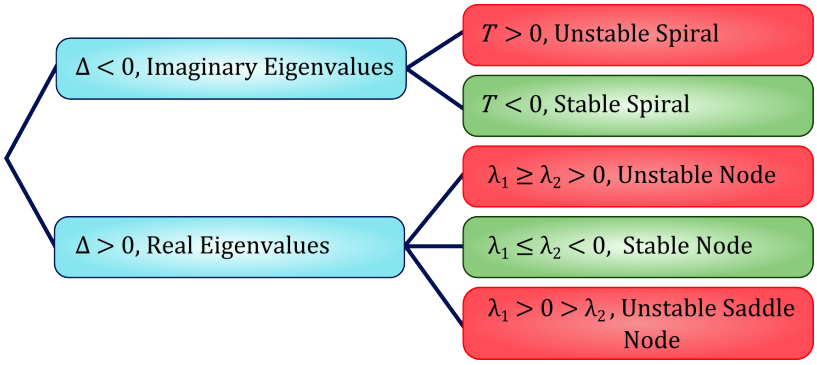

Figure C.1: Eigenvalues relationship to stability for two eigenvalues. T and Δ relate to Equation C.9. Red box indicates unstable, Green box indicates stable solution

C.2 Removing Impossible Options

Given Figure C.1 should the system not contain an eigenvalue that is both real and positive then the bifurcation point becomes the trivial solution described in Section C.3. This section will show that for $c = 0.2$ and $\beta > 0$, it is not possible for the system to be both real and positive. First for the system to be real the discriminant needs to be greater than zero, $\Delta > 0$. Thus, Equation C.10 must be true.

$$\left(\frac{c^2}{\beta^2} - 1\right)^2 - 4\beta^2 > 0 \tag{C.10}$$

Thus,

$$\frac{1}{\beta^4}\left(c^2 - \beta^2\right)^2 - 4\beta^2 > 0 \tag{C.11}$$

$$\left(c^2 - \beta^2\right)^2 - 4\beta^6 > 0 \tag{C.12}$$

$$c^4 - 2c^2\beta^2 + \beta^4 - 4\beta^6 > 0 \tag{C.13}$$

Finally, by rearranging Equation C.10 it can be found that Equation C.14 must be true.

$$\beta^6 - \frac{1}{4}\beta^4 + \frac{c^2}{2}\beta^2 - \frac{c^4}{4} < 0 \tag{C.14}$$

To determine when Equation C.14 is true as a function of β the critical points need to be found.

$$f(\beta) = \beta^6 - \frac{1}{4}\beta^4 + \frac{c^2}{2}\beta^2 - \frac{c^4}{4} \tag{C.15}$$

$$f'(\beta) = 6\beta^5 - \beta^3 + c^2\beta = 0 \tag{C.16}$$

$$\beta\left(\beta^4 - \frac{1}{6}\beta^2 + \frac{c^2}{6}\right) = 0 \tag{C.17}$$

$$\beta\left(\beta^2 - \frac{1}{10}\right)\left(\beta^2 - \frac{1}{15}\right) = 0 \tag{C.18}$$

Therefore, the critical points of Equation C.15 are as follows:

$$\beta = 0, \beta = \pm\sqrt{\frac{1}{10}}, \beta = \pm\sqrt{\frac{1}{15}} \tag{C.19}$$

Substituting the critical points (Equation C.19) back into Equation C.15 (with c = 0.2) gives the locations $(\beta, f(\beta))$ of the turning points:

$$\begin{array}{cc} & \left(0-4\times10^{-4}\right) \\ \left(\sqrt{\frac{1}{10}},1.185\times10^{-4}\right) & \left(-\sqrt{\frac{1}{10}},1.185\times10^{-4}\right) \\ \left(\sqrt{\frac{1}{15}},1\times10^{-4}\right) & \left(-\sqrt{\frac{1}{15}},1\times10^{-4}\right) \end{array}$$

Thus, because of the shape of a β^6 graph there is only two roots. These roots are symmetrical, therefore (β^2-a) is a factor.

$$(\beta^2-a)(\beta^4+b_1\beta^2+b_2)=0 \tag{C.20}$$

Thus,

$$\beta^6+(b_1-a)\beta^4+(b_2-ab_1)\beta^2-ab_2=\beta^6-\frac{1}{4}\beta^4+\frac{c^2}{2}\beta^2-\frac{c^4}{4} \tag{C.21}$$

By equating like terms the common factor term, a, can be found.

$$\begin{array}{lll} \beta^4: \quad (b_1-a)=-\frac{1}{4} & \therefore & b_1=a-\frac{1}{4} \\ \beta^2: \quad (b_2-ab_1)=\frac{c^2}{2} & \therefore & b_2=\frac{c^2}{2}+ab_1 \\ \beta^0: \quad -ab_2=-\frac{c^4}{4} & \therefore & a\left(\frac{c^2}{2}+a\left(a-\frac{1}{4}\right)\right)=\frac{c^4}{4} \\ & & \frac{c^2}{2}a+a^2\left(a-\frac{1}{4}\right)=\frac{c^4}{4} \\ & & a^3-\frac{1}{4}a^2+\frac{c^2}{2}-\frac{c^4}{4}=0 \end{array} \tag{C.22}$$

Finally, $a=0.0297416$ when $c=0.2$. Thus, the root is located at $\beta=\pm\sqrt{a}=\pm0.17246$. This means that the function is only ever less than zero on the interval $(-0.17246,0.17246)$, given the shape of a β^6 graph. Ie. the eigenvalue is real on the β interval $(-0.17246,0.17246)$. Next, the case of the eigenvalue

being positive ($\lambda > 0$) will be considered.

$$\frac{T \pm \sqrt{\Delta}}{2} > 0 \tag{C.23}$$

Therefore there exists two cases to be examined separately. The minus case will be examined first.

$$\begin{aligned} T - \sqrt{\Delta} &> 0 \\ -\left(\frac{c^2}{\beta^2} - 1\right) - \sqrt{\Delta} &> 0 \\ 1 - \frac{c^2}{\beta^2} - \sqrt{\Delta} &> 0 \\ 1 &> \frac{c^2}{\beta^2} + \sqrt{\Delta} \end{aligned} \tag{C.24}$$

Given that c and β are positive and $\sqrt{\Delta}$ needs to be defined as positive and real, c^2/β^2 must be less than or equal to 1, thus

$$\frac{c^2}{\beta^2} \leq 1 \quad \therefore \quad \beta \geq c \tag{C.25}$$

In this case since the eigenvalue is only ever real on the interval $(-0.17246, 0.17246)$ and $\beta \geq 0.2$ for the eigenvalue to be positive, it is not possible here for the eigenvalue to be both positive and real. Second, the plus case will be examined.

$$\begin{aligned} T + \sqrt{\Delta} &> 0 \\ \sqrt{\Delta} &> -T \\ \sqrt{\left(\frac{c^2}{\beta^2} - 1\right)^2 - 4\beta^2} &> \frac{c^2}{\beta^2} - 1 \end{aligned} \tag{C.26}$$

In order to square both sides, the knowledge that if $y < \sqrt{x}$ then $y^2 \cdot sign(y) < x \cdot sign(x)$ must be used. In this case y must be positive since it is real and we

have already shown that $\beta < c$ must be the case for both positive and real, thus:

$$\begin{aligned} \left(\frac{c^2}{\beta^2} - 1\right)^2 - 4\beta^2 &> \left(\frac{c^2}{\beta^2} - 1\right)^2 \\ -4\beta^2 &> 0 \\ \beta^2 &< 0 \end{aligned} \tag{C.27}$$

However, $\beta^2 \not< 0$, thus, for this model and $c = 0.2$ it is not possible for the model to both be real and positive.

C.3 Finding the transition (Bifurcation point)

Following this the only way for the model to transition between stable and unstable is for the trace to equal zero ($T = 0$). This will give the bifurcation point criteria.

$$\begin{aligned} T = 0 &= -\left(\frac{c^2}{\beta^2} - 1\right) \\ 0 &= \frac{c^2}{\beta^2} - 1 \\ \therefore \quad c &= \pm\beta \end{aligned}$$

Again since β is only considered positive, then the bifurcation will occur at $\beta = c$.

Bibliography

Anantharam, A., Tian, Y., and Palmer, L. G. (2006). Open probability of the epithelial sodium channel is regulated by intracellular sodium. *Journal of Physiology*, 574(2):333–347.

Bailey, R. (2017). ThoughtCo: Gyri and Sulci of the Brain.

Bartocci, E., Corradini, F., Entcheva, E., Grosu, R., and Smolka, S. A. (2008). CellExcite: An efficient simulation environment for excitable cells. *BMC Bioinformatics*, 9(SUPPL. 2):1–13.

Beeman, D. (2005). Introduction to Realistic Neural Modeling. *Brains, Minds and Media*, 2.

Biography.com (2014). *Santiago Ramón y Cajal . Epistolario*. PhD thesis.

Bygravel, F. L. and Benedetti, A. (1996). What is the concentration of calcium ions in the Endoplasmic Reticulum? *Cell Calcium*, 19:547–551.

Calcagno, C., Lobatto, M. E., Robson, P. M., and Millon, A. (2016). Vascular cells in blood vessel wall development and disease. *Diagn Microbiol Infect Dis.*, 28(10):1304–1314.

Champneys, A. R., Kuznetsov, Y. A., Paffenroth, R. C., Fairgrieve, T. F., Oldeman, B. E., and Wang, X. (2000). Auto 2000 : Continuation and Bifurcation Software. page 212.

Charles, A. (1994). Glia-Neuron Intercellular Calcium Signaling. *Dev Neurosci*, 16(3-4).

Cloud, G. C. and Markus, H. S. (2003). Diagnosis and management of vertebral artery stenosis. *QJM - Monthly Journal of the Association of Physicians*, 96(1):27–34.

Crank, J. (1975). *The Mathematics of Diffusion*. Clarendon Press, Brunel University Uxbridge, second edition.

Dani, J. W., Chernjavsky, A., and Smith, S. J. (1992). Neuronal activity triggers calcium waves in hippocampal astrocyte networks. *Neuron*, 8(3):429–440.

Dawson, S. P., Keizer, J., and Pearson, J. E. (1999). Fire-diffuse-fire model of dynamics of intracellular calcium waves. *Biochemistry*, 96(May):6060–6063.

Doi, S., Tanaka, M., Inoue, J., Pan, Z., and Tsumoto, K. (2010). *Computational Electrophysiology*. A First Course in In Silico Medicine. Springer Japan.

Dokos, S. (2017). Modelling Organs, Tissues, Cells and Devices.

Donaldson, I. M. L. (2010). Cerebri anatome: Thomas Willis and his circle. *Journal of the Royal College of Physicians of Edinburgh*, 40(3):277–279.

Dormanns, K. (2015). Computational models of neurovascular coupling. *Thesis*.

Dormanns, K., von Disseldorp, E., Brown, R., and David, T. (2015). Neurovascular Coupling and the Influence of Luminal Agonists via the Endothelium. *Journal of Theoretical Biology*, 364:49–70.

Drion, G., Franci, A., Seutin, V., and Sepulchre, R. (2012). A novel phase portrait for neuronal excitability. *PLoS ONE*, 7(8):1–14.

Dupont, G., Falcke, M., Kirk, V., and Sneyd, J. (2016). Models of Calcium Signalling.

Dupont, G. and Goldbeter, A. (1993). One-pool model for Ca2+ oscillations involving Ca2+ and inositol 1,4,5-trisphosphate as co-agonists for Ca2+ release. *Cell Calcium*, 14(4):311–322.

Dupont, G. and Goldbeter, A. (1994). Properties of intracellular Ca2+ waves generated by a model based on Ca(2+)-induced Ca2+ release. *Biophysical journal*, 67(6):2191–2204.

Endoh, T. (2004). Characterization of modulatory effects of postsynaptic metabotropic glutamate receptors on calcium currents in rat nucleus tractus solitarius. *Brain Research*, 1024(1-2):212–224.

Endresen, L. P., Hall, K., Hoye, J. S., and Myrheim, J. (1998). A Theory for the Membrane Potential of Living Cells.

Ermentrout, G. and Rinzel, J. (1996). Analysis of Neural Excitability and Oscillations.

Fabricius, M., Jensen, L. H., and Lauritzen, M. (1993). Microdialysis of interstitial amino acids during spreading depression and anoxic depolarization in rat neocortex. *Brain Research*, 612(1-2):61–69.

Falcke, M. (2003). On the role of stochastic channel behavior in intracellular Ca2+dynamics. *Biophysical Journal*, 84(1):42–56.

Fall, C. P., Marland, E. S., Wagner, J. M., and Tyson, J. J. (2002). Computational Cell Biology:. *Interdisciplinary Applied Mathematics, Springer.*, Vol. 20.

Farr, H. and David, T. (2011). Models of neurovascular coupling via potassium and EET signalling. *Journal of Theoretical Biology*, 286:13–23.

Feindel, W. (1962). Thomas Willis (1621-1675) - The Founder of Neurology. *Canadian Medical Association Journal*, 87:289–296.

Félétou, M. and San, R. (2011). *The Endothelium: Part 1: Multiple Functions of the Endothelial Cells - Focus on Endothelium - Derived Vasoactive Mediators.* Morgan & Claypool Life Sciences.

Fernández, V., Llinares-Benadero, C., and Borrell, V. (2016). Cerebral cortex expansion and folding: what have we learned? *The EMBO Journal*, 35(10):1021–1044.

Filosa, J. A. and Blanco, V. M. (2007). Neurovascular coupling in the mammalian brain. *Experimental Physiology*, 92(4):641–646.

Filosa, J. A., Morrison, H. W., Iddings, J. A., Du, W., and Kim, K. J. (2016). Beyond neurovascular coupling, role of astrocytes in the regulation of vascular tone. *Neuroscience*, 323:96–109.

FitzHugh, R. (1961). Impulses and Physiological States in Theoretical Models of Nerve Membrane. *Biophysical Journal*, 1(6):445–466.

Gerstner, W., Kistler, W. M., Naud, R., and Paninski, L. (2014). *Neuronal Dynamics: From single neurons to networks and models of cognition*. Cambridge University Press, UK.

Goldbeter, A., Dupont, G., and Berridge, M. J. (1990). Minimal model for signal-induced Ca2+ oscillations and for their frequency encoding through protein phosphorylation. *Proceedings of the National Academy of Sciences of the United States of America*, 87(February):1461–1465.

Gonzalez-Fernandez, J. M. and Ermentrout, B. (1994). On the origin and dynamics of the vasomotion of small arteries. *Mathematical Biosciences*, 119:127–167.

Greiner, W., Neise, L., and Stocker, H. (1997). *Greiner N - Thermodynamics and Statistical Mechanics*. Springer.

Guckenheimer, J. and Kuehn, C. (2009). Homoclinic orbits of the fitzhugh-nagumo equation: The singular-limit. *Discrete and Continuous Dynamical Systems - Series S*, 2(4):851–872.

Hackney, C. M. (2005). The Concentrations of Calcium Buffering Proteins in Mammalian Cochlear Hair Cells. *Journal of Neuroscience*, 25(34):7867–7875.

Hamdi, S., Schiesser, W. E., and Griffiths, G. W. (2007). Method of Lines , Part I : Basic Concepts Some PDE Basics. *Scholarpedia, 2(7):2859.*, 2:1–41.

Harris, F. E. (2014). Mathematics for Physical Science and Engineering. *Mathematics for Physical Science and Engineering*, pages 593–612.

Hawkins, B. T. and Davis, T. P. (2005). The Blood-Brain Barrier / Neurovascular Unit in Health and Disease. *Pharmacological reviews*, 57(2):173–185.

Herculano-Houzel, S. (2009). The human brain in numbers: a linearly scaled-up primate brain. *Frontiers in Human Neuroscience*, 3(November):1–11.

Hersh, R. (2013). *The Courant-Friedrichs-Lewy (CFL) Condition*. Springer Science+Business.

Hilborn, R. C., Brookshire, B., Mattingly, J., Purushotham, A., and Sharma, A. (2012). The transition between stochastic and deterministic behavior in an excitable gene circuit. *PLoS ONE*, 7(4).

Hodgkin, A. and Huxley, A. (1952). A quantitative description of membrane current and its application to conduction and excitation in nerve. *J Physiol*, (117):500–544.

Holloway, S. and Richardson, N. (2008). *Dynamics: Handbook of surface science*. Elsevier, first edition.

Hsu, C. H., Yang, T. H., and Yang, C. R. (2009). Diversity of traveling wave solutions in FitzHugh-Nagumo type equations. *Journal of Differential Equations*, 247(4):1185–1205.

Iadecola, C. (2017). The Neurovascular Unit Coming of Age: A Journey through Neurovascular Coupling in Health and Disease. *Neuron*, 96(1):17–42.

Jäkel, S. and Dimou, L. (2017). Glial Cells and Their Function in the Adult Brain: A Journey through the History of Their Ablation. *Frontiers in Cellular Neuroscience*, 11(February):1–17.

Johny, J., Plank, M. J., and David, T. (2015). *Self-regulation of agonist induced calcium dynamics by vascular smooth muscle cell*. PhD thesis.

Keener, J. and Sneyd, J. (2009). *Mathematical Physiology; I: Cellular Physiology*. Springer-Verlag New York, Inc., 2 edition.

Kenny, A., David, P. T., and Plank, M. J. (2016). Calcium Dynamics and Wave Propagation in Coupled Cells. Master's thesis.

Koenigsberger, M., Sauser, R., Lamboley, M., Bény, J.-L., and Meister, J.-J. (2004). Ca2+ dynamics in a population of smooth muscle cells: modeling the recruitment and synchronization. *Biophysical journal*, 87(July):92–104.

Kostova, T., Ravindran, R., and Schonbek, M. (2004). FitzhughNagumo Revisited: Types of Bifurcations, Periodical Forcing and Stability Regions By a Lyapunov Functional. *International Journal of Bifurcation and Chaos*, 14(03):913–925.

Krupa, M., Sandstede, B., and Szmolyan, P. (1997). Fast and Slow Waves in the FitzHugh Nagumo Equation. *Journal of Differential Equations*, 133:49–97.

Kwee, R. M. and Kwee, T. C. (2007). Virchow-Robin Spaces at MR Imaging. *RadioGraphics*, 27(4):1071–1086.

Lauritzen, M., Dreier, J. P., Fabricius, M., Graf, R., Hartings, J. A., and Strong, A. J. (2011). Clinical relevance of cortical spreading depression in neurological disorders: migraine, malignant stroke, subarachnoid and intracranial hemorrhage, and traumatic brain injury. *Clinical Neurophysiology*, 122(1):S15.

Liu, W. and Van Vleck, E. (2006). Turning points and traveling waves in FitzHugh-Nagumo type equations. *Journal of Differential Equations*, 225(2):381–410.

Lodish, H., Berk, A., Zipursky, S., and Al., E. (2000). *Molecular Cell Biology: Overview of Neuron Structure and Function*. New York, 4th edition.

Malmivuo, J. and Plonsey, R. (1995). *Bioelectromagnetism: Principles and Applications of Bioelectric and Biomagnetic Fields*. New York Oxford University Press, New York.

McConnell, H. L., Kersch, C. N., Woltjer, R. L., and Neuwelt, E. A. (2017). The translational significance of the neurovascular unit. *Journal of Biological Chemistry*, 292(3):762–770.

Metz, R. P., Patterson, J. L., and Wilson, E. (2011). *Vascular Smooth Muscle Cells: Isolation, Culture, and Characterization*. Humana Press, Totowa, NJ.

Michaelis, L. and Menten, M. L. (1913). Die Kinetik der Invertinwirkung. *Biochem Z*, 49(February):333–369.

Michiels, C. (2003). Endothelial cell functions. *Journal of Cellular Physiology*, 196(3):430–443.

Montagne, A., Zhao, Z., and Zlokovic, B. V. (2017). Alzheimer 's disease: A matter of blood - brain barrier dysfunction? *Journal of Experimental Medicine*, 214(11):3151–3169.

Morris, C. and Lecar, H. (1981). Voltage oscillations in the barnacle giant muscle fiber. *Biophysical Journal*, 35(1):193–213.

Nagumo, J., Animoto, S., and Yoshizawa, S. (1962). An active pulse transmission line simulating nerve axon. *Proc. Inst. Radio Engineers*, 50:2061–2070.

Nedergaard, M., Ransom, B., and Goldman, S. A. (2003). New roles for astrocytes: Redefining the functional architecture of the brain. *Trends in Neurosciences*, 26(10):523–530.

Nur Adila Faruk Senan (2017). A brief introduction to using ode45 in MATLAB.

O'Connor, J. P. B. (2003). Thomas Willis and the background to Cerebri Anatome. *Journal of the Royal Society of Medicine*, 96(3):139–43.

Pace, N., editor (2015). *Neurocritical Care in Anaesthesia : Prepare for the FRCA , 1st Edition*. Elsevier, Glasgow UK, 1st edition.

Parthimos, D., Edwards, D. H., and Griffith, T. M. (1999). Minimal model of arterial chaos generated by coupled intracellular and membrane Ca2+ oscillators. *The American journal of physiology*, 277(22):H1119–H1144.

Piccolino, M. (1998). Animal electricity and the birth of electrophysiology: the legacy of Luigi Galvani. *Brain research bulletin*, 46(5):381–407.

Purves, D., Augustine, G. J., Fitzpatrick, D., Katz, L. C., LaMantia, A.-S., McNamara, J. O., and Williams, S. M. (2001). *Neuroscience, 2nd edition*. Sunderland (MA): Sinauer Associates;.

Quarton, C. G., Melnechuk, T., and Schmitt, F. O. (1967). *The Neurosciences. A Study Program*. Rockefeller Univ. Press.

Raju, T. N. (1999). The Nobel Chronicles. *The Lancet*, 354:22205.

Roussel, M. R. (2005). Stability Analysis for ODEs. *Vorlesung*.

Sanderson, M. J., Charles, A. C., Boitano, S., and Dirksen, E. R. (1994). Mechanisms and function of intercellular calcium signaling. *Molecular and Cellular Endocrinology*, 98(2):173–187.

Sarmin, E. and Chudov, L. (1963). On the stability of the numerical integration of systems of ordinary differential equations arising in the use of the straight line method. *USSR Computational Mathematics and Mathematical Physics*, 3(6):1537–1543.

Scatliff, J. H. and Johnston, S. (2014). Andreas Vesalius and Thomas Willis: Their anatomic brain illustrations and illustrators. *American Journal of Neuroradiology*, 35(1):19–22.

Schumacher, K. and Friml, J. (2009). Cell biology by the numbers. *Current opinion in plant biology*, 12(6):651–652.

Schwiening, C. J. (2012). A brief historical perspective: Hodgkin and Huxley. *Journal of Physiology*, 590(11):2571–2575.

Serrano-López, R., Cuesta-López, S., Tapia-Júdez, O., and Fradera, J. (2013). Physics of non-steady state diffusion of lightweight atoms in a heavy atom matrix. Introducing an open-source tool for simulated-experiments in fluid mechanics.

Shampine, L. F. and Reichelt, M. W. (1997). The MATLAB ODE Suite. *SIAM Journal on Scientific Computing*, 18(1):1–22.

Sofroniew, M. V. and Vinters, H. V. (2010). Astrocytes: Biology and pathology. *Acta Neuropathologica*, 119(1):7–35.

Stern, M. D. (1990). Theory of Excitation-Contraction Coupling in Cardiac Muscle. *Biophysical Society*, 63:497–517.

Syková, E., Nicholson, C., and Sykova, Eva; Nicholson, C. (2008). Diffusion in brain extracellular space. *Physiological reviews*, 88(4):1277–1340.

The American Heritage (2007). The American Heritage® Medical Dictionary; synaptic cleft. (n.d.). *The American Heritage Medical Dictionary.*

Thul, R. (2014). Translating intracellular calcium signaling into models. *Cold Spring Harbor Protocols*, 2014(5):463–471.

Ustun, C. (2005). Erratum: NEUROwords: Dr. Thomas Willis' famous eponym: The circle of Willis. *Journal of the History of the Neurosciences*, 14(1):16–21.

Volpe, P., Villa, A., Podini, P., Martini, A., Nori, A., Panzeri, M. C., and Meldolesi, J. (1992). The endoplasmic reticulum-sarcoplasmic reticulum connection: distribution of endoplasmic reticulum markers in the sarcoplasmic reticulum of skeletal muscle fibers. *Proceedings of the National Academy of Sciences of the United States of America*, 89(13):6142–6.

Weerakkody, D. Y., Gaillard, A. F., and Al., E. (2017). Vertebral artery. *Radiopaedia*, rid: 4858.

Wilkins, M. and Sneyd, J. (1998). Intercellular spiral waves of calcium. *Journal of Theoretical Biology*, 191(3):299–308.

Zhao, Z. and Gu, H. (2017). Transitions between classes of neuronal excitability and bifurcations induced by autapse. *Scientific Reports*, 7(1):1–15.

Declaration

I declare that this dissertation is my own unaided work. It is being submitted for the degree of Doctor of Philosophy at the University of Canterbury. It has not been submitted for any other degree or examination in any other University.

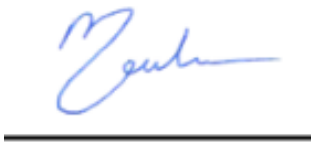

Michelle L. Goodman